On the Spatial Structure and Properties of Cold Neutral Hydrogen Gas In the Milky Way

Callum Lynn

A thesis submitted for the degree of

Doctor of Philosophy

The Australian National University

Research School of Astronomy & Astrophysics

April 2026

To my family, friends and mentors who have all guided me on this journey

Disclaimer

I hereby declare that the work undertaken in this thesis has been conducted by me alone, except where indicated in the text. I conducted this work between February 2022 and April 2026, during which period I was a PhD student at the Australian National University. This thesis, in whole or any part of it, has not been submitted to this or any other university for a degree.

This thesis has been compiled as a Thesis by Compilation in accordance with relevant ANU policies. The works are included as main chapters of this thesis as follows.

The first main chapter, Chapter 2, presents work from "Considerations with stacking absorption spectra: cold H I gas in cirrus region of the Milky Way" by C. Lynn, A. Marchal, N. M. McClure-Griffiths, Marc-Antoine Miville-Deschênes, C. E. Murray, H. Nguyen, J. Dempsey, E. Di Teodoro, J. Th van Loon, J. M. Dickey, M-Y. Lee, G. Joncas, Yik Ki Ma, N. M. Pingel, S. Stanimirović, I. Kemp, S. Gibson, and H. Dénes published in press in the Monthly Notices of the Royal Astronomical Society, 2025, MNRAS, 536, 4, 3538–3553. The work is presented exactly as in the publication, consisting of approximately 10,000 words. I worked alongside other members of the GASKAP-HI team to prepare and reduce the pilot survey data used in this work, including the GASKAP-HI emission map. I carried out all of the analysis, including the application of the spectral stacking and decomposition for H i emission-absorption sightlines. I have written the manuscript, with insightful feedback and suggestions from the co-authors.

The second main chapter, Chapter 3, presents the contents "Spatial structure of multiphase Galactic gas via structure functions of H I absorption and emission" by C. Lynn, N. M. McClure-Griffiths, A. Marchal, A. Seta, A. J. M. Thomson, Marc-Antoine Miville-Deschênes, H. Nguyen, J. Dempsey, J. Th van Loon, N. M. Pingel, G. Park, M-Y. Lee, B. Lee, D. Leahy, J. M. Dickey, G. Joncas, Yik Ki Ma, S. Stanimirović, I. Kemp, S. Gibson, H. Dénes, and K. Jameson, submitted to the Monthly Notices of the Royal Astronomical Society at the time of this writing. The work presented here is exactly as in the submission, consisting of approximately 10,000 words. I carried out all of the analysis, including the application of structure function code to the GASKAP-HI survey data set. I have written the manuscript, with insightful feedback and suggestions from the co-authors.

The third main chapter, Chapter 4, presents the contents "Spatial structure of the H I cold neutral medium in a Galactic Rayleigh-Taylor Instability: effects on H I phase decomposition with spatial resolution" by C. Lynn, N. M. McClure-Griffiths, A. Marchal, Marc-Antoine Miville-Deschênes, H. Nguyen, and N. M. Pingel, which is currently in preparation for submission to the Monthly Notices of the Royal Astronomical Society, and consists of approximately 7000 words at the time of writing. The H I emission data presented in this work was produced and imaged by the GASKAP-HI Survey Builders. I carried out all of the analysis, including the Gaussian decomposition of the H I emission field in this chapter and comparison with 3D dust maps. I have written the manuscript, with insightful feedback and suggestions from the co-authors.

On behalf of all the co-authors of these papers, I declare that I have made significant contribution to each of these journal articles and have written the text of the papers myself, except where indicated otherwise.

Callum Lynn

13 August 2026

Acknowledgements

It feels like only yesterday that a young Callum began the journey to pursue a PhD in Astronomy at the ANU. Yet at the same time, February 2022 feels like a lifetime ago, with the past four years filled with countless incredible memories and people I would love to thank. While that list would take an entire thesis in itself, I would especially like to express my gratitude to those who have played a significant role in assisting me complete this journey.

Firstly, I am deeply grateful to my primary supervisor, Naomi McClure-Griffiths. During my undergraduate studies at ANU six years ago, I first met Naomi when she taught my first undergraduate astronomy course, opening my eyes to studying astronomy academically. Since then, Naomi has been nothing but an incredibly supportive and patient supervisor. Whether I had questions about research, the world of conferences or simply life itself, she has been an invaluable mentor in shaping my research journey, as I grew from a young, naive and anxious undergraduate student, to a slightly less young, slightly less naive researcher. She has been an amazing role model, not just in terms of the kind of researcher I wish to be, but the kind of person I want to be.

I would like to thank Antoine Marchal, one of my supervisors who has been invaluable in assisting me and always being a source of great encouragement. His constant availability has been an immense source of comfort especially during periods where I felt I was falling behind, or when code or research questions required a second opinion. I am also grateful to my other supervisors, Marc-Antoine Miville-Deschênes, Hiep Nguyen, and Nickolas Pingel. Marc-Antoine hosted my visit to LPENS in Paris for a few months as part of my PhD, and his hospitality and research discussions were a major highlight in my degree. While not an official supervisor, I would also like to specifically thank Amit Seta, who has been an incredible source of knowledge with structure functions and turbulence of the interstellar medium.

More broadly I would like to thank the radio research group at ANU. The friendly atmosphere during meetings has been an amazing place to share research ideas and explore new research avenues. Visiting conferences together has always made talks, that would otherwise be nerve-wracking, more fun and enjoyable.

Outside of my research group, I am grateful for all of the other students of Mount Stromlo who have taken on this research journey alongside me. They have really made Stromlo a second home and have given me a sense of belonging. My office-mates, Maja and Lindsey, have been an immense comfort through the day-to-day life of my PhD, and I am not sure where I would be without their support.

Sabrina, despite only being at ANU for a few months, has become an invaluable friend and a great role model throughout my time here. I would also like to thank my other PhD friends, Neco, Marcie, Hye-Jin, Madi, Ben, Hilay, Sarah B., Bailey, Jamie, Shin-Jeong, Patrick, Zach, Eric, Neelesh, Jason, Sophie, Lewis, Daniela, Rafif, Diego, Fatma, Alex, Sarah A., Anell, Valentina, Bella, Lyla, Radhika, and Qianhui. Whether you were someone I met when I just started at Stromlo, or someone I met when compiling this thesis, I will always cherish the memories we've made together, from writing retreats and beach trips, to watching shows and movies together.

I am also grateful for my non-Stromlo friends, many of whom I met during our undergraduate time at ANU. Special thanks to Tiffany, who has been an incredible friend. The many laughs we have shared over the years during our study sessions and quests to find a functional soft-serve ice cream machine or find the nearest dog park have been some of my favourite University memories. I am immensely glad we stay in touch despite being halfway across the world from each other, and greatly enjoy our catch-ups when I attend conferences in Europe. I would also like to thank Murray, Piper, Emma, Rachael, Nick, Josh, Sophie, Jaxsen, Dylan, Lachie, and Julia. I will always be fond of the many boardgames nights and DnD sessions, and many TV show binge-watches that have been a great way to catch up as we all venture on different paths in life.

My family has been the main motivation for everything I do in life. This achievement is as much theirs as it is mine. I would like to thank my parents who have sacrificed so much to ensure me and my brother have obtained the lives we have. It's not everyday you get to say you love what you do for a living, and that is all thanks to my parents' tireless support. I am especially grateful for them always listening without exception to my late-night rants when research has gotten tough, helping me avoid the spiral of negative thoughts. I would also like to thank my brother, and I have greatly enjoyed the time we have spent together during my PhD, both online and in person. I am deeply grateful for my family always being by my side when I need it most.

Abstract

The formation of stars is still one of the most illusive problems in modern astrophysics. Currently, despite its long period of study, there still remains no consensus on the dominant processes that control the rate of star formation. Neutral hydrogen (H I), being the most abundant element in the Universe, provides an important tracer, both for large scale galactic morphology and as the fundamental building block of stars. With this in mind, improving our knowledge of the physical properties of H I and its transition between warm and cold phases is key to understanding the cycle of star formation and chemical enrichment in the Milky Way. Despite ongoing efforts, there still remains great uncertainty on the physical properties of cold and warm H I due to observational constraints of previous surveys. Presented here in this thesis are attempts to address questions surrounding the phase distribution and spatial structure of H I through detailed analysis of H I absorption and emission of the Milky Way from the Galactic Australian Square Kilometre Array Pathfinder H I Survey (GASKAP-HI).

The first component of the thesis makes use of the unparalleled source density of the Australian Square Kilometre Array Pathfinder (ASKAP) radio telescope, using the ~ 500 sightlines where H I 21-cm absorption was detected in the Milky Way at high Galactic latitudes, and the ~ 200 sightlines with no detections. From these sightlines, the signal-to-noise is reduced through stacking sightlines to detect warmer temperature gas in absorption. A warmer phase of gas was detected with a temperature of ~ 1300 K gas ubiquitous throughout the region, along with a lack of temperature variation spatially across the plane-of-sky. The work also provides a test for the efficacy of stacking H I spectra to detect higher temperature gas useful for future studies, determining that stacking, while producing lower limits on optical depth measurements, still allows for accurate measurements of temperature for components previously hidden under noise.

For the second component of the thesis, I have analysed the spatial variation of neutral hydrogen cold gas density across the plane-of-sky through computing structure functions of the detected GASKAP-HI absorption sightlines. Since the combination of absorption and emission data allows for a complete picture of the radiative transfer process, we were able to study the spatial structure of both the cold and warm phases of neutral hydrogen in a more accurate way compared to previous attempts relying solely on H I emission where separation of the phases is less trivial. We found that the warm and CNM follow different power-law slopes (2-D power spectrum slopes of -2.6 vs -2.3 respectively), with both phases following slopes shallower than that of Kolmogorov turbulence (-3.6). The CNM has a shallower

slope due to more power existing on smaller spatial scales, where the cold gas is formed through condensation and shocks. Since the combination of emission and absorption sightlines allows for the computation of spin temperatures, I have also, for the first time, calculated the structure function of temperature of cold H I gas across the plane-of-sky. We found the structure function slope of the spin temperatures to be flat, implying that the temperature of cold gas is random across the plane-of-sky, and not tied to any specific physical H I structures. While this result requires higher sensitivity observations to confirm, the randomness of H I spin temperatures has also been observed in other fields such as when measuring H I temperature as a function of Galactic radius. Comparing with MHD simulations, we find that the flatness of the structure function may indicate potential uncharacterised errors in the calculation of spin temperatures, and the need for a review of the currently accepted method for estimating temperatures for potential improvements.

For the final portion of the thesis, I present work focussed on characterising instabilities found in the H I emission data within the survey range of GASKAP-HI. Through Gaussian decomposition tools such as ROHSA, I was able to separate out spatially coherent maps of the individual neutral H I phases. While not as accurate as the combination of emission and absorption sightlines, this method offers a good estimation for a spatially resolved map of the cold and warm neutral medium to study their interactions, something which discretised absorption data is unable to obtain. The cold gas is concentrated within small scale structures undergoing Rayleigh-Taylor instabilities, buried within a large-scale Galactic filament, with the warmer, more diffuse phases of H I gas enveloping the structure. The mean CNM mass fraction of the filament is approximately 0.14 ± 0.11. Using the correlation between H I and dust to estimate physical distances to the structure, two wavelength scales of the Rayleigh-Taylor instabilities are observed, with average size-scales of 4 and 0.9 parsecs respectively. The work also investigates the effects of resolution on estimating cold gas mass fractions, since extra-galactic observations lack the spatial resolution of Milky Way surveys. Through convolving the field and applying ROHSA Gaussian decomposition, I find the average mass fraction of gas pertaining to the instability does not vary with spatial resolution, while the maximum mass fraction along a line-of-sight decreases with decreasing spatial resolution, likely due to beam smearing effects. The decomposition does not detect CNM mass fractions as high as other Galactic H I absorption surveys, due to having lower resolution than the point-source resolution of absorption sightlines. The results confirm the reliability of mean cold gas mass fractions made of gas in extragalactic bodies, despite not fully resolving the small-scale cold gas structures. However, the lack of a plateau in peak CNM mass fraction towards high spatial resolution suggests the small-scale structure of the CNM exists on scales smaller than the current physical resolution of ~ 0.03 parsecs.

Contents

List of Figures

List of Tables

Chapter 1

Introduction

"I know that I am mortal, a creature of a day; but when I search in the multitudinous revolving spirals of the stars my feet no longer rest on the earth, but, standing by Zeus himself, I take my fill of ambrosia, the food of the gods."

- Claudius (Ptolemy) Ptolemaeus (100–170 CE)
Anthologia Palatina (9.577)

1.1 The Interstellar Medium

The interstellar medium (ISM) comprises of the matter that lies between the stars residing in our Galaxy. The matter of the ISM is a combination of gas, dust grains and cosmic ray particles. Of the gas, approximately 71% is hydrogen, 28% is helium and the remainder being heavier elements.

The ISM within our Galaxy contains a wide range of temperatures and densities, driven by local differences in heating and cooling mechanisms and dynamical processes. Within this wide range, observations have classified the ISM into distinct phases based on chemical and physical properties. The ISM can be categorised into five over-arching phases based on chemical and physical properties: the hot inter-cloud medium (HIM), warm ionised medium (WIM), atomic warm neutral medium (WNM), atomic cold neutral medium (CNM) and molecular gas. These physical properties of each phase are approximately described in Table 1.1.

In this thesis the primary focus is the transition between the WNM and CNM. The WNM is known to be the diffuse, volume-filling fraction of the ISM, containing roughly 32−64% of the Galaxy's H I mass, and $\sim 30\%$ of the ISM's volume (McClure-Griffiths et al. 2023). The kinetic temperature of the warm gas ranges from $4000 - 8000$ K, with densities of around 0.5 cm^{-3}. The CNM, on the other hand, ranges from $25 - 250$ K in temperature, and fills only $\sim 1 - 4\%$ of the ISM's volume.

Table 1.1: Properties of the phases of the ISM (Tielens 2005)

Phases	T (K)[a]	n_H (cm^{-3})[b]	ϕ_V (%)[c]	H (pc)[d]	Gas State
HIM	10^6	0.003	50%	3000	Ionised
WIM	8000	0.1	25%	900	Ionised
WNM	8000	0.5	30%	220	Neutral Atomic
CNM	80	50	1%	94	Neutral Atomic
Molecular	10	> 200	0.05%	75	Molecular

[a]Typical kinetic temperature
[b]Typical gas number density
[c]Volume Filling Factor, which have typically large uncertainties
[d]Gaussian scale height.

However with its higher density of ~ 50 cm^{-3} (Wolfire et al. 2003), the CNM's mass fraction is only slightly less than that of the WNM, at around $28 - 40\%$ of the mass of Galactic H I. While the CNM is typically described as "clouds" for educational purposes, the cold gas of the Galactic ISM is found to be ubiquitous, forming sheets and filaments (Gibson 2002; Heiles & Troland 2003). Between the two phases of the WNM and CNM lies a thermally unstable portion of gas named aptly the unstable neutral medium (UNM), but also referred to as the lukewarm neutral medium (LNM). With temperatures of $250 - 4000$ K (Heiles & Troland 2003; Roy et al. 2013b; Murray et al. 2015; McClure-Griffiths et al. 2023), the UNM forms $\sim 20 - 28\%$ of the H I mass in the Solar Neighbourhood. The temperature ranges and percentage masses for the H I phases are summarised in Table 1.2.

Each of these phases constitute distinct stages of the baryon cycle, a path by which gas is recycled within galaxies and star formation is regulated. Warm ionised material eventually cools to become neutral. This warm neutral medium cools further through a mixture of turbulence and dynamical processes such as colliding flows to become unstable, before forming the denser cold neutral medium, forming large scale filaments and sheets (Audit & Hennebelle 2005; Hennebelle et al. 2008; Vazquez-Semadeni 2012; Saury et al. 2014; Kobayashi et al. 2023). In regions with enough shielding from UV radiation of massive stars, the cold neutral gas can be dense enough to combine into molecular hydrogen, the building block from which stars form. The stars live out their lifespans before inevitably releasing their material upon their death via supernovae explosions. The ionised gas from these stars is released out into the ISM for the cycle to repeat. Despite molecular hydrogen being the direct fuel for stars, each step of the baryon cycle is an important regulator for their creation and by extension, so is every phase of gas.

Table 1.2: Properties of the phases of the H I (McClure-Griffiths et al. 2023)

H I Phase	T (K)[a]	ϕ_M (%)[b]
CNM	25 – 250	28 – 40
UNM	250 – 4000	20 – 28
WNM	4000 – 8000	32 – 64

[a]Kinetic temperature Range
[b]Typical Mass Fraction Range in ISM

1.2 The Phases of Neutral Hydrogen (H I)

The thermodynamic properties of neutral hydrogen are best defined by the balance between heating and cooling mechanisms from both radiative and dynamical processes. The heating rate per unit volume for a gas with number density n is described mathematically as $n\Gamma$ (erg cm^{-3} s^{-1}), where Γ is the heating function, independent of temperature and density of the gas (to first-order approximation). The cooling mechanisms of the ISM are ultimately produced via the collision of particles radiating energy. As a result, the cooling rate is more strongly dependent on density than the heating rate, and can be defined by $n^2\Lambda(T)$ (erg cm^{-3} s^{-1}), where $\Lambda(T)$ is the cooling function, which is a function of the temperature of the gas. Regions of thermal equilibrium are found through the balance of the heating and cooling rates. As the cooling rate is dependent on temperature, the thermodynamic equilibrium of the ISM is therefore also temperature dependent. The heating and cooling rates of different sources as a function of density are shown in Figure 1.1.

The dominant heating process at all densities where hydrogen is in its neutral state is photoelectric heating from small dust grains and larger molecules, such as polycyclic aromatic hydrocarbons (PAHs) (Field 1965; Wolfire et al. 1995, 2003). Towards the higher densities, H_2 heating also plays a role (Bialy & Sternberg 2019). At lower densities, where WNM typically exists, cosmic rays and X-ray heating become the significant components in the heating of the ISM. The responsible radiation for the photoelectic effect and heating stems from far-ultraviolet photons with energies < 13.6 eV, which is below the energy threshold for ionising neutral hydrogen atoms.

The dominant cooling processes of the ISM however are more diverse, but all involve converting the kinetic energy of the gas into radiation. For H I, cooling is driven by spectral line emission from collisionally excited transitions, mainly the fine structure transitions emitted in the far-infrared. For the CNM at cooler temperatures, the dominant cooling source is the fine structure line of CII at 158 μm. Towards the higher densities of CNM, the spectral lines of CI at 370 μm and 609 μm become

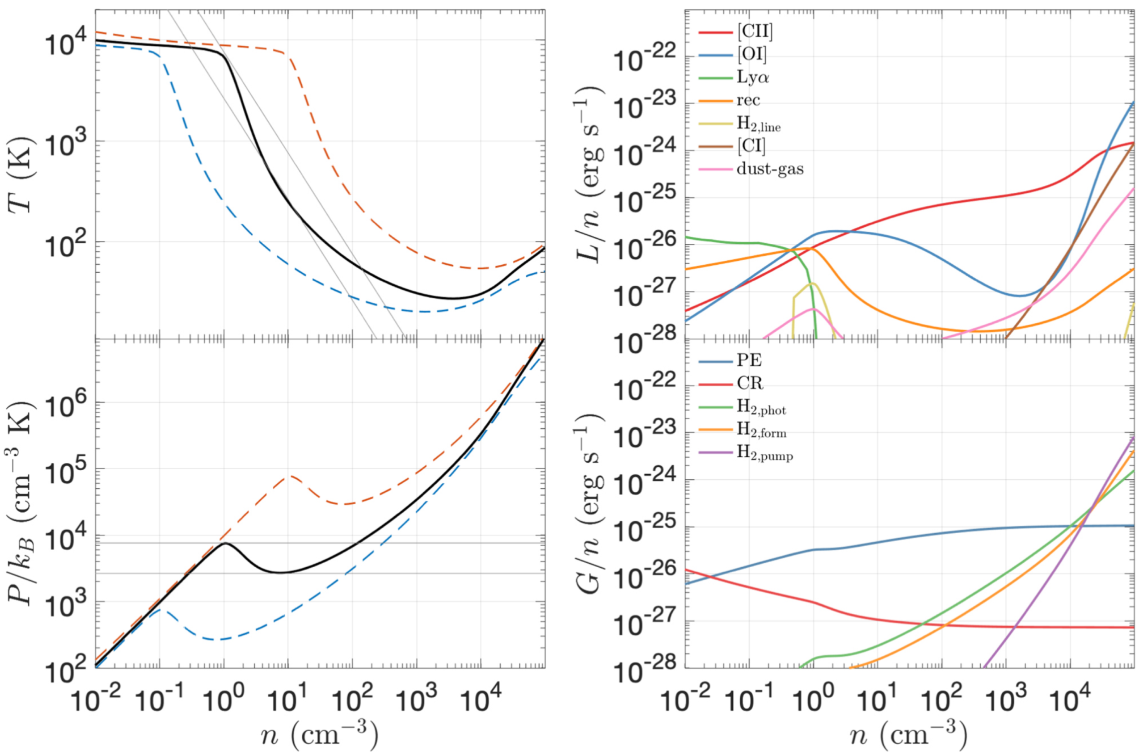

Figure 1.1: The temperature (top left), pressure (bottom left), heating rates (top right) and cooling rates (bottom right) per hydrogen atom as a function of volume density (taken from Bialy & Sternberg 2019). The solid lines assume a solar metallicity and UV radiation intensity of 1 (relative to Galactic levels) and ionisation rate per hydrogen atom of $\zeta_{-16} = \frac{\zeta}{10^{-16}\,\mathrm{s}^{-1}} = 1$. The grey diagonal and horizontal lines in the temperature and pressure diagrams respectively highlight the maximum and minimum pressure for a medium where both CNM and WNM can co-exist. The dashed red and blue lines show functions for UV radiation intensity of 0.1 and 10 relative to Galactic levels and ionisation rates of $\zeta_{-16} = 0.1$ and $\zeta_{-16} = 10$ per hydrogen atom, respectively.

increasingly more effective, along with H_2 cooling (Bialy & Sternberg 2019). For the WNM at higher temperatures but still below 8000 K, the CII and OI fine structure lines are the main sources of cooling. Towards even lower densities, recombination lines and emission of H I Lyman-α lines become important. Since the cooling processes mentioned all involve collisions, their cooling rates are proportional to the gas density squared (n^2).

Through the balance between heating and cooling processes, phase diagrams of the temperature and pressure of the ISM in thermal equilibrium can be produced, shown also in Figure 1.1. Several theoretical studies have described the multiphase nature of the ISM. The work from Field (1965) explored the initial framework to describe the criteria for thermal instabilities within the ISM. Later, Wolfire et al. (1995) and Wolfire et al. (2003) modelled heating and cooling mechanisms to study thermal equilibrium within the ISM. The phase diagram of pressure as a function of density displays a function with two positive gradient regions and one negative. Above this function, cooling is the dominant mechanism over heating, and below this function heating processes dominate. The positive-gradient regions ($dP/dn > 0$) correspond to the two stable phases of H I, with the CNM and WNM at higher and lower densities, respectively. Both phases are also able to co-exist in a narrow range of thermal pressures, with the maximum, $P_{\rm max}$, determined by the warm section, and the minimum, $P_{\rm min}$, determined by the cold section. The minimum and maximum pressures for a multiphase medium to exist are such that $P_{\rm max} \leq 3P_{\rm min}$ Field et al. (1969). For the solar neighbourhood, the stable pressure range where both CNM and WNM can co-exist is found to be $1500 < P_k < 10^4$ cm^{-3} K, with the upper limit lying closer to around 3000 cm^{-3} K (Field et al. 1969; Wolfire et al. 2003). Beyond this region, if $P > P_{\rm max}$, all gas is CNM, and if $P < P_{\rm min}$, all gas is WNM.

The phase diagram displayed in Figure 1.1 also shows functions for differing ionisation rates, highlighting that even if properties of the ISM differ from that of the local Solar neighbourhood, the phase diagrams always show a characteristic “bump”. This ”bump” is a local maximum where the gradient changes direction, forming a negative gradient portion ($dP/dn < 0$), spanning over different densities depending on the specific properties of the region of the ISM in question. For example, with lower metallicities (e.g. around 0.1 Solar), or if dust abundance is reduced by a similar amount, the photoelectric heating is less effective, leading to a shift in the equilibrium function where CNM exists at lower temperatures (Bialy & Sternberg 2019). The negative-gradient branch corresponds to gas from the unstable phase, whereby any perturbation from the thermal equilibrium line quickly push the gas to either of the two stable phases, depending on if there is more heating or cooling in the local environment. It should be noted the neutral phases of the CNM, UNM and WNM are not true thermodynamic phases, which require free-energy minimisation to separate, but are instead quasi-phases arising from the balance between heating and cooling mentioned above. However, the term "phase" has been used as the traditional nomenclature for these categories of gas since their discovery.

1.2.1 The Formation of Cold Gas

One major caveat to the theoretical models described earlier for heating and cooling in the ISM is that they are static in nature (McKee & Ostriker 1977; Wolfire et al. 2003; Bialy & Sternberg 2019). This means they ultimately lack a full description on the origin of the density fluctuations required to trigger thermal instabilities that form the UNM, and hence the CNM in the first place. Some theories as to the main drivers of CNM formation include colliding flows, compression of the WNM through thermal instabilities, and turbulence. Due to the complex nature of the ISM, it is likely these different processes all work together but at different scales. As the cooling of warm diffuse gas is a pivotal step in the formation of over-densities which lead to star formation (Ostriker et al. 2010; Clark et al. 2012), understanding the mechanisms which produce the CNM is critical to our understanding of the evolution of galaxies on both short and cosmological time-scales.

Due to the number of dynamical processes involved in the ISM, numerical simulations are often required to probe the mechanisms which lead to the production of the CNM. Early simulations demonstrated that compression of the WNM in a converging flow can trigger the phase transition and formation of cold structures in H I (Hennebelle & Pérault 1999, 2000). More recent simulations have also found compression to assist in stabilising the pressure regime of environments to where WNM and CNM can co-exist (Kim & Ostriker 2017; Hill et al. 2018). Convergence has been shown to naturally occur in compressible trans-sonic flows, triggering local condensation so long as the fluid is thermally bi-stable (Porter et al. 1994). The compression of the WNM in this scenario (assuming the flow is transonic) increases the density such that gas cools rapidly to merely tens of degrees. Kelvin-Helmholtz and Rayleigh-Taylor instabilities then fragment these cold gas pockets further into smaller clumps of gas, with sizes on the order of 0.1pc (Audit & Hennebelle 2005; Heitsch et al. 2006). Beyond this, thermal equilibrium is provided by the ram pressure and thermal pressure of the enveloping WNM. Under some circumstances the compression will force the density to increase to the conditions found in molecular clouds (Vázquez-Semadeni et al. 2006; Banerjee et al. 2009). The works mentioned increased the density of the WNM through a sustained ram pressure, which is hard to physically justify within the environment of the ISM. Other methods of producing pockets of CNM include shock waves propagating into the WNM, with thermal instabilities faster than the duration of the shock forming instances of the CNM in the post-shock region (Koyama & Inutsuka 2000, 2002).

Turbulence is a main driver for the evolution of the ISM (McKee & Ostriker 2007) and plays an important role in the condensation of H I gas. Currently, turbulence is thought to be injected and driven on a wide variety of spatial scales, before cascading down to smaller scales. This theory is supported by the fractal structure of the ISM (Stutzki et al. 1998; Stanimirovic et al. 1999; Elmegreen et al. 2001). Studies have found that large scale injection of turbulence can be produced by the accretion of the circumgalactic medium of galaxies and with other galactic-scale instabilities (Klessen & Hennebelle 2010; Krumholz & Burkhart 2016). Self-gravity and gravity-driven instabilities injected at large scales are also an important effect (Krumholz et al. 2018; Fensch et al. 2023). On the other hand, stellar outflows, supernova explosions and other forms of stellar feedback are the likely origins of smaller scale injection of turbulence (Krumholz et al. 2006; Zamora-Avilés et al. 2012; Padoan et al. 2016).

When looking to see whether observed turbulent motions of the WNM in the ISM alone can produce a phase transition, it was found that WNM at typical densities, temperatures and turbulent motions do not transit to CNM gas, even with the aid of stronger turbulent motions, which have higher turbulent velocities (Saury et al. 2014). Instead, stronger turbulent motions lead to an increased duration in the existence of gas in the unstable LNM regime. Weaker turbulent motions on the other hand tend to produce larger, denser and colder clouds of gas (Audit & Hennebelle 2005). The property that most greatly affects whether or not cold gas is formed however is the initial density of the WNM. Simulations with an initial WNM density above 1.5 cm^{-3} show condensation, with the final amount of CNM increasing with density. This initial increase in density can only exist due to some converging flow which increases the density of the region as mentioned earlier.

While these studies demonstrate compression from converging flows to be a main driver for the condensation of neutral gas, the origin of these converging flows remains uncertain. Possible explanations include a wide range of phenomena: from outflows of gas, to supernova explosions producing shock fronts. These events are transient in nature, and produce dynamically stable cold structures more suddenly and are easier to physically justify than the continuous ram pressure implemented in previous studies.

All of this work points to turbulence and thermal instabilities being important mechanisms in the formation of the CNM.

1.3 Observing Neutral Hydrogen (H I)

Neutral hydrogen atoms have the potential to emit a small amount of radiation via the hyperfine spin-flip transition between states with different proton and electron spin alignments. Atoms in the higher-energy triplet ($F = 1$) hyperfine state are often approximated as having parallel proton and electron spins. These higher-energy atoms can spontaneously transition to the lower-energy singlet ($F = 0$) state, often approximated as having anti-parallel spins. This transition emits a photon with a frequency of $1,420$ MHz, which lies within the range of frequencies observable with ground-based radio telescopes. The rate at which the spin-flip transition occurs was theorised in the 1940's by H.C. van de Hulst (van de Hulst 1945) and was revised later by Shklovsky in 1949 (Shklovsky 1982), with their estimate for the probability of the transition being off the currently accepted value by a factor of 4. The currently accepted value for the probability of the spin-flip transition occuring is approximately 2.85×10^{-15} s^{-1} (Wiese & Fuhr 2009), with a single atom making a transition on average every 12 million years. Such a small probability of occurring means this transition is near impossible to observe within a laboratory on Earth naturally. However, due to the shear abundance of hydrogen within our Universe, the 21-cm line has been observed with great success to trace the baryonic matter of the Universe.

The 21-cm line was first observed by a combination of groups in the early 1950's. Ewen and Purcell from the United States (Ewen & Purcell 1951), followed by Muller and Oort from the Netherlands (Muller & Oort 1951), both detected the existence of H I in our own Galaxy through spectra closely centred on the 21-cm line. Further confirmation came from Christiansen and Hindman in 1952 (Christiansen & Hindman 1952), who formed the first comprehensive map of H I 21-cm sightlines of the southern sky, analysing the variation in H I emission as a function of distance from the Galactic plane. From the 1970's, attention turned towards the outer Galaxy as surveys probed the variation of H I at large Galactic-radii (Henderson et al. 1982). The first few decades of H I radio astronomy utilised single dish telescopes that over time grew larger to achieve both greater resolution and sensitivity. The angular resolution of a telescope, θ can be related to the wavelength of light observed, λ and the telescope dish's diameter, D, such that:

$$\theta = 1.22\frac{\lambda}{D}\,, \tag{1.1}$$

where θ is given in radians. This fact was the main driver for the construction of telescopes with increased diameter, as state-of-the art telescopes of the time moved from 18 metres in Parkes, Australia to a 64 metre dish built in 1961, to the 305 metre diameter dish at Arecibo in Puerto Rico in 1963. With each passing decade, the sky coverage and angular resolution of H I surveys has increased by a factor of around 2 (McClure-Griffiths et al. 2023). The most recent state-of-the-art single dish telescopes include the Five-hundred-meter Aperture Spherical Telescope (FAST) located in China (Nan et al. 2011; Li et al. 2013).

With the increased resolution of telescopes came the trade-off of mapping increasingly smaller regions of the sky within the same time. Due to observational limitations, Galactic H I astronomy had reached a plateau by the late 1970's, with technological improvements needed to improve upon surveys further. Instead, H I astronomy focused on extragalactic surveys through advent of synthesis interferometer imaging techniques allowing for similar resolutions to that of observations of the Milky Way with single-dish telescopes. With the advent of "mosaicing" with interferometers and through the combination of single-dish data, interferometric surveys became more prominent, due to their longer baselines providing higher resolution than single-dish alternatives. Such telescopes include the Australian Telescope Compact Array (ATCA; Nelson 1992) in Australia built in the latter half of the 20th century and the Australian Square Kilometre Array Pathfinder (ASKAP; Hotan et al. 2021), built this century. Surveys made of the Milky Way in H I emission and absorption using the telescopes mentioned above are discussed in Section 1.4.

1.3.1 Radiative Transfer of H I

If the populations of hydrogen atoms with the higher and lower energy states of the spin flip transition have number densities of n_2 and n_1, respectively, then the ratio of hydrogen atoms in each state can be described by the Boltzmann equation:

$$\frac{n_2}{n_1} = \frac{g_2}{g_1} e^{\frac{-h\nu}{kT_s}}, \tag{1.2}$$

where ν is the frequency of the spin-flip transition at $1,420$ MHz, and g_2 and g_1 are the statistical weights of the two energy states, equal to 3 and 1, respectively. T_s represents the spin-flip analogue of the excitation temperature of the atoms. While T_s is statistical in nature, in practice it is very close to the kinetic temperature of H I gas T_k at temperatures below ~ 1000 K (Seon & Kim 2020). As such, calculating T_s has become a useful practice for estimating the temperatures of H I on the colder end of the ISM's temperature range. For the higher temperatures of the WNM however, collisions are not able to thermalise the 21-cm transition, leading to the condition that $T_s < T_k$ (Field 1958; Liszt 2001). While T_s is a useful physical property to understand the properties of H I, it cannot be directly measured from observations of H I emission. Instead, observations measure brightness from H I gas in the form of a temperature measurement known as the brightness temperature, T_B.

For the 21-cm line, the radiative transfer equation can be approximated by the Rayleigh-Jeans limit ($h\nu \ll kT$) and written in terms of the brightness temperature as:

$$\frac{dT_B(v)}{d\tau(v)} = T_s - T_B(v)\,, \tag{1.3}$$

where τ is the opacity of the gas along the line-of-sight and T_s is the spin temperature based on the number ratio of the hydrogen atom's spin states. In the idealistic scenario of a single gas cloud along a line-of-sight, the radiative transfer equation can be solved to define the brightness temperature measured by the a telescope as:

$$T_B(v) = T_s(1 - e^{-\tau(v)}) + T_{bg}e^{-\tau(v)}\,, \tag{1.4}$$

where T_{bg} is the temperature of the background radiation from any sources behind the cloud. Sources that contribute to this background temperature include bright extragalactic radio sources, the radiation from the Cosmic Microwave Background at 2.725 K, and the Galactic diffuse synchrotron background towards the direction of the source. If $T_s < T_{bg}$, the H I gas cloud is seen in absorption, and if $T_s > T_{bg}$, the cloud is seen in emission.

Assuming the background source is negligible, if one is interested in the total number of H I atoms along a sightline (or over velocity), we can calculate the column density of H I gas, defined by:

$$N_{\mathrm{H\,I}} = C\int \frac{\tau(v)T_B(v)}{(1 - e^{-\tau(v)})}\,dv \tag{1.5}$$

where $C = 1.823 \times 10^{18}$ cm^{-2} K^{-1} (km s^{-1})$^{-1}$. In the case the gas is optically thin, with $\tau \ll 1$, the column density simplifies to the following:

$$N_{\mathrm{H\,I,thin}} = C\int T_B(v)\,dv\,. \tag{1.6}$$

Through the assumption that H I gas is optically thin, we can therefore estimate the total number of H I atoms along a sightline through only measuring T_B.

1.3.2 Decomposition of Absorption and Emission Sightlines

Studies involving the combination of emission and absorption sightlines allow for the measurement of optical depths and hence can lead to calculating true column densities of H I gas that do not rely on the optically thin assumption from Equation 1.6. Many methods exist for combining absorption and emission sightlines to determine extra quantities like spin temperature. For example, original methods used measurements of the gradient from plotting absorption and emission spectra against each other (Mebold et al. 1997; Dickey et al. 2003). More recent methods use assumptions that each velocity channel contains a different spin temperature Roy et al. (2013a); Lee et al. (2015) or use assumptions of a single harmonic-mean spin temperature along a full sightline (Kanekar et al. 2011; Murray et al. 2018). Despite these different methods, spectral decomposition has remained the more prominent and powerful tool to separate components of H I gas and determine their individual properties (Heiles & Troland 2003; Stanimirović et al. 2014; Lee et al. 2015; Murray et al. 2015; Nguyen et al. 2024). One such study that outlined a formalism for joint decomposition of absorption and emission sightlines is Heiles & Troland (2003).

The H I absorption sightlines require a bright background continuum source (such that $T_s < T_{bg}$). However, this requirement limits us from observing emission along the same direction due to the dominance of the background source. To overcome this limitation, we observe emission sightlines close to the detection of absorption on the plane-of-sky, and make the assumption that the emission and absorption spectra sample the same gas population. The absorption measurements are therefore known as "on-source" measurements, and the emission sightlines are referred to as "off-source", with their respective brightness temperatures written as:

$$T_{B,\,\mathrm{on}}(v) = (T_{bg,\,\mathrm{sky}} + T_c)e^{-\tau_v} + T_s(1 - e^{-\tau_v}) \tag{1.7}$$

$$T_{B,\,\mathrm{off}}(v) = T_{bg,\,\mathrm{sky}}e^{-\tau_v} + T_s(1 - e^{-\tau_v})\,, \tag{1.8}$$

where $T_{bg,\,\mathrm{sky}}$ is the temperature of the blank sky (including both the radiation from the Cosmic Microwave Background at 2.725 K, and the Galactic diffuse synchrotron background towards the direction of the source). T_c is the brightness temperature of the radio continuum source. In reality, the emission spectrum may vary significantly at different positions around the absorption source, and can also be contaminated if the emission sightline is taken within the beam of the original absorption measurement. To avoid this, several off-source measurements are used, typically creating a ring around the absorption source to average out these effects and make an estimate for an "expected" emission spectrum at the position of the absorption source.

It is through the combination of the "on-source" and "off-source" sightlines that we can then calculate the optical depth spectra via:

$$e^{-\tau_v}(v) = \frac{T_{B,\,\mathrm{on}}(v) - T_{B,\,\mathrm{off}}(v)}{T_c}\,. \tag{1.9}$$

Since we now have two equations and two unknown parameters of optical depth and spin temperature, the combination of emission and absorption sightlines allows for the direct measurement of these properties, and more importantly, distinguishing between the gas phases of H I.

Through work pioneered by Heeschen (1955) for H I emission and Muller (1957) for absorption, H I spectra have been best described mathematically by the sum of Gaussian components, which in the case of optical depth, each component is described as:

$$\tau(v) = \tau_0\, e^{-\frac{(v-v_0)^2}{2\sigma^2}}\,, \tag{1.10}$$

where τ_0, v_0 and σ are the Gaussian's amplitude, central velocity, and dispersion, respectively. In the case where more than one component is needed to describe a signal, the total spectrum of N components can be expressed as:

$$\tau(v) = \sum_{n=1}^{N} \tau_{0,n}\, e^{-\frac{(v-v_{0,n})^2}{2\sigma_n^2}}\,. \tag{1.11}$$

The method prescribed in Heiles & Troland (2003) for decomposition absorption and emission sightlines begins with the Gaussian decomposition of the absorption sightline in a form similar to Equation 1.11. The components fitted from absorption are then used in a fit of the corresponding emission spectrum, along with extra components fitted to represent warmer gas that is too optically thin to be observed in absorption. As such the emission spectrum can be described through the combination of a $T_{B,\,\mathrm{CNM}}$ and $T_{B,\,\mathrm{WNM}}$ for the cold gas and warm gas respectively, such that:

$$T_B(v) = T_{B,\,\mathrm{CNM}}(v) + T_{B,\,\mathrm{WNM}}(v)\,, \tag{1.12}$$

where $T_{B,\,\mathrm{CNM}}$ and $T_{B,\,\mathrm{WNM}}$ are each expressed as:

$$T_{B,\,\mathrm{CNM}}(v) = \sum_{n=1}^{N} T_{s\,,n}\,(1 - e^{-\tau_n(v)})\,e^{-\sum_1^M \tau_m(v)} \tag{1.13}$$

$$T_{B,\,\mathrm{WNM}}(v) = \sum_{k=1}^{K} [\mathcal{F} + (1-\mathcal{F})\,e^{-\tau(v)}]\,T_{0,\,k}\,e^{-\frac{(v-v_{0,k})^2}{2\sigma_k^2}}\,, \tag{1.14}$$

where the CNM and WNM spectra contain N and K components respectively. Example spectra from the 21-SPONGE survey (Murray et al. 2015) that have previously been fit using this process are shown in Figure 1.2. The value of $\mathcal{F}$ defines the fraction of WNM gas that lies in-front of the absorption CNM clouds, with $(1 - \mathcal{F})$ representing the fraction of gas behind. M represents the number of CNM components that are located in-front of the nth cloud. While this method creates additional parameters to fit, which can lead to a more degenerate solution, the model is ultimately more physically motivated with ordering clouds along a sightline compared to simple Gaussian decomposition. In the work of Heiles & Troland (2003), the values for $\mathcal{F}$ were set to discrete values of 0, 0.5, or 1 to avoid long computation times, with the final values for the fit determined by the average between these different models.

One main concern with Gaussian decomposition is the potential for over-fitting through adding too many components. To alleviate these problems, more recent works improve upon the Heiles and Troland method through the addition of testing chi-squared values of the fit. The number of components is usually decided by the point at which the addition of more components causes a sharp decline in improvement of the chi-squared test (Murray et al. 2015).

The Gaussian parameters from these decompositions can be attributed to physical characteristics of the H I gas along a line of sight. For example, the central velocity, v_0, represents the bulk velocity of the gas, and since the intrinsic linewidth of the 21-cm line is small (Condon & Ransom 2016), the dispersion, σ, describes the dispersion from random motions from the thermal and turbulent motions of the H I gas.

While the Heiles and Troland method has become a staple for analysing H I in the Milky Way and nearby galaxies, it still remains limited due to the degeneracy of Gaussian decomposition and the arbitrary ordering of components along a sightline

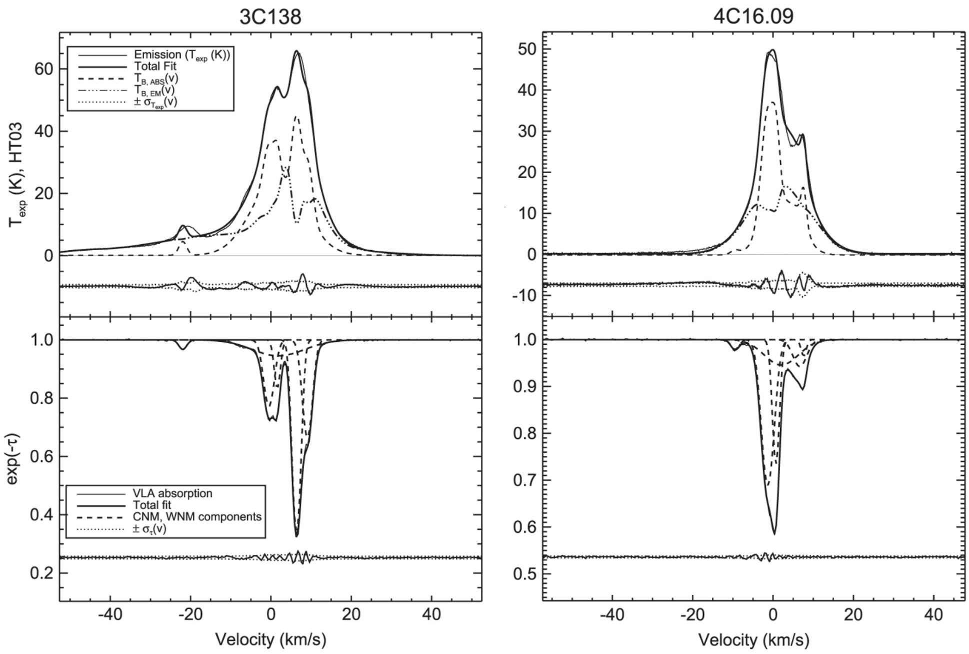

Figure 1.2: H I emission and absorption spectra from two sample sightlines from the 21-SPONGE survey (extracted from Figure 3 of Murray et al. 2015). The spectra were fit following methods from the work of Heiles and Troland 2003, prescribed in Section 1.3.2. The absorption spectra are fit with Gaussian components. The emission spectra are fit using Gaussian components with central velocities and dispersions similar to those from the absorption spectra, alongside additional emission-only components. Residuals of the fits are shown in the bottom of each panel.

after fitting. More recently, Bayesian forward fitting methods, such as CARIBOU[1], are currently being developed which model parcels of gas along a sightline and compute radiative transfer to fit H I emission and absorption spectra. This version of fitting spectra provides a more more physically motivated model compared to fitting Gaussians to spectra which we receive after being affected by radiative transfer over hundreds of parsecs. These forward fitting models are also able to fit more physical characteristics such as kinetic temperature and three-dimensional number density, compared to original Gaussian decomposition that fits brightness temperature and optical depths.

1.3.3 Quantifying Spatial Structure

Single sightlines of H I emission and absorption can reveal important information about H I gas properties and their phase separation along pathlengths through the ISM, but they yield no information about the spatial variation of these properties on the plane-of-sky. The spatial variation of ISM gas is an especially crucial point for constraining the physics of interstellar turbulence Elmegreen & Scalo (2004), which is also a key driver in the formation of molecular clouds (Hennebelle & Falgarone 2012). Instead of Gaussian decomposition, statistical tools are required to quantitatively describe the spatial variations of H I gas across the plane-of-sky.

One of the most common techniques used for analysing H I emission and the spatial variation and turbulent properties of H I gas is the spatial power spectrum (SPS). The SPS is a tool used to describe the variation in properties as a function of spatial scale. Since H I emission data lacks a third spatial dimension of depth, studies focus mostly on the two-dimensional field of H I column density and its variation across the plane-of-sky. For a two-dimensional field, $I(\mathbf{x})$, the SPS $P(k)$ is constructed through the Fourier transform such that:

$$P(k) = \int\int \langle I(\mathbf{x}) I(\mathbf{x}') \rangle \, e^{i\mathbf{L}\cdot k} \, d\mathbf{L} \,, \tag{1.15}$$

where k is the spatial frequency, and $\mathbf{L} = \mathbf{x} - \mathbf{x}'$ is the distance between two points on the image. If ISM gas is under the influence of turbulence, fluctuations in H I column density (as defined in Equations 1.5 and 1.6) are expected to form a power-law slope, $P(k) \propto k^{\gamma}$ that are tied to the physical three-dimensional density and velocity fluctuations of the field (Scalo 1987; Lazarian & Pogosyan 2000). The SPS can also be related to the form of turbulence driving a medium, injecting energy at the turnover scale where driving occurs which then cascades down to

[1] https://github.com/tvwenger/caribou_hi

smaller scales before dissipating out of the system (Colman et al. 2022). While both velocity and density fluctuations likely contribute to the overall slope, it is currently thought that SPS slopes measured are primarily due to density fluctuations so long as it is measured over a large enough velocity range (Lazarian & Pogosyan 2000; Yuen et al. 2021). As such, the SPS can be a valuable tool for understanding the spatial structure of H I gas within regions of the ISM, with shallower slopes implying more power, and hence more structure, exists on smaller scales compared to steeper slopes.

Historically, the SPS has been utilised on various tracers of the ISM in both our Galaxy and extragalactic bodies (Crovisier & Dickey 1983; Green 1993; Plume et al. 2000; Dickey et al. 2001; Burkhart et al. 2010; Pingel et al. 2013, 2018). H I SPS of the Milky Way have typically been fit with a single power-law slope ranging from $\gamma = -4.0$ to -2.5 (Blagrave et al. 2017; Pingel et al. 2018). The slope has been found to be relatively consistent across the plane-of-sky, with only surveys at higher Galactic latitudes forming shallower power-law slopes (McClure-Griffiths et al. 2023). SPS of dust on the other hand, which is strongly correlated with the amount of total hydrogen, typically has a shallower slope ranging from $\gamma = -2.9$ to -2.7 (Pingel et al. 2018). The shallower slope aligns with the fact that dust also traces molecular hydrogen which is denser and exists within self-gravitating, supersonic mediums on smaller scales than H I. In incompressible fluids without self-gravity, density power-law slopes are expected to follow an index of $-11/3$, known as Kolmogorov turbulence (Kolmogorov 1941). However, in astrophysical contexts, cold H I gas is formed through shocks and compressions that create more power on smaller spatial scales (Beresnyak et al. 2005; Kowal & Lazarian 2007; Burkhart et al. 2010), slopes of the CNM are typically shallower than Kolmogorov turbulence. Kolmogorov turbulence is based on non-magnetohydrodynamic turbulence, and other turbulence models that integrate magnetic fields are usually better baselines for comparison such as the Iroshnikov-Kraichnan (IK) or the Goldreich-Sridhar (GS) models (Iroshnikov 1963; Kraichnan & Nagarajan 1967; Goldreich & Sridhar 1997).

Many H I SPS studies have not detected a turnover scale within their survey ranges, ranging from physical scales of ~ 0.01 to a few tens of parsecs. The lack of a turnover scale, implies that H I turbulence is likely driven through mechanisms acting on scales larger than the H I structures being observed (Pingel et al. 2013, 2018). While SPS have been calculated across large portions of the sky, such as with the GALFA-HI survey (Mittal et al. 2023), rolling kernel techniques have also been developed, measuring SPS slopes within subregions of the Small and Large Magellanic Clouds through rolling a spatial kernel over an image (Szotkowski et al. 2019).

Effects such as the multiphase nature of H I can heavily influence the slope of the H I SPS (Koch et al. 2020; Körtgen et al. 2021; McClure-Griffiths et al. 2023). Observational biases such as telescope resolution and noise also influence the SPS, motivating the need for surveys of Milky Way H I gas with higher spatial resolution and sensitivity.

One main drawback of the SPS on H I emission maps is that these fields use the optically thin limit to compute H I column densities, and as such are biased against regions of high optical depth where cold gas primarily exists. While one could solve this issue with absorption-emission pairs, these measurements do not fully sample the sky. The SPS requires a spatially-resolved field to form a complete Fourier transform. The structure function can be used instead to analyse the spatial variation of discrete dataset such as H I absorption sightlines. The structure function is a powerful diagnostic that quantifies the variation of a particular field as a function of physical length scale. For some spatially dependent parameter $f(\mathbf{x})$ and as a function of scale $r = |\mathbf{r}|$, the second-order structure function with a 2-point stencil, $\mathrm{SF}_2^{\mathrm{2pt}}(\mathrm{f}, \mathbf{r})$ can be written as (Haverkorn et al. 2004; Seta et al. 2023):

$$SF_2^{2pt}(f, \mathbf{r}) = \langle |f(\mathbf{x}+\mathbf{r}) - f(\mathbf{x})|^2 \rangle, \tag{1.16}$$

where $\mathbf{x}$ is the two-dimensional position vector over which the average, $\langle\rangle$, is computed. Structure functions typically form single power-law slopes up until a break-scale, known as the correlation length scale. This correlation length scale measures the point beyond which the field is no longer spatially correlated and plateaus at a value proportional to the standard deviation of the sample (Seta et al. 2023). For the second-order structure function, this plateau point is equal to $2\sigma^2$, where σ is the standard deviation of the sample used.

The structure function power-law slope can be analytically related to the slope of the SPS, assuming the structure function is properly sampled with enough data points. For a two-dimensional field, the power-law slope, α of a structure function, $\mathrm{SF} = A\, r^{\alpha}$, can be equated to the power-law slope, γ, of a SPS such that $\gamma = \alpha + 2$ (Deshpande et al. 2000; Seta et al. 2023). This makes the structure function a very useful tool in the context of using H I absorption to calculate optical-depth corrected column densities to form SPS of true H I column densities.

Many subfields have implemented the structure function, ranging from extragalactic ISM studies (Lee et al. 2025), to works on the structure of interstellar magnetic fields (Haverkorn et al. 2008; Stil et al. 2011; Livingston et al. 2021). Structure functions of H I optically thin column density have been implemented across subregions of galactic bodies such as the Small Magellanic Cloud, finding correlation-length scales on a median scale of 50 parsecs, measuring the scale of small-scale turbulence (Lee et al. 2025). The slope of H I column density structure functions has also been found to be strongly correlated to regions of stellar-feedback.

Within our Galaxy, the structure function has primarily been implemented on H I absorption across single background sources that are spatially resolved such as the radio galaxy Cassiopeia A (Deshpande et al. 2000). This limits studies in the spatial variation of optical depth to AU-scales up to single-parsec scales (Roy et al. 2010, 2012; Dutta et al. 2014). These works have typically observed optical depth structure functions with power-law slope values ranging from 0.3 to 0.8. The positive power law slopes imply greater variability on larger scales. Due to the small-scales these structure functions probe, the structure of these optical depth variations are likely due to cold H I gas within the ISM. Structure functions involving multiple H I absorption sources have been historically limited due to a lack of high-density, statistically significant samples across the plane-of-sky. Likewise, structure functions of optical depth-corrected column densities have also been limited.

Despite this, both the SPS and structure function are valuable tools for probing the spatial structure of gas and the scales at which turbulence drives the ISM.

1.4 H I Surveys of the Milky Way

1.4.1 H I Emission

Due to its close proximity, the Milky Way has always been the primary laboratory for observing the ISM with high spatial resolution. From Section 1.3.1, we know that brightness temperature observed by telescopes is a direct proxy for the amount of hydrogen along most optically thin sightlines. As such, H I observations have had a historical preference for cataloguing H I emission to study the spatial and velocity structure of H I within the Galaxy.

Throughout the 20th century, H I surveys have been observed with mostly single-dish radio telescopes with the end of this period culminating in the Leiden-Argentine-Bonn (LAB) collaboration (Kalberla et al. 2005), providing a whole-sky survey with 30-arcminute angular resolution and a velocity resolution of 1 km s^{-1}. Around this time, engineers had developed multi-beam receivers and applied them to radio telescopes. With this advancement, survey time was decreased allowing for higher sensitivity observations to be made across wide regions of the sky. The combination of these pieces of technology with large single-dish telescopes, such as the Parkes, Effelsberg and Arecibo telescopes, produced surveys with resolutions better than 16 arcminutes. The Parkes Galactic All-Sky Survey (GASS; McClure-Griffiths et al. 2009; Kalberla et al. 2010; Kalberla & Haud 2015a) and the Effelsberg-Bonn H I survey (Winkel et al. 2010) in particular were combined to form the HI4PI Survey (HI4PI Collaboration et al. 2016), a full-sky H I emission survey with 16-arcminute resolution. This survey allowed for statistically complete studies of H I phase distributions to be completed on different regions of the sky with the same survey data and sensitivity. More recently, the GALFA-HI survey from the Arecibo telescope produced the highest-resolution single dish observations of the Milky Way at 4-arcminute angular resolution and 0.2 km s^{-1} velocity resolution (Peek et al. 2011, 2018). While the survey observed only portions of the sky, it still enabled the study of features with fine velocity gradients seen in H I emission.

At the turn of the 21st century, the technique of interferometric mosaicing enabled for the overlapping of field of view from many observations at once. Originally proposed by Ekers & Rots (1979) and first implemented in the Australia Telescope Compact Array (ATCA) by Sault (1994), interferometric surveys were now able to observe larger areas of the sky and hence larger angular scales than their single-dish counterparts. After this, interferometric mosaic surveys were then merged with single-dish observations, first achieved by Stanimirovic et al. (1999). The resulting H I cubes contained greater U-V plane coverage that allowed for more signal on a greater range of angular scales. Examples of telescope surveys that implemented this technique include northern-sky surveys such as the Canadian Galactic Plane Survey (CGPS; Taylor et al. 2003) from the Dominion Radio Astrophysical Observatory's (DRAO) Synthesis Telescope and the DRAO's H I Intermediate Galactic Latitude Survey (DHIGLS: Blagrave et al. 2017), as well as observations of the southern-sky like the aptly named Southern Galactic Plane Survey (SGPS; McClure-Griffiths et al. 2005).

To obtain even higher resolutions, dishes in an interferometer must be further away from each other, mimicing a larger single dish telescope. However, there is a trade-off between this distance, known as the longest baseline, and the brightness sensitivity of the observation. With this in mind, as higher spatial resolutions were achieved, the spatial extent of survey regions become smaller and smaller to maintain similar brightness sensitivity to previous work, alongside pragmatic observing schedules (McClure-Griffiths et al. 2023). More recent focus thus led towards the Galactic plane and other key regions of the sky, such as that of the THOR survey (Beuther et al. 2016; Wang et al. 2020), with its goal of improving the Very Large Array Galactic Plane Survey (VGPS; Stil et al. 2006) to a spatial resolution of 20-arcseconds per beam. A notable outlier to this trend focussing on the construction of interferometers and smaller survey regions is the currently ongoing CRAFTS survey utilising the FAST single-dish in China (Zhang et al. 2021). Due to the telescope's large diameter, the CRAFTS survey is producing H I emission maps of the Galaxy with 4-arcminute angular resolution and 0.2 km s^{-1} spectral resolution. The survey will be observing large regions of the sky with its current data release having already observed a total 4500 square-degrees of sky.

1.4.2 H I Absorption

While H I emission surveys are fundamental in observing the spatial structure of H I gas within our Galaxy, it is through the combination of H I absorption that the full radiative transfer equation can be deciphered.

H I absorption is especially powerful in its ability to constrain the CNM and its properties, since cold gas has typically higher optical depths compared to the other phases, becoming optically thick ($\tau \gg 1$) at column densities of around 10^{21} cm^{-2} and greater (McClure-Griffiths et al. 2023). Observations from the second-half of the 20th century were able to detect the CNM with relative ease (Hughes et al. 1971; Knapp & Verschuur 1972; Radhakrishnan & Goss 1972; Lazareff 1975; Belfort & Crovisier 1984; Braun et al. 1992). However the most notable single-dish absorption survey is that of the Millennium Arecibo 21 Centimeter Absorption-Line Survey (Heiles & Troland 2003), observing a total of 79 H I absorption and emission sightline pairs over the full sky. These spectra were decomposed spectrally using the method from Section 1.3.2 into cold components observed in both emission and absorption, with an example spectra shown in Figure 1.3.

One concern with all-sky surveys, is that with sightlines along the Galactic plane at low latitudes, many velocity components complicate the spectra, increasing the likelihood of degenerate decomposition solutions. An example of a low-latitude spectra from the Millenium survey is shown in Figure 1.3. This issue is also combined with the fact that velocity structures do not necessarily reflect 3-dimensional density structures. From numerical simulations (Hennebelle & Audit 2007; Kim et al. 2014), it has been shown that recovering spin temperatures accurately strongly depends on the pathlength of gas observed and hence Galactic latitude, with low Galactic latitudes of less than $|b| < 20$ degrees only having a 53% accuracy of determining spin temperature (Murray et al. 2017). Higher Galactic latitudes greater than $|b| > 50$ degrees had all velocity structures matching with corresponding density structures. This finding has led to most H I absorption surveys being focused on higher Galactic latitudes where sightlines are simpler and over shorter pathlengths of gas.

As mentioned in Section 1.3.2, emission spectra paired with absorption sightlines need to be in close proximity on the plane-of-sky to the background source in order for the approximation holds that the two sightlines probe similar gas. With this in mind, interferometers are more preferred for H I absorption studies due to their superior spatial resolution to that of single-dish telescopes, as they resolve out the large spatial scales, focussing on the small scale structures where cold gas typically resides. One complication that emerges from the matching of emission and absorption sightlines is the difference in beam sizes between the two, with past interferometric surveys of H I emission having beam resolutions on the order of arcminutes, whereas the H I absorption has a beam-size more similar to the background radio source, which is often a point-source (McClure-Griffiths et al. 2023). The increased sensitivity and stable spectral baselines of interferometers has also enabled attempts to study not just the CNM in absorption but also the UNM and WNM, which both have very low typical optical depths ($\tau < 10^{-2.5}$). To achieve high-enough sensitivity for the detection of these warmer phases, longer observation times are also usually required, resulting in only a few sightlines being chosen to avoid long survey observing schedules. Some studies have detected gas along a few sightlines with spin temperatures within the regime of the WNM (Carilli et al. 1998; Dwarakanath et al. 2002; Murray et al. 2014). Other surveys that have not yielded direct detections have instead made upper limit estimates on the WNM's temperature (Mebold et al. 1982; Heiles & Troland 2003; Kanekar et al. 2003, 2011; Roy et al. 2013b). Work using the Arecibo Observatory has identified structures with temperatures ranging from $T_s = 400-900$ K, within the regime of the UNM (Begum et al. 2010). Likewise, sightlines observed with the Westerbork Synthesis Radio telescope and ATCA have also detected UNM components (Roy et al. 2013a,b). More notably however was the 21-SPONGE Survey (Murray et al. 2014, 2015, 2018), which utilised the Karl G. Jansky Very Large Array to produce high-sensitivity observations of absorption lines with sensitivities of $\sigma_\tau < 1 \times 10^{-3}$ along each sightline. In total, H I absorption was measured against 58 bright radio background sources. Combined with H I emission data from the Arecibo telescope, spin temperatures were able to be calculated, ranging across all H I phases. Murray et al. (2014) in particular utilised techniques of stacking spectra to improve signal to noise even further, reaching sensitivities of $\sigma_\tau \sim 2 \times 10^{-4}$, and detecting warm H I gas at ~ 7000 K, likely a result of the thermalisation of Lyman-alpha scattering. Detections of H I gas with these high temperatures and sensitivities are therefore crucial for not just improving our understanding of the properties of H I phases, but also placing constraints on the energy balance of the ISM such as with the Lyman-alpha radiation field. Most recently,

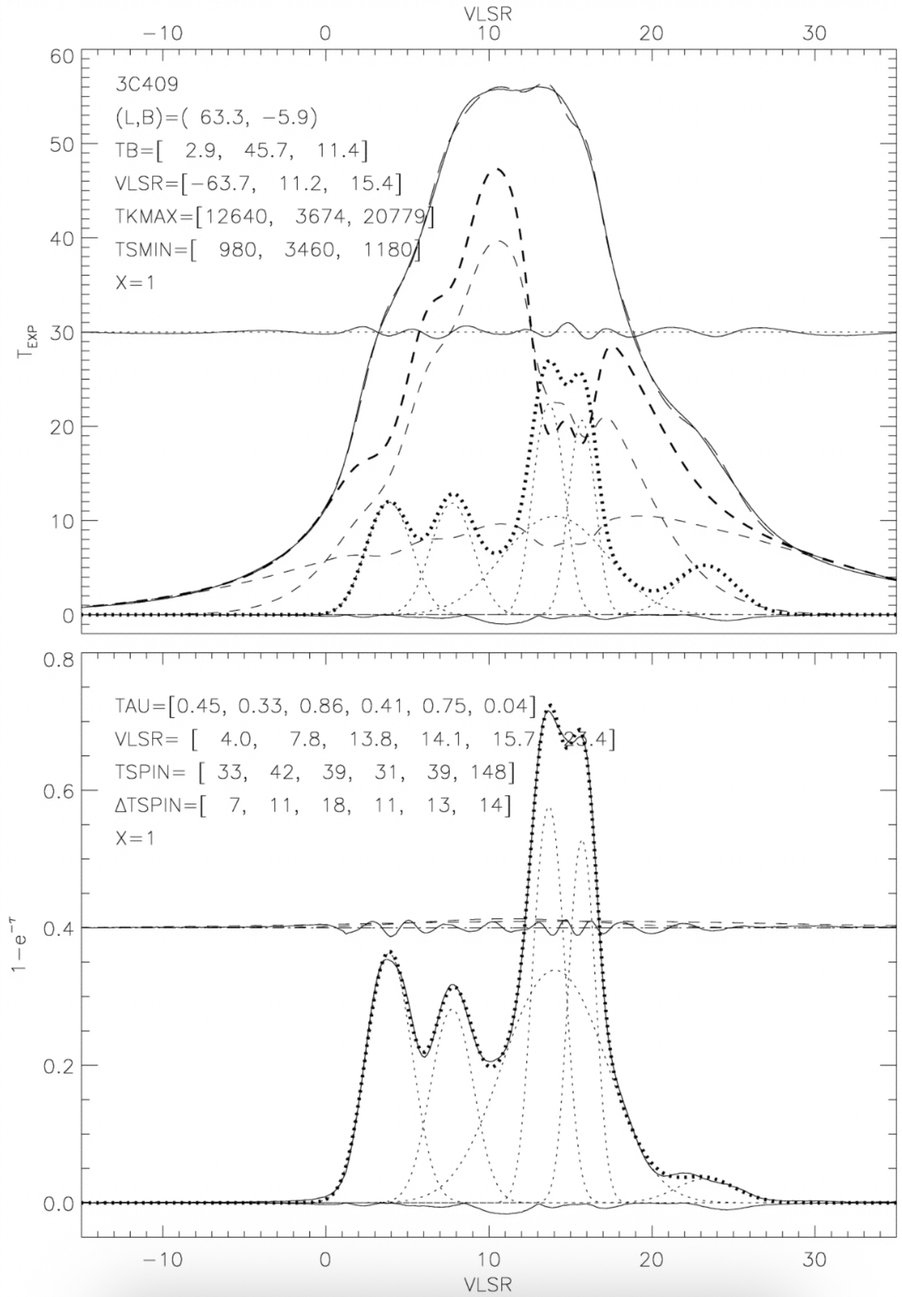

Figure 1.3: H I emission (top) and absorption (bottom) spectra from a sample sightline of the Millenium Survey at low Galactic latitude (extracted from Figure 7 of Heiles & Troland 2003). The spectra were fit following methods, prescribed in Section 1.3.2. Top: The emission spectra (solid line), fit using Gaussian components with central velocities and dispersions similar to those from the absorption spectra (totalling to the bold dotted line), alongside additional emission-only components (totalling to the bold dashed line). Bottom: The absorption spectrum (bold dotted line), fit with Gaussian components (thin dotted lines). Residuals of the fits and the negative of the noise of the total spectra are shown along the middle and at the bottom of each panel, respectively. The Gaussian properties of each component are written in the square brackets.

the MACH survey (Murray et al. 2021) has searched for H I absorption within a relatively small field-of-view between Galactic latitudes of $b = (30°, 62°)$ and longitudes of $l = (60°, 110°)$. The survey detected 42 bright background sources, greatly improving the background source density compared to previous absorption surveys. However, due to the region being diffuse and with relatively low column densities compared to regions of similar Galactic latitude, the survey found very few sightlines with optical depths greater than 1, and very low CNM mass fractions close to zero.

Despite the past ~ 70 years of H I absorption surveys observing the Milky Way, our knowledge is still ultimately held back by observational limitations. The main downside of absorption compared to emission surveys is the requirement of a bright background source, which is usually that of a quasar or bright radio galaxy. Figure 1.4 showcases the combined sightlines of all previous Milky Way H I absorption surveys overlaid on a H I column density map of the Milky Way, computed in the optically thin regime. While the number of sightlines of H I absorption through the Milky Way is much higher than that of extragalactic bodies (Pingel et al. 2022), our understanding of the temperature of H I, which can only be achieved through the combination of absorption and emission sightlines, is limited to the ~ 400 sightlines of gas currently observed from major surveys (McClure-Griffiths et al. 2023). In contrast to these past surveys, the recent MeerKAT Absorption Line Survey (MALS) has captured close to 19,000 absorption sightlines (Gupta et al. 2025) of Milky Way H I gas. However, each sightline has a velocity resolution of approximately 5.5 km s^{-1}, and is not reliable for separating out H I phases, especially cold gas features that typically have narrower linewidths. Thus these ~ 400 sightlines with high spectral resolution previously discussed represent our best current attempts at observing cold gas in the diffuse interstellar medium. Comparison between observations and simulations of ISM physics are also therefore limited by this same inconvenience of a limited number of sightlines through the Galaxy and the ~ 1300 Gaussian components decomposed from them. As such, the need for instruments that are able to produce high sensitivity observations is crucial to drastically improve the source density of background sources required for absorption and hence, the separation and study of H I phase properties.

1.5 The GASKAP-HI Survey

The Galactic Australian Square Kilometre Array Pathfinder H I Survey (GASKAP-HI, Dickey et al. 2013; Pingel et al. 2022) is a survey of H I spectral line emission

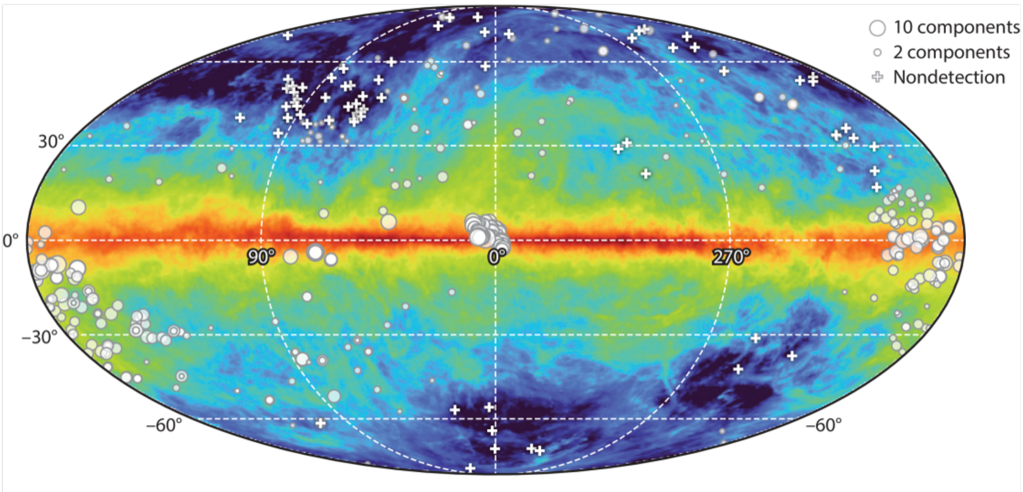

Figure 1.4: H I absorption spectra source locations from all Milky Way H I absorption surveys prior to the ASKAP telescope, overlaid on a map of H I column density over a velocity range from −75 to 75 km ss^{-1} from the HI4PI survey (Ben Bekhti et al. 2016). The white crosses are non-detections of H I absorption, while the white circles are absorption detections, with their size corresponding to the number of components along the sightline. Coordinates are in Galactic latitude and longitude (from Figure 3 of McClure-Griffiths et al. 2023).

and absorption using the Australian Square Kilometre Array Pathfinder (ASKAP) telescope (Hotan et al. 2021). The goal of the survey is to observe the Magellanic system and portions of the Milky Way at a spatial resolution of 30-arcseconds and frequency resolution $\Delta\nu = 1.15$ kHz, resulting in a velocity resolution of $\Delta v = 0.244$ km s^{-1}. Combining the high spatial resolution data of the ASKAP telescope with the short baseline data from the single dish measurements from the GASS using the Parkes 64-metre telescope (McClure-Griffiths et al. 2009; Kalberla et al. 2010; Kalberla & Haud 2015a) provides a survey with approximately 30 times the spatial resolution of previous single-dish H I surveys, and 5 times the spatial resolution of previous interferometric surveys of the Galactic plane. The main benefit of the ASKAP telescope however is its ability to simultaneously map H I absorption and emission at similar resolutions compared to previous surveys that had resolution mismatches between the two datasets. It is worth noting however that most absorption sources are unresolved and as such the absorption measurements trace a much narrower sightline than the emission. The main advantage of the equal resolutions is instead the increased H I emission resolution enabling emission gas to be measured more closely to the absorption source on the plane-of-sky for radiative transfer methods discussed in Section 1.3.2. While telescopes such as the Very Large Array (VLA) (Heeschen 1981; Perley et al. 2009) and MeerKAT (Jonas & MeerKAT Team 2016) have similar capabilities, they do not have the wide field-of-view for fast surveying. The VLA specifically also lacks enough short baseline telescopes compared to ASKAP to form strong emission sensitivity. This makes the GASKAP-HI survey ideal for measuring emission sightlines near absorption sources to produce more accurate emission-absorption sightline pairs.

While the survey is currently ongoing, the Pilot survey has completed, mapping the sky towards the Magellanic system, including the Small and Large Magellanic Clouds and the Magellanic Stream and Bridge. The survey's spectral extent covers line-of-sight velocities ranging from $v = 100$ km s^{-1} to -400 km s^{-1} to cover both the Magellanic system and the Milky Way foreground. The Pilot survey consists of 10 individual 20-hour observations of 5 degree $\times$ 5 degree fields combined into a mosaic covering an area of approximately 250 square-degrees. The field spans a Galactic latitude range of $b = (-45°, -27°)$ and a Galactic longitude range of $l = (270°, 305°)$. The combined mosaic for the Pilot survey is shown in Figure 1.5. The Milky Way gas covered by the GASKAP-HI Pilot survey contains two nearby large-scale filaments, known as the Reticulum and Hydrus filaments (Kamal Youssef & Grenier 2024; Nguyen et al. 2024; Lynn et al. 2025). These filaments are highlighted in Figure 1.5, making up majority of the contribution to the H I column density in the region. The remainder of the gas within the field is more diffuse, enveloping the filamentary structures.

Within the area of the Pilot survey, H I absorption spectra were extracted towards 2714 background continuum sources whose flux densities were higher than 15 mJy at a spectral frequency of 1.4 GHz (Dempsey et al. 2022). From these 2714 bright background sources, 462 contained absorption features strong enough to be observed beyond a 3σ detection threshold, and at least one neighbouring channel containing at least a detection beyond 2.8σ. The filtering process results in the two absorption sightlines per square-degree with detected H I absorption. 12 sightlines from the detected sample were removed since their opacity spectra were saturated and thus had indeterminate measurements with large uncertainties. From Figure 1.5, there is a noticeable gap in absorption features to the bottom left, due to the observational complications with the survey leaving the underlying fields too noisy to detect absorption features.

The 462 H I absorption sightlines detected within the Pilot survey already rival the total number of sightlines across the entire sky from the collection of previous high spectral resolution H I absorption surveys. Work done by Nguyen et al. (2024) utilised the method of Heiles & Troland (2003) outlined in Section 1.3.2 to spectrally decompose the H I absorption spectra along with nearby emission spectra that were at least one beam radii away from the absorption source on the plane-of-sky.

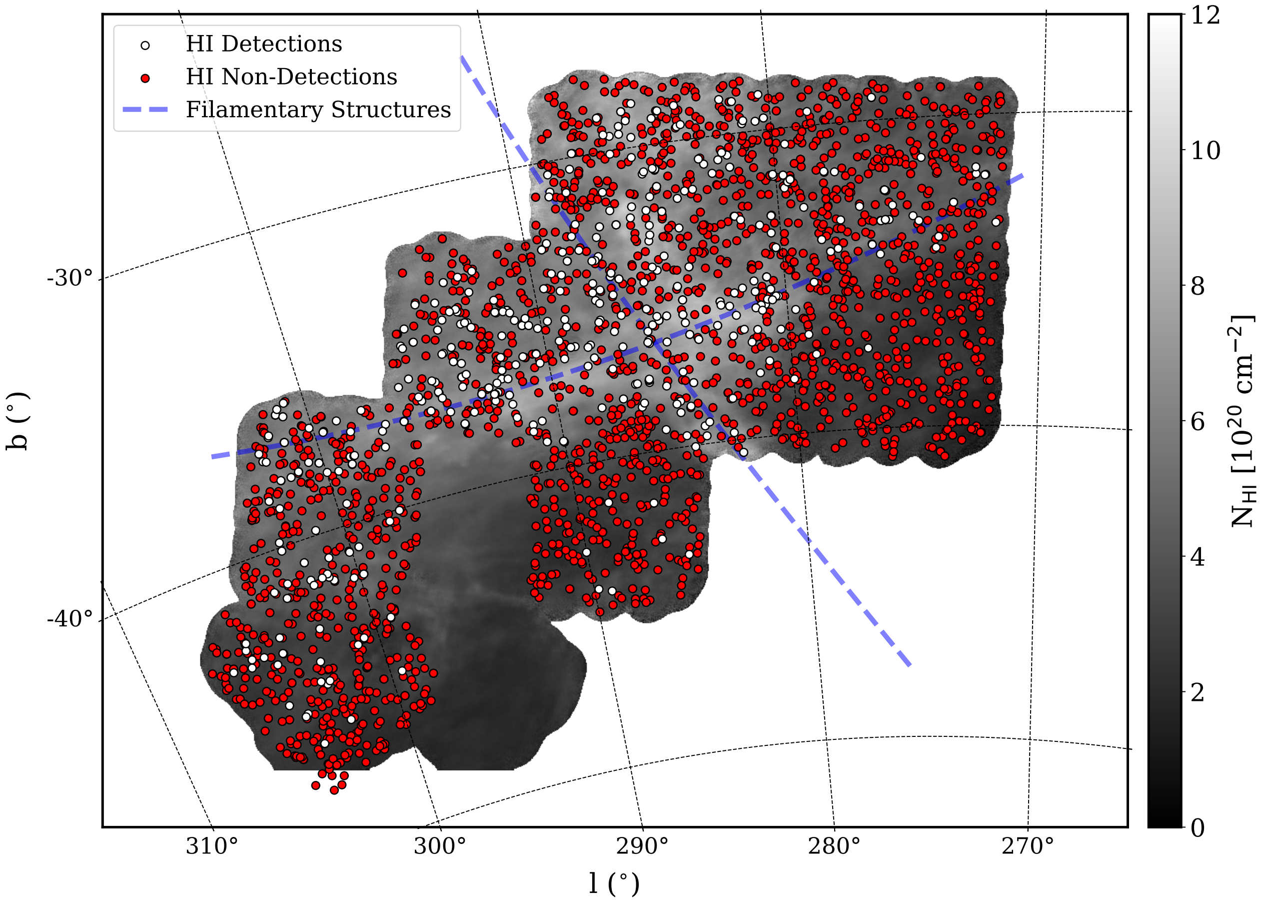

Figure 1.5: H I Column density from the combined Mosaic of the 10 fields from the GASKAP-HI Pilot Survey (Nguyen et al. 2024; Lynn et al. 2025). Detections of cold H I gas in absorption over the velocity range $-50 < v_{\rm LSRK} < 50$ km s^{-1} are annotated with white circles. Sightlines with non-detections of H I absorption are marked by red circles. The blue dashed lines indicate the arcs of two H I filaments in this region of the Milky Way: Reticulum and Hydrus in the vertical and horizontal direction respectively (Kamal Youssef & Grenier 2024).

1.6 Thesis Motivation

Previous H I surveys in both emission and absorption have illuminated us on the large-scale structure of our Galaxy (Heiles & Troland 2003; Murray et al. 2015, 2021). Our knowledge of the properties of H I phases and their temperature and turbulent properties have assisted in fine-tuning theoretical models and numerical simulations. The MACH survey produced a survey of H I absorption with high background source density, however due to the location chosen, very little CNM gas was observed. The GASKAP-HI survey on the other hand, probes a region of the ISM more generic to the solar neighbourhood, resulting in hundreds of sightlines of detected H I absorption and high source density across the plane-of-sky Nguyen et al. (2024). The abundance of sightlines will enable us to explore several key avenues that have been historically limited, biasing our knowledge of the H I phases and their spatial variation.

1.6.1 Spatially Mapping H I Temperature

While H I emission surveys have created high resolution, spatially resolved maps of the H I column density of the Milky Way, H I gas temperature remains more of a mystery, due to its reliance on absorption sightlines and bright background sources. One major limitation has been the very few sightlines where H I gas warmer than the CNM has been detected in absorption (Carilli et al. 1998; Dwarakanath et al. 2002). The lack of temperature measurements across the plane-of-sky of UNM and WNM gas has restricted us in our understanding of temperature variation of H I gas within galaxies. Some studies have attempted to alleviate this through spectral stacking of dozens of sightlines across the entire plane-of-sky (Murray et al. 2014). This allows for the detection of warmer gas phases, and the study of their global properties and average temperatures. However, these global stacks are averaging sightlines in entirely different hemispheres, where gas is likely not physically connected or influenced by the same dynamical processes. As such, these single stacked spectra hide the spatial variation of temperature within our Galaxy. Spectral stacks of emission-absorption sightlines within localised fields have not yet been attainable due to limitations on source finding. With the GASKAP-HI Pilot survey however, the large sample of sightlines within a small field of view now allows for localised spectral stacking, and an attempt to map the temperature variation of gas warmer than the CNM across the plane-of-sky.

1.6.2 Spatial Structure of CNM and WNM

While H I absorption surveys have targeted key locations of molecular cloud regions and other places of interest due to their higher concentrations of CNM gas (Stanimirović et al. 2014; Nguyen et al. 2019), these are often on relatively small scales, and result in a couple dozen sightlines at most per survey. Some studies have used H I absorption from single background sources to develop small-scale optical depth maps, resulting in studies of the spatial structure of cold gas over AU to single parsec scales (Deshpande et al. 2000; Roy et al. 2010, 2012; Dutta et al. 2014). Studies of cold gas over scales greater than this have been limited due to a lack of a statistically significant sample of H I absorption sightlines within a given localised region.

The lack of sightlines has resulted in a heavy reliance on optically thin column density measurements for quantitative analyses such as spatial power spectra and structure functions (Pingel et al. 2018; Lee et al. 2025). One avenue that has not been explored is attempting to derive spatial power spectrum slopes of H I column density in the optically thick regime. With the large sample of emission-absorption sightlines provided by the GASKAP-HI survey, phase decomposition with full radiative transfer information is also possible, allowing for a more accurate analysis of the structure of H I phases within the Milky Way compared to previous work relying solely on H I emission (Kalberla & Haud 2015a; Martin et al. 2015).

1.6.3 CNM Decomposition vs Resolution

H I emission-based phase decomposition through tools such as ROHSA have provided a revolution in our understanding of H I phases in not just our Galaxy but also nearby extagalactic bodies such as the Small and Large Magellanic Clouds. ROHSA in particular is a Gaussian decomposition tool designed to model H I emission spectra of full emission maps. Through the addition of spatial regularisation parameters in its fitting cost function, the ROHSA algorithm is able to ensure fits of neighbouring sightlines are similar to form more spatially correlated phase decomposition compared to other methods (Marchal et al. 2019). While the tool was originally developed with Milky Way gas in mind, the lower physical resolutions when observing gas within extragalactic bodies means CNM gas structures are often not resolved. Despite the use of ROHSA with these lower physical resolutions of approximately 8 parsecs, there has not yet been a comprehensive study on the effect of spatial resolution with separating H I phases and deriving CNM mass fractions accurately. The high resolution GASKAP-HI survey provides us with many interesting locations with small-scale instabilities to test whether decomposition tools are powerful enough to determine the global statistics of the H I phases in other galaxies without knowledge on their small-scale structure.

1.7 Thesis Outline

In this thesis, with the use of the data sets from the GASKAP-HI Pilot survey, alongside other wavelength data such as dust, I address several open questions: How does stacking H I spectra affect measurements of spin temperature of gas previously undetected on single H I absorption sightlines? What is the spatial structure and variation of cold gas absorption properties across the plane-of-sky within localised regions? And how accurate are Gaussian decompositions of H I emission maps when cold gas is no longer spatially resolved?

In Chapter 2, I present an observational study stacking H I spectra from the Milky Way observations of the GASKAP-HI Pilot Survey. Through tests with both real data and toy models, we determine how effective stacking spectra is for accurately measuring the temperature of residual gas. We also detect warmer gas not previously detected along single sightlines.

Chapter 3 entails the study of the spatial variation of H I absorption properties across the plane-of-sky. Through the combination of absorption and emission, I use the full radiative transfer description to form structure functions of the opacity-corrected column density to more accurately measure the spatial power law of H I compared to solely with H I emission. For the first time the structure function of spin temperature of H I is produced, to quantify the spatial variation of H I cold gas temperature within the Local solar neighbourhood.

Chapter 4 provides the details of new observations from the GASKAP-HI survey of Milky Way gas towards the Small Magellanic Cloud. Within this region, I investigate the variation of cold gas properties as a function of spatial resolution, specifically of a cold gas filament, to test the efficacy of phase separation for extra-galactic counterparts where cold gas is not resolved.

Chapter 5 summarises my results, and plans the future directions for this work.

Chapter 2

Considerations with Stacking Absorption Spectra

Context and Contribution

This chapter presents the contents "Considerations with stacking absorption spectra: cold H I gas in cirrus region of the Milky Way" by C. Lynn, A. Marchal, N. M. McClure-Griffiths, Marc-Antoine Miville-Deschênes, C. E. Murray, H. Nguyen, J. Dempsey, E. Di Teodoro, J. Th van Loon, J. M. Dickey, M-Y. Lee, G. Joncas, Yik Ki Ma, N. M. Pingel, S. Stanimirović, I. Kemp, S. Gibson, and H. Dénes published in press to the Monthly Notices of the Royal Astronomical Society, 2025, MNRAS, 536, 4, 3538–3553, available on https://doi.org/10.1093/mnras/stae2818. The work is presented here exactly as in the publication. I worked alongside other members of the GASKAP-HI team to prepare and reduce the pilot survey data used in this work, including the GASKAP-HI emission map. I carried out all of the analysis, including the application of the spectral stacking and decomposition for H I emission-absorption sightlines. I have written the manuscript, with insightful feedback and suggestions from the co-authors.

Abstract

We use the Milky Way neutral hydrogen (H I) absorption and emission spectra from the Galactic Australian Square Kilometre Array Pathfinder (GASKAP) Phase II Pilot survey along with toy models to investigate the effects of stacking multi-component spectra on measurements of peak optical depth and spin temperature. Shifting spectra by the peak in emission, "primary" components shifted to 0 km s^{-1} are correctly averaged. Additional components on individual sightlines are averaged with non-centred velocities, producing a broader and shallower "secondary" component in the resulting stack. Peak optical depths and brightness temperatures of

the secondary components from stacks are lower limits of their true average values due to the velocity offset of each component. The spin temperature however is well correlated with the truth since the velocity offset of components affects the emission and absorption spectra equally. Stacking 462 GASKAP absorption-emission spectral pairs, we detect a component with a spin temperature of 1320 ± 263 K, consistent with gas from the unstable neutral medium and higher than any previous GASKAP detection in this region. We also stack 2240 pilot survey spectra containing no Milky Way absorption, revealing a primary narrow and secondary broad component, with spin temperatures belonging to the cold neutral medium (CNM). Spatially binning and stacking the non-detections across the plane-of-sky by their distance from CNM absorption detections, the primary component's optical depth decreases with distance from known locations of cold gas. The spin temperature however remains stable in both components, over an approximate physical plane-of-sky distance of ~ 100 pc.

2.1 Introduction

Neutral hydrogen (H I) is the most abundant element in the Universe, making it an important tracer for large-scale galactic morphology. Because H I is the building block of stars, understanding its temperature in the current epoch of the interstellar medium (ISM) is crucial to our understanding of the current state of star formation in the Milky Way.

Through a combination of observations and theory, H I has been best described with a bi-stable model with two stable temperature regimes: the warm neutral medium (WNM), $T_s \sim 4000 - 8000$ K in the Solar neighbourhood, filling most of the H I volume, and the cold neutral medium (CNM), $T_s \sim 25 - 250$ K, that exists in dense cold clumps enveloped by the WNM. Between these two temperature regimes lies the thermally unstable neutral medium (UNM), a region thought to be produced by the condensation of the WNM via thermal instability (Field 1965; Field et al. 1969; Wolfire et al. 1995, 2003; Hennebelle & Pérault 1999, 2000; Audit & Hennebelle 2005).

Observationally, the CNM is the easiest of the three phases to detect in absorption, even through low sensitivity observations, due to its typically high optical depth and column density (Lazareff 1975; Dickey et al. 1977; Crovisier et al. 1978; Heiles & Troland 2003; Mohan et al. 2004; Roy et al. 2013a; Begum et al. 2010). However, the UNM and WNM, due to their lower opacity, require high sensitivity observations and instruments to be observed in absorption (Carilli et al. 1998; Dwarakanath et al. 2002; Patra et al. 2018). Therefore, most of their physical properties have been estimated from H I emission alone, decomposed through methods of Gaussian decomposition (Haud 2000; Nidever et al. 2008; Lindner et al. 2015; Kalberla & Haud 2018; Riener et al. 2019; Marchal et al. 2019; Marchal & Miville-Deschênes 2021).

It is only recently with advances in absorption survey sensitivity and field-of-view that we have the number of sightlines to be able to stack Galactic H I absorption spectra to improve their signal-to-noise. Using absorption sources from the first half of the 21-SPONGE survey, Murray et al. (2014) stacked the spectra from 19 sightlines with Milky Way H I absorption to improve the optical depth sensitivity to the point of detecting the Milky Way's WNM in absorption ($\sigma_\tau \approx 2.6 \times 10^{-4}$). The spin temperature of this component was approximately 7200^{+1800}_{-1200} K. With the completed 21-SPONGE survey catalogue, Murray et al. (2018) conducted a similar stacking process, detecting a spin temperature of $\sim 10^4$ K. While this was one of the first steps in using stacking techniques with H I absorption, the 21-SPONGE survey is limited both in the small number of sightlines used as well as sources being located vast distances from each other on the plane-of-sky, yielding an average of gas that may not physically be interacting or connected.

In this work, we make use of recent observations of Galactic absorption and emission in the direction of the Magellanic system ($-45° < b < -25°$, $270° < l < 300°$). The gas of the Milky Way in this direction forms two distinct filamentary structures overlapping each other (Nguyen et al. 2024; Lynn et al., in preparation). The H I survey in this region of the sky comes from the pilot phases of the Galactic Australian Square Kilometre Array Pathfinder (GASKAP) survey, observing the region with a spatial resolution of 30 arcsec (Dickey et al. 2013). Using the absorption pipeline for GASKAP described in Dempsey et al. (2022), the absorption survey searched in an unbiased manner across the full plane-of-sky survey range, producing a large number of 462 detections of Galactic H I absorption.

While the individual detections sightlines are used for studying the physical and spatial properties of cold gas in the cirrus gas of the Milky Way (Nguyen et al. 2024; Lynn et al., in preparation), we instead focus on utilising stacking both the detections sightlines, as well as the non-detections of Galactic H I absorption. Through stacking these two samples independently, we probe the global properties of the gas that lies beyond the sensitivity limits of individual spectra through GASKAP's current operational sensitivity, revealing the higher temperature phases of H I gas in this region of the sky. The large number of the non-detections also allows for stacking sources based on their spatial distribution to investigate differences across the sky, a technique that was not possible previously.

In this work, we present analysis of the optical depth and spin temperature of H I gas in the Milky Way towards the Magellanic system and the spatial distribution of these properties through stacking the detection and non-detection sources from the GASKAP Pilot Phase II observations (Nguyen et al. 2024). The chapter is organised as follows. Section 2.2 presents the data used in this work. In Section 2.3, we provide a theoretical background on stacking lines-of-sights with multiple Gaussian components and the consequences for extracted parameters. Section 2.4 investigates stacking the detection spectra after subtracting the already detected cold gas components from Nguyen et al. (2024). Section 2.5 then describes the stacking analysis of our GASKAP non-detection catalogue using (i) the whole sample, and (ii) spatially distinct bins based on their proximity to known locations of cold gas. A discussion and summary are provided in Sections 2.6 and 2.7.

2.2 Data

2.2.1 Observations

We made use of observations from the GASKAP-HI Pilot Phase II survey using the Australian Square Kilometre Array Pathfinder (ASKAP) (Dickey et al. 2013). The observations were taken from 2021 October (SBID 33047) to 2022 April (SBID 38845) with each field gaining 10 h of exposure. The Pilot Phase II observations comprise ten 25 square-degree adjacent fields of view covering the entire Large Magellanic Cloud, Small Magellanic Cloud, as well as the whole Magellanic Bridge. Put together, the fields form a large mosaic from which we have analysed the background sources seen in absorption against the Milky Way foreground gas that was mapped at local velocities.

2.2.2 Source Catalogues

Detections

Nguyen et al. (2024) utilised the GASKAP absorption pipeline developed by Dempsey et al. (2022) to process 2714 sources of H I absorption and their spectra. Twelve of these absorption spectra were saturated and removed from the sample. The remaining 2702 sources selected had a background source flux, S_{cont}, greater than 15 mJy. Of these spectra, 462 were deemed to contain detections of H I absorption from gas pertaining to the Milky Way, defined as having a point above 3σ and a neighbouring channel above 2.8σ. Nguyen et al. (2024) used Gaussian

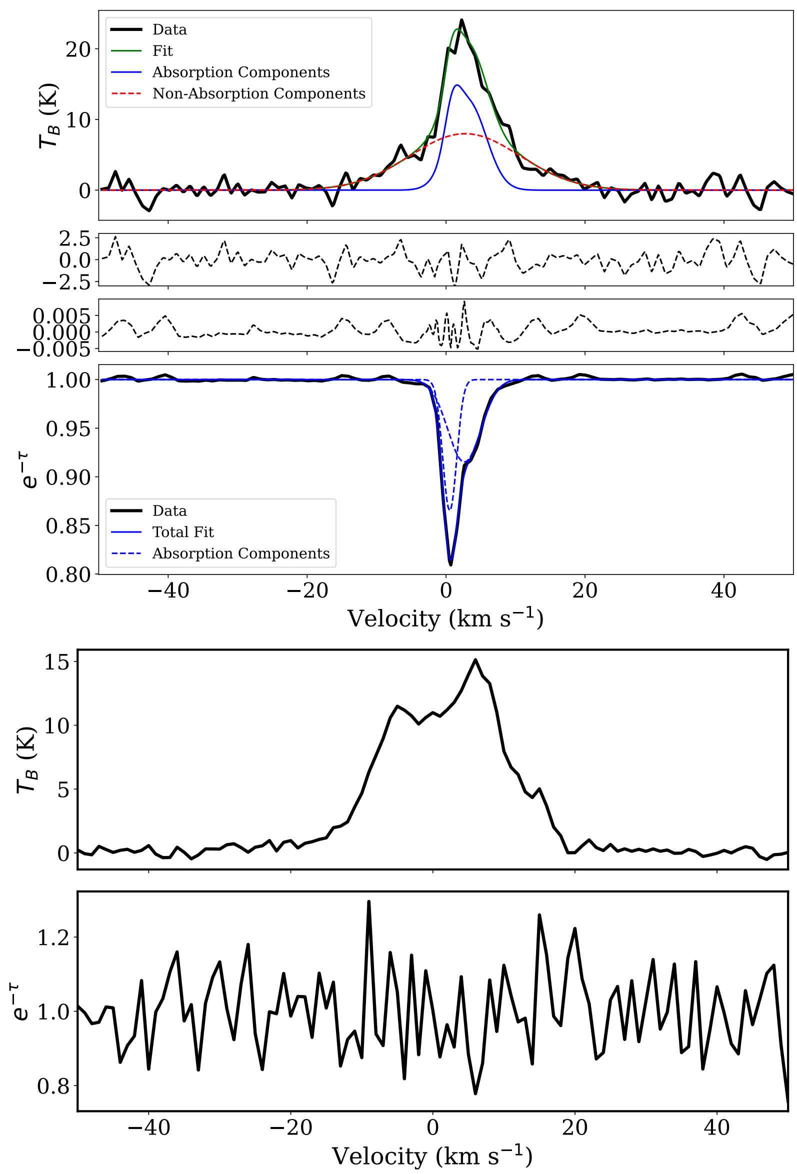

Figure 2.1: Top panels: Brightness temperature T_B in units of kelvin of the absorption source J040848-750719 from the detection catalogue (top), and its corresponding absorption profile $e^{-\tau}$ (bottom). The coloured lines show the Gaussian decomposition as documented in Nguyen et al. (2024), with the fit of the Gaussian components found in absorption (dashed blue lines) along with their total contribution in emission (solid blue), an additional component added in emission tracing warm gas not found in absorption (dashed red) and the total fit of the emission profile (green). Bottom panels: Brightness temperature T_B (top) and its corresponding absorption profile (bottom) of a randomly selected line-of-sight with no detected Galactic H I absorption.

Table 2.1: Sample of GASKAP Pilot Phase II non-detection parameters.

Source	l (°)	b (°)	σ_τ [a] ($\times 10^{-3}$)	$v_{\rm peak}$ [b] (km s^{-1})
J055932−634614	273.2	−29.8	244.5	2
J044109−631421	273.9	−38.5	158.0	12
J053738−624208	272.0	−32.3	93.3	6
J060128−624704	272.0	−29.6	204.9	−1
J053234−631640	272.7	−32.8	149.0	5
J060038−674747	277.8	−29.7	154.8	−5
J003524−732222	304.5	−43.7	116.5	0
J044926−691203	280.7	−35.9	88.5	3
J050107−691737	280.5	−34.9	190.4	4
J013229−734122	299.0	−43.1	238.4	1

Notes:
[a]: Mean rms noise in optical depth over all velocity channels.
[b]: Line-of-sight velocity of the peak in brightness temperature.

decomposition to then analyse the spin temperature and optical depth properties of the cold gas in these detection sightlines.

Relevant for this work, Fig. 2.1 (top panels) displays one of these absorption detections (bottom) against the radio source J040848-750719 and its associated emission spectra interpolated around the source (top). It is noteworthy that there are multiple peaks seen in absorption against this source. The blue and red lines show the modelled contribution from the cold and warm gas obtained following the methodology prescribed in Heiles & Troland (2003).

The mean rms noise of the detection sample is approximately $\sigma_\tau = 4.2 \times 10^{-2}$ and a median of around 3.1×10^{-2}, around 15 times higher than the noise level of individual channels in more sensitive observations like 21-SPONGE (Murray et al. 2014, 2018). However, the main advantage with the GASKAP survey is the order of magnitude increase in the number of sightlines available to stack.

Non-detections

In this work, we also used the remaining 2240 sources where there were no detections of H I absorption with a signal-to-noise greater than 2.8 in multiple neighbouring channels. Hereafter, we will refer to them as the non-detection sample. An example of an absorption-emission pair selected randomly from the non-detection sample is shown in Fig. 2.1 (bottom panels). While the sensitivity of the absorption profile is too low to detect any features, the associated emission spectrum shows prominent peaks, one of which is relatively narrow, that reveal the presence of CNM gas mixed within the warmer phases of the ISM (i.e., the UNM and the WNM).

Table 2.1 lists the source name, Galactic coordinates l and b, average rms noise σ_τ over all velocity channels, and velocity at the peak brightness temperature $v_{\rm peak}$ of ten sample entries of the 2240 non-detection source catalogue. The mean rms noise of the non-detections is $\sigma_\tau = 0.18$ with a median rms noise of approximately 0.14. The noise level of the GASKAP absorption sightlines is several orders of magnitude higher than that of 21-SPONGE (Murray et al. 2018). However, similar to the detection sample, this noise level increase is countered by having two orders of magnitude more sources than that used in the stacking analysis in Murray et al. (2014, 2018).

Flux versus Sensitivity

A comparison between the two data sets of detections and non-detections is shown in Fig. 2.2, comparing their background source flux and the mean rms noise of their absorption spectra. Detections and non-detections are shown in orange and blue, respectively. We note that the detections typically have higher background source fluxes, where there is a higher probability of the line-of-sight (LOS) producing a detection of absorbing gas. Most of the detections are within the same parameter space as the non-detections. However when the noise level is greater than $\sigma_\tau \sim 3 \times 10^{-1}$, the spectra are too noisy for any gas regardless of its opacity to produce a signal beyond the $\sim 3\sigma$ signal-to-noise requirement of a detection.

Since the non-detections spectra have similar background source fluxes to most of the detections, there is nothing intrinsically different about these spectra other than the higher noise levels. Thus, while the non-detection sources did not meet the criteria for being used in regular absorption analysis (Dempsey et al. 2022; Nguyen et al. 2024), they should nonetheless still contain astrophysical signals buried within their noise.

2.2.3 Emission Data

To pair these absorption sightlines with emission data, we made use of the H I emission data provided by the GASKAP Pilot surveys as mentioned in Section 2.2.1. The emission data have a beamsize of 30 arcsec and native spectral resolution of 0.24 km s^{-1}. For noise reduction, the emission and absorption spectra were binned spectrally by a factor of 4 to a spectral resolution of $\sim$ 1 km s^{-1}. As the emission sightline located at the position of H I absorption is affected by the absorbing feature, emission spectra from nearby sightlines on the plane-of-sky were used instead, assuming that the gas within this distance is similar. These emission sightlines also have to be far away enough from each other that beam smearing does not affect their average. For this purpose, we used a method similar to that of Nguyen et al. (2024). For each absorption sightline, approximately 20 emission sightlines were selected around the absorption feature, within an annulus of inner-radius 1 beam-radius and outer-radius 2.5 beam-radii, ensuring each is at least 1 beam-radius from other sightlines. These emission sightlines are then averaged, weighted by the inverse of their plane-of-sky distance from the absorption sightline at the centre.

Fig. 2.3 shows the locations of the absorption sightlines, including both detections and non-detections at Milky Way velocities in the velocity range $-50 < v < 50$ km s^{-1} overlaid onto the column density map of the region taken from the Galactic All-Sky survey computed in the optically thin limit (GASS, surveyed with the Parkes telescope with a beam size of 16′ and 1 km s^{-1} spectral resolution; McClure-Griffiths et al. 2009; Kalberla et al. 2010; Kalberla & Haud 2015a). The column density map highlights the vertical and horizontal H I filamentary structures in the region, defined by high H I column density and high brightness temperature (Lynn et al., in preparation).

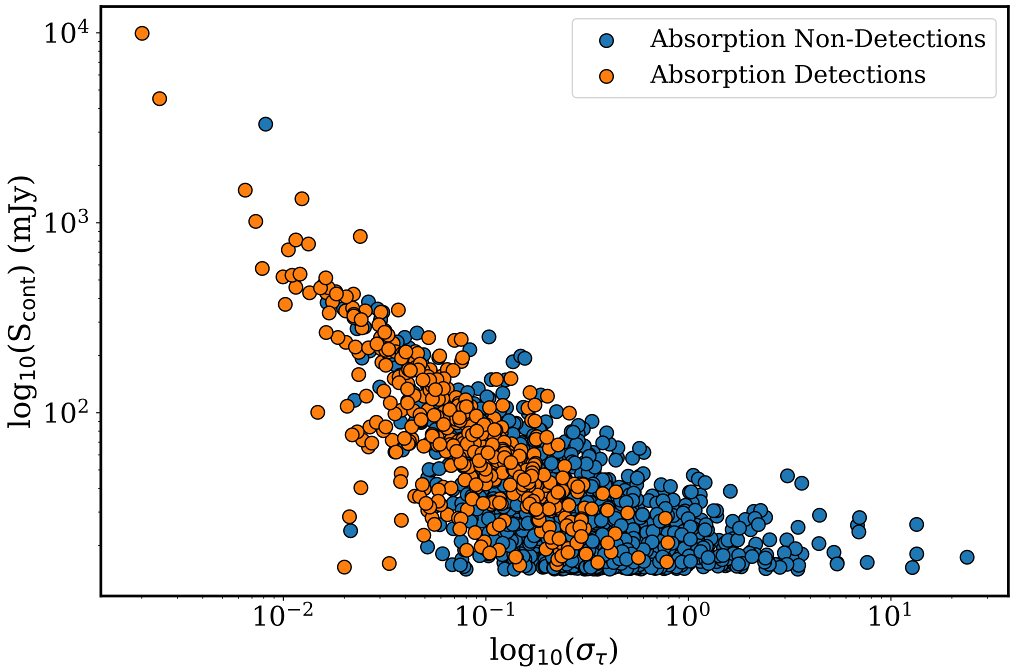

Figure 2.2: Scatter plot of the background source flux, S_{cont}, versus the optical depth noise, σ_τ, for each source of the 2240 non-detections (blue) and the 462 detections (orange) of Milky Way H I absorption. All sources, regardless of detection, have a background flux higher than the cut-off of 15 mJy (Dempsey et al. 2022).

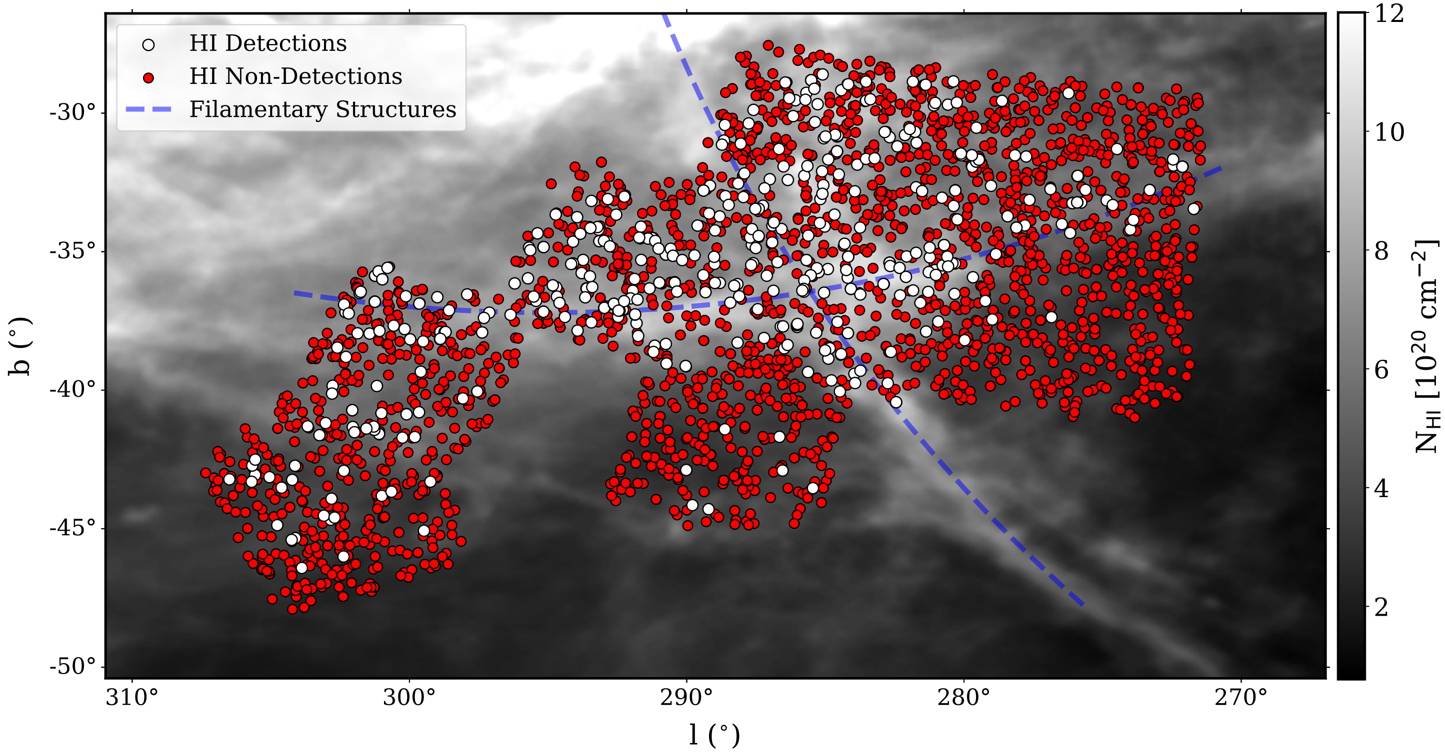

Figure 2.3: Spatial distribution of background sources from the GASKAP-H I absorption survey overlaid on a grey-scale map of the column density of H I gas computed in the optically thin limit from the GASS survey (McClure-Griffiths et al. 2009; Kalberla et al. 2010; Kalberla & Haud 2015a). Detections of cold gas in the velocity range $-50 < v < 50$ km s^{-1} are annotated with white circles. Sightlines with non-detections of cold gas in absorption are shown with red circles. The blue dashed lines indicate the arcs of the vertical and horizontal H I filaments in this region of the Milky Way (Lynn et al., in preparation).

2.3 Stacking Considerations

When stacking multiple spectra to produce an approximate average spectra over a region, one needs to take into consideration the effects of averaging multiple Gaussian components that are potentially misaligned in velocity. In this section, we explore, through use of the GASKAP detection sample, the biases introduced by mixing complex multiphase emission and absorption spectra through stacking.

2.3.1 Velocity Alignment

When stacking spectra, the first thing we must consider is how to account for effects like Galactic rotation, or bulk motions of gas that could displace components in line-of-sight velocity. For this work we explore shifting the emission and absorption spectra such that the peak brightness temperature is centred on 0 km s^{-1}. The peak in emission typically traces cold gas and so shifting to centre this ensures that at least the bulk of H I cold gas is centred on the same velocity when stacking. With sightlines containing single components, this method of shifting perfectly aligns all components to produce a true average spectrum. We note that in reality some minor deviations are present between the peak in emission and absorption that are typically on the order of $1-2$ km s^{-1}, as observed in the GASKAP detections (Nguyen et al. 2024). These deviations are due to a combination of the difference in noise-levels between the emission and absorption spectra as well as the emission and absorption spectra probing slightly different gas as they are not along the same sightline. These effects cause some uncertainty in the central velocity of the peak of absorption and its alignment with the peak in emission. However, the $1-2$ km s^{-1} deviation is negligible compared to the $\sim 10-15$ km s^{-1} variation in central velocities of cold components in this region of the sky (Nguyen et al. 2024).

Other methods in the past have utilised shifting by the first velocity moment (Murray et al. 2014, 2018) producing similar results with single components as this simplifies to centring by the peak. However, the two shifting methods deviate when we consider sightlines with multiple components. As shown in the example detection spectra of Fig. 2.1, the most sensitive detection sources showcase multiple components: a narrow primary component aligned well to the peak in the respective emission profile and a slightly broader secondary component offset in velocity. Therefore, velocity shifting needs to be able to accommodate for the existence of multiple clouds along a sightline. In a multiphase medium with multiple components per sightline, none of the components along a line-of-sight will be perfectly centred to 0 km s^{-1} if shifted by the first velocity moment. When stacking these partially shifted spectra, the key features of colder and warmer phases will be heavily mixed together.

Since in a general stacking case, we are unsure of the number of components in each sightline prior to stacking, shifting by the first velocity moment will make it difficult to separate out the phases of H I through Gaussian decomposition. If we shift instead by the peak in emission, we avoid these problems, as we standardise the individual sightlines such that the bulk of cold gas (traced by the peak in emission and henceforth referred to as the "primary component") is centred to the same velocity. While additional components at other local maxima will be mixed together since their central velocities are not accounted for (producing what will be referred to as the "secondary component"), shifting in this manner allows for easier separation of the phases of H I with a major part of the cold phase aligned in velocity at 0 km s^{-1} prior to stacking.

2.3.2 Stacked Spectrum

The GASKAP detection sample provides a unique opportunity to test how stacking affects measured properties, given that the sightlines are all in the same plane-of-sky location, and sightlines contain multiple cold components (Nguyen et al. 2024).

Our stacking analysis follows the procedure described in Murray et al. (2014), where they formed a stack of 19 absorption spectra from the 21-SPONGE survey, after subtracting Gaussian fits for cold gas, to investigate properties of the WNM. For this section, however, we are using the un-subtracted detection spectra as observed, containing all the phase information of the ISM to compare the stack with the average properties of the individual sightlines.

The stacked spectrum was obtained by taking the average of the sample weighted by the noise of each absorption spectrum, with weights $\tau_{\rm res}/\sigma_\tau^2$ (Treister et al. 2011) to favour spectra with lower noise. The weights simplify to $1/\sigma_\tau$ since $\sigma_\tau \propto T_{\rm B}$ and for constant temperature, $\tau_{\rm res} \propto T_{\rm B}$ (Murray et al. 2014). The same weights were applied in the stack of the emission spectra. Fig. 2.4 shows the stacked emission and absorption spectra (top and bottom panel, respectively). The absorption stack produces a two-component profile; a deep, narrow, primary component, and a broad secondary component.

2.3.3 Gaussian Decomposition

To properly Gaussian decompose the stacked spectra, we implemented the method prescribed in Heiles & Troland (2003) to model their spin temperatures individually. Two Gaussian components were fitted to the absorption stacked spectrum.

The fitting parameters were then used to model the amplitude of their emission counterparts, allowing for a ± 1 km s^{-1} deviation in their central velocities and 10 per cent deviation in their widths. An additional broader Gaussian component was added to fit the signal in emission to ensure the column density of the fit was not lower than that of the original data from GASKAP, and that the correction factor, $R = N_{\mathrm{H\,I}}/N^{*}_{\mathrm{H\,I}}$, was greater than one, where $*$ denotes the column density computed in the optically thin regime. The additional component in emission represents gas from the WNM that is not able to be detected in absorption due to the insufficient optical depth sensitivity of our stack. The resulting decomposition is displayed in Fig. 2.4. It should be noted that a potential bias in adding only a single emission-only component is that it under-represents the spin temperature of the absorption feature. Adding additional components to fit the same data would lead to them being narrower in width and shallower in amplitude, allowing the absorption components to more closely fill the emission at the peak. This higher amplitude in brightness temperature would lead to a higher recorded spin temperature.

When solving the radiative transfer equation of the line, we accounted for each possible permutation of the broader emission component being in either the foreground or background relative to the colder components seen in absorption along the LOS. For the fraction of warm gas in the background (and hence absorbed by the cold gas infront of it), we used three values: 0, 0.5, and 1. Averaging these solutions to the radiative transfer yielded the mean spin temperatures. The primary and secondary component of the total stacked spectrum using all 462 detection sources have a mean spin temperature of $T_s = 68 \pm 7$ K and 159 ± 58 K, peak optical depth of $\tau_{\mathrm{peak}} = 0.160 \pm 0.033$ and 0.040 ± 0.007, and full-width half-maximum (FWHM) of 3.4 ± 1.4 km s^{-1}, and 12.5 ± 1.1 km s^{-1},, respectively. The uncertainties are produced through a method of bootstrapping, where new samples of 462 detection spectra were sampled from the original 462 sightlines with replacement. Repeating the stacking and fitting process of the new sample, and repeating this 10^5 times, the standard deviations of the above measurements of T_s, τ_{peak}, and FWHM were computed.

2.3.4 Comparison of Stack versus Original Sample

To examine the effect of stacking spectra on the measurements properties of spin temperature, optical depth, and FWHM, we can compare these values to that of the individual detection sightlines, using the properties extracted by Nguyen et al. (2024). Following the discussion in Section 2.3.1, absorption detection components located closest spectrally to the peak in emission in each detection sightline are con-

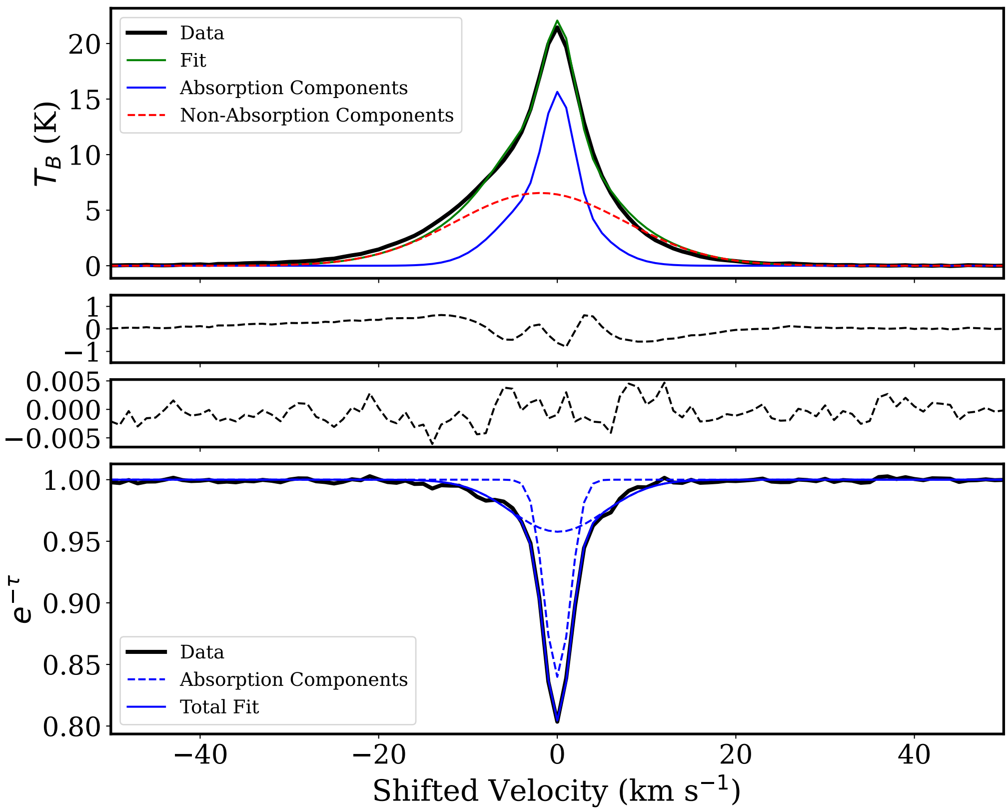

Figure 2.4: Top: Weighted-mean emission profile of the stacked GASKAP detection spectra. The original stacked spectrum is shown in black and the model of the joint Gaussian decomposition in green. The model is made by the addition of the emission produced by the narrow and broad components (shown in blue), and an additional broad component required to complete the fit (shown by the red dashed line). Middle: Residual profiles of the emission (middle top) and absorption (middle bottom) fits. Bottom: Weighted-mean absorption profile of the stacked GASKAP detections. The original stacked spectrum is shown in black. The narrow and broad components' absorption fits are shown by the blue dashed lines, with their total contribution to the absorption profile shown in the solid blue line.

sidered primary components. The remaining absorption components are collected as the secondary components in each spectra. Fig. 2.5 shows the comparison between the observed peak τ, FWHM, and spin temperatures of both stacked components and the distribution of the individual sightlines' primary and secondary components. We generate the weighted mean of these individual sightline properties using the same weighting of the inverse of the optical depth noise that produced the stacks. The uncertainty in these means were calculated by adding the uncertainty of the mean and the systematic errors in quadrature. The systematic errors were approximated as the mean of the uncertainties of individual sightline values in $\tau_{\rm peak}$, FWHM and $T_{\rm s}$. When considering the overlap of the errors in the stacked values and that of the mean individual values, we find that the primary component's optical depth and FWHM are both accurate representations of an average value. However when it comes to the secondary component, the observed peak optical depths lies below the mean of the individual sightline peak τ measurements that produced them. Conversely, the FWHM measurements observed in the secondary component's stack lie above the mean FWHM of the individual sightline components.

The reason for this discrepancy between the secondary component's stacked values compared to the mean properties of the individual sightlines comes from the velocity offset of components. Since the components are slightly offset in velocity from each other, the width of the resulting stacked Gaussian will be wider than the average of the individual Gaussians. Due to the total flux of all the components being conserved in the average stack, if the width of the Gaussians is increased, to compensate the amplitude of the resulting stacked Gaussian must diminish. Therefore, regardless of the severity of the range of central velocities of secondary components in individual sightlines, the peaks will always be lower limits and their widths always greater than the average of the individual components themselves.

The primary components on the other hand, aligned with the peak in emission, are shifted correctly to roughly 0 km $\rm s^{-1}$ with some minor deviation due to possible slight offset between absorption and emission peaks in velocity (as mentioned in Section 2.3.1). As such the primary component's lack of a noticeable velocity offset leads to the stacked result representing a relatively accurate average of the peak optical depth and FWHM.

When calculating the spin temperatures of the components, the primary component's stack and mean values are well aligned along with their uncertainty envelopes. The secondary component's values are also similar. While their uncertainty envelopes do not perfectly align, it should be noted that due to the potential biases in spin temperature by only including one emission component (as mentioned in Section

2.3.2), it is likely we are undersampling the error in the observed stacked temperature. Therefore we conclude that both the primary and secondary components' spin temperatures are well aligned with the means of the original distributions. This is due to the fact that since the velocity offset of components is equal in both emission and absorption, the peaks of emissions and absorption are affected in a similar way. Since the spin temperature is found through the division between peaks in brightness temperature and optical depth, the velocity offset effect is cancelled out, resulting in a spin temperature that is well correlated to the true average temperature of the individual sightlines' components. An exploration into this velocity offset effect is explored in Appendix A.1.1 where toy models are used instead of real detection data, yielding similar results.

2.3.5 Theoretical Implications

From stacking the detection sample and comparing the result with the individual sightline properties (as well as through the use of toy models in Appendix A.1.1), we find several effects to be considered.

The uncertainty of the true peaks and widths of the stacked components means we should be cautious when calculating secondary information extracted from emission-absorption pair stacks that use these values such as the FWHM, corresponding turbulent Mach numbers and mass fractions, as they become unreliable.

This is especially true for extragalactic observations, where individual sightlines' beamsizes pass through much larger portions of a galaxy than Galactic observations. The large amount of extragalactic ISM material mixed together at various velocities will broaden the Gaussian components in a similar manner to that of the secondary component explored in this section, with individual sightlines acting as a pseudo-stack of the region. As a result, a similar effect will occur and peak optical depth measurements of extragalactic sources should take this lower-limit effect into account when determining results.

The rest of this work will calculate and report parameters including the peak optical depth, FWHM and spin temperature. However, other quantities such as the turbulent Mach number, column density and mass fraction will not be discussed as they develop large uncertainties, as mentioned above.

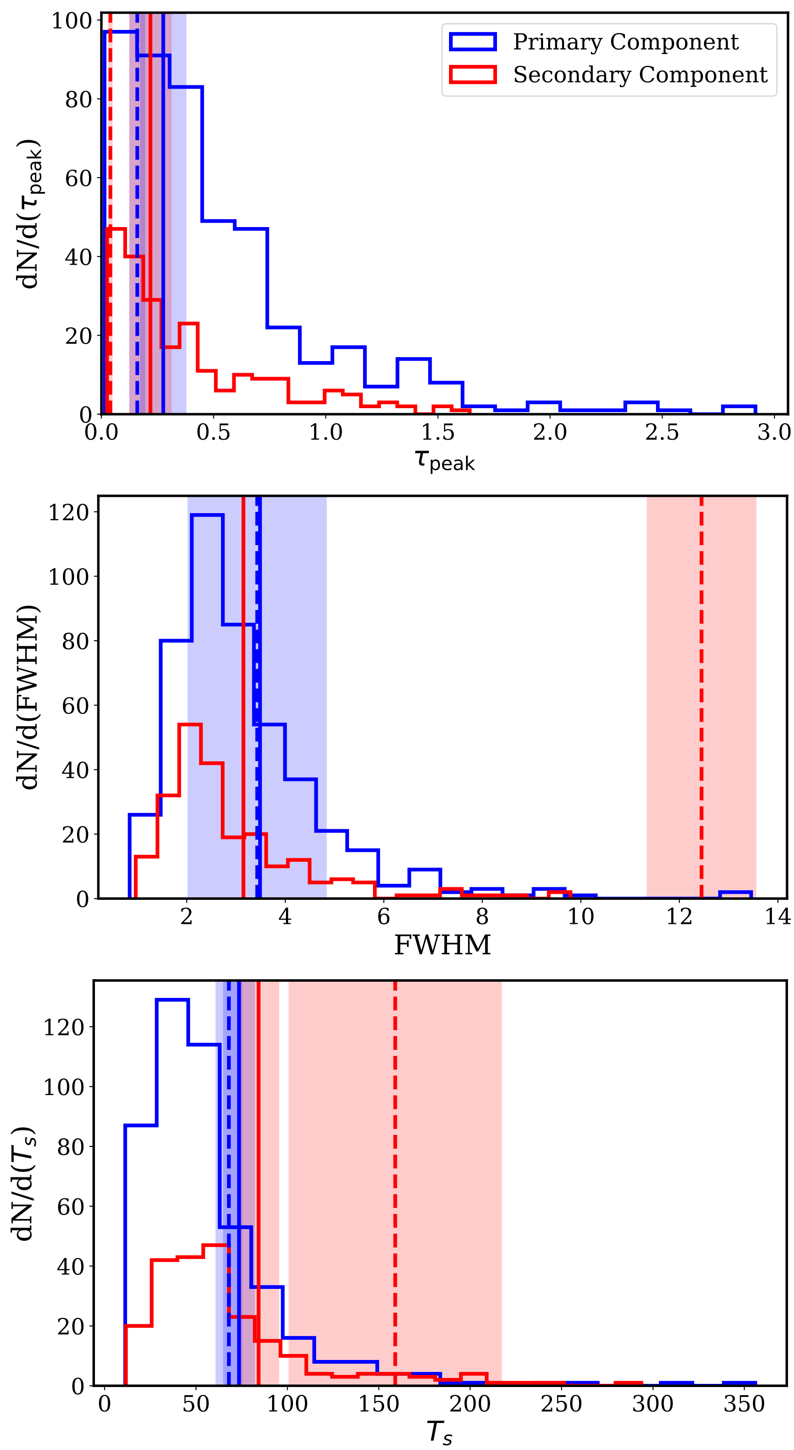

Figure 2.5: Distributions of the peak optical depth (top), FWHM (middle), and spin temperature (bottom) of individual absorption components found by Nguyen et al. (2024). The components are separated into primary components (blue), which are aligned with the peak in their corresponding emission spectra, and secondary components (red), containing additional components offset from the emission peak. The solid vertical lines represent the mean of these distributions in their respective colours. The dotted lines highlight the values obtained from the detection stack in Fig. 2.4 with the shaded regions representing the uncertainties of both the mean and observed stacked values.

2.4 Stacking Model-Subtracted Detections

In this section, we investigate the existence of higher temperature H I gas in the region of the GASKAP-HI Pilot survey by stacking the GASKAP detection spectra after subtracting the cold gas already detected from Nguyen et al. (2024).

2.4.1 Model Subtraction

Higher temperature phases of H I tend to have weaker signals in absorption due to lower optical depths. In order to detect these higher temperatures in absorption, we must first subtract the cold gas already detected from individual sightlines. For each of the 462 detection sightlines, Nguyen et al. (2024) catalogues the fitted model parameters of the cold gas detected in absorption and emission. The modelled Gaussian absorption and emission components, $\tau_i(v)$ and $T_{\mathrm{B},i}$ (where i indicates the ith component) were subtracted from the respective spectra from which they were detected to produce 462 residual absorption spectra, $\tau_{res}(v) = \tau(v) - \Sigma\tau_i(v)$, and residual emission spectra $T_{\mathrm{B},res}(v) = T_{\mathrm{B}}(v) - \Sigma T_{\mathrm{B},i}(v)$.

2.4.2 Stacked Spectrum

Since we have removed the majority of the signal through subtracting the cold gas components, we no longer have information about the velocity of the remaining underlying absorption hidden beneath the noise in individual detection spectra. We follow the same procedure as in Section 2.3.1, relying on the GASKAP emission data to align the spectra before performing the stack to account for Galactic rotation and large scale bulk motions in the region.

To produce the stacked model-subtracted emission and absorption spectra, we use the same weighting as in Section 2.3.2 following Murray et al. (2014). The resulting stacked emission and absorption spectra are shown in Fig. 2.6. The rms noise of the stacked spectrum is $\sigma_\tau = 1.1 \times 10^{-3}$, calculated from taking the standard deviation of 30 empty channels in the post-shifting velocity range $-50 < v < -20$ km s^{-1}. The stacked detection spectra's noise level is almost 40 times smaller than the mean rms noise of the individual detection sightlines ($\sigma_\tau = 4.2 \times 10^{-2}$) and nearly 30 times smaller than their median rms noise ($\sigma_\tau = 3.1 \times 10^{-2}$). The stacked absorption profile has an equivalent width (EW) in the velocity range $-50 < v < 50$ km s^{-1} of $\mathrm{EW} = \int_{-50}^{50} (1 - e^{-\tau})\, dv = 0.12$km s^{-1} (Murray et al. 2014).

To ensure that our stack is not plagued by any outlying spectra and the detected component of the stack is not produced by only a few dominant narrow profiles in the average, we conducted two bootstrapping Monte Carlo simulation experiments (Wall

& Jenkins 2003; Murray et al. 2014) to test for variations in the stack's EW. First, we repeated the stacking analysis on a new sample of 462 sources randomly chosen from our original 462 sightlines with replacement. Repeating this analysis 10^5 times, we computed the EW for each trial. The distribution of these EW values is shown in Fig. 2.7. The distribution is Gaussian, with a mean value of $\langle EW \rangle = 0.12 \pm 0.02$ km s^{-1} (68 per cent confidence), suggesting that the EW computed from the original sample is consistent with being drawn from a parent population of spectra with a comparable mean and is not influenced by outlying spectra. Secondly, we produced a similar EW distribution where in each trial we inverted (multiplied by -1) half of our randomly selected sample. The distribution, also shown in Fig. 2.7, is centred around 0 km s^{-1}, consistent with no signal. The result verifies that our stack does not produce a false signal.

We used the method described in Section 2.3.2 to decompose the stacked spectrum and determine the properties of the remaining gas. The stacked spectrum produces a single wide component in absorption, with a peak optical depth of $\tau_{\rm peak} = (6.6 \pm 0.5) \times 10^{-3}$, FWHM of 16.3 ± 1.4 km s^{-1}, and $T_s = 1320 \pm 263$ K. The uncertainties in these values were evaluated by repeating the same fitting procedure to each of the 10^5 trials of the bootstrapping sample used earlier. These uncertainties are larger than those from the variation of the fraction of background warm gas in the radiative transfer solution.

2.5 Stacking Non-Detections

Stacking the detection spectra is useful for investigating higher temperature gas in sightlines where we know cold gas already exists. However, the GASKAP survey has the unique opportunity to use 2240 non-detection spectra in the same region on the sky that likely also contains information about the multiphase ISM buried within their noise. In this section, we investigate stacking the GASKAP non-detection spectra to reveal more information about cold gas in this region of the Milky Way.

2.5.1 Velocity Alignment

Since there is no information about the velocity of the underlying absorption line hidden beneath the noise in individual non-detection spectra, we rely on the peak in the GASKAP emission data to align them before performing the stack to account for Galactic rotation and large scale bulk motions in the region (as explained in Section 2.3.1).

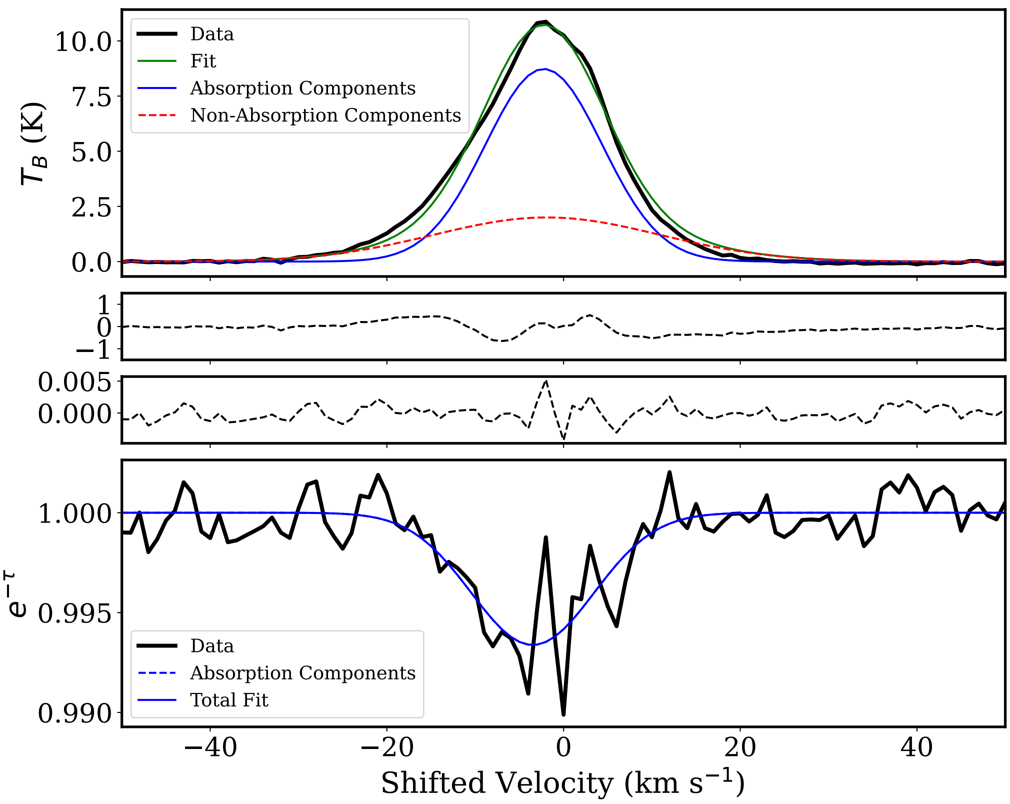

Figure 2.6: Top: Weighted-mean emission profile of the stacked GASKAP detection spectra after subtracting the cold gas models in individual sightlines from Nguyen et al. (2024). The original stacked spectrum is shown in black and the model of the joint Gaussian decomposition in green. The model is made by the addition of the emission produced by the absorption component (shown in blue), and an additional broad component required to complete the fit (shown by the red dashed line). Middle: Residual profiles of the emission (middle top) and absorption (middle bottom) fits. Bottom: Weighted-mean absorption profile of the stacked GASKAP non-detections. The original stacked spectrum is shown in black. The absorption fit is shown by the solid blue line.

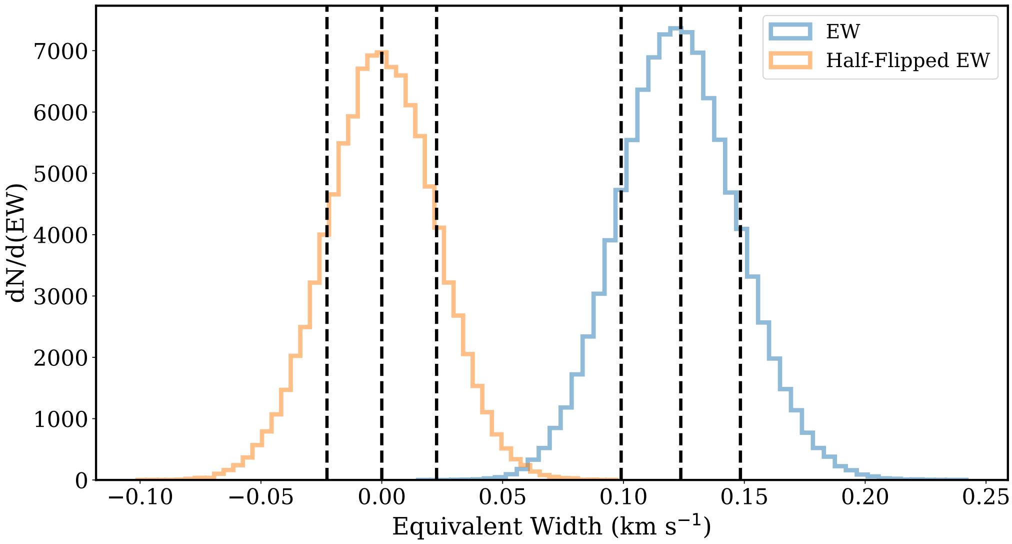

Figure 2.7: Histograms of the EW distribution from 10^5 trials of bootstrapping, randomly sampling 462 spectra from the model-subtracted detection sample derived in Section 2.4.1, with possibility of replacement. The blue histogram displays the distribution of EW values from the trials, with a mean of $\langle \mathrm{EW} \rangle = \langle \int_{-50}^{50} (1 - e^{-\tau}) \; dv \rangle = 0.12 \pm 0.02$ km s^{-1} (68 per cent confidence). The orange histogram displays the same random trials except with half of the spectra inverted (multiplied by -1) before stacking to test for contamination from outlying spectra. The mean of the orange distribution is 0.00 ± 0.02 km s^{-1} (68 per cent confidence). The vertical dotted line crossing the middle of the blue histogram represents the EW of the original stack (EW$=$ 0.12 km s^{-1}). The dotted line along the middle of the orange histogram represents the expected mean of 0 km s^{-1} for the half-inverted stack EW. The additional dashed lines mark the 68 per cent confidence interval for the two distributions.

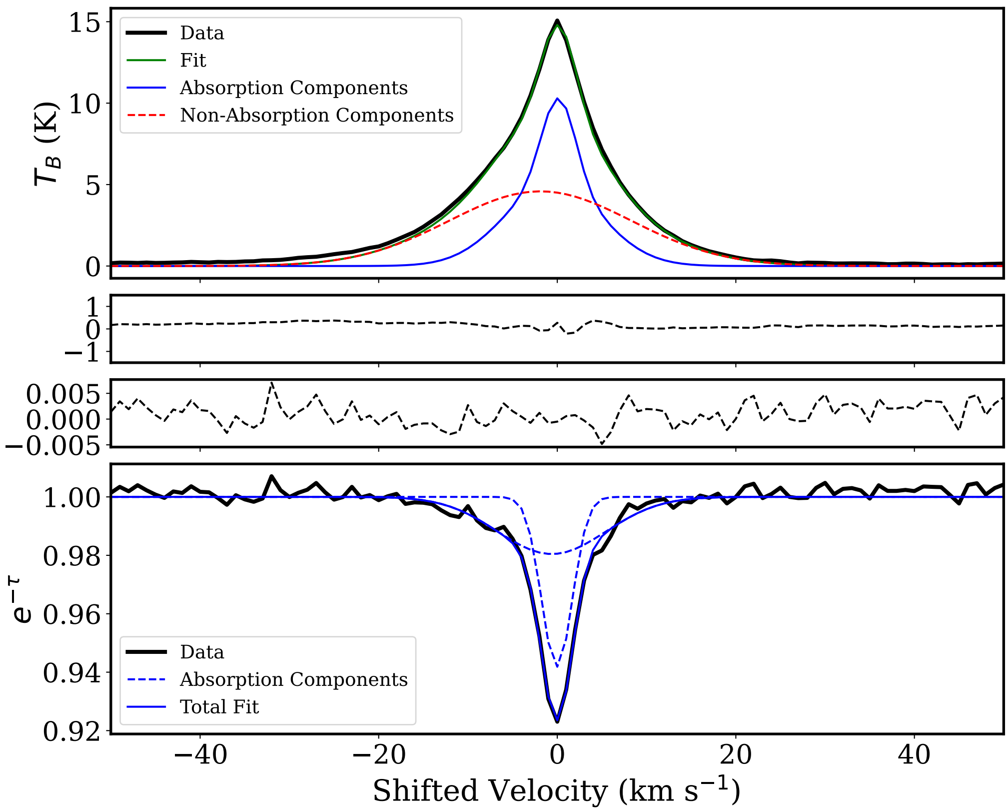

Figure 2.8: Top: Weighted-mean emission profile of the stacked GASKAP non-detections. The original stacked spectrum is shown in black and the model of the joint Gaussian decomposition in green. The model is made by the addition of the emission produced by the narrow and broad components (shown in blue), and an additional broad component required to complete the fit (shown by the red dashed line). Middle: Residual profiles of the emission (middle top) and absorption (middle bottom) fits. Bottom: Weighted-mean absorption profile of the stacked GASKAP non-detections. The original stacked spectrum is shown in black. The narrow and broad components' absorption fits are shown by the blue dashed lines, with their total contribution to the absorption profile shown in the solid blue line.

2.5.2 Stacked Spectrum

For the non-detection stack, we follow the same stacking analysis used in previous sections for the detection sample in Section 2.4.2. The top and bottom panels in Fig. 2.8 show the stacked emission and absorption spectra of the non-detection sample, respectively. The high sensitivity of the absorption stack reveals a two-component profile; a deep narrow primary component resembling absorption profiles of the CNM seen in the detection catalogue, and a broad secondary component.

The rms noise of the stacked absorption profile is $\sigma_\tau = 2.0 \times 10^{-3}$, calculated by taking the standard deviation of 30 empty channels in the post-shifting velocity range $-50 < v < -20$ km s^{-1}. The noise level has decreased from the original mean of $\sigma_\tau = 1.7 \times 10^{-1}$ for the non-detections by nearly two orders of magnitude. The absorption stack's noise level is also approximately 15 times lower than that of the median noise level ($\sigma_\tau = 3.1 \times 10^{-2}$) of the single lines-of-sight classified as detections in the GASKAP-HI absorption survey (Nguyen et al. 2024). The stacked absorption profile has an equivalent width (EW) in the velocity range $-50 < v < 50$ km s^{-1} of EW $= \int_{-50}^{50} (1 - e^{-\tau})\, dv = 0.44$ km s^{-1} (Murray et al. 2014).

To ensure that our stack is not plagued by any outlying spectra and that the primary component of the stack is not produced by only a few dominant narrow profiles in the average, we conducted the same two bootstrapping Monte Carlo simulation experiments used in Section 2.4.2. We completed the stacking analysis on a new sample of 2240 sources randomly chosen from our original 2240 sightlines with replacement. The process was repeated 10^5 times, with the EW computed in each trial. The distribution of EW values is shown in Fig. 2.9. The distribution is Gaussian, with a mean value of $\langle EW \rangle = 0.41 \pm 0.06$ km s^{-1} (68 per cent confidence), suggesting that the EW computed from the original sample is consistent with being drawn from a parent population of spectra with a comparable mean and is not influenced by outlying spectra.

We produced an additional EW distribution where in each trial we inverted (multiplied by -1) half of our randomly selected sample. The distribution, also shown in Fig. 2.9, is centred around 0 km s^{-1}, consistent with no signal. From this result, we conclude our stack does not produce a false signal.

Since there are multiple components within this stacked absorption spectrum, we followed the method described in Section 2.3.2 to decompose the spectra and calculate the gas' properties, tabulated in Table 2.5.3. The primary and secondary component of the total stacked spectrum using all 2240 sources have a mean spin temperature of $T_s = 98 \pm 12$ K and $T_s = 255 \pm 106$ K, respectively. The uncer-

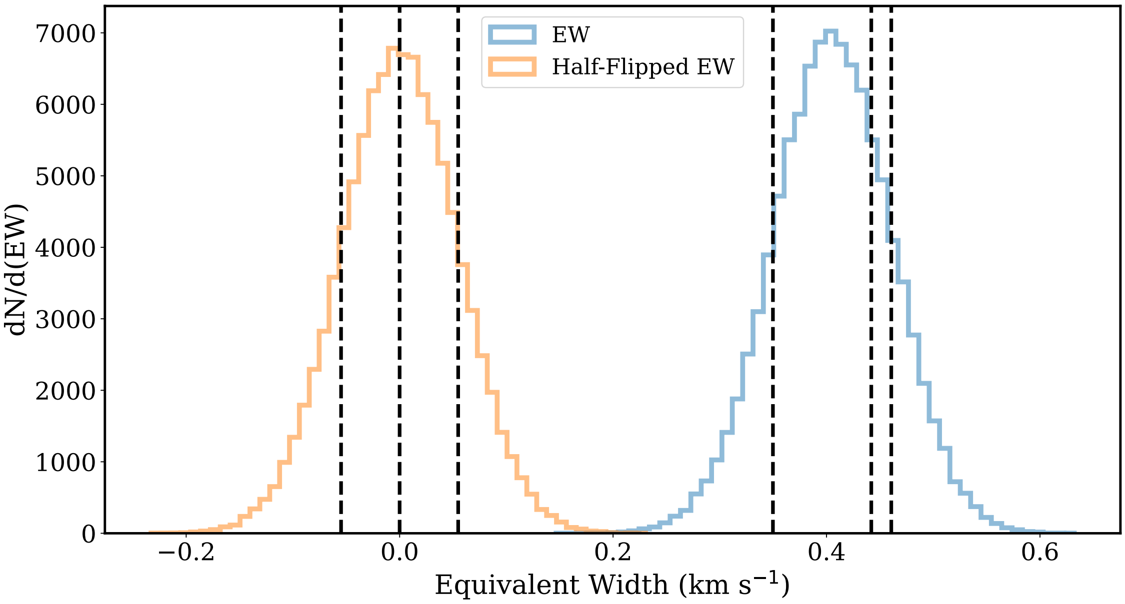

Figure 2.9: Histograms of the EW distribution from 10^5 trials of bootstrapping, randomly sampling 2240 spectra from the total non-detection sample with possibility of replacement. The blue histogram displays the distribution of EW values from the trials, with a mean of $\langle \mathrm{EW} \rangle = \langle \int_{-50}^{50} (1 - e^{-\tau})\, dv \rangle = 0.41 \pm 0.06$ km s^{-1} (68 per cent confidence). The orange histogram displays the same random trials except with half of the spectra inverted (multiplied by -1) before stacking to test for contamination from outlying spectra. The mean of the orange distribution is 0.00 ± 0.05 km s^{-1} (68 per cent confidence). The vertical dotted line crossing the middle of the blue histogram represents the EW of the original stack (EW= 0.44 km s^{-1}). The dotted line along the middle of the orange histogram represents the expected mean of 0 km s^{-1} for the half-inverted stack EW. The additional dashed lines mark the 68 per cent confidence interval for the two distributions.

tainties were evaluated by repeating the same fitting procedure on the 10^5 trials of the bootstrapping sample used above. These uncertainties are larger than those from the variation of the fraction of background warm gas in the radiative transfer solution.

2.5.3 Spatial Distribution of Stacked Features

Given the large number of sources that have been obtained within GASKAP's relatively narrow field of view of the Magellanic system, we have the unique opportunity to search for any spatial variation in the absorption stack profile. In this work, we have chosen to bin the data by increasing source density of detections, allowing us to assess how the profile's peak optical depth and spin temperature change with distance from known locations of CNM gas. Since regions of cold gas typically show higher column densities, this also acts as a probe for binning by column density (as shown in Table 2.5.3).

Table 2.2: Fitted parameters for the total non-detection stack and spatially binned stacks

Bin	N[a]	n[b] (deg^{-2})	N_{tot} ($\times 10^{20}$ cm^{-2})	σ_τ [c] ($\times 10^{-3}$)	Peak τ ($\times 10^{-3}$)	FWHM (km s^{-1})	T_s (K)
Total	2240	0.97±0.76	4.2	2.0	60±10	4.0±1.1	98±12
Non-detections					¿20±10**	¡14.2±1.9**	255±106
1	374	0.08±0.06	2.5	7.0	- *	- *	- *
2	373	0.32±0.09	3.1	7.8	46±20	3.0±1.5	75±26
					¿17±6**	¡13.5±3.6**	306±117
3	373	0.66±0.11	4.0	7.8	87±9	4.1±1.8	77±26
4	373	1.02±0.12	4.8	7.8	62±27	2.7±1.5	89±24
					¿40±15**	¡10.2±4.3**	135±215
5	373	1.48±0.15	5.5	8.1	107±10	5.6±0.7	99±7
6	374	2.28±0.34	6.2	12.2	187±16	6.1±0.3	88±6

Notes:
[a]Number of non-detection sources.
[b]Mean plane-of-sky number density of detection sources.
[c]Mean rms noise over 30 velocity channels from approximately -50 to -20 km s^{-1}.
*Due to the low signal-to-noise of the data in bin 1, a fit could not be made.
**As discussed in Section 2.3, optical depths and FWHM of the secondary components in shifted stacks are lower limits and upper limits respectively.

Binning by Source Density of Detections

One parameter of interest is how the profile's peak optical depth and spin temperature change with distance from known locations of CNM gas. To probe this, we first used the locations of the 462 H I detections of Milky Way absorption in this region (Nguyen et al. 2024) to create a kernel probability distribution function (PDF) of known cold gas. We convert the density values of the PDF into source density of detections in units of sources per square-degree. We attribute to each non-detection a value corresponding to the source density grid at the non-detection's spatial location.

The non-detections were then binned into six equally sized populations based on their respective PDF values. The six regions created from this binning process are displayed via the contour map in Fig. 2.10, overlaid by the location of absorption detections shown in white used to calculate the source density map and the filamentary structures marked in Figure 2.3 for context.

The spatial distribution of the individual non-detection sources after binning is displayed in Fig. 2.11, overlaid onto the column density map from the GASS H I emission survey. Binning using this source density metric highlights a concentric diamond-configuration centred on the Galactic filament cross, marking it as a region densely populated by CNM detections. With each of these bins of non-detections, we repeated the same methodology of stacking their absorption and emission spectra and fitting them using Gaussian decomposition as done in Sections 2.4.2 and 2.5.2 to extract their physical properties. We repeated this using the same Monte Carlo bootstrapping process as done previously to determine uncertainties.

The Gaussian decomposition of each bin is shown in Fig. 2.12. Table 2.5.3 displays the physical properties obtained including the total column density of the bins, $N_{\rm tot} \approx 1.823 \times 10^{18} \int T_{\rm B}\, dv$, peak optical depth, spin temperature and FWHM of each component. We note that with each bin getting closer to regions of cold gas (bin 1 to bin 6 increasing in source density), the total column density also increases, allowing us to also probe the variation of the absorption features with column density simultaneously.

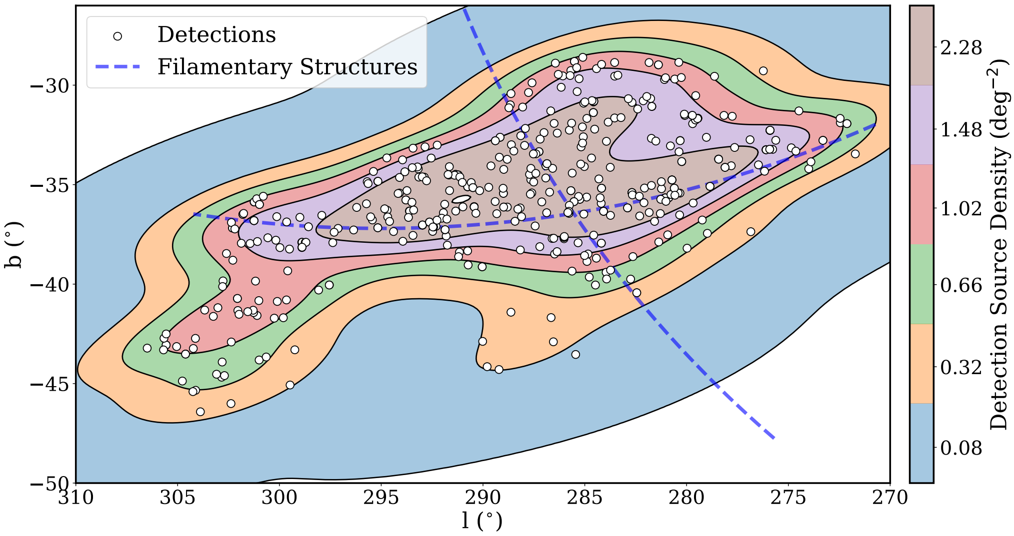

Figure 2.10: A 2-dimensional contour plot of the source density of Milky Way H I detections found through the GASKAP Pilot II survey towards the Magellanic system (Nguyen et al. 2024). The contours are created based on a kernel density PDF using the spatial location of the detected sources (shown with white circles). The levels of the contours separate the 6 equally sized bins of non-detection sources, highlighting regions of higher absorption source density on the plane-of-sky towards the centre of the H I filamentary structure observed in Fig. 2.3. The dotted blue lines indicate the H I filaments from Fig. 2.3 for context.

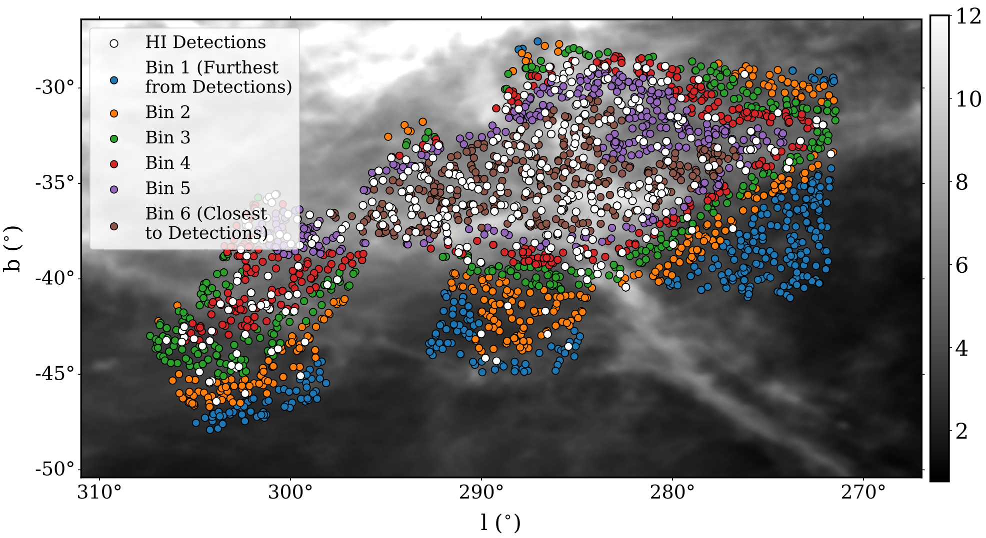

Figure 2.11: Spatial distribution of the non-detection sources coloured based on their respective contour level from the contour regions shown in Figure 2.10. We define the bins $1-6$ starting from the outer regions of the survey, with higher bin numbers probing regions with higher source density of H I absorption, as highlighted with the locations of the 462 Milky Way H I absorption detections marked with white circles. The background is a grey-scale of the Milky Way H I column density in the region of the sky from the GASS survey (McClure-Griffiths et al. 2009; Kalberla et al. 2010; Kalberla & Haud 2015a).

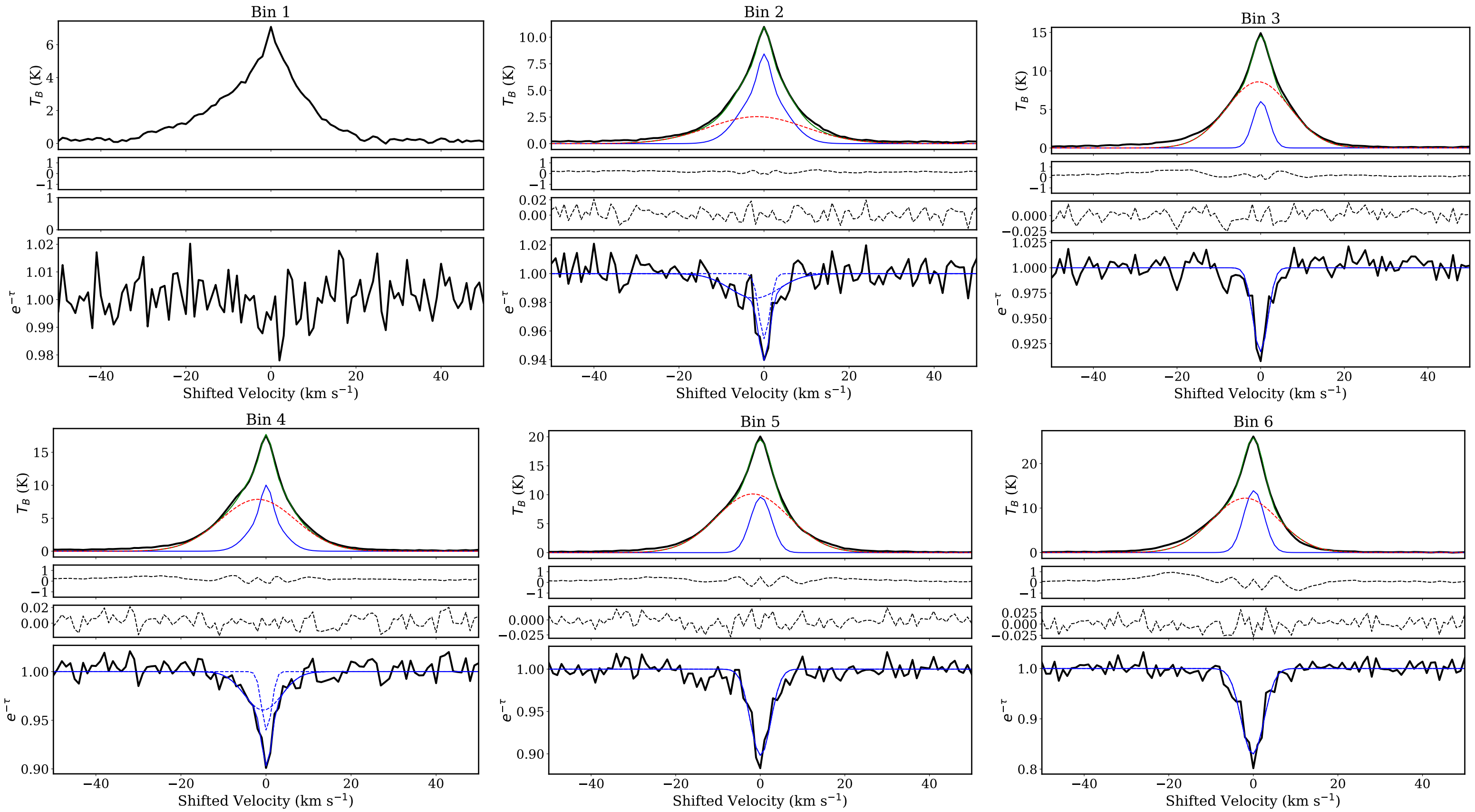

Figure 2.12: H I emission and absorption stacked profiles of the spatially binned groups of spectra from Fig. 2.11 and their Gaussian decompositions using the method from Heiles & Troland (2003). The layout and colour scheme used is similar to that used in Fig. 2.8. We note a secondary component is detected in bins 2 and 4, whereas the primary component exists in all bins except for bin 1, increasing in amplitude in absorption from bins 2 to 6 with increased detection source density. Due to the signal-to-noise being inconsistent between bins, bin 1 could not be fitted with a statistically significant Gaussian component.

The primary component's peak optical depth diminishes from approximately $\tau_{\rm peak} = (187 \pm 16) \times 10^{-3}$ to $(46 \pm 20) \times 10^{-3}$ as the bins of non-detections move outwards, away from regions of known cold gas, before disappearing in the bin most distant from the GASKAP detections. This trend is supported further with the left plot of Fig. 2.13 highlighting the variation of peak τ of the primary component in each bin, as it decreases the further we move from the filament structure. The peak optical depth values from the detection sample stack in Section 2.3.2 is also displayed, representing the closest available bin in our GASKAP sample to cold gas. We find the detection stack value agrees with the trend of the primary components in the non-detection bins.

The secondary component values on the other hand appear to plateau in peak optical depth, with the value in bin 4 being relatively similar to that of the detection sample stack in the central region of the filament structure. While this is a lower limit of the true average (as discussed in Section 2.3), the plateau is still noteworthy considering these lower limits are linearly correlated with their true counterparts (as shown in Appendix A.1.1).

We note that due to variation of signal-to-noise between each bin, bin 1's signal-to-noise was too low to consistently Gaussian decompose the stack during the Monte Carlo process used in this work. As a result, uncertainties could not be calculated for this bin. Therefore, we treat bin 1 as a non-detection of H I absorption.

The right panel of Fig. 2.13 shows the FWHM of the two absorption components in each bin. We note the primary component's FWHM is consistent with that of the total stack. The secondary component's FWHM, while an upper limit, also seems consistent with the value of the total stack (except for an outlier in bin 4). With the flux of these stacked components being conserved, the FWHM upper limit is related to the lower limit of the peak optical depth. As such, this implies that the FWHM upper limit is also linearly correlated with the true average FWHM (similar to the optical depth as mentioned earlier). Therefore, while we can not confirm that the true FWHM in each bin is similar to the total stack, we can conclude that the bins' values are at least similar to each other.

Fig. 2.14 displays the variation of T_s for the primary and secondary components with distance from cold gas. We find that both the primary and secondary components remain relatively consistent in temperature regardless of distance or changes in detection source density, and notice no overall trend. There is however a minor decline in the secondary component's spin temperature as they approach the value of the detection stack from Section 2.3.2. Regardless, the spin temperatures of the two components still align well with those of the total stack, with most bins' components falling within 1σ (68 per cent confidence) of the total stack's values. One might argue that the stability in spin temperature could be caused by the additional component added in emission during the fitting process accommodating any changes in the absorption properties. However, since the linewidths of the broad and narrow components (see values tabulated in Table 2.5.3), and hence their $T_{k,\mathrm{max}} = 121\sigma_v^2$ remain relatively consistent, similar to their spin temperatures, it is likely that this trend of constant spin temperature is physical and not a byproduct of the fitting process.

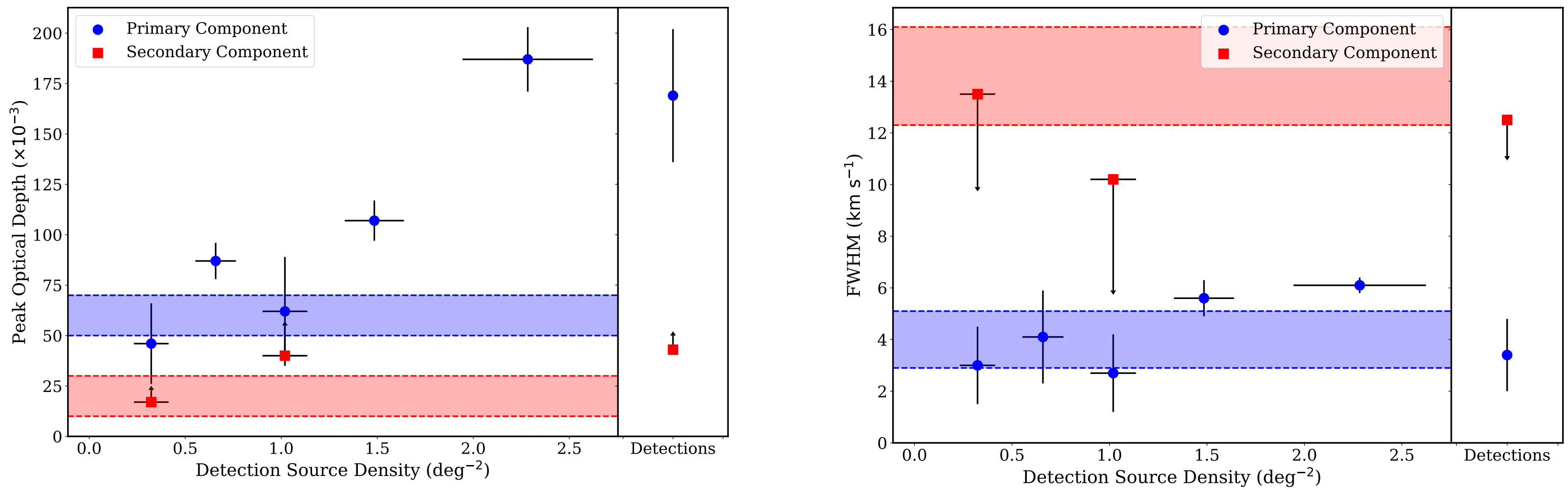

Figure 2.13: Properties of the Gaussian decompositions of the stacked profiles binned in Section 2.5.3 (bin 1 not shown). Left: Plot of the peak τ values for the primary components (blue circles) and secondary (red squares) components from each of the stacked absorption profiles. The primary component increases in peak τ as the stacked spectra get closer to regions of known cold gas, and increase at a faster rate relative to the secondary component, whose lower limit remains relatively stable in peak optical depth. The blue and red shaded regions represent the peak optical depth of each component in the total stack from Fig. 2.8 within 1σ. The optical depths of the detection sample stack from Section 2.3.2 are shown to the right, and agree with the trends from the non-detection bins as they approach colder gas. Right: Plot of the FWHM for the primary (blue circles) and secondary (red squares) components from each of the bins' stacked profiles. The FWHM of the primary component in each bin is consistent with that of the total stack, shown in the shaded region. The secondary component's upper limit of the FWHM is also relatively consistent, except for the outlier in bin 4. The FWHM's of the detection sample stack from Section 2.3.2 are shown to the right, and agree with values of those from the non-detection bins.

2.6 Discussion

Previous absorption surveys have typically used deep observations in single LOS locations (Carilli et al. 1998; Dwarakanath et al. 2002; Patra et al. 2018) or observations in a widespread field (Heiles & Troland 2003; Murray et al. 2018). In this work however, we have taken advantage of the unbiased observational capabilities of ASKAP to observe the spatial distribution of the properties of cirrus H I gas in the relatively small region of the Milky Way toward the Magellanic system.

2.6.1 Spin Temperature

In Section 2.4, stacking the residual detection spectra reveals a broad component with a spin temperature of 1320 ± 263 K. This is representative of gas from the UNM, and is much higher than the highest temperature detected by Nguyen et al. (2024) from the 462 individual detection sightlines. Since this is a stacked average of the detection spectra, which are sampled in an unbiased manner across the spatial span of the GASKAP survey range, this component represents an average of the UNM temperature within this region of the sky. The component's spin temperature is consistent with average UNM temperatures found from previous surveys that observed relatively diffuse gas ($\sim 800 \pm 570$ K from Heiles & Troland 2003 and $\sim 600 \pm 480$ K from Murray et al. 2018).

The fact that this broader UNM component appears simultaneously in the same region of sky as the cold components found in both Nguyen et al. (2024) as well as this work supports previous findings that CNM structures are typically surrounded by a broader warmer feature such as colder UNM (Kalberla & Haud 2018) and that they are interlinked as part of a continuous range of H I properties, with the UNM being a transitional stage between the stable phases.

From the spin temperatures of the components in the total non-detection H I stack in Fig. 2.8, we are able to discern that both the primary and secondary components with temperatures of 98 ± 12 and 255 ± 106 K originate from gas belonging to the CNM ($T_s <\sim 250$ K). We note that both values are higher than the mean spin temperature of ~ 50 K for the components found in single lines-of-sight (Nguyen et al. 2024). This discrepancy is likely due to the sightlines used being non-detections and as such did not contain deep absorption profiles of colder denser gas like those classified as detections. However, only a few instances of warmer gas still within the regime of CNM and under 250 K were found in the detection survey. This upper regime of cold gas has optical depths beyond the sensitivity of the current Pilot survey and as such were only found through stacking in this work to reduce

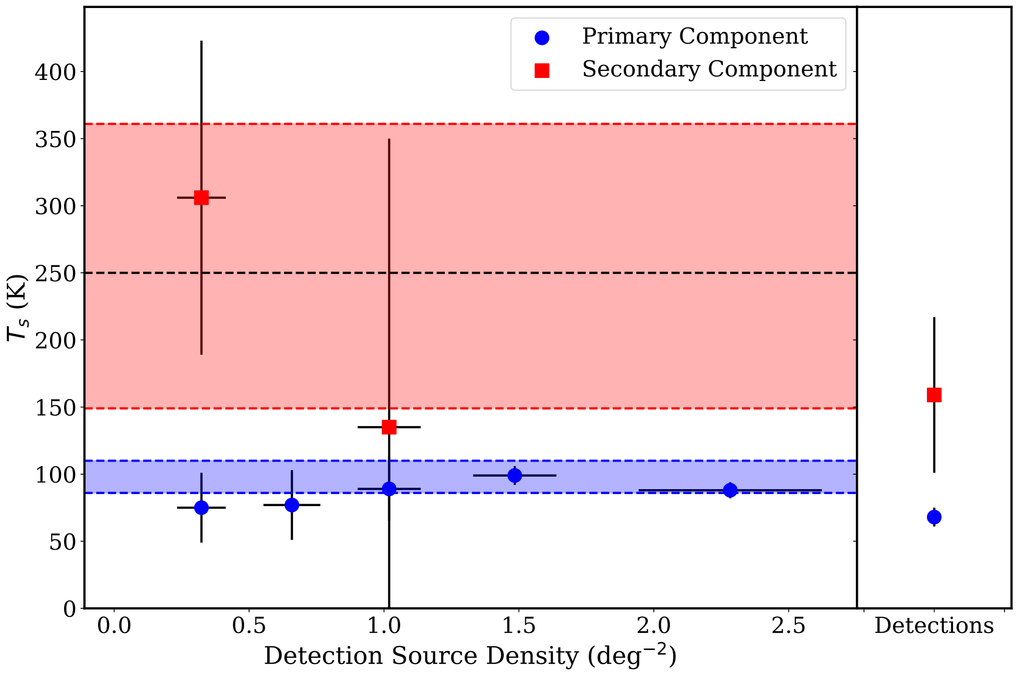

Figure 2.14: Variation of the spin temperature values for the primary (blue circles) and secondary (red squares) components from each of the stacked profiles binned in Section 2.5.3 (bin 1 not shown). The black line denotes the cutoff between CNM and UNM used in this work of $\sim$ 250 K. The primary component remains relatively consistent in spin temperature regardless of the region being probed. Both components align with their counterparts in the total stack, shown in the shaded regions with their widths indicating the 1σ standard deviation. The spin temperatures of the detection sample stack from Section 2.3.2 are shown to the right, and align with those from the non-detection bins.

the signal-to-noise. The primary component's spin temperature also aligns with the average CNM spin temperature of 80 ± 60 K from the Millenium survey (Heiles & Troland 2003) and 71 ± 52 K from the more recent 21-SPONGE survey (Murray et al. 2018) albeit slightly warmer. This indicates that while probing more diffuse gas than typical past H I absorption surveys, the CNM spin temperatures remain relatively consistent.

The secondary component's higher spin temperature of a warmer CNM gas seems to indicate that the sensitivity reached by the stacked spectrum is high enough to detect and quantify the properties of warmer cool gas throughout the entire region of the GASKAP survey. As shown in Section A.1.1, while the observed spin temperature of primary and secondary components is well correlated with the true average, we do not have any information as to the dispersion of the individual spin temperatures that form these averages. Due to the range of thermal pressures allowing a two-phase medium, the CNM temperature predicted can theoretically range from ~ 20 to 350 K in Solar neighbourhood conditions (Wolfire et al. 2003). While the upper limit of stable spin temperatures for the CNM is a function of dust extinction (McClure-Griffiths et al. 2023), we can only safely conclude that this secondary component at approximately 250 K is at the rough boundary of the cold and unstable regime of the neutral ISM. We conclude that the secondary component likely contains a mixture of warmer CNM and cooler UNM.

Unlike the detection sample stack, the non-detections when averaged did not reveal any gas with temperatures above ~ 1000 K. This is likely because the UNM component's optical depth found in the detection sample residual stack resides close to the $\sim 3\sigma$ detection threshold with the non-detection stack's noise level. Since the detection and non-detection sightlines are close in location and span the same small patch-of-sky, it is likely such a component could be found with the non-detections with longer exposure time and hence a reduced noise profile.

The WNM has been observed in absorption in the past (Carilli et al. 1998; Murray et al. 2014; Patra & Roy 2024); however, our large sample of absorption signals when stacked only yield components with spin temperatures belonging to the CNM in the non-detection stack and UNM in the detection stack. This is in contrast to recent work observing WNM temperatures up to 10^4 K in H I absorption at optical depth sensitivities close to that of the absorption stack in this work at $\sigma_\tau \approx 1 - 2 \times 10^{-3}$ (Patra & Roy 2024). This could point to a lack of WNM in this region relative to other regions on the sky, especially with the field dominated by 2 large cold dense filamentary structures (Nguyen et al. 2024; Lynn et al., in preparation). Another possibility is that the WNM in this region resides at higher optical depths than normal. Adding to this is the optical depth sensitivity of our absorption profile stack being an order of magnitude lower than that of more sensitive observations like the 21-SPONGE stacking analysis of Murray et al. (2018) ($\sigma_\tau \approx 10^{-3}$ versus the 21-SPONGE stack sensitivity of $\sigma_\tau \approx 2 \times 10^{-4}$). Despite not detecting the WNM in absorption, we can define an upper limit on the peak optical depth of the WNM in this region of the sky of approximately $\tau_{\rm peak,WNM} \lesssim 3.3 \times 10^{-3}$ using the $\sim 3\sigma$ detection threshold of the fitting algorithm when applied to the residual detection spectra stack in Section 2.4.

2.6.2 Non-Detections Spatial Variation

To determine whether the temperature and optical depth trends observed in Section 2.5.3 reflect changes in the true density and relative abundance of the H I phases, we looked to dust. Since at high Galactic latitudes the total amount of hydrogen is mostly in the neutral phase, dust is a good tracer of H I at high latitudes (Low et al. 1984; Boulanger et al. 1996; Lenz et al. 2017). Converting dust extinction densities from three-dimensional (3D) dust maps to total hydrogen densities (dominated by H I) therefore allows us to probe any variations to 3D H I density between each of the 6 bins defined in Figs 2.10 and 2.11.

Recently, work by Edenhofer et al. (2024) has produced a local 3D dust extinction map ranging from 69 pc to 1.2 kpc from the Sun with an angular resolution of 14′ and a varying distance resolution, from 0.4 to 7 pc. We used the coordinates of the sightlines used in the non-detection absorption stacks and collected, using the `dustmaps`[1] package, all of their respective sightlines in the 3D dust map for each of the six spatial bins used in Section 2.5.3.

We followed the procedure described in O'Neill et al. (2024) to convert the differential extinction measurements $A'_{ZGR_{23}}$, defined in terms of unitless extinction ZGR_{23} (Zhang et al. 2023), into densities of total hydrogen atoms H (molecular gas included) given by:

$$n_{\rm H} = C \times A'_{ZGR_{23}} \,, \tag{2.1}$$

where $C = 1653\,{\rm cm}^{-3}$. The binned $n_{\rm H}$ sightlines were then averaged, weighted by the same $1/\sigma_\tau$ values as used in the stacks of Section 2.5.3. These weighted-mean $n_{\rm H}$ spectra are shown in Fig. 2.15.

We find that the collections of sightlines further away from regions of known cold gas and with a lower detection source density (i.e., bin 1) contain a noticeably lower peak with lower $n_{\rm H}$ densities compared to the regions close to the filament and known cold

[1] https://dustmaps.readthedocs.io/

gas (i.e., bin 6) with the density spectra's peaks increasing in amplitude the higher the detection source density. This trend supports our findings in Section 2.5.3 where the cold gas optical depth disappears drastically as we move away from the filaments (shown in the left plot of Fig. 2.13). It is interesting to note that the n_{H} spectra contain two local maxima, implying the existence of multiple physically separated layers of H I, especially in the bins closer to the location of cold gas. This result aligns well with the fact that absorption sightlines in the region contain multiple cold clouds along individual sightlines and that the region contains two distinct filament structures at different physical distances (Nguyen et al. 2024).

The fact that the optical depth of the primary cold component found in the non-detection stack increases as we move closer to the regions with higher densities of cold gas detections (matching the value of the detection stack used in Section 2.3.2), also highlights the unbiased nature of the GASKAP absorption survey in determining regions with higher amounts of cold gas.

The primary component's spin temperature on the other hand remains relatively stable across the region, with the value in each bin staying close to the value of the total stack as shown in Fig. 2.14. Since the primary component traces the peak in emission, which typically accounts for the bulk of cold gas, this result seems to suggest there is little structural variation of the CNM's temperature across this region of the sky. Assuming that the H I absorption lies at the same physical distance as the peak in the weighted mean dust extinction spectra, the average physical distance to each H I absorption location is approximately 240 ± 48 pc (as shown in Fig. 2.15). Using this physical distance along with the angular extent of the entire GASKAP Pilot survey of $\sim 25°$, the temperature of cold gas within this region of the Milky Way does not vary over a plane-of-sky distance of $\sim 100 \pm 20$ pc. We note that due to the width of the Local Bubble's shell in the LOS direction, this length scale likely reflects only the plane-of-sky direction and not the depth along the LOS.

The secondary component's lower limit of optical depth exhibits negligible spatial variation from each bin compared to the bulk of the cold gas in the primary components. The optical depth plateaus in the middle bins at a value close to that in the detection stack in Section 2.3.2 as shown in Fig. 2.13. The spin temperature of the secondary component also shows a similar trend as shown in Fig. 2.14. However, due to the lack of sample size, detecting a secondary component in only 2 of the 6 non-detection bins, we cannot make any conclusions on the spatial variation of the secondary component's properties with any confidence.

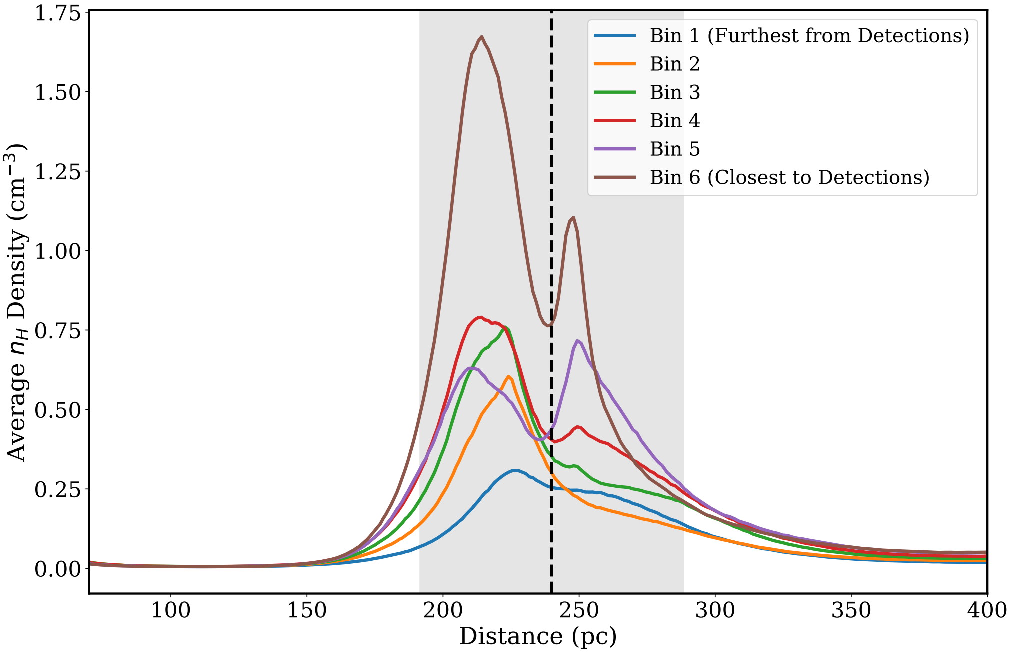

Figure 2.15: Weighted-mean of $n_{\rm H}$ along the sightlines of each of the 6 bins described in Section 2.5.3. The dust densities were converted from the Edenhofer et al. (2024) 3D dust map to total hydrogen densities using a conversion factor of 1653 cm^{-3} (O'Neill et al. 2024). Note as the spatial bins sample sightlines further away from the known regions of cold gas (from bin 6 to 1), we observe a decrease in the peak density of total hydrogen and by extension a decrease in the amount of colder phases of H I as we are observing at high Galactic latitudes (Lenz et al. 2017). The vertical dashed line represents the average distance of maximum $n_{\rm H}$ in the 2240 non-detection sightlines ($\sim 240 \pm 45$ pc), with the grey region indicating the 1σ standard deviation.

2.7 Summary

We present analysis using the recent Milky Way GASKAP Phase II Pilot survey's H I absorption detection sample investigating the effect of multiple components along individual sightlines on resulting stacked spectra and reported measurements such as the spin temperature and optical depth. Taking these effects into consideration, we report the results of stacking the Milky Way H I absorption and emission spectra from both the detection and non-detections of the GASKAP survey towards the Magellanic system. The main conclusions of this work are as follows:

- When stacking multicomponent H I absorption and emission spectra, any secondary components not centred before stacking create a signal with a peak optical depth lower than the true average value. The FWHM of the component is conversely an upper limit to conserve the total flux of the individual stacked components.
- Due to the velocity offset being equal in emission and absorption, the spin temperature from a stack of secondary components is still well correlated with average of the individual components.
- Stacking the residual spectra of the 462 GASKAP absorption detection sightlines to improve the total signal-to-noise, we detected gas in H I absorption with a spin temperature of $\sim 1320 \pm 263$ K belonging to the UNM.
- From stacking the 2240 non-detection GASKAP spectra to find gas hidden within the noise of individual sightlines, we detected the existence of a primary narrow and secondary broad component in H I absorption.
- Both the primary and secondary component can be attributed to averaged CNM fields in this region of the sky, with a spin temperature of approximately 98 ± 12 and 255 ± 106 K respectively.
- When spatially binning these non-detections by their plane-of-sky distance from known regions of cold gas, the primary CNM component varies noticeably in optical depth by almost an order of magnitude, decreasing with distance from the locations of known cold gas.
- The change in the primary cold component's optical depth is also reflected in the change in the mean peak extinction density traced by dust over the same lines-of-sight.
- The spin temperatures of cold gas components in each bin remain constant and within 1σ of the spin temperature values from the stack of all 2240 non-

detections regardless of their spatial location, over a physical plane-of-sky distance of ~ 100 pc.

In the near-future, the GASKAP survey will observe the same fields discussed in this work with longer exposure times, yielding a higher signal-to-noise ratio and sensitivity. Assuming the same number of sources are found as a conservative estimate, the signal-to-noise of all the absorption stacks throughout this work should improve by almost an order of magnitude. From this, we will then approach a signal-to-noise rivalling that of the stacked 21-SPONGE spectra (Murray et al. 2014, 2018) and will be able to detect higher spin temperature components, possibly even belonging to the WNM.

Acknowledgements

This scientific work uses data obtained from Inyarrimanha Ilgari Bundara/the Murchison Radio-astronomy Observatory. We acknowledge the Wajarri Yamaji People as the Traditional Owners and native title holders of the Observatory site. CSIRO's ASKAP radio telescope is part of the Australia Telescope National Facility (https://ror.org/05qajvd42). Operation of ASKAP is funded by the Australian Government with support from the National Collaborative Research Infrastructure Strategy. ASKAP uses the resources of the Pawsey Supercomputing Research Centre. Establishment of ASKAP, Inyarrimanha Ilgari Bundara, the CSIRO Murchison Radio-astronomy Observatory and the Pawsey Supercomputing Research Centre are initiatives of the Australian Government, with support from the Government of Western Australia and the Science and Industry Endowment Fund. This research is supported by an Australian Government Research Training Program (RTP) Scholarship. This research was partially funded by the Australian Government through the Australian Research Council through the award of an Australian Laureate Fellowship (project number FL210100039) to NMc-G. The authors acknowledge Interstellar Institute's programme "II6" and the Paris-Saclay University's Institut Pascal for hosting discussions that nourished the development of the ideas behind this work. EDT was supported by the European Research Council (ERC) under grant agreement no. 10104075.

This research made use of `Astropy`, a community-developed core Python package for astronomy (Astropy Collaboration et al. 2013), `NumPy` (van der Walt et al. 2011), `matplotlib`, a Python library for the publication of quality graphics (Hunter 2007), and `SciPy` (Virtanen et al. 2020).

Data Availability

The GASKAP-HI Pilot survey data are available on the CSIRO ASKAP Science Data Archive[2] (CASDA). The non-detection data set and auxiliary data products from this article will be shared on reasonable request to the corresponding author.

[2] https://research.csiro.au/casda/

Chapter 3

Spatial structure of multiphase Galactic gas via structure functions of H I absorption and emission

Context and Contribution

This chapter presents the contents "Spatial structure of multiphase Galactic gas via structure functions of H I absorption and emission" by C. Lynn, N. M. McClure-Griffiths, A. Marchal, A. Seta, A. J. M. Thomson, Marc-Antoine Miville-Deschênes, H. Nguyen, J. Dempsey, J. Th van Loon, N. M. Pingel, G. Park, M-Y. Lee, B. Lee, D. Leahy, J. M. Dickey, G. Joncas, Yik Ki Ma, S. Stanimirović, I. Kemp, S. Gibson, H. Dénes, and K. Jameson, submitted to the Monthly Notices of the Royal Astronomical Society at the time of this writing. The work presented here is exactly as in the submission. I carried out all of the analysis, including the application of structure function code to the GASKAP-HI survey data set. I have written the manuscript, with insightful feedback and suggestions from the co-authors.

Abstract

We investigate the plane-of-sky spatial structure of multiphase neutral hydrogen (H I) gas in the cirrus regions of the Milky Way's interstellar medium using the unparalleled density of absorption measurements from the Galactic Australian Square Kilometre Array Pathfinder H I (GASKAP-HI) Phase II Pilot survey. The Pilot survey observes the Reticulum-Hydrus filamentary region. Low optical depth values are ubiquitous throughout the region. High optical depths appear closer to the filaments, but not within. No spatial correlation was found between cold neutral medium (CNM) spin temperature and plane-of-sky location across the $\sim$ 100 pc wide region. We compute structure functions of the CNM column density and integrated optical depth, which have power-law slopes of 0.34 ± 0.12 and 0.23 ± 0.10, respectively. The column density of residual gas not found in absorption from the unstable neutral medium (UNM) and warm neutral medium (WNM) forms a broken power-law structure function. For spatial separation greater than 3 to 4 pc, the slope is 0.66 ± 0.07, characterising turbulence in the interstellar medium (ISM). For smaller separations, the slope is flat, due to noise becoming dominant. The equivalent power spectrum slope of CNM and UNM+WNM H I column densities is ~ -2.3, and ~ -2.6 respectively, providing unbiased measurements of the power-law slopes of CNM gas and residual warm gas in the Milky Way's ISM. For the first time we also compute the structure function of cold H I spin temperature, forming a flat power-law slope, implying CNM spin temperature is spatially uncorrelated between $\sim$ 0.4 and $\sim$ 100 pc across the plane-of-sky. Comparing with numerical simulations, the flatness is likely due to the errors in current methods of computing spin temperature not being accurately quantified, and observational bias from the noise of H I absorption and emission observations.

3.1 Introduction

Neutral hydrogen (H I) plays a crucial role in the evolution of galaxies. With H I providing the fuel reservoir for the formation of molecular clouds (Clark et al. 2012; Klessen & Glover 2016), the neutral to molecular gas transition is critical to our understanding of star formation. However, this fundamental step that leads to the formation of star-forming material and the physical processes involved are still poorly understood. Understanding the physical structure of H I gas, particularly cold H I, is therefore necessary to our overall understanding of the multiple physical processes in the Galaxy (McClure-Griffiths et al. 2023).

H I has historically been best modelled as a bi-stable medium of two stable temperature ranges: the cold neutral medium (CNM, $T_s \sim 50-250$ K), comprising the dense clumps within the ISM, and the warm neutral medium (WNM, $T_s \sim 4000-7000$ K), filling the majority of the volume of the ISM and enveloping the CNM. Between these two stable phases of gas lies the unstable neutral medium (UNM), which also occupies a significant fraction of the ISM's volume, produced by the thermal instability and condensation of warm gas (Field 1965; Field et al. 1969; Wolfire et al. 1995, 2003; Hennebelle & Pérault 1999, 2000; Audit & Hennebelle 2005).

While the amount of H I gas within the Galaxy has been explored since the discovery of H I itself, measuring the temperature of H I in the ISM is less trivial, and by extension the separation of H I into more detailed phase descriptions. The difficulty lies in requiring both absorption and emission measurements in the same location of the sky to measure the spin temperature of gas along a sightline (Heiles & Troland 2003). Observationally, the CNM is easiest to detect in absorption due to its high density and optical depth. However, these measurements are restricted by the requirement of chance alignment of radio-bright background sources in the sky. As such, understanding the spatial structure of cold gas within the ISM has been limited (McClure-Griffiths et al. 2023; Lynn et al. 2025).

In the past, techniques to separate H I phases and analyse their spatial structure have used H I emission data, focussing on two main methods: Gaussian spectral decomposition of H I emission surveys separating features by the components' velocity dispersion (Lindner et al. 2015; Marchal et al. 2019; Bhattacharjee et al. 2024), and machine-learning CNN models trained on synthetic H I observations (Murray et al. 2020; Nguyen et al. 2025a). However, the main disadvantages of these techniques is that neither use radiative transfer or physics-based approaches to model the physics of the gas before separating phases. The former relies on the total spectral broadening that is comprised of both thermal and turbulent motions, and the latter trains on ISM simulations that, due to computational limitations, involve approximations and are missing some physical processes expected in the Milky Way. The simulations also use analytical models to resolve processes below their physical resolution such as small-scale cooling mechanisms, adding more potential biases when training CNN models. With this in mind, combining absorption and nearby emission sightlines to complete the radiative transfer equation along a sightline is currently the best method for properly diagnosing the temperature of cold H I gas and hence their phase description.

The main downside to using absorption-emission sightline pairs to probe the ISM is the lack of high area density coverage and hence a lack of uniform spatially sampled information across the sky. However, spatial techniques such as structure functions can be used to provide useful diagnostics on the structure and amount of gas concentrated on different physical scales. The structure function is a method of quantifying the variation of a particular field or property as a function of physical length scale (Seta & Federrath 2024), and has been used in numerous subfields, from extragalactic ISM studies (Deshpande et al. 2000; Lee et al. 2025) to works on Faraday rotation measures (Haverkorn et al. 2008; Stil et al. 2011; Livingston et al. 2021). However given the poor Galactic absorption source density of past surveys and lack of statistically significant sample sizes, analysing the spatial structure of the CNM of the Milky Way and its scale-dependence directly through absorption has not been possible until now (McClure-Griffiths et al. 2023). Recent advancements in absorption sensitivity and field-of-view, now allow us to map out nearby H I features with hundreds of absorption sightlines and detections of the CNM in a relatively small region of the sky (Nguyen et al. 2024; Lynn et al. 2025). We are now at a point where structure functions of phase-separated gas via spin temperature measurements via are possible.

In this work, we use observations of Galactic absorption and emission from the Galactic Australian Square Kilometre Array Pathfinder (GASKAP) survey (Dickey et al. 2013; Hotan et al. 2021; Pingel et al. 2022). The pilot phases of the survey observed a region towards the Magellanic system ($-45° < b < -25°$, $270° < l < 300°$). The Milky Way gas in this portion of sky forms two large filamentary structures overlapping each other on the plane-of-sky (Nguyen et al. 2024; Lynn et al. 2025). The observations resulted in a 30 arcsec spatial resolution in emission (Dickey et al. 2013). Nguyen et al. (2024) used the absorption pipeline for GASKAP, outlined in Dempsey et al. (2022) to search the region in an unbiased manner across the full extent of the pilot survey, producing a catalogue of 462 detections of Galactic H I absorption.

In this paper, we present analysis on the spatial and spectral properties of optical depths and H I column densities via structure functions of the detected CNM gas within the GASKAP pilot phase II survey region (Nguyen et al. 2024). With the advent of high source density absorption source finding, we are able to also, for the first time, calculate the structure function of spin temperature of cold gas in the Milky Way's ISM.

The chapter is organised as follows. Section 3.2 presents the data used in this work. In Section 3.3, we investigate the 1-dimensional spatial analysis of cold gas properties with Galactic latitude, as well as qualitative analysis of the spatial distribution of properties across the GASKAP Pilot region. Section 3.4 provides theoretical framework for structure functions, before applying them to the optical depth, CNM column density and spin temperature of cold gas. A discussion of the results and their interpretations, along with comparisons to the residual warm column density and total column density are provided in Section 3.6, with comparison to numerical simulations in Section 3.6.2, followed by a summary in Section 3.7.

3.2 Data

3.2.1 Observations

This work uses observations from the GASKAP-HI Pilot Phase II survey (Dickey et al. 2013) using the Australian Square Kilometre Array Pathfinder (ASKAP, Hotan et al. 2021). The survey includes ten 25-square degree fields covering the Large Magellanic Cloud, Small Magellanic Cloud and the Magellanic Bridge, observed from October 2021 (SBID[1]) to April 2022 (SBID 38845). Each of the fields observed totalled 10 hours of integration, providing an rms noise level of approximately $\sigma_{T_{\mathrm{B}}} \approx$ 1.1 K (1.6 mJy/beam) per 0.89 km s^{-1} channel (Pingel et al. 2022). The fields are all combined with single dish data from the GASS survey over the same region of the sky (McClure-Griffiths et al. 2009; Kalberla et al. 2010; Kalberla & Haud 2015a). The combined mosaic of these fields provides a large field of view of the diffuse Milky Way gas in this region of the sky at local velocities from −50 to 50 km s^{-1} (shown in Figure 3.1). The GASKAP-HI Pilot survey observes a region dominated by two large-scale filaments forming a cross: Reticulum in the vertical direction (near the Reticulum constellation) and Hydrus in the horizontal direction (near the Hydrus constellation, Kamal Youssef & Grenier 2024). The H I filaments are defined as regions with high H I column density and brightness temperature, with lengths of 23 and 33 degrees within the spatial extent of the GASKAP-HI pilot survey for the vertical and horizontal filaments, respectively.

[1]SBID: Scheduling Block ID, as defined on the CSIRO ASKAP Science Data Archive (CASDA)

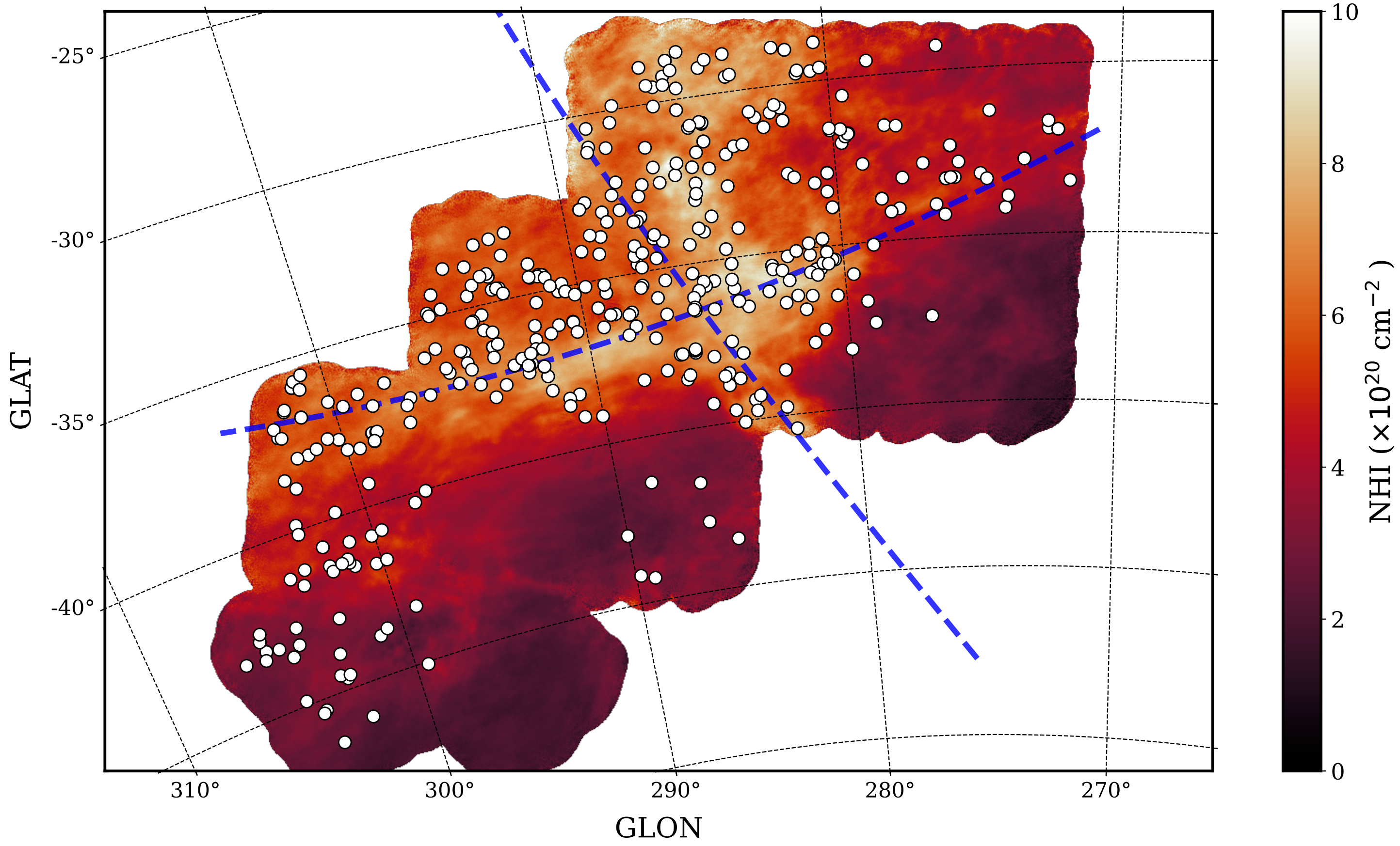

Figure 3.1: Spatial distribution of background sources from the GASKAP-HI absorption survey overlaid on a map of the column density of H I gas computed in the optically thin limit from the GASKAP Pilot survey. Detections of cold gas in the velocity range $-50 < v_{\mathrm{LSRK}} < 50$ km s^{-1} are annotated with white circles. The blue dashed lines indicate the arcs of two H I filaments in this region of the Milky Way: Reticulum and Hydrus in the vertical and horizontal direction respectively (Kamal Youssef & Grenier 2024).

3.2.2 H I Absorption Source Catalogue

Nguyen et al. (2024) created a catalogue of 462 sightlines containing detections of H I absorption in the Milky Way velocity range from −50 to 50 km s^{-1} using the GASKAP absorption pipeline (Dempsey et al. 2022). The detections were defined as sightlines with background source flux greater than 15 mJy, and having an optical depth value above 3σ and a neighbouring channel above 2.8σ where σ is the rms-noise of the spectra. From this catalogue, the sightlines were decomposed into Gaussian components to measure spin temperatures and optical depths of the CNM gas in the region (Nguyen et al. 2024), with 690 absorption components detected with spin temperatures less than ~ 350 K. The locations of these 462 detection sightlines are shown in Figure 3.1, with their line-of-sight velocities matching with that of the H I emission from the Reticulum and Hydrus filaments. The mean rms noise of the detection sightlines in optical depth, τ, is approximately $\sigma_\tau = 4.2 \times 10^{-2}$, with a median of around 3.1×10^{-2}. While the noise of these sightlines is higher than more sensitive samples, such as those from 21-SPONGE (Murray et al. 2014, 2018), the benefit of this dataset is the unprecedented sample size within a small field-of-view of the Milky Way's high Galactic latitude gas and the denser source grid of continuum background sources this produces of $\sim$ 12 sources / square-degree (Nguyen et al. 2024; Lynn et al. 2025).

3.3 Spatial Distribution

In this section, we present an analysis of the plane-of-sky spatial variation of absorption and emission properties of peak optical depth and spin temperature, using the H I detection sightlines from Nguyen et al. (2024). We start with a one-dimensional qualitative analysis along Galactic latitude before using quantitative techniques such as the structure function in further sections.

3.3.1 Galactic Latitude

Previous surveys have observed an overall decrease in the amount of H I gas as one moves away from the Galactic plane (Dickey & Lockman 1990). In Figure 3.2, we show the variation of $N_{\rm H\,I} \sin|b|$ of cold components as a function of $sin|b|$ for the Milky Way GASKAP absorption survey, comparing it with the values of previous Galactic H I surveys catalogued into BigHICat (McClure-Griffiths et al. 2023). The $\sin|b|$ factor corrects for the path length and is equivalent to an inclination correction when working with external galaxies. We find that when the GASKAP-HI and BigHICat catalogues are combined, the binned average follows a similar trend to the original fit of $N_{\mathrm{HI}} = 3.84 \times 10^{20} \mathrm{cosec}|b|\ \mathrm{cm}^{-2}$ (Heiles & Jenkins 1976; Dickey & Lockman 1990) that used optically thin H I emission data available at the time.

Due to the filamentary structures within the region of the GASKAP survey, the column densities found are higher than the average for the probed absolute Galactic latitude. This is contrasted with results from the MACH survey (Murray et al. 2021), where points at a similar absolute Galactic latitude in the northern sky sit below the Dickey & Lockman (1990) fit (also shown in Figure 3.2). While H I column density is a local property that varies between regions, the difference between the MACH and GASKAP surveys, each observing large regions of cirrus gas, indicates a lack of plane-parallel symmetry. The Galactic latitude extent of the GASKAP pilot survey positions our data in the latitude region where peak $N_{\mathrm{H\,I}}$ column densities are found in the disk, before decreasing rapidly at the highest Galactic latitudes due to the cavity of the Local Bubble becoming a dominant feature (Dickey & Lockman 1990).

3.3.2 Plane-of-Sky Distribution

While 1-dimensional analysis with Galactic latitude is useful for analysing variation in the context of the Milky Way's disk, 2-dimensional spatial analysis is required to link variation in properties to specific physical structures on the plane-of-sky. In Figure 3.3, we show the spatial distribution of the peak optical depths and spin temperatures of the 690 cold components from the GASKAP absorption sightlines detected by Nguyen et al. (2024). These points are overlaid on the GASKAP H I column density map of the Pilot survey in the optically thin limit.

We see that low optical depth components are ubiquitous throughout the region, lying both inside and outside of the filamentary structures. Higher optical depth components seem to be closely tied to the filaments and regions of higher column density. However, the highest optical depth values are not found within the H I filamentary structures (i.e., close to the core of the filamentary cross), which instead contain mostly low optical depth values. The highest values are instead positioned at the interface between the filaments' edges and the rest of the diffuse ISM. This implies the possibility that the filaments could be comprised of superpositions of many small cold structures along the line-of-sight, forming higher column densities, while the filament edges contain fewer, larger, coherent structures. However with a lack of line-of-sight distance information with similar resolution to the plane-of-sky this remains to be determined. While the optical depth contains spatial structure, with some parts being denser than others, there is no clear spatial trend for the spin temperature, appearing to be random across the plane-of-sky.

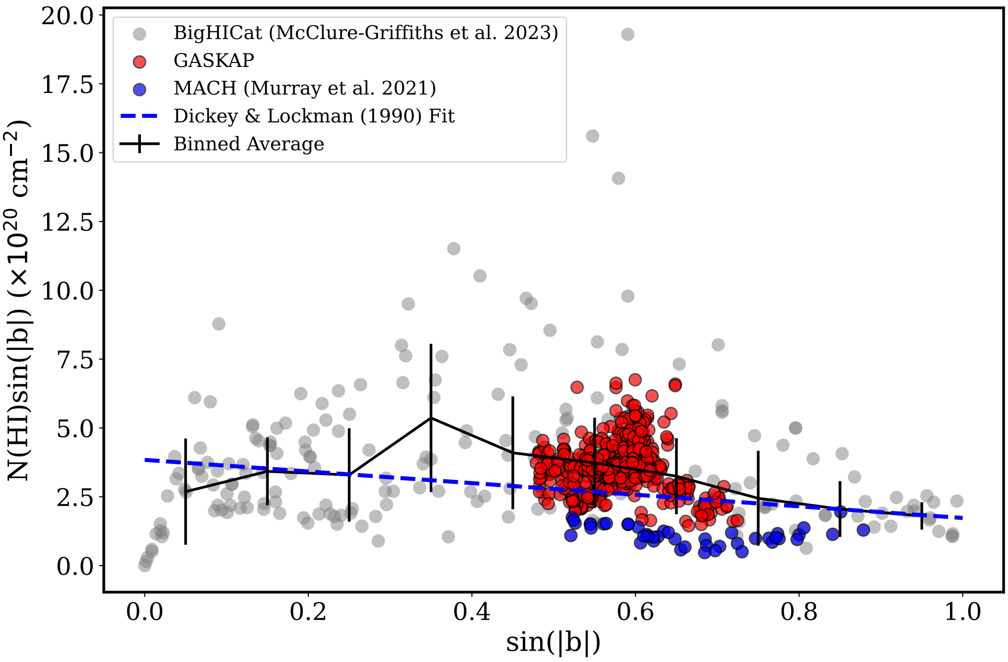

Figure 3.2: Variation of $N_{\mathrm{H\,I}} sin|b|$ of cold components as a function of $\sin|b|$. The cold components from the GASKAP Pilot survey are shown in red, and the combined measurements from previous surveys are highlighted in grey (McClure-Griffiths et al. 2023). The binned average of the combined dataset of GASKAP and the Big H I Catalogue are shown in black, and align well with the previous results and the original fit made by Dickey & Lockman (1990), shown by the dashed line. The GASKAP sightlines trace typical column densities, but are positioned above the Dickey & Lockman (1990) fit as opposed to points from the MACH survey (Murray et al. 2021) at similar absolute latitudes, shown in blue, indicating a lack of symmetry about the Galactic plane.

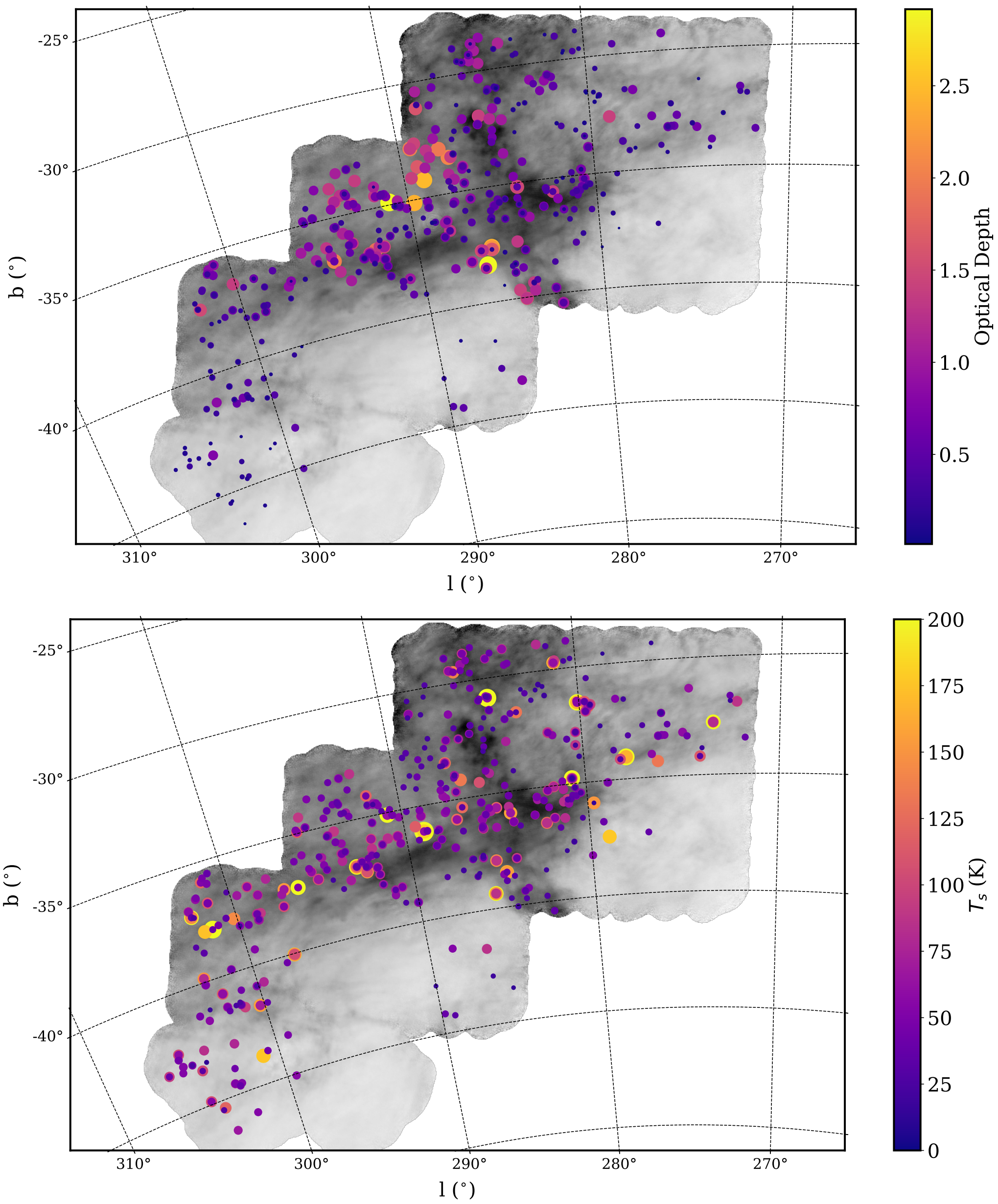

Figure 3.3: Spatial distribution of the peak optical depth (top) and spin temperature (bottom) of the cold components decomposed from Nguyen et al. (2024). The values are overlaid on top of a mosaic of the GASKAP-HI column density map of the Pilot surveys. The values of the points are represented by both the colour and size of the points. On visual inspection, we find low optical depths are uniformly dispersed but high optical depths are restricted to the edges of the large-scale filaments. Spin temperatures however, show no spatial correlations or trends, appearing random across the plane-of-sky.

To investigate this further, we examine the properties of H I gas as a function of distance from the two large-scale H I filaments: Reticulum and Hydrus, mentioned in Section 3.2.1. Figure 3.4 shows the distributions of the line-of-sight integrated quantities: column density, cold gas mass fraction, and the opacity correction factor between optically thin and thick H I column density, with respect to the angular distances to the nearest of the two filaments. All of the integrated properties of the 462 H I absorption sightlines decrease with increasing distance from the filaments, as would be expected with an overall decrease in gas density.

We also compared the component-based properties of spin temperature, peak optical depth, and full-width half-maximum (FWHM), shown in the bottom row of Figure 3.4. When looking at the quantities for individual cold Gaussian components, we find very little variation in the spin temperature and FWHM with distance from the filaments. However, the peak optical depth, acting as a density metric, appears to decrease away from the filaments. This suggests that while the presence of cold gas varies with distance from filamentary structures, the gas' other physical properties such as temperature and velocity dispersion do not significantly.

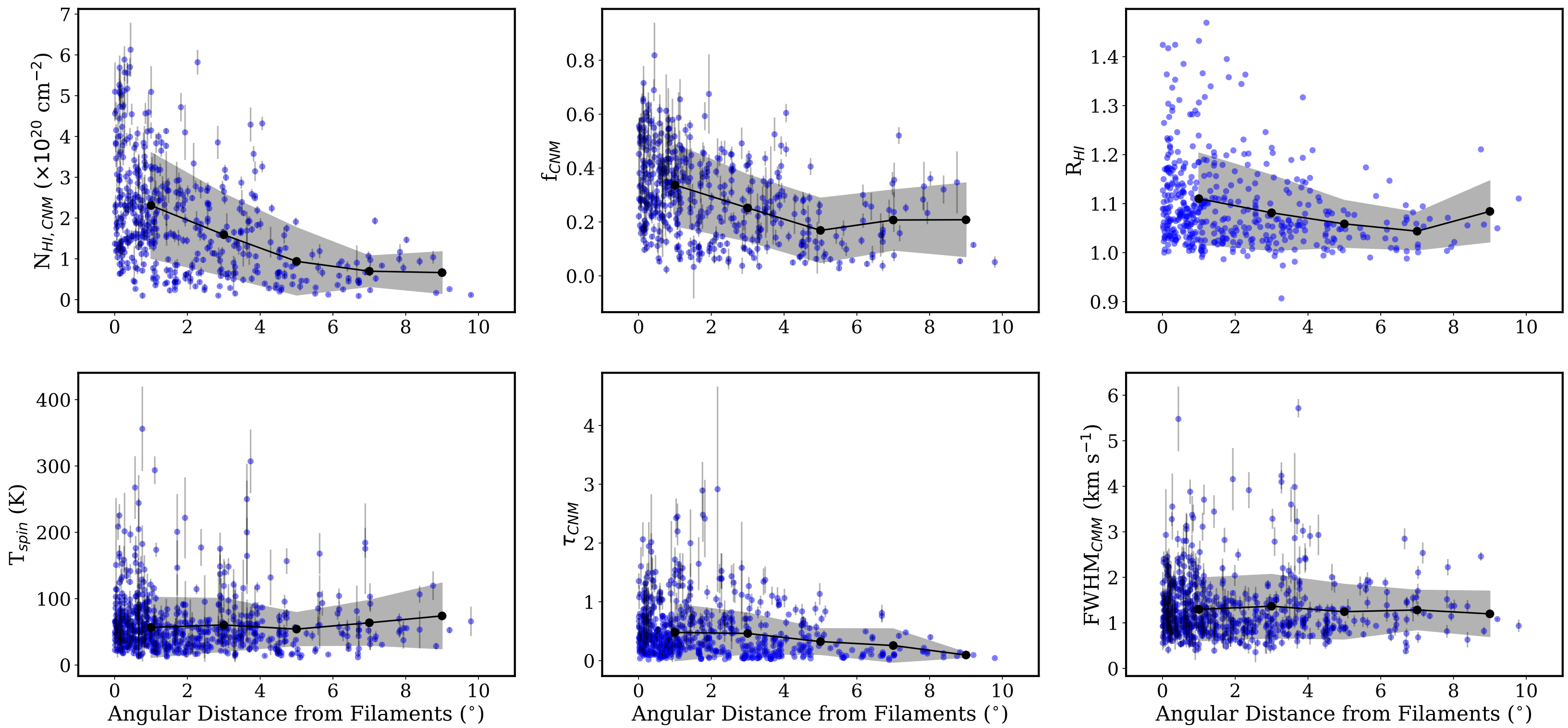

Figure 3.4: Collection of H I gas properties from the MW absorption sightlines as a function of their distance from the two Reticulum and Hydrus filaments in the region of the GASKAP Pilot Survey. Top: line-of-sight average properties of the CNM column density, CNM mass fraction, and H I opacity correction factor. Bottom: Variation of the individual cold components' spin temperature, peak optical depth, and full-width half-maximum. The black points represent the binned-averaged with bin-widths of 2 degrees, and the shaded regions indicate their standard deviations.

3.4 Structure Functions

3.4.1 Theoretical Framework

In addition to looking at the variation of properties by distance from filaments discussed above, we can also look to determine if there is any spatial correlation in the absorption properties, and if so, over what angular scales. As discussed previously, the structure function is a powerful diagnostic to explore the dependence of a discrete quantity (such as pencil-beam absorption measurements) on spatial length scale. For some spatially dependent parameter $f(\mathbf{x})$ and as a function of scale $r = |\mathbf{r}|$, the second-order structure function with a 2-point stencil, $\mathrm{SF}_2^{(2\mathrm{pt})}(f, \mathbf{r})$ can be expressed as (Haverkorn et al. 2004; Seta et al. 2023):

$$SF_2^{2pt}(f, \mathbf{r}) = \langle |f(\mathbf{x} + \mathbf{r}) - f(\mathbf{x})|^2 \rangle, \tag{3.1}$$

where $\mathbf{x}$ is the two-dimensional position vector over which the average, $\langle\rangle$, is computed.

Second-order multi-point structure functions, like the 3-point stencil version, are useful as they are more accurate in capturing smaller scale fluctuations. Comparing different stencils is therefore crucial for properly determining the trustworthiness of the second-order structure function and its slope as it extends towards smaller scales (Stutzki et al. 1998; Lazarian & Pogosyan 2008; Seta et al. 2023; Seta & Federrath 2024; Lee et al. 2025).

With similar parameters to the 2-point stencil, the 3-point structure function, $\mathrm{SF}_2^{(3pt)}(f, \mathbf{r})$, is defined as:

$$SF_2^{3pt}(f, \mathbf{r}) = \langle |f(\mathbf{x} + \mathbf{r}) - 2f(\mathbf{x}) + f(\mathbf{x} - \mathbf{r})|^2 \rangle. \tag{3.2}$$

We choose to use the 2-point stencil as the main point of study in this work, with the 3-point stencil used for verification, especially at smaller scales.

Typically, when the length scales being probed by the structure function become large enough, the field will no longer experience growth in its variance, and the function will observe a plateau, past which there is no longer any scale-dependence or correlation between points. For the second-order structure function, the value the structure function converges to is $2\sigma^2$ for the 2-point stencil and $6\sigma^2$ for the 3-point stencil (Seta et al. 2023), where σ is the standard deviation of the discrete data points of the dataset used. For this to be observed, the region being examined must be large enough and include the size-scale where this break occurs, known as the correlation length scale.

We calculate the structure functions presented in this work using the `Structure-Function` Python software package[2]. The package uses the functions described above, with the error in the structure function computed using Monte-Carlo error propagation to calculate the means in each bin, along with their 16th and 84th percentile errors. The Monte-Carlo procedure assumes the input data and errors follow a Gaussian distribution. The package also corrects for the error in the dataset through subtracting the structure function of the errors themselves (Haverkorn et al. 2004).

3.4.2 Integrated Quantities

Since H I cold components along a sightline are distinguished spectrally, we have no information on their individual line-of-sight distance. As such, we are unable to create three-dimensional structure functions with third spatial dimension of line-of-sight depth. Instead, we compute two-dimensional structure functions across the plane-of-sky using integrated line-of-sight quantities from the 462 total sightlines from the GASKAP Pilot Survey (Nguyen et al. 2024). For this work, we focus on the integrated optical depth ($\tau_{\rm LOS}$), optically thick-corrected H I column density ($N_{\rm H\,I}$) for the CNM, and column density-weighted average line-of-sight spin temperature ($T_{s,\,\rm avg}$). These quantities are defined as:

$$\tau_{\rm LOS} = \int \tau(v)\, dv, \tag{3.3}$$

$$N_{\rm H\,I} = 1.823 \times 10^{18}\,{\rm cm}^{-2} \int \frac{\tau(v)\, T_B(v)}{1 - e^{-\tau(v)}}\, dv, \tag{3.4}$$

$$T_{s,\,\rm avg} = \frac{\sum_i T_{s,i}\, N_{\rm H\,I,\,\it i}}{\sum_i N_{\rm H\,I,\,\it i}}, \tag{3.5}$$

where T_B is the brightness temperature of the H I emission from only the cold components found in Nguyen et al. (2024), and $T_{s,i}$ and $N_{\rm H\,I,\,\it i}$ are the spin temperature and column density of the i-th cold component decomposed by Nguyen et al. (2024) for the sightline, respectively.

Using the framework described in Section 3.4.1, we compute the 2-point structure functions of the integrated optical depth, CNM column density, and average LOS spin temperature for the 462 GASKAP sightlines. The structure functions are shown

[2]Thomson, Alec (2024): StructureFunction. CSIRO. v1. Software https://doi.org/10.25919/dkwn-mg50

in Figure 3.5. Due to the relatively high uncertainties in some integrated optical depth measurements, a noise cut was made to only include data points with percentage errors less than 0.6. Doing so removed 50 sightlines, with a resulting dataset of 412 measurements (see Appendix A.2.1).

The structure functions of the integrated optical depth and column density have a power-law trend over all spatial scales covered by the GASKAP pilot survey. On the largest scales, the structure function for the column density shows a sharp decrease, as seen in Figure 3.5. This is due to a small and statistically insignificant number of pairs at these scales made from opposite corners of the survey region. Therefore the dip is unreliable and is not of physical origin. The average line-of-sight spin temperature however, produces a flat structure function, indicating its variation has no dependence on spatial scale within the scale range probed by the GASKAP survey.

The structure functions of all three quantities are fitted using single power-law functions, defined as:

$$SF(r) = A\, r^{\alpha}\,, \tag{3.6}$$

since there is no scale that shows a break in the power-law to form a plateau (and flat power-law in the case of the mean spin temperature). The bin representing the largest scale is ignored when fitting, along with bins with too few pairs (defined in this work as bins containing < 10 pairs) to focus only on statistically significant bins. The fitted values and their uncertainties are tabulated in Table 3.1. The errors of the parameters are determined through the quadratic sum of the uncertainty in the original fit, and the statistical uncertainty, calculated through the standard deviation of parameter fits when fitting sub-samples of the structure function bins (see Appendix A.2.2 for more information).

The density proxies of integrated optical depth and column density both show non-zero power-law indices of 0.19 ± 0.08 and 0.31 ± 0.05, respectively, which agree within the uncertainties of their 3-point structure function counterparts.

The 2-point spin temperature structure function however is close to zero, with a slope of 0.10 ± 0.2, reaching down to the smallest scales probed by the current dataset. The 3-point stencil also forms a flat slope of 0.05 ± 0.05. Since the 3-point structure function is more sensitive to and reliable at smaller scales (Seta et al. 2023; Lazarian & Pogosyan 2008), we choose to focus on the 3-point structure function over the 2-point stencil for the spin temperature.

For completeness, the same process was also completed for the 690 individual cold

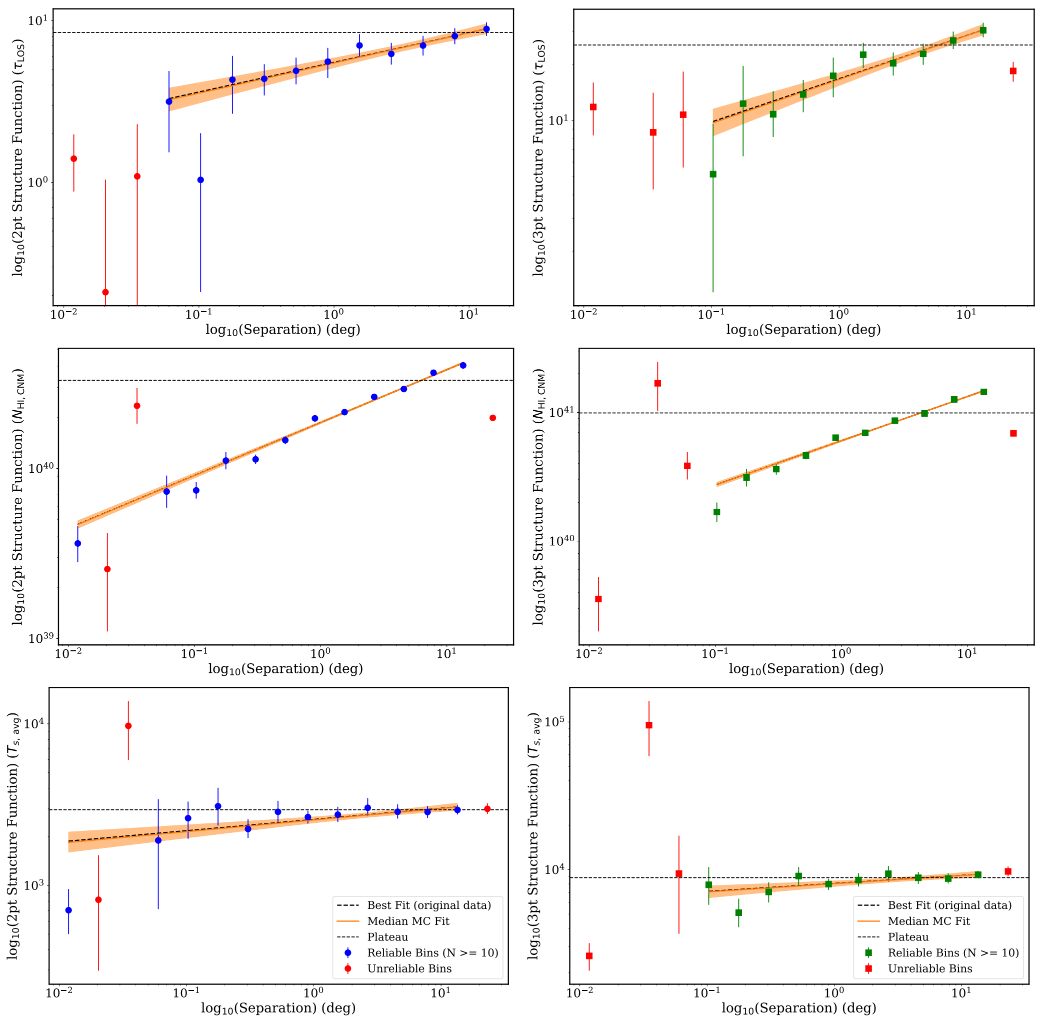

Figure 3.5: Combined log-log plots of the binned average 2-point (left) and 3-point (right) structure function measurements for the integrated optical depth, τ_{LOS} (top), H I column density, $N_{\mathrm{H\,I}}$ (middle), and column density-weighted average LOS spin temperature, $T_{s,\,\mathrm{avg}}$ (bottom) of the 412 sightlines of the GASKAP Pilot survey (after applying noise cutoffs), calculated in Section 3.4.2. The 2-point and 3-point structure functions are marked in the blue circles and green squares, respectively, with the red points indicating bins with low sampling and which are hence unreliable. The orange lines indicate the power-law fits, with the shaded region marking 1 standard deviation. The plateau points are marked by the dotted black lines, equal to $2\sigma^2$ for the 2-point structure function and $6\sigma^2$ for the 3-point structure function, where σ is the standard deviation of the original sample (Seta et al. 2023).

components catalogued in Nguyen et al. (2024) across the 462 sightlines. Due to the region of the high Galactic latitude of the GASKAP pilot survey, the sightlines observed are simple spectrally, and as such, the structure functions using the individual components show similar shapes to the integrated quantities discussed above, and are hence not shown.

Table 3.1: Fitted parameters for the 2-point and 3-point structure functions calculated in Section 3.4.2, fitted with a single power-law function (Equation 3.6).

Structure Function	Amplitude (A)	Slope (α)
$\tau_{\rm LOS}$ (2-point)	5.49 ± 0.72	0.19 ± 0.08
$\tau_{\rm LOS}$ (3-point)	16.78 ± 1.72	0.23 ± 0.10
$N_{\rm H\,I,\mathit{CNM}}$ (2-point)	$(1.86 \pm 0.10) \times 10^{40}$ cm^{-4}	0.31 ± 0.05
$N_{\rm H\,I,\mathit{CNM}}$ (3-point)	$(6.04 \pm 0.71) \times 10^{40}$ cm^{-4}	0.34 ± 0.12
$T_{s,\,\rm avg}$ (2-point)	2600 ± 2100 K^2	0.10 ± 0.2
$T_{s,\,\rm avg}$ (3-point)	8100 ± 700 K^2	0.05 ± 0.05

3.4.3 Warm and Total $N_{\text{H I}}$

To compare the cold gas structure functions to the broader context of the cirrus ISM in this region of the sky, we also examined the opacity-corrected column densities of the remaining warmer gas of UNM and WNM not fit in absorption, and the total opacity-corrected $N_{\text{H I}}$, both derived from the Gaussian decomposition completed by Nguyen et al. (2024) of the emission spectra at the same locations of the absorption sightlines. The total column densities were calculated in both the optically thin and thick regime. Similar to the integrated optical depth values mentioned previously, data-points with high percentage noise needed to be removed from the optically thick and warm column density datasets. Sightlines with percentage errors above 0.4 were ignored, leading to 9 and 16 values being removed from each dataset, forming datasets of 453 and 446 sightlines, respectively (see Appendix A.2.1).

We computed structure functions of these three metrics using the same methodology outlined in the above sections, with their fitted parameter values displayed in Table 3.2. The structure function of the column density of the remaining warm gas not found in absorption is shown in Figure 3.6. Both the 2-point and 3-point structure functions were fit with a broken power law, defined as:

$$SF(r) = \begin{cases} A\, r^{\alpha_1} & \text{if } r < r_b \\ A\, r_b^{\alpha_1}\, (\frac{r}{r_b})^{\alpha_2} & \text{if } r \geq r_b\,, \end{cases} \tag{3.7}$$

where the break point for the power law lies at r_b. For the 2-point stencil, we observe a flat power law of 0.06 ± 0.12 (0.00 ± 0.12 in the 3-point stencil) until a break point of approximately 0.90 ± 0.20 degrees (0.90 ± 0.12 degrees). After this break point, the warm gas develops a power law slope of 0.59 ± 0.06 (0.66 ± 0.07). The errors for the fitted parameters were determined similar to the integrated quantities of the cold gas in Section 3.4.2.

Table 3.2: Fitted parameters for the 2-point and 3-point structure functions calculated in Section 3.4.3 for the column densities of warm gas not found in absorption, fitted with a broken power-law function (Equation 3.7), and the optically thin and thick column densities of the GASKAP absorption sightlines (Nguyen et al. 2024), fitted with a single power-law function (Equation 3.6)

Structure Function	Amplitude (A)	Slope 1 (α_1)	Slope 2 (α_2)	Break (r_b) (degrees)
$N_{\mathrm{H\,I},WNM}$ (2-point)	$(0.78 \pm 0.14) \times 10^{40}$	0.06 ± 0.12	0.59 ± 0.06	0.90 ± 0.20
$N_{\mathrm{H\,I},WNM}$ (3-point)	$(2.42 \pm 0.37) \times 10^{40}$	0.00 ± 0.13	0.66 ± 0.07	0.90 ± 0.12
$N_{\mathrm{H\,I},thin}$ (2-point)	$(1.71 \pm 0.32) \times 10^{40}$	0.47 ± 0.16	-	-
$N_{\mathrm{H\,I},thin}$ (3-point)	$(5.24 \pm 1.53) \times 10^{40}$	0.54 ± 0.34	-	-
$N_{\mathrm{H\,I},thick}$ (2-point)	$(1.67 \pm 0.31) \times 10^{40}$	0.59 ± 0.09	-	-
$N_{\mathrm{H\,I},thick}$ (3-point)	$(5.31 \pm 0.45) \times 10^{40}$	0.65 ± 0.09	-	-

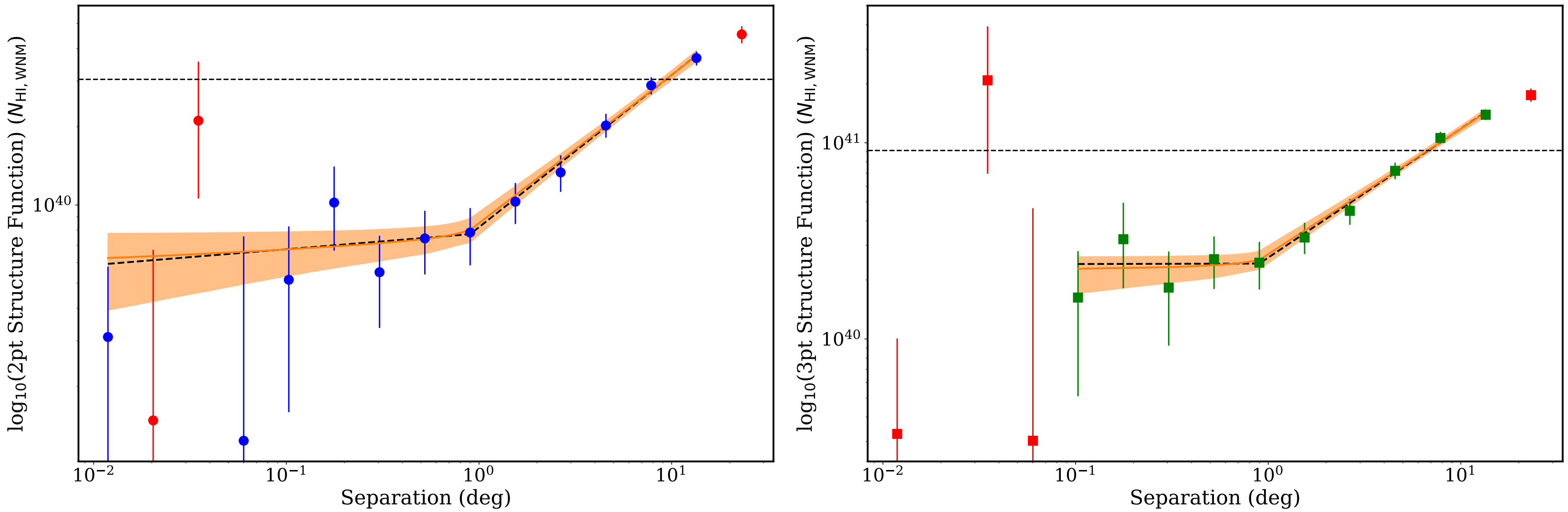

Figure 3.6: Log-log plots of the binned average 2-point (left) and 3-point (right) structure function measurements for the H I column density of the remaining warm gas, $N_{\mathrm{H\,I},WNM}$ not fit in absorption from the 446 sightlines of the GASKAP Pilot survey (after applying noise-cutoffs), calculated in Section 3.4.3. The 2-point and 3-point structure functions are marked in the blue circles and green squares, respectively, with the red points indicating bins with low sampling and which are hence unreliable. The orange lines indicate the power-law fits, with the shaded region marking 1 standard deviation. The plateau points are marked by the dotted black lines, equal to $2\sigma^2$ for the 2-point structure function and $6\sigma^2$ for the 3-point structure function, as in Figure 3.5.

Figure 3.7 displays the structure functions for the optically thin and thick total $N_{\mathrm{H\,I}}$ along the GASKAP absorption sightlines. In both the 2-point and 3-point stencils, single power laws were fit to the data as no break or correlation length scale was apparent. The slope of the optically thin column density was approximately 0.47 ± 0.16 and 0.54 ± 0.34 in the 2-point and 3-point stencil respectively. The optically thick column density structure function yielded power law slopes of 0.59 ± 0.09 and 0.65 ± 0.09 with the same stencils. The fitted parameters' errors were calculated in the same way as those from Section 3.4.2.

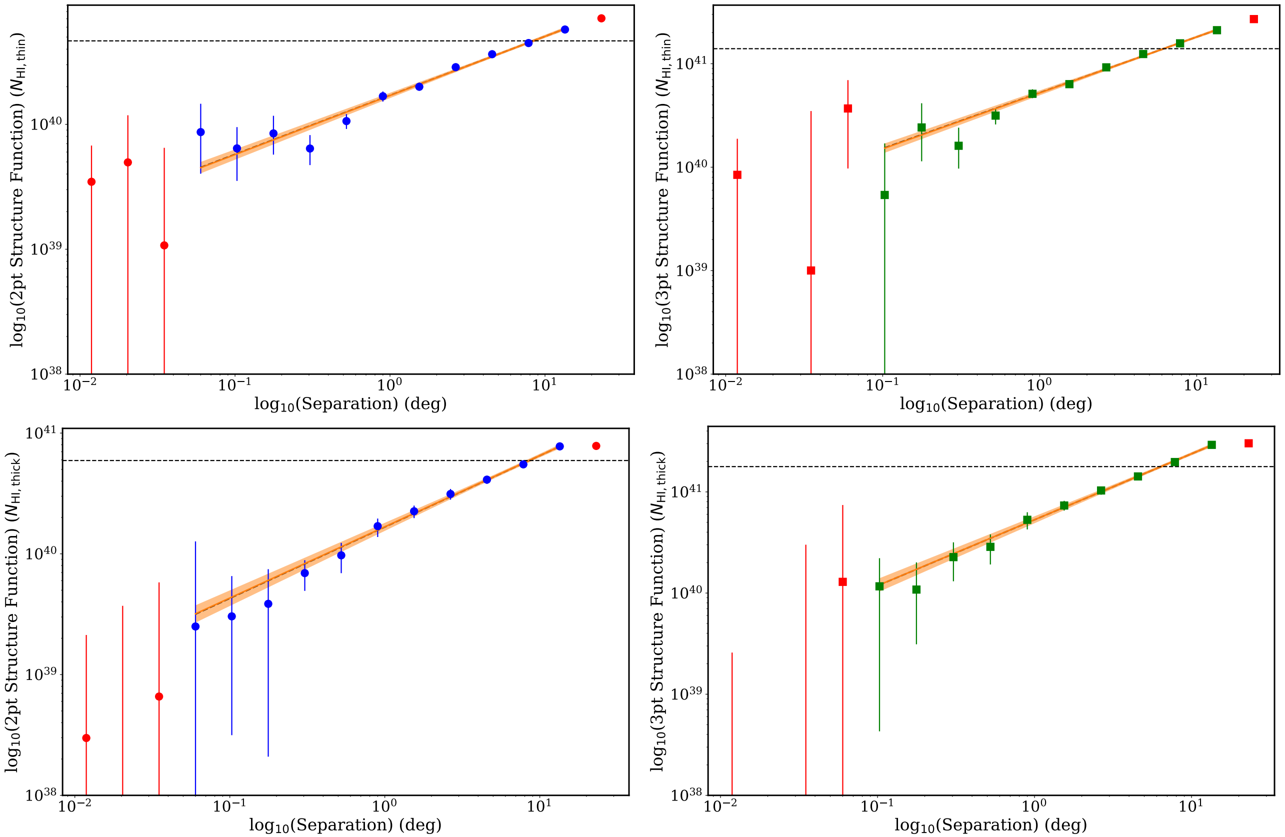

Figure 3.7: Log-log plots of the binned average 2-point (left) and 3-point (right) structure function measurements for the total H I column density $N_{\text{H I},WNM}$ from the 453 sightlines of the GASKAP Pilot survey in the optically thin (top) and thick (bottom) regime (after applying noise-cutoffs), calculated in Section 3.4.2. The 2-point and 3-point structure functions are marked in the blue circles and green squares, respectively, with the red points indicating bins with low sampling and which are hence unreliable. The orange lines indicate the power-law fits, with the shaded region marking 1 standard deviation. The plateau points are marked by the dotted black lines, equal to $2\sigma^2$ for the 2-point structure function and $6\sigma^2$ for the 3-point structure function, where σ is the standard deviation of the original sample (Seta et al. 2023).

3.5 Spatial Power Spectrum of H I Emission

Assuming the structure function is properly sampled with enough data points, the power-law slopes can be analytically related to the power-law slope of an equivalent spatial power spectrum of the same field taken over the fully spatially sampled data (Deshpande et al. 2000; Seta et al. 2023). The spatial power spectrum is a similar statistical tool to the structure function, having been applied to observations of various tracers of the ISM, in both Galactic and extragalactic environments (Plume et al. 2000; Dickey et al. 2001; Burkhart et al. 2010; Pingel et al. 2013, 2018). The power-law slopes provide information on the relative amount of structures as a function of spatial scale and can be related to models of turbulence through comparison with numerical simulations (Burkhart et al. 2010).

With this in mind, we can use the H I emission field of the GASKAP pilot survey discussed earlier in Section 3.2.1 to compute a spatial power spectrum of the region used in this work for direct comparison with the structure function power-law slopes. To compute the spatial power spectrum, we used the same methodology described in Pingel et al. (2018), which computed power spectra of different ISM tracers of the Perseus molecular cloud. The methodology described computes the 2-dimensional spatial power spectrum that assumes azimuthal symmetry about the centre of the modulus image of the Fourier transform to take median values as a function of radius from the centre of the image of the Fourier plane. The use of median values instead of mean values is justified by the existence of bright pixels along the axes of the modulus image caused by the Gibbs phenomenon (Pingel et al. 2018). Following this method, we computed the spatial power spectrum for the optically thin column density of H I emission for the GASKAP Pilot survey, shown in Figure 3.8.

The errors in the median values for the power spectrum were calculated by employing the median absolute deviation (MAD) method (Pingel et al. 2018). For some distribution X that depends on a univariate data set made from individual samples $(X_1, X_2, ...X_n)$ is defined as:

$$\mathrm{MAD} = \mathrm{median}(|X_i - \mathrm{median}(X)|), \tag{3.8}$$

The MAD method is more robust compared to typical standard deviations in avoiding the bias from outliers (such as the high pixel values from the Gibbs phenomenon) and from differing sample sizes at different spatial scales in the image. The computed spatial power spectrum, $P(k)$, can be modelled as (Marchal et al. 2021):

$$P(k) = B(k) \times P_0 k^{\gamma} + N_0 N(k), \tag{3.9}$$

where P_0 is the amplitude of the single power-law, γ is the scaling exponent, $B(k)$ is the spatial power spectrum of the beam of the observing instrument, defined as a Gaussian of FWHM = 30 arcseconds, and $N(k)$ is the noise estimated from the spatial power spectrum of empty channels of the PPV (position-position-velocity) cube of the survey, with N_0 being a scaling factor for fitting. The resulting fitted power spectrum has a power-law slope of 2.87 ± 0.20.

3.6 Discussion

In Section 3.4.2, we found the 2-point structure functions of the integrated optical depth and column density of the 412 GASKAP absorption sightlines both produced power-law structures, with slopes of 0.19 ± 0.08 and 0.31 ± 0.05, respectively.

Assuming the structure function is properly sampled with enough data points, the power-law slopes can be analytically related to the power-law slope of an equivalent power spectrum of the same field taken over fully spatially sampled data. If a structure function of H I column density can be expressed as $\mathrm{SF}(\mathrm{N}_{\mathrm{H\,I}}) \sim r^{\alpha}$, the equivalent power spectrum, $\mathcal{P}(N_{\mathrm{H\,I}})$ can be expressed as $\mathcal{P}(N_{\mathrm{H\,I}}) \sim k^{-\alpha-2}$ (Deshpande et al. 2000; Seta et al. 2023) where we convert to the spatial power spectrum of a two-dimensional field. Using this conversion, the power spectrum of the CNM detected through absorption within the GASKAP pilot survey region yields a slope of ~ -2.3, and the optical depth spatial power spectrum would have a slope of ~ -2.2. For spatial power spectra of H I column densities, it has been found that the power-law slope traces that of the three-dimensional density field, so long as the medium's depth is on the order of the transverse scale in the image (Miville-Deschênes et al. 2003). From dust measurements of the filamentary region, we know this criteria holds (Lynn et al. 2025). Therefore, we find the CNM slope in this work is shallower than that of a typical Kolmogorov slope of ~ -3.6 for an incompressible fluid (Pingel et al. 2018). This deviation aligns with the idea that the cold neutral medium is compressible and formed through shocks and supersonic turbulence that in turn create small-scale density enhancements (Beresnyak et al. 2005; Kowal & Lazarian 2007; Burkhart et al. 2010).

Previous H I emission surveys have separated the phases of H I gas based on the FWHM of Gaussian components. Martin et al. (2015) for example used data from the GBT H I Intermediate Galactic Latitude Survey (GHIGLS). By separating Gaussian components into the two stable phases of the WNM and CNM, they found the two phases had power spectrum slopes of approximately -2.6 to -3.2 for the WNM and -1.9 for the CNM. Kalberla & Haud (2019) however, performed a similar separation using H I emission data from the HI4PI survey, this time including the UNM as a potential category. The CNM gas that was separated yielded a power spectrum slope of around −2.5. The CNM slope from the HI4PI survey agrees more closely with our value from the GASKAP pilot survey absorption data, implying the need for the UNM to be included in models of the ISM. This constant requirement for including the UNM also aligns with previous work demonstrating the existence of UNM gas within the GASKAP pilot survey region (Lynn et al. 2025).

As mentioned earlier, the main drawback of these previous surveys using spectral decomposition of H I emission data is that no radiative transfer information is used. Instead, gas is separated based on components' FWHM which contain both thermal and turbulent contributions. In addition to this, H I emission uses an optically thin approximation, not taking into account the full optically thick regime where CNM gas typically exists. With this in mind, this work, focussing on absorption-emission pairs with full radiative transfer, constitutes a more accurate probe of the structure function and power spectrum of the CNM.

Similar studies of H I absorption structure functions have utilised optical depth maps over individual resolves background sources. While each work has looked at different sources and hence portions of gas in the sky, structure functions of optical depth maps of foreground gas have power-law slopes typically within the range of 0.3 to 0.8 across AU scales up to scales of a few parsecs (Deshpande et al. 2000; Roy et al. 2010, 2012; Dutta et al. 2014). Deshpande et al. (2000) for example, mapped optical depth across the background source of Cassiopeia A, finding a structure function slope of approximately 0.75 over a physical range of 0.02–4 parsecs. Dutta et al. (2014) also found optical depth structure function slopes of around 0.81 ± 0.13 towards the absorption source 3C 138 across scales of $5-40$ AU. The H I optical depth slopes found in this work of approximately 0.2 ± 0.1 are shallower in comparison, and align more with the slope from Roy et al. (2012) of ~ 0.33 over scales of $5-100$ AU. The shallower slope could be explained by the dominant cold filaments in the region and their anisotropic structure (Lynn et al. 2025). This anisotropy would lead to the power spectrum of turbulence to become shallower than that of typical three-dimensional turbulence, and hence the slope of the structure functions for H I absorption properties (Roy et al. 2009, 2012).

In both the optical depth and CNM column density structure functions we do not detect any correlation length scale within the scale range probed, beyond which the structure function flattens. We therefore conclude the correlation length scale, where cold gas sightlines become no longer related to each other, must exist on scales equal to or larger than the spatial extent of GASKAP of ~ 25 degrees.

From dust measurements of the filamentary region, the distance to the Reticulum and Hydrus filaments is approximately 240 ± 45 pc (Edenhofer et al. 2024; Kamal Youssef & Grenier 2024; Lynn et al. 2025; Nguyen et al. 2025b). Combining this physical distance with the angular extent of the GASKAP survey of $\sim 25°$, the physical plane-of-sky spatial extent of the GASKAP Pilot survey is approximately 100 ± 20 pc. The smallest angular bin confidently sampled by the 3-point stencil structure function is around 0.1 degrees, with a physical size-scale of ~ 0.4 pc for the local filaments. Assuming the absorption sources that constructed the structure function are in the vicinity of the filaments, the correlation length scale for the CNM must therefore be greater than ~ 100 pc or less than 0.4 pc.

3.6.1 Spin Temperature

The temperature structure function, on the other hand, remains flat, with the 3-point structure function yielding a power-law slope of 0.05 ± 0.05, as discussed in Section 3.4.2. The flatness of the spin temperature 3-point structure function suggests that there is no scale-length dependence of the variation of spin temperature between the spatial scales of ~ 0.4 to ~ 100 pc within the survey region. This aligns with the qualitative analysis from Section 3.3.2 where no structures could be detected based on spin temperature. Flat structure functions can also be produced by randomly arranged values within a field, as well as a scenario with values derived from a Gaussian distribution. The flatness could also imply the correlation scale is much smaller than what the GASKAP survey's resolution probes. Based on these points, we conclude that the spin temperatures of the GASKAP Pilot survey show no signs of dependence with spatial-scale within the spatial extent and resolution capabilities of the survey.

The GASKAP pilot survey's region is rectangular in shape across Galactic coordinates, and the absorption sightlines are predominantly towards filaments which align with particular directions on the plane-of-sky. These elements could lead to potential bias of our study in the form of anisotropy of the absorption sources found in the survey. This lack of isotropy would mean our structure functions would be biased towards particular directions across the plane-of-sky, along the major filaments in the region. To ensure the flat spin temperature structure function is not affected by this, we randomly swap the spin temperatures among the absorption sightlines (see Appendix A.2.3). The resulting structure function is also flat, and suggests that the location of our discrete sightline sample does not bias the structure function. It should be noted that the anisotropy from the orientation of the two dominant filaments in the region may also affect the slope of the spatial power spectra of column density discussed in this work, but this effect cannot currently be separated or quantified given the uncertainty levels in the fitted power-law slopes.

3.6.2 Synthetic Observations

Since spin temperature structure functions have not been achievable in previous H I absorption surveys, we look towards synthetic observations from numerical simulations to test if they can replicate flat spin temperature structure functions and find potential physical origins. For this work, we look to the TIGRESS MHD simulations (Kim & Ostriker 2017). Specifically, we use the MHD-PI version (Kado-Fong et al. 2020), which models a slice through a Milky Way-like galactic plane at a galactic radius similar to our Sun. The benefit of the MHD-PI version over other iterations of the TIGRESS simulations is the post-processing with adaptive ray-tracing to transfer UV from the sources such as star clusters. This added step leads to more accurate density calculations for H I modelling. The simulations reach a z-height of ±3584 pc with 2 pc resolution. The total H I column density is shown in Figure 3.9.

To create an analogous synthetic observation to the GASKAP survey, we choose to look through the bottom half of the simulation from the Galactic mid-plane. This view point mimics a Milky Way-like galaxy from the perspective an observer within the Galactic disk, such as the Sun, towards high galactic latitude gas. It is worth noting that this is more idealised than reality, where the Sun would sit within the simulation and the sightlines observed would be from a spherical coordinate system centred on the point-of-view (Kim et al. 2019). The resulting column density field of this sub-region is shown in Figure 3.10.

Within this subfield, we choose 200 pc wide boxes to limit the spatial extent down to the GASKAP survey's physical size scales, also indicated in the right side of Figure 3.10. Since the sightlines used in this work to construct the structure functions in Section 3.4.2 were based on absorption sightlines of cold gas, we restrict the simulation to only include cells with kinetic temperatures, $T_k < 500$ K.

We used the z direction as our line-of-sight and v_z as our line-of-sight velocity for each cell. From this, we created synthetic H I spectra of brightness temperature, T_B and optical depth τ using the methodology from Kim et al. (2014), assuming $T_s \approx T_k$ (Seon & Kim 2020). The 200 pc boxes used in our analysis were chosen are highlighted in Figure 3.10. These regions were chosen to compare to the GASKAP survey due to their combination of bright filamentary regions with more diffuse gas on the periphery.

From these resulting synthetic observations, 500 sightlines were randomly chosen that contained cold gas. Distributions of the brightness temperature and optical depth values from these synthetic sightlines for each region before the temperature cut are shown in Figure 3.11, compared with the values from the GASKAP-HI absorption spectra used in this work. We find that the values from the TIGRESS regions are similar to that of the GASKAP-HI spectra, meaning they capture similar gas properties to the GASKAP-HI survey fields. Since a full component separation with radiative transfer is computationally expensive, we choose to instead use the harmonic mean-weighted spin temperature, $\langle T_s \rangle$, defined as (Kim et al. 2014; Murray et al. 2018):

$$\langle T_s \rangle = \frac{\int \tau(v) \cdot T_s(v) dv}{\int \tau(v) dv} = \frac{\int \tau(v) \cdot \frac{T_B(v)}{(1-e^{-\tau(v)})} dv}{\int \tau(v) dv}. \tag{3.10}$$

While the harmonic mean-weighted spin temperature is typically skewed towards slightly warmer phases by excess emission that is harder to detect in absorption buried in the noise, the restriction of gas temperatures in our synthetic data to a maximum of 500 K alleviates this concern. We calculate the harmonic mean-weighted spin temperature for each of our 500 sightlines.

Following the procedure from Section 3.4.1, we produced a structure function of the harmonic mean-weighted spin temperature for each of the chosen regions, shown in Figure 3.12. We find that the synthetic data consistently produces a spin temperature structure function with a non-zero power law slope. The correlation length scale of the spin temperature is also observed, with the structure functions of each region reaching their plateau points within the spatial extent of the 200 pc box-size. However, when we introduce the observational noise of the GASKAP pilot survey ($\sigma_{T_B} \sim 1.25$ K), and optical depth noise randomly sampled from the absorptions sightlines from Nguyen et al. (2024)), the structure function slope disappears, as shown in Figure 3.12.

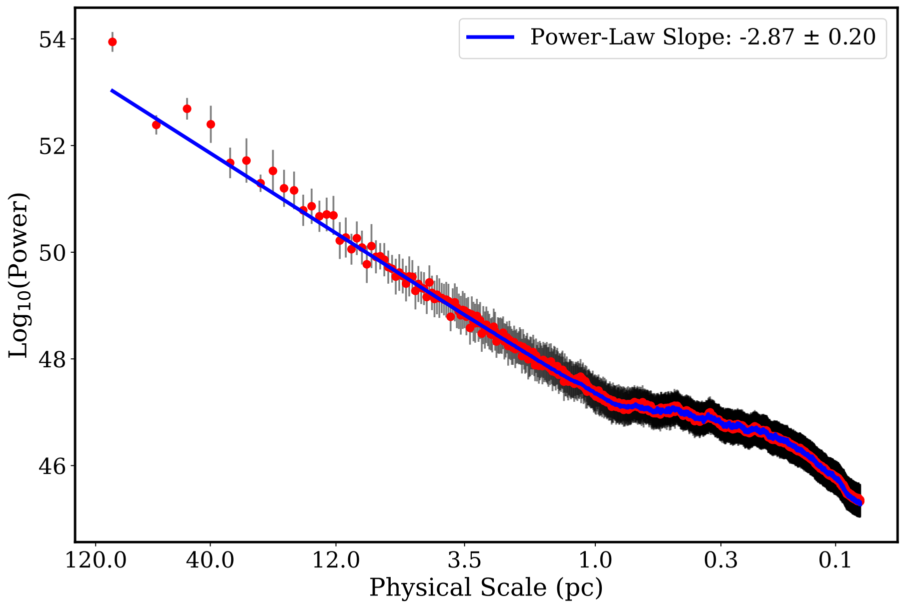

Figure 3.8: Spatial Power Spectrum of the H I column density map for the GASKAP Pilot survey, displayed in Figure 3.1. The blue line indicates the single-power-law fit described in Section 3.5.

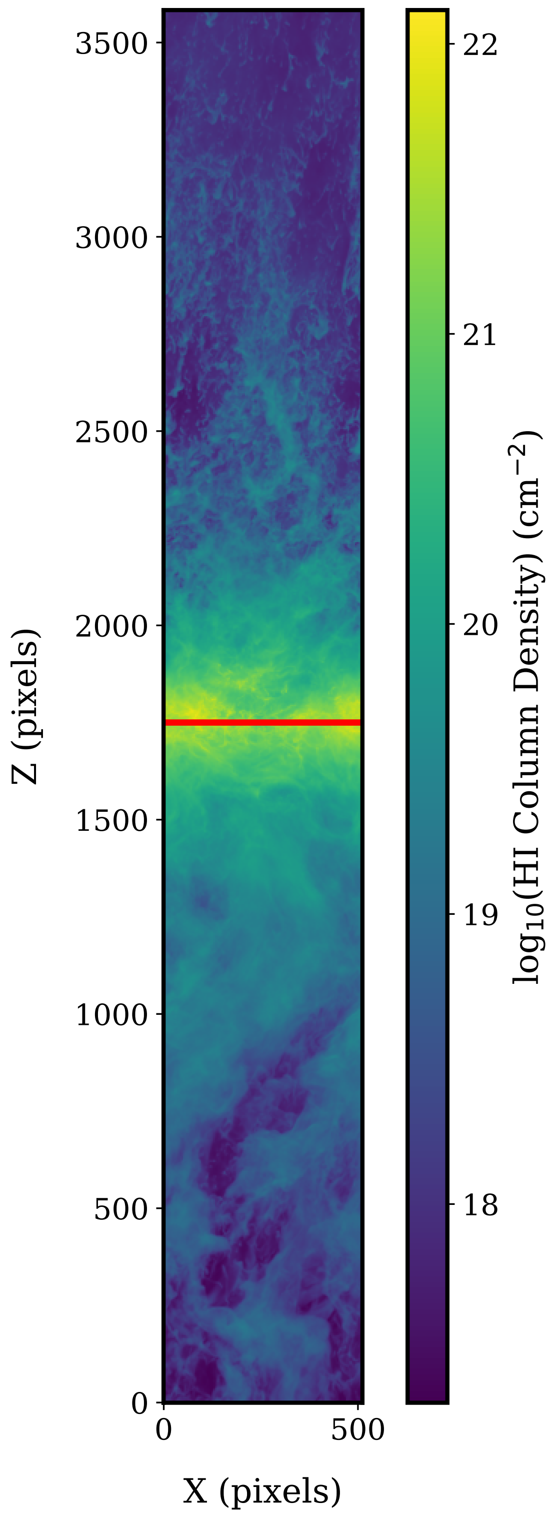

Figure 3.9: H I column density map from the total TIGRESS MHD-PI simulation (Kim & Ostriker 2017; Kado-Fong et al. 2020) of a cutout of a Milky-Way-like galactic plane. The red line indicates the cutoff where data below was used for the synthetic observation looking towards gas at high Galactic latitude from the perspective of the red line.

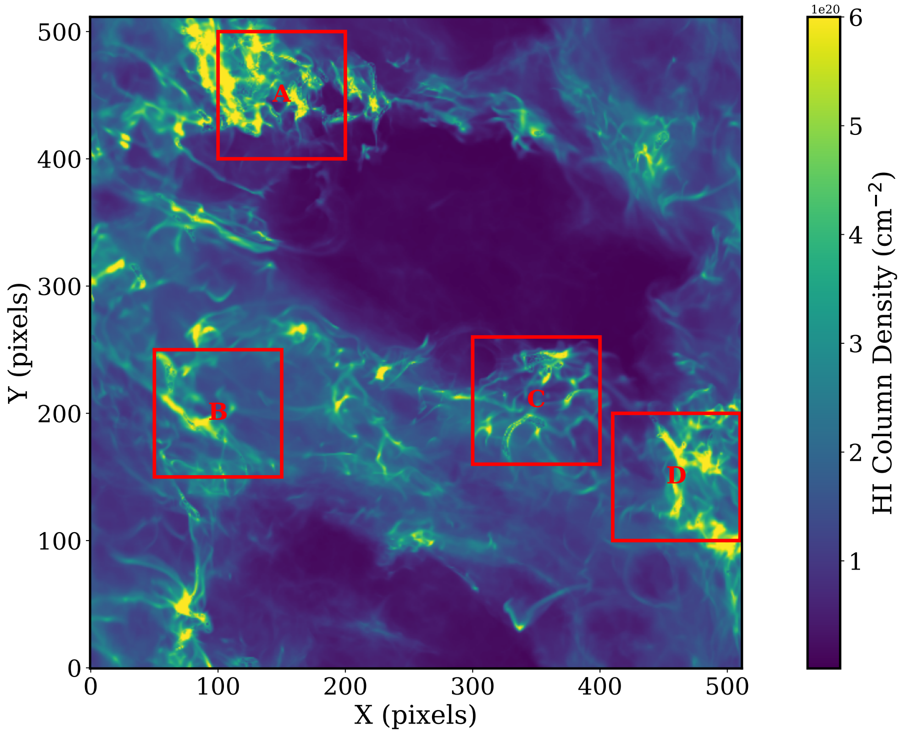

Figure 3.10: Synthetic observation of H I column density of the TIGRESS Simulation (Kim & Ostriker 2017; Kado-Fong et al. 2020) from the point-of-view of the mid-plane, as shown in Figure 3.9. The red boxes indicates the 200 pc regions used for the structure function comparison in Section 3.6.2.

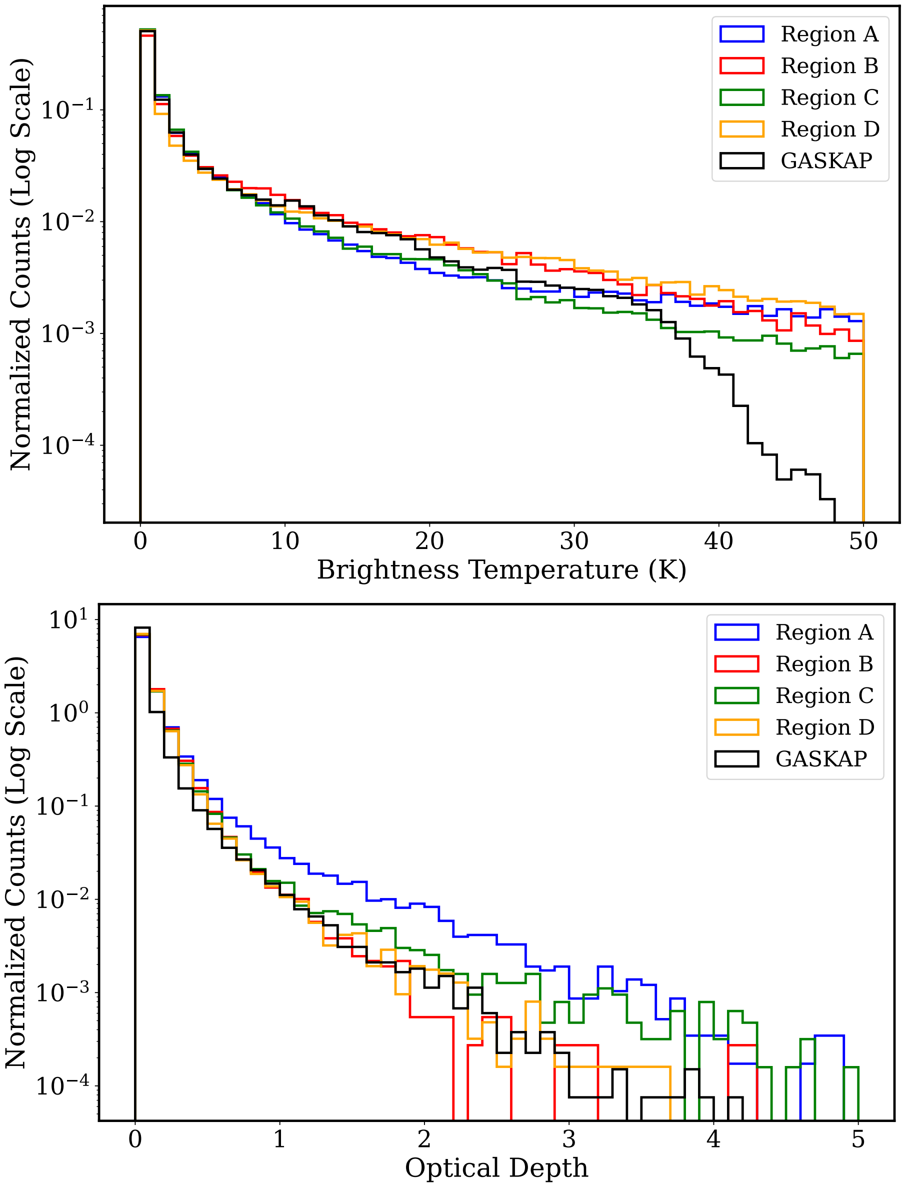

Figure 3.11: Distributions of the brightness temperature (top) and optical depth (bottom) values for each of the regions highlighted in Figure 3.10, compared with the values from the GASKAP-HI absorption spectra used in this work. The values used are from the entire spectra from -50 to 50 km s^{-1}.

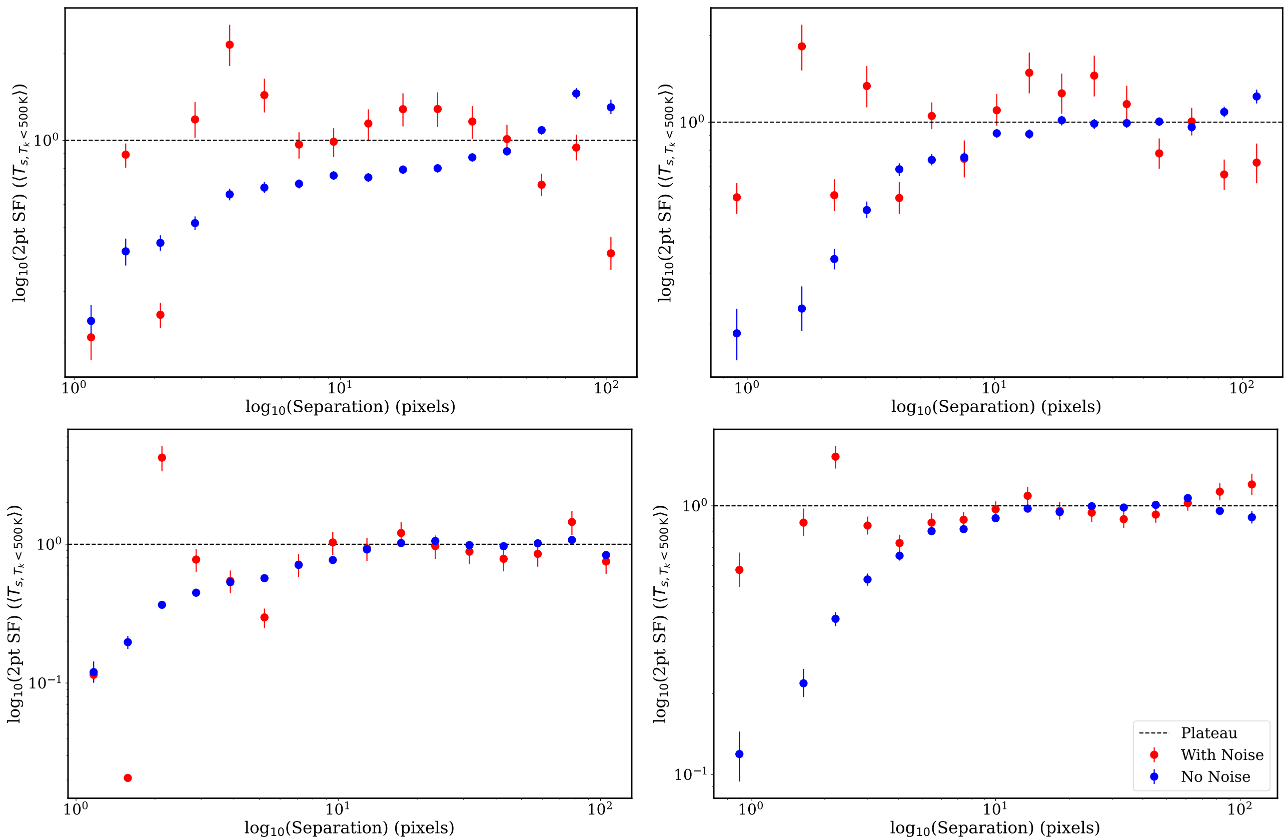

Figure 3.12: Normalised structure functions of the TIGRESS simulation using data from the H I synthetic observation and regions A (top left), B (top right), C (bottom left), and D (bottom right) shown in Figure 3.10. The blue points are the structure function of the TIGRESS line-of-sight harmonic mean-weighted spin temperature of gas with $T_k < 500$ K as given through radiate transfer. The red points are from the same sightlines, but with brightness temperature and optical depth errors added similar to the GASKAP survey. Both structure functions are normalised for comparison by the plateau point of the 2-point structure function equal to $2\sigma^2$ (Seta et al. 2023).

With this same result occurring in multiple regions throughout the TIGRESS simulation, we conclude that a main reason for the spin temperature structure function being flat in the GASKAP pilot survey is due to the spin temperature values being dominated by observational noise. We also produced similar structure functions from the TIGRESS simulation for the optically thick column density and integrated optical depth for cells with $T_k < 500$ K. These quantities were calculated using Equations 3.3 and 3.4. The structure functions for these quantities are shown in Appendix A.2.4. The difference between the structure functions of these quantities of the true values and when GASKAP-level noise is added is negligible. This implies that the structure functions of column density and integrated optical depth in Section 3.4.2 for cold H I gas are not affected by noise as much compared to the average line-of-sight spin temperature.

While the noise levels of the GASKAP pilot survey explain the flatness of the spin temperature structure function, they do not explain the narrow error bars of each of the bins, since high noise levels should cause large uncertainties in the bins' values. This implies that the overall uncertainties given to the spin temperature values from Nguyen et al. (2024) may be underestimating the true errors involved in the calculation. The method for calculating the spin temperature is based on the method provided by Heiles & Troland (2003), where there are multiple effects and processes whose errors are not properly quantified, such as the fraction of cold gas being in front of warmer phases, and the difference in location of absorption and emission sightlines probing slightly different gas. Such effects are hard to quantify properly, and may lead to the total spin temperature distribution of the GASKAP sample simply following a Gaussian distribution because of the uncertainty in temperature estimates rather than a physical reason. In order to properly test the effects of errors in spin temperature calculations, future work will need to focus on applying new tools and techniques based on physics-based forward models such as `CARIBOU`[3], rather than spectral decomposition techniques.

3.6.3 CNM vs Warm and Total $N_{\mathrm{H\,I}}$

In Section 3.4.3, we calculated the structure function for the column density of warmer H I gas not observed in absorption by Nguyen et al. (2024). The resulting structure function (shown in Figure 3.6) produced a broken power law, which was flat until a break at around 0.9 degrees. Using the average line-of-sight distance to this cirrus H I gas of $\sim 240 \pm 45$ pc from earlier, this angular distance becomes a physical plane-of-sky distance of approximately $3 - 4$ pc. The flatness of the

[3] https://github.com/tvwenger/caribou_hi

structure function is likely due to the structure function reaching a comparable level to the structure function for the rms noise of the separated WNM column densities and is thus non-physical (see Appendix B of Lee et al. 2025). The structure function's power law after the break of ~ 0.66 can be converted into a spatial power spectrum slope of ~ -2.6 for a 2-D field. The slope is shallower than that of the turbulent cascade in an idealised Kolmogorov incompressible fluid of around $\sim -11/3$, or an equivalent compressible turbulence with a low density contrast. This slope is also found in the 3-point stencil of the optically thick total column density, as shown in Figure 3.7. Gas in a transonic regime, typical of the WNM, has been shown to follow a density-field power-law slope similar to Kolmogorov (Kim & Ryu 2005). The discrepancy between this and our result likely stems from the inclusion of gas from the UNM, which would exist on scales between the CNM and WNM as a transitionary stage between the two, and so the combined power law would be shallower than if it was solely WNM gas. Additionally, as mentioned earlier, the anisotropic structure from the large-scale filaments in the region of the survey could influence the power spectra, leading to shallower slopes than three-dimensional turbulence Roy et al. (2009, 2012). The single power law of ~ 0.65 seen in the total column density does not exhibit any breaks as seen in the warm gas only structure function due to better noise characteristics. Combined with the fact that this slope is equivalent to the WNM only column density slope at larger scales, this implies the structure function of the total column density is not sensitive to the fluctuations of the CNM, since the warmer H I phases remain the dominant mass fraction of the cirrus ISM. It should be noted this result likely relies on the individual region in question and the location's relative amounts of CNM and WNM. The total column density slopes from the structure functions also agree with the spatial power spectrum computed from the optically thin emission of the GASKAP Pilot Survey from Section 3.5 of approximately -2.9. The structure function slopes are slightly shallower, likely stemming from the sightline locations being biased towards regions of cold gas where absorption was detected. However overall they still match within standard deviations and as such provide a useful confirmation of the conversions between structure functions and spatial power spectra for this work.

Comparing the column density structure function slopes of all of the phases, we can conclude that the CNM, while subdominant in the total column density structure function, has a shallower slope than the warmer phases, with more power existing on smaller scales where the CNM resides. This agrees with the picture of the CNM existing as small dense clumps enveloped in a warmer medium. However, all phases, including the warmer H I gas, follow slopes shallower than idealised Kolmogorov turbulence. While this disagrees with large-scale Milky Way H I spatial power spectrum analysis of optically thin emission (Pingel et al. 2018), this discrepancy has been observed in regions with large amounts of cold gas (Martin et al. 2015; Kalberla & Haud 2019).

3.7 Summary

We present analysis of the spatial distribution and structure of the multiphase neutral interstellar medium gas within the Milky Way towards the Magellanic system via the recent Milky Way GASKAP Phase II Pilot survey's 462 H I absorption detection sightlines. We report the results of both qualitative descriptions of cold gas property's spatial variation, as well as the application of structure functions to quantify the spatial dependence of cold gas properties typically observed. We contextualise this with structure functions of the warmer phases and total H I gas. The main conclusions of this work are as follows:

- The optically thick H I column densities of cold gas observed via absorption in the GASKAP pilot survey agree with large scale Milky Way disk models, decreasing with increasing Galactic latitude.
- Qualitatively, the lowest peak optical depth values of the 690 cold components from the pilot survey are ubiquitous throughout the region and not dependent on any physical features. High peak optical depth values however are dominated towards the central Hydrus and Reticulum filaments, and in regions towards the Galactic plane.
- Integrated line-of-sight quantities such as H I column density, the cold gas mass fraction, and the optically thick-to-thin correction factor decrease in value with plane-of-sky angular separation from the Reticulum and Hydrus filaments, implying the majority of cold gas is held within the dense filaments. Peak optical depths of individual components also exhibit this trend.
- The spin temperature and full-width half-maximium of cold gas components do not vary with angular separation from the two filaments.
- Using structure functions, the H I column density and integrated optical depth form single power-laws with slopes of 0.34 ± 0.01 and 0.23 ± 0.04, respectively. The correlation length scale of the two fields is not observed, implying the scale at which cold gas becomes unrelated must be greater than the survey's physical range of ~ 100 pc across the plane-of-sky or smaller than 0.4 pc, at the limit of what is currently confidently probed.
- The structure function of the mass-weighted mean spin temperature however,

is flat, implying spin temperature is spatially uncorrelated across the GASKAP survey's spatial extent. However, this effect is likely due to observational bias and the noise-levels of the survey.

- The structure function of column densities of warm and unstable neutral medium residual gas not observed in absorption yields a broken power law, being flat and below a plane-of-sky length scale of $\sim 3-4$ pc. The flat power law regime is dominated by the noise in the column density measurements and is hence not physical.
- The total H I column density structure function forms a single power law with a slope of $\sim 2/3$, equal to the warmer phases' slope. This implies the total column density structure function is not sensitive to the cold neutral medium at the scales probed in the GASKAP survey.
- All column density structure functions form slopes shallower than that of Kolmogorov turbulence, due to this being a region largely influenced by cold dense anisotropic filaments, and being a region of cold gas formation on smaller scales.

In the near-future, the GASKAP survey will observe the pilot survey fields used in this work with longer integration times. This, in addition to more fields being observed over the next few years, will yield a much larger data set to analyse the spatial distribution of absorption properties, and over larger scales. This will allow for more detailed exploration to observe the correlation length scale of the CNM, and the warmer phases which both appear to be larger than the current survey's largest scales. The higher count of sightlines will also allow the smaller scale bins to be more statistically significant, letting us probe smaller scales towards the beam size of the ASKAP itself.

The GASKAP survey will also be observing different Galactic environments, such as towards the Galactic Plane. Probing different environments of the interstellar medium will enable us to determine what scales the warm H I column density structure function breaks and whether the scale is universal, or dependent on the local physical processes in the region.

With more physics-based forward modelling tools being developed to fit H I 21-cm spectra such as `CARIBOU`, calculating spin temperature through different methods will allow us to test the unquantifiable uncertainties involved in current emission-absorption fitting methods. Such updated methods will allow for a re-analysis of structure functions of temperature to either confirm or deny the trends observed here in this work.

Acknowledgements

GASKAP-HI is partially funded by the Australian Government through an Australian Research Council Australian Laureate Fellowship (project number FL210100039 awarded to NM-G). AS is supported by the Australian Research Council through the Discovery Early Career Researcher Award (DECRA) Fellowship (project DE250100003) funded by the Australian Government and the Australia-Germany Joint Research Cooperation Scheme of Universities Australia (UA–DAAD, 2025–2026). B.L. acknowledges support by the NRF, grant Nos. RS-2022-NR069020.

This research made use of `Astropy`, a community-developed core Python package for astronomy (Astropy Collaboration et al. 2013), `NumPy` (van der Walt et al. 2011), `matplotlib`, a Python library for the publication of quality graphics (Hunter 2007), and `SciPy` (Virtanen et al. 2020).

Chapter 4

Effects on H_I Phase Decomposition with Spatial Resolution in a Local Galactic Filament

Context and Contribution

This chapter presents the contents "Spatial structure of the H I cold neutral medium in a Galactic Rayleigh-Taylor Instability: effects on H I phase decomposition with spatial resolution" by C. Lynn, N. M. McClure-Griffiths, A. Marchal, Marc-Antoine Miville-Deschênes, H. Nguyen, N. M. Pingel, which is currently in preparation for submission to the Monthly Notices of the Royal Astronomical Society. The H I emission data presented in this work was produced and imaged by the GASKAP-HI Survey Builders. I carried out all of the analysis, including the Gaussian decomposition of the H I emission field in this chapter and comparison with 3D dust maps. I have written the manuscript, with insightful feedback and suggestions from the co-authors.

Abstract

We detect small-scale Rayleigh-Taylor instabilities within a local Galactic Filament using new H I emission observations from the Galactic Australian Square Kilometre Array Pathfinder H I (GASKAP-HI) Survey. Two wavelength scales are detected within the instability of 4 and 0.9 parsecs, with the smaller representing the critical wavelength below which smaller wavelengths are suppressed. Through Gaussian decomposition of the H I spectra, we separate the H I phases based on their spectral linewidth. The mean cold neutral medium (CNM) mass fraction of the filament is

0.14 ± 0.11, with the highest values concentrated within the peaks of the instabilities present. The peak CNM mass fraction is lower than those from Galactic H I absorption surveys due to the surveys bias towards regions where CNM is detected, as well as the low volume filling fraction of the CNM within the ISM. Through convolving the field to lower resolutions and applying Gaussian decomposition, we find that H I phase separation tools like ROHSA produce the same mean CNM mass fraction regardless of spatial resolution, likely with the requirment of high spectral resolution and spectra that can be described with few Gaussian components. The peak CNM mass fraction decreases with decreasing resolution due to beam-smearing and a loss of detail of small-scale CNM structures. No plateau is detected in peak CNM mass fraction at high spatial resolution, implying the CNM is still not fully resolved at physical resolutions of ~ 0.03 parsecs.

4.1 Introduction

Learning the properties of the cold neutral medium (CNM) is fundamental to our understanding of the formation of molecular clouds and star formation (Clark et al. 2012; Kim & Ostriker 2017). Due to its high optical depth, the CNM has typically been described through observations of H I absorption where it is easy to detect (Heiles & Troland 2003; Murray et al. 2015). While H I absorption surveys provide accurate phase separation and temperature estimates when combined with H I emission sightlines, they still ultimately lack the spatially resolved data of H I emission maps. To avoid the reliance on bright background sources to obtain absorption spectra, many works have focused on techniques for phase decomposition of H I emission data (Lindner et al. 2015; Marchal et al. 2019; Bhattacharjee et al. 2024). The main method for doing so is through Gaussian decomposition and categorising the components by their velocity dispersions. In more recent years, machine-learning tools have also been developed, trained on synthetic H I observations (Murray et al. 2020; Nguyen et al. 2025a), however Gaussian Decomposition is still commonly used. One decomposition tool in particular, developed by Marchal et al. (2019) is ROHSA, a Gaussian decomposition algorithm that has the added benefit of spatial coherence. Through this addition, neighbouring sightlines are forced to have similar Gaussian decompositions to match the smoothness of H I signals between pixels.

ROHSA has been applied to many H I emission surveys, both Galactic and extragalactic (Marchal & Miville-Deschênes 2021; Marchal et al. 2021; Taank et al. 2022; Buckland-Willis et al. 2025), producing estimates on H I phase mass fractions and turbulent Mach numbers. These observational measurements are then used to inform numerical simulations to better test theories of the dynamical processes in the ISM. However, one key issue that has not been properly explored with these Gaussian decomposition techniques is their reliance on spatial resolution. Galactic gas is typically close enough to obtain parsec resolution, especially at high Galactic latitudes (Miville-Deschênes et al. 2017; Marchal et al. 2021; Lynn et al. 2025). The best extra-galactic H I emission surveys on the other hand, even to nearby dwarf galaxies of the Magellanic system, currently have physical resolutions of approximately 8 parsecs per beam (Pingel et al. 2022; Lee et al. 2025). From observations of thermal instability scales in the Galactic ISM, the condensation of CNM triggers on scales smaller than 15 pc Marchal et al. (2021). Therefore, in many regions of extra-galactic bodies, H I emission surveys do not resolve the small-scale structure of the CNM. It is uncertain how Gaussian decomposition tools can estimate properties such as the CNM mass fraction of gas for lower physical resolutions. In order to test this, we require high resolution Galactic H I emission surveys, where the resolution can be reduced towards that of extra-galactic surveys. From this it can be seen how losing knowledge of small-scale features affects estimates on the CNM mass fraction compared to reality.

The Galactic Australian Square Kilometre Array Pathfinder H I (GASKAP-HI) Survey is currently observing high Galactic latitudes, producing high resolution H I emission maps (Dickey et al. 2013; Hotan et al. 2021; Pingel et al. 2022). A 50-hour observation of Milky Way foreground gas towards the Small Magellanic Cloud provides a 30 arcsecond resolution map. The high spectral resolution of 0.5 km s $^{-1}$ makes it ideal for detecting components of cold gas which have typically narrower line-widths Nguyen et al. (2024). Within this region lies a sub-region of a long Galactic filament with sharp velocity features. In this work, we use these observations to explore the effects spatial resolution has on Gaussian decomposition of high Galactic latitude H I emission fields and to determine if these methods are reliable when cold H I gas is not spatially resolved. With the high resolution of the GASKAP-HI survey, we also are able to study the small-scale structure of the CNM embedded within local filaments at sub-parsec resolution, compared to previous Galactic H I emission surveys that were limited to parsec resolution such as the HI4PI survey HI4PI Collaboration et al. (2016).

The chapter is organised as follows. Section 4.2 presents the data used in this work. In Section 4.3, we discuss the algorithm of ROHSA and the choices made in this work to decompose the data. Section 4.4 presents the results from the best fit of ROHSA, along with the phase separation of the filament sub-region and calculations of the CNM mass fraction. In Section 4.4.4 we use dust maps to contextualise the location of this filament and make estimates on the wavelength of instabilities present. A discussion of the results is presented in Section 4.5, including a comparison to H I absorption surveys and to CNM mass fractions when varying the spatial resolution of H I emission maps. Section 4.6 summaries the results of this work.

4.2 Data

4.2.1 Observations

The data in this work makes use of H I emission observations from the GASKAP-HI survey towards the Small Magellanic Cloud (SMC). Seven 8-hour observations were made, consisting of SBID[1] 67521, 68329, 68408, 68827, 68979, 69111, and 69152, over a period from November to December of 2024. Concatenating all 7 observations resulted in an approximately 50-hour observation of a 5×5 square-degree field towards the SMC with a beam-size of 30 arcseconds. The total cube is comprised of 4500×4500 spectra, each with 1639 velocity channels from line-of-sight velocity of -300 to 500 km s^{-1} at 0.5 km s^{-1} spectral resolution. For the purposes of this work, we created a sub-cube of this region spanning a line-of-sight velocity range of -30.1 to 30.4 km s^{-1} to cover gas belonging to the Milky Way foreground, resulting in a cube with 125 velocity channels. The sub-cube created for this work was also focused spatially on the main Milky Way gas within this region of sky, a portion of a Galactic filament. The H I column density of the field is shown in Figure 4.1, alongside a H I column density map from the GASS survey (McClure-Griffiths et al. 2009; Kalberla et al. 2010; Kalberla & Haud 2015b) covering the same region and its surroundings for context. The filament exists over only a few velocity channels from 6 to 15 km s^{-1}, with a brightness temperature map of the same region at a single velocity of ~ 10.8 km s^{-1} shown in Figure 4.2. The filament is prominent in the region, containing scalloping-like features with narrow linewidths, making it an interesting region to probe the H I phase transition and the formation of cold gas structures.

[1]SBID: Scheduling Block ID, as defined on the CSIRO ASKAP Science Data Archive (CASDA)

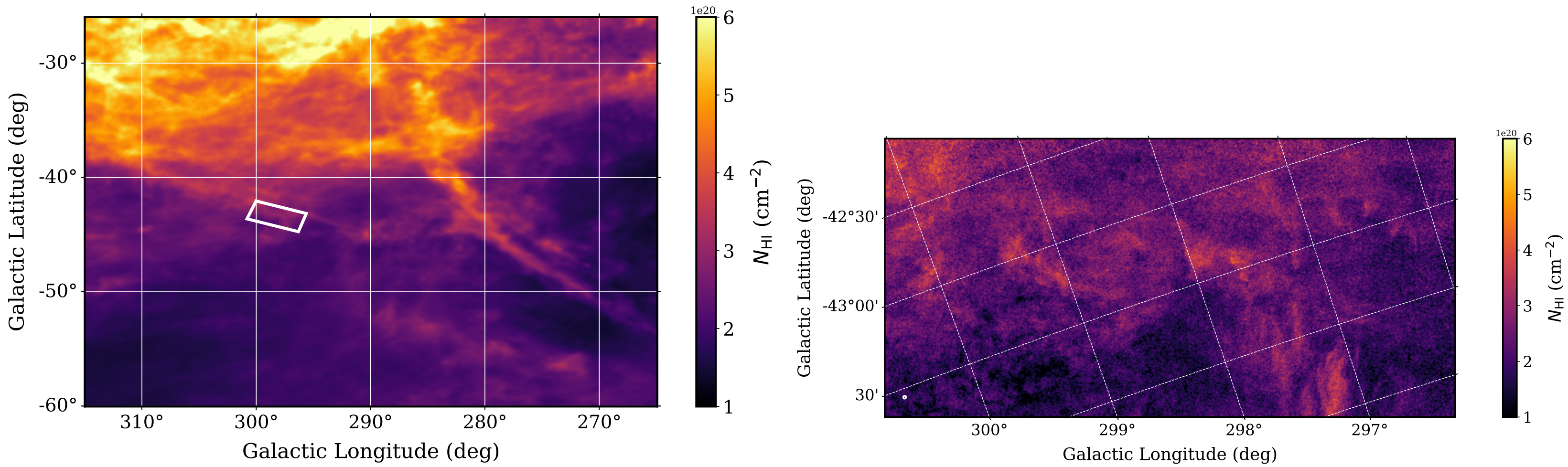

Figure 4.1: H I column density maps calculated over line-of-sight velocities from −30 to 30 km s^{-1}. Left: Map from the GASS survey (McClure-Griffiths et al. 2009; Kalberla et al. 2010; Kalberla & Haud 2015a) towards the Reticulum and Hydrus filamentary structures. The white box highlights the region of the filamentary structure discussed in this work. Right: Map from the GASKAP-HI survey of the region highlighted in the larger field-of-view. The white circle in the bottom-left corner indicates the beam-size of the survey at 30 arcseconds per beam.

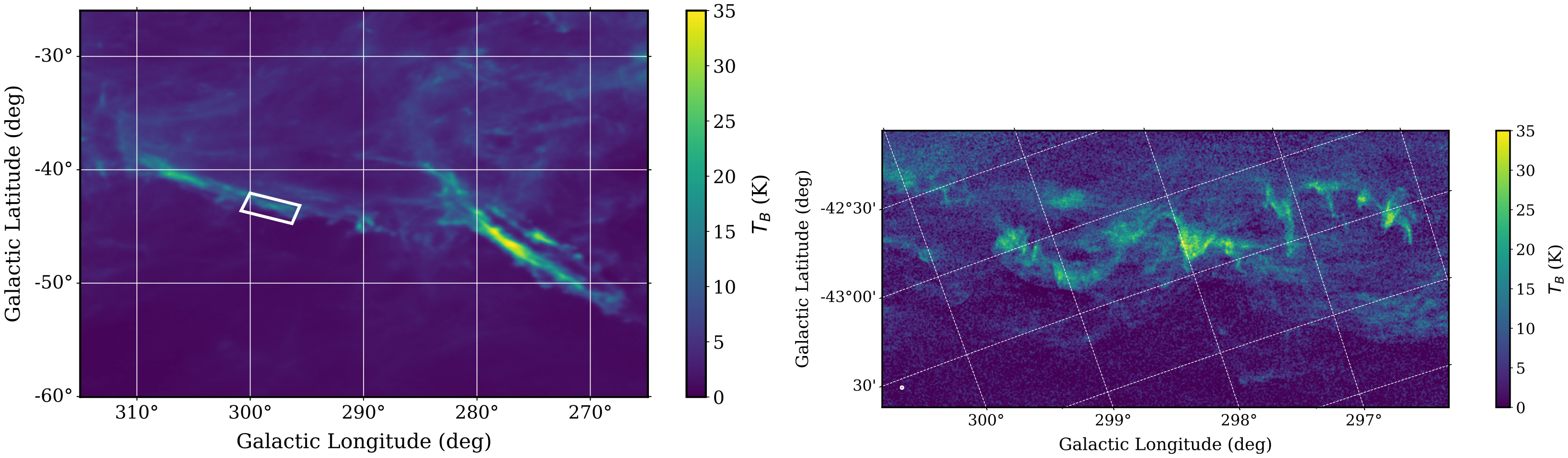

Figure 4.2: H I emission maps of the fields in Figure 4.1 at a line-of-sight velocity of $\sim$ 10.8 km s^{-1}. Left: Map from the GASS survey (McClure-Griffiths et al. 2009; Kalberla et al. 2010; Kalberla & Haud 2015a) towards the Reticulum and Hydrus filamentary structures. The white box highlights the region of the filamentary structure discussed in this work. Right: Map from the GASKAP-HI survey of the region highlighted in the larger field-of-view. The white circle in the bottom-left corner indicates the beam-size of the survey at 30 arcseconds per beam.

4.2.2 Noise Estimation

Since we are focussing on a specific sub-region of the GASKAP-HI survey, it is necessary to measure local estimations of the noise to use later in this work. We use an empirical method of obtaining the noise of the H I emission data-cube, using "emission-free" velocity channels where no H I emission is observed Buckland-Willis et al. (2025). We selected velocity channels in this data cube with 30 channels with $v > 16.3$ km s^{-1} and 20 channels with $v < -20.4$ km s^{-1} that were observed as free of Milky Way emission. These 50 velocity channels out of 125 (40%) were used to measure the rms-noise of each pixel of the data-cube. The median rms-noise in the field was 1.9 K.

4.3 Spectral Decomposition

We performed the spectral decomposition of the subfield of the GASKAP-HI survey used in this work using the publicly available Gaussian decomposition code, ROHSA (Marchal et al. 2019), designed to facilitate phase separation of the 21-cm line. The benefit of using a tool such as ROHSA is that the cost-function takes into consideration the spatial coherency of the H I signal, where H I spectra are similar to their neighbours.

The application of ROHSA requires the user choosing values for the number of Gaussians, N, fitted and the hyper-parameters used in weighting the cost function, defined by Marchal et al. (2019). The cost function, $J(\theta, v)$, over the positional axes, θ, and spectral axis, v, of the data-cube, is defined as:

$$J(\theta, v) = L(\theta, v) + \frac{1}{2}\sum_{n=1}^{N} \lambda_A||DA_n||_2^2 + \lambda_\mu||D\mu_n||_2^2 + \lambda_\sigma||D\sigma_n||_2^2 + \lambda'_\sigma||\sigma_n - m_n||_2^2 , \quad (4.1)$$

where λ_A, λ_μ, λ_σ, and λ'_σ are the hyper-parameters of ROHSA that govern the level of restriction on the spatial variance of the fitted Gaussian parameters A (amplitude), μ (central velocity), and σ (velocity dispersion), and m represents the mean value of μ for each of the Gaussians fit to the data.

The choices for the hyper-parameters need to be adapted for each dataset used based on the physical size of the structure and the complexity of the H I spectra (Marchal et al. 2021). Similar to previous usages of the code, we set the parameters (λ_a, λ_μ, λ_σ) to be the equal to each other for a more efficient search of the parameter-space, since they control similar terms of the cost function regarding spatial coherence (Taank et al. 2022), and it has been previously shown that the hyper-parameters λ_v and λ_σ affect the overall fit less than the other parameters (Buckland-Willis et al. 2025). In searching the parameter-space, we varied the hyper-parameters over 4 orders of magnitude (from values of 0.1 to 100) to find the lowest hyper-parameter values before the reduced Chi-squared (χ^2_{red}) showed a decline in improvement. The lowest hyper-parameters were chosen as they were less restrictive in fitting the data. The number of Gaussians chosen to fit the data was determined through a similar approach, finding the smallest number of Gaussians able to fit the data. The hyper-parameter λ'_σ minimises the variance of the velocity dispersion for each Gaussian field. The ideal λ'_σ value allows for enough freedom to fit the data whilst collecting the sightlines into clusters of similar velocity dispersions, representing the different H I phases.

4.3.1 Error Estimation

Since errors estimates are not obtained from the output of ROHSA, we instead follow the method outlined in Section 4.2.2 of Taank et al. (2022). This involves the quadratic sum of three different methods for estimating errors and testing the stability of the solution. The methods involve either perturbing the initial field before fitting with ROHSA or altering the first initial fit made by the algorithm. The first method involves adding random noise (based on the empty channels of the field) to the original data before fitting with ROHSA using the same hyper-parameters as the best-fit solution. The second method takes the original cube and varies the hyper-parameter values over a uniform distribution by up to a maximum of 10% around the best-fit solution. The third method uses the original data and varies the initial guess ROHSA uses to fit the top-level solution. The initial guess is varied by selecting different starting values for the Gaussian parameters of the fit. The range of values used in this method are based on the full-width half-maximum (FWHM) of the distribution of fitted values for each Gaussian of the best-fit solution. Each of these methods are repeated 100 times to generate 300 total realisations. We then computed the standard deviations of each Gaussian parameter from the 100 realisations of each method. The total uncertainty, σ_{tot}, from these methods was then calculated via:

$$\sigma_{tot} = \sqrt{\sigma_{rn}^2 + \sigma_{hp}^2 + \sigma_{ig}^2}\,, \tag{4.2}$$

where σ_{rn}, σ_{hp}, and σ_{ig} are the uncertainties from the first, second and third methods, respectively.

4.4 Results

4.4.1 Best Fit Model

From the methodology described in the previous section, we determined the field in this work was best described with ROHSA using 4 Gaussians and hyper-parameters of $\lambda_a = \lambda_v = \lambda_\sigma = 10$, and $\lambda'_\sigma = 100$. The resulting mean properties of the 4 Gaussians across the field are listed in Table 4.1. The amplitude, centroid velocity and velocity dispersion maps for each of the components are shown in Figure 4.3.

Table 4.1: Mean fitted parameters for the 4 Gaussians decomposed in Section 4.4.1.

Gaussian	Amplitude (A)	Central Velocity (v_0)	Dispersion (σ_v)
G_1	4.96 K	11.74 km s $^{-1}$	1.55 km s $^{-1}$
G_2	4.73 K	0.17 km s $^{-1}$	1.68 km s $^{-1}$
G_3	4.27 K	0.71 km s $^{-1}$	6.90 km s $^{-1}$
G_4	0.69 K	-16.40 km s $^{-1}$	6.63 km s $^{-1}$

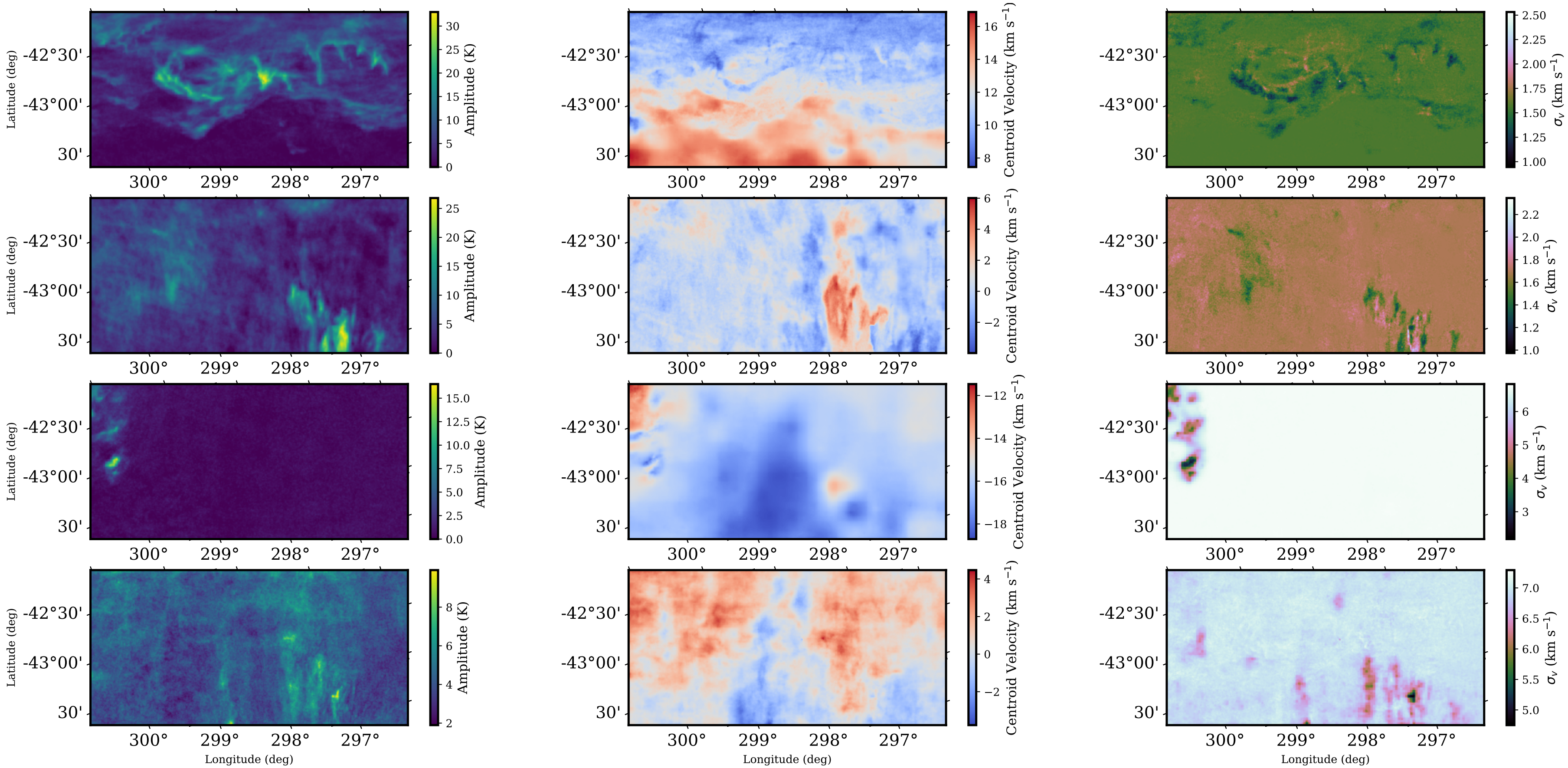

Figure 4.3: Collection of fields for the amplitude (left), central velocity (middle) and velocity dispersion (right) of each Gaussian fields (G_1, G_2, G_3, and G_4) fitted from the HI emission data discussed in Section 4.2.1 using ROHSA. The mean values for each field are documented in Table 4.1.

When calculating the error from ROHSA, it has been previously shown that the initial guess variation was the largest source of error when fields are more complex and use many Gaussian components Taank et al. (2022). Due to the simplicity of the field in this work and only requiring 4 Gaussians to fully describe the data, we find that varying the third error method of varying the initial guess is not a dominant influence on the uncertainty of ROHSA, similar to previous work on H I clouds in the SMC Buckland-Willis et al. (2025). This is likely due to Gaussian decomposition degeneracy decreasing when fewer Gaussians are used to fit.

When looking at the central velocity maps of the four Gaussians decomposed from the data, we find that only the Gaussian with the narrowest velocity-dispersion map, G_1, is aligned in velocity-space with the original filament shown in Section 4.2.1. The central velocity of this Gaussian also appears relatively constant across the field where bulk of the filamentary gas is present, as shown in the top of Figure 4.3. The amplitude field of this narrow Gaussian also appears to show more contrast compared to the velocity dispersion field of the same Gaussian, which appears constant across the field apart from the locations with the highest amplitude. The second Gaussian, G_2 also has a relatively low velocity dispersion, however it represents gas at a different central velocity to the filament, and is connected to regions outside of that probed in this work. The other Gaussian fields of G_3 and G_4 appear more diffuse both spatially, and spectrally with higher velocity dispersions, and are separated in velocity from the original filament.

4.4.2 Phase Classification

The 4 components are categorised into H I phases by their mean maximum kinetic temperature, $\langle T_k \rangle$, computed through the following (Draine 2011):

$$\langle T_k \rangle = 121 \langle \sigma \rangle^2, \tag{4.3}$$

where $\langle \sigma \rangle$ is the mean dispersion of each component. This categorisation assumes that the dispersion of the components originates solely from the thermal broadening of the gas, with no turbulent-broadening. As this is not the case in reality, this kinetic temperature estimate serves as an upper limit on the true temperature of the gas. We find two CNM components ($\langle T_k \rangle \approx 290$ K and 340 K), and two components belonging to warmer temperature gas ($\langle T_k \rangle \approx 5300$ and 5800 K). If we assume that the warmer components are transonic with a turbulent Mach number of 1 (Kim & Ryu 2005), the kinetic temperature estimates would instead be approximately 1325 and 1450 K respectively. Due to the wide range of potential temperatures these components could be without reliable turbulent velocity information, we define these components as a mix of unstable neutral medium (UNM) and warm neutral medium (WNM). If we make the same assumption with the CNM components of being transonic, their temperatures would be ~ 70 and ~ 85 K respectively. Since the CNM has been measured to be typically supersonic (Murray et al. 2015, 2021), these temperatures could be even lower. As mentioned earlier, the coldest CNM component appears to be the main component of the filament observed in Section 4.2.1, whilst the warmer components are separate and represent more diffuse gas enveloping the feature.

4.4.3 Column Density and Mass Fraction Maps

To calculate the column density ($N_{\rm H\,I}$) contribution from each of the 4 Gaussian components, we assume the gas is in the optically thin regime such that Roberts (1975):

$$N_{\rm H\,I}(x,y) = 1.823 \times 10^{18} \int T_B(x,y,v)\, dv\,, \tag{4.4}$$

where $T_B(x,y,v)$ represents the brightness temperature maps formed from the Gaussian components. The optically thin assumption is safe in the case of this work as from H I absorption studies, opacity correction for column densities below 10^{21} cm^{-2} are found to be less than 1.05 (Dempsey et al. 2022; Nguyen et al. 2024). Since we are dealing with Gaussian components along a velocity axis, the above equation can be simplified for each Gaussian such that the column density can instead be calculated via:

$$N_{\rm H\,I,\mathit{n}} = 1.823 \times 10^{18}\,{\rm cm}^{-2}\sqrt{2\pi}\,{\rm A_n(x,y)}\,\sigma_{\rm n}{\rm (x,y)}, \tag{4.5}$$

where A_n and σ_n are the amplitude and velocity dispersion maps for the n-th Gaussian component. In Figure 4.4, we show the H I column density maps of the 4 components separated with ROHSA discussed in Section 4.4.1. We note the CNM component traces sharper and smaller-scale structures while the warmer-phase components appear more extended and cover diffuse gas surrounding the colder gas.

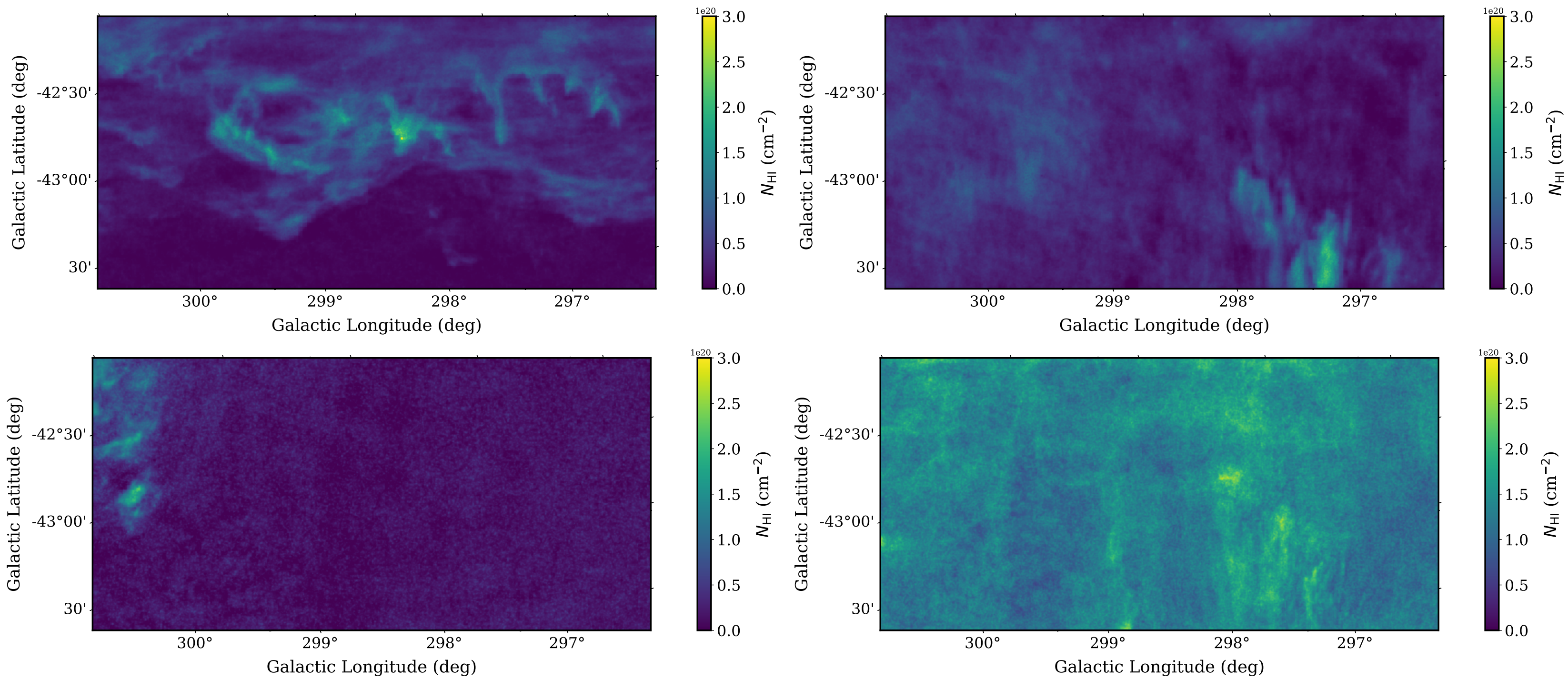

Figure 4.4: H I column density maps for each of the 4 Gaussian fields, G_1 (top left), G_2 (top right), G_3 (bottom left), and G_4 (bottom right), decomposed in Section 4.4.1, calculated using Equation 4.5.

The CNM mass fraction is a useful diagnostic to search for regions dominated by cold gas. In order to calculate the CNM mass fraction, we divide the column density map of the CNM component by the total H I column density of all the components combined, such that:

$$f_{\mathrm{CNM}} = \frac{N_{\mathrm{H\,I,CNM}}}{N_{\mathrm{H\,I,tot}}}\,, \tag{4.6}$$

where $N_{\mathrm{H\,I,tot}} = N_{\mathrm{H\,I,CNM}} + N_{\mathrm{H\,I,UNM}} + N_{\mathrm{H\,I,WNM}}$. For the purposes of this work, we choose to only include the G_1 Gaussian in the CNM mass fraction since it is the main contributor to the filament and the other cold Gaussian G_2 contains non-filament gas at a separate line-of-sight velocity. Hence for this work the CNM mass fraction is calculated via:

$$f_{\mathrm{CNM}} = \frac{N_{\mathrm{H\,I,G_1}}}{N_{\mathrm{H\,I,G_3}} + N_{\mathrm{H\,I,G_4}}}\,. \tag{4.7}$$

This will also assist in the direct comparison of CNM mass fraction and resolution later in Section 4.5.1 when beam smearing affects the accurate separation of Gaussians. The resulting CNM mass fraction map for the field is shown in Figure 4.5. The mean CNM mass fraction is approximately 0.14 ± 0.11 where the uncertainty is measured by 1 standard deviation. We find the field contains the highest CNM mass fractions within the filament, forming finger-like structures such as those in the top right of the field, perpendicular to the orientation of the large-scale filament that is horizontal across the field in this work, as viewed from the larger field-of-view of previous surveys, as seen in Figure 4.1. Ultimately the CNM mass fraction map appears strongly correlated with the column density maps of the CNM fields, aligning with how the column density of the other phases are consistent in across this region of the filament.

4.4.4 Instability Wavelengths

Several structures within the CNM fields of this region form structures with peaks and troughs, similar to that of a Rayleigh-Taylor instabilities within superbubbles and cloud complexes (McClure-Griffiths et al. 2003; Miville-Deschênes et al. 2017). These instabilities are especially seen within the G_1 field, where most of the cold gas within the filament has been fitted. The wavelength of the peaks can be measured across the plane-of-sky and is shown in Figure 4.6, where we utilise the column density of the G_1 gaussian field from Figure 4.4. We observe two distinct wavelength regimes. One is a larger-scale feature, with wavelengths of each section estimated to be approximately 57.8 arcminutes and 1.09 degrees across the plane-of-sky. The other stems from the smaller-scale "finger"-like features seen in the top right of the field, with wavelengths of approximately 20.2, 10.1, and 12.1 arcminutes across the plane-of-sky.

To convert these angular distances into physical plane-of-sky distances we can make use of three-dimensional (3D) Galactic dust maps towards the region. Most of the total hydrogen gas at high Galactic latitudes is in the neutral phase, making dust a good tracer of H I at high latitudes (Low et al. 1984; Boulanger et al. 1996; Lenz et al. 2017). Similar to the work done in Lynn et al. (2025), we can convert dust extinction densities from the 3D dust map from Edenhofer et al. (2024), providing locations of dust over distances of 69 pc to 1.2 kpc from the Sun with an angular resolution of 14′ and a varying distance resolution, from 0.4 to 7 pc. We use the coordinates of the field in this work to form mean dust extinction spectra. Following the procedure described in O'Neill et al. (2024), we convert the differential extinction measurements $A'_{ZGR_{23}}$, defined in unitless extinction ZGR_{23} (Zhang et al. 2023), to densities of total hydrogen atoms H including molecular gas, given by:

$$n_{\mathrm{H}} = C \times A'_{ZGR_{23}}\,, \tag{4.8}$$

where $C = 1653\,\mathrm{cm}^{-3}$. The mean dust spectra in units of total hydrogen density, is shown in Figure 4.7. The dust spectrum is comprised of a single peak, with negligible hydrogen beyond a distance of approximately 400 parsecs. The peak of the hydrogen density is at approximately 215 ± 2 parsecs. We assume that the H I column density from the filament seen in Figure 4.1 forms the peak observed in the dust spectra. This assumption is supported by the fact that if the median H I column density of approximately 4×10^{20} cm^{-2} was concentrated within a filament with a line-of-sight depth of 10 parsecs, this would result in a H I number density of approximately ~ 13 cm^{-3}. The only place we observed a hydrogen density this high in the total hydrogen density spectra is the peak at 215 parsecs in Figure 4.7.

Since the dust spectra peak lies close in distance to the edge of the Local Bubble, the filament in this work is likely tied to gas of the Local Bubble Wall. Since the Local Bubble is not a perfect sphere, certain regions are such that the normal to the surface has a component along the plane-of-sky, which are the components of the instabilities observed in this work. To confirm the structure's connection to the bubble wall, we make use of 3D models of the Local Bubble from O'Neill et al. (2024), made using the 3D dust maps from Edenhofer et al. (2024). We selected 4 sightlines along the filament, shown in Figure 4.8. At the coordinates of these points,

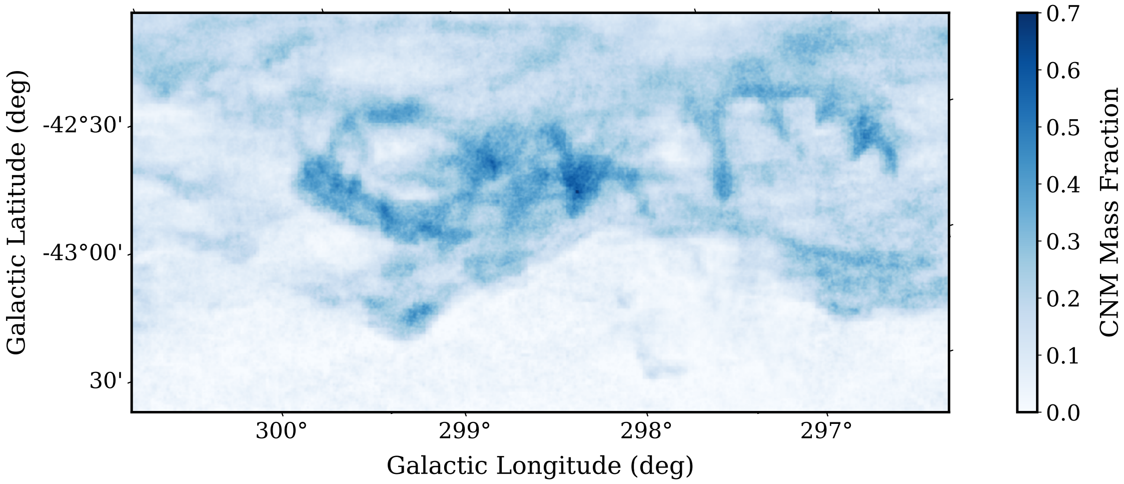

Figure 4.5: CNM mass fraction map of the GASKAP-HI field discussed in Section 4.2.1 using the Gaussian G_1 described in Section 4.4.1.

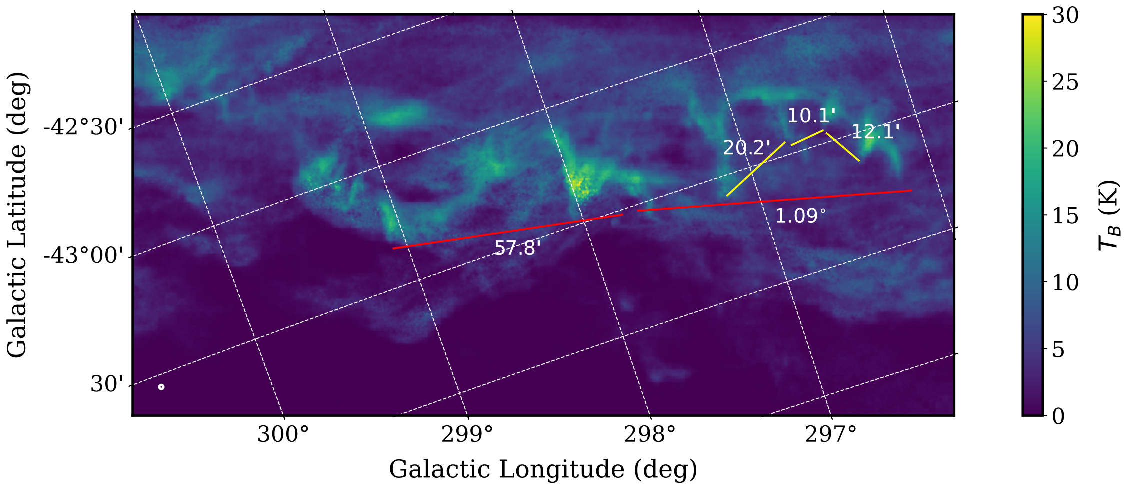

Figure 4.6: H I channel map of the Gaussian field G_1 produced in Section 4.4.1 at a velocity of 10.5 km s^{-1}. Large-scale and small-scale instability wavelength are mapped with the red and yellow lines, respectively. The angular distances between the peaks for each wavelength are also labelled.

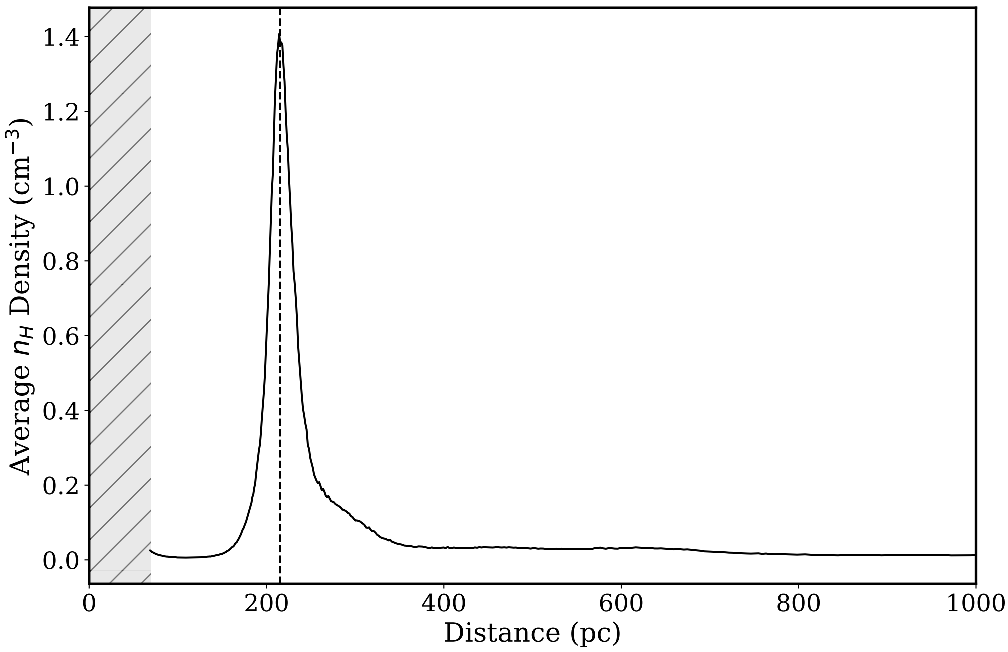

Figure 4.7: Weighted-mean of $n_{\rm H}$ along the sightlines within the region of the field shown in the right side of Figure 4.1. The dust densities were converted from the Edenhofer et al. (2024) 3D dust map to total hydrogen densities using a conversion factor of 1653 cm^{-3} (O'Neill et al. 2024). The grey, dashed region marks the nearby distances below 69 parsecs which lack data. The vertical dashed line represents the distance of maximum $n_{\rm H}$ in the region ($\sim 215 \pm 2$ pc).

we obtain distance spectra of both the dust maps from Edenhofer et al. (2024), as well as distance spectra of the modelled Local Bubble wall in these directions. These spectra are also shown in Figure 4.8. We find that along all sightlines, the peak of the dust spectra matches well with the 3D model of the Local Bubble wall. Since there is no other dust along this sightline out to 1000 parsecs, we can conclude that this filament is likely a structure tied to the wall of the Local Bubble.

The large-scale wavelength of the instability has a mean angular distance of $\lambda = 1.02 \pm 0.06$ degrees, and the small-scale instability has a mean wavelength of 14.1 ± 4.4 arcminutes. With the distance to the filament being approximately 215 parsecs, we find the large-scale mode of the instability has a mean wavelength of approximately $\lambda \approx 4$ parsecs and the small-scale mode has an average wavelength of around $\lambda \approx 0.9$ parsecs. We make approximate measures here as since the dust maps resolution is much lower relative to the resolution of the GASKAP-HI survey, we are unable to make estimates on the orientation of the filament using line-of-sight distances. If the filament is not parallel to the plane-of-sky, the observed structure would be shorter than reality. As such, these measurements should be taken as lower-limit estimates for instability wavelengths within this region. this in mind, the small-scale mode of the instability of 0.9 parsecs is of a similar order of magnitude to previous periodic structures found in our Galaxy, such as that in the DRACO Cloud complex of 2.2 parsecs (Miville-Deschênes et al. 2017), but much smaller than those within the Galactic chimney of ~ 70 parsecs (McClure-Griffiths et al. 2003). While both of these instabilities are detected from structures ~ 500 parsecs and ~ 6.5 kilo-parsecs from us respectively, this is the first time we have detected parsec-scale Rayleigh-Taylor instabilities in H I within the Local Bubble Wall.

The smaller-scale instability likely stems from the larger instability due to the fractal nature of Rayleigh-Taylor instabilities (Schulreich & Breitschwerdt 2022). The smallest observed mode of the Rayleigh-Taylor instability is the critical wavelength, below which magnetic fields permeating the instability suppress smaller scale modes parallel to the field's direction (Chandrasekhar 1961; McClure-Griffiths et al. 2003). Modes perpendicular to the magnetic field direction, known as interchange modes, remain unaffected and are unstable at all scales (Stone & Gardiner 2007). The smallest-scale wavelength observed in this work of 0.9 parsecs is therefore an upper limit estimate on the critical wavelength of this Rayleigh-Taylor instability, as even smaller instabilities could be present but not resolved with current observational resolutions. Since we only have observations of a single epoch, we are unable to make accurate calculations as to the acceleration the filament is undergoing in order to produce this instability.

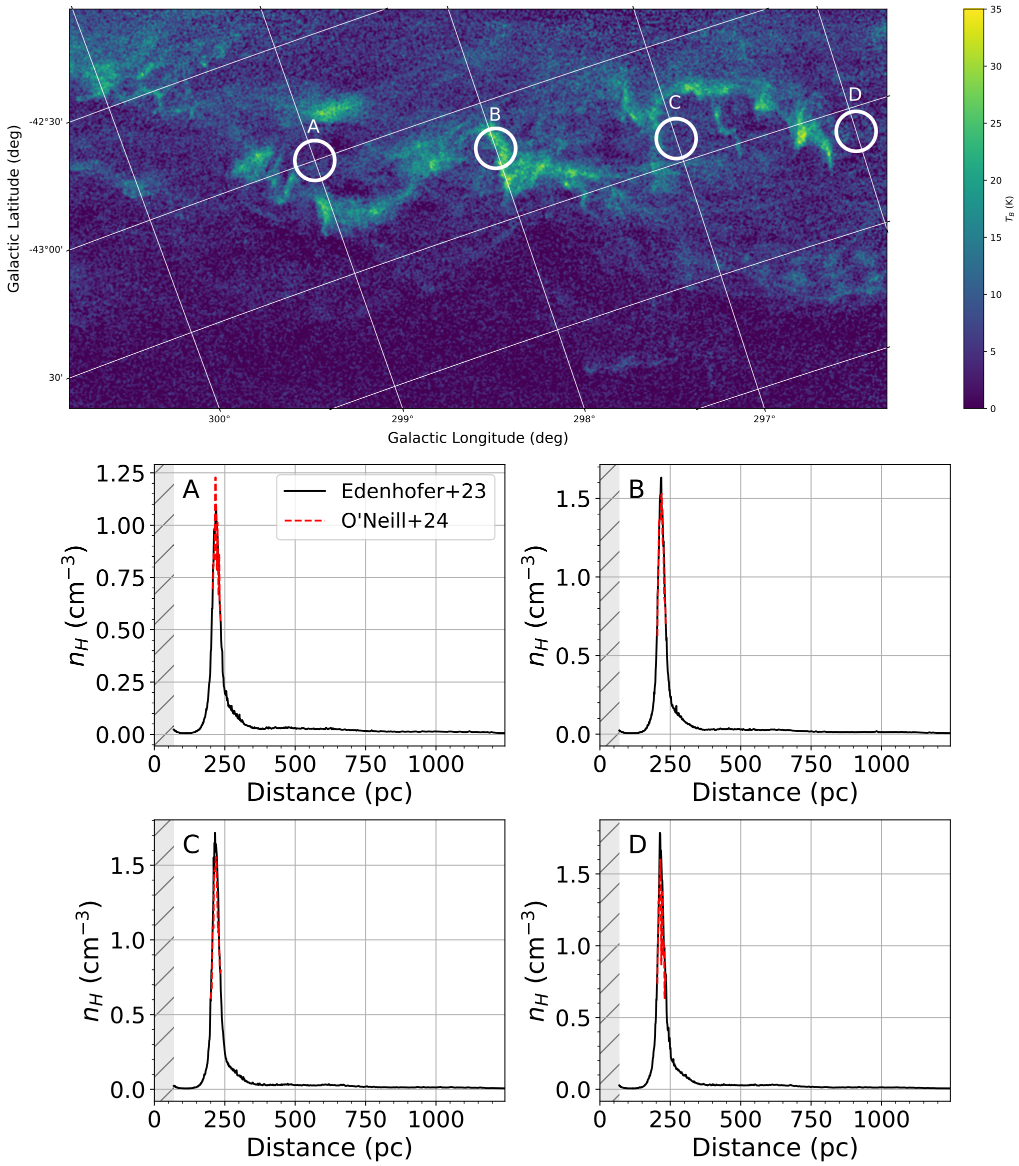

Figure 4.8: Top: H I emission map of the field discussed in Section 4.2.1 at a line-of-sight velocity of $v \sim 10.8$ km s^{-1}, as shown in the right of Figure 4.2. The 4 red circles mark the sightlines chosen in Section 4.4.4 to compare the 3D total hydrogen density spectra with the 3D model of the Local Bubble Wall from O'Neill et al. (2024). Bottom: Total hydrogen density spectra from the 4 sightlines chosen as a function of distance, derived through the method in Section 4.4.4 from the Edenhofer et al. (2024) dust map. The grey, dashed region marks the nearby distances below 69 parsecs which lack data. The red-dashed line maps the equivalent total hydrogen density spectra of the 3D model of the Local Bubble Wall from O'Neill et al. (2024).

4.5 Discussion

In Section 4.4.3, we found that the region in this work had a mean CNM mass fraction of approximately 0.14 ± 0.11. This value is lower than what is typically found in H I absorption surveys targetting high Galactic latitudes, especially like the GASKAP-HI absorption measurements in regions nearby on the plane-of-sky (Nguyen et al. 2024; Lynn et al. 2025). To compare the distribution of CNM mass fractions in this work with those of previous surveys, we form a 1-dimensional probability distribution function of the map from Figure 4.5. This histogram is displayed in Figure 4.9 alongside CNM mass fraction distributions from the HI absorption surveys of the GASKAP-HI Pilot survey (Nguyen et al. 2024), Millenium Survey (Heiles & Troland 2003), and 21-SPONGE survey (Murray et al. 2018). Despite the sightlines observed in each survey probing different regions of gas across the sky, the H I absorption surveys all contain approximately even distributions of CNM mass fractions, with a gradual decline around approximately $f_{CNM} \sim 0.6$. In contrast, the ROHSA decomposition in this work has CNM mass fractions concentrated towards the lower values, with a steep drop-off in CNM mass fraction after $f_{CNM} \sim 0.3$. The H I absorption survey is governed primarily by the location of bright background sources, independent of the local Milky Way gas itself. However, since these surveys only contain sightlines with detections of CNM gas, they would ultimately be biased towards regions with higher CNM mass fractions, and as such lead to a more skewed representation of CNM mass fraction. In contrast, the ROHSA decomposition's high concentration of low CNM mass fraction sightlines is likely due to the typically low volume filling factor of the CNM in the ISM Marchal & Miville-Deschênes (2021).

4.5.1 CNM Mass Fraction vs Resolution

As discussed earlier in this work, while ROHSA and other Gaussian decomposition techniques have been utilised across a wide range of H I surveys in both Galactic and extra-galactic contexts, tests on the effect of resolution on measured CNM mass fractions have been limited. With even the nearest extra-galactic bodies of the Magellanic system, current spatial resolution with state-of-the-art telescopes result in H I emission maps with physical resolutions of approximately 8 parsecs per beam Pingel et al. (2022). The scales at which thermal instabilities form cold H I gas has been found observationally to be on the order of ~ 15 parsecs in select regions of the Galaxy (Marchal et al. 2021). Since the CNM structures formed are on scales smaller than the thermal instabilities themselves, extra-galactic observations leave much of the small-scale CNM structure unresolved.

To explore whether resolution impacts the overall CNM mass fractions observed from emission line observations, we perform Gaussian decomposition with ROHSA of the field in this work convolved to different spatial resolutions. We convolve the field in Section 4.2.1 using a Gaussian beam of 1 arcminute, 2 arcminutes, 4 arcminutes, 8 arcminutes, 16 arcminutes, 32 arcminutes, 64 arcminutes, and 128 arcminutes, producing 8 maps in total. These maps were then re-binned to have the same number of pixels per beam as the original data-product to avoid over-sampling of the data. The reason for convolving to the final resolution of 128 arcminutes is that for the specific filament in this work, the physical resolution at 128 arcminutes results in a physical resolution of approximately 7.8 parsecs per beam, which is very similar to the 8 parsecs per beam physical resolution of the SMC provided by the GASKAP-HI survey (Pingel et al. 2022). Matching these physical resolutions will allow for a direct comparison of CNM mass fractions obtained when using ROHSA on the SMC completed in the past (Buckland-Willis et al. 2025) with the potential CNM mass fractions if sub-parsec physical resolution were possible.

The H I column density maps of each of these convolved fields are displayed in Figure 4.10. We note that with decreasing resolution, the field slowly loses flux through beam smearing of the image, with the sharp features of the original field becoming undetectable. This loss of flux is due to an edge effect as the main power that is conserved is towards the centre of the image, with the edges losing power more quickly from the introduction of zero values from outside the field-of-view.

From each of these fields, we extracted a sample spectra, shown in Figure 4.11, to observe the variation in the strength and properties of the H I signal in the region with resolution. We find that as resolution decreases, the amplitudes of the peaks found in the H I emission spectra decrease. Eventually the peaks become blurred into single broader Gaussians through beam-smearing, at which point narrow features are not longer detectable, espectially at beam-sizes larger than 16 arcminutes.

For each of shown in Figure 4.10, we repeat the Gaussian decomposition via ROHSA completed in Section 4.3 as was done on the original 30 arcsecond resolution field. For the purpose of direct comparison we choose to use the same hyper-parameter values on each of the convolved fields as was found with the best fit of the original map in Section 4.4.1 with $\lambda_a = \lambda_v = \lambda_\sigma = 10$, and $\lambda'_\sigma = 100$. This allows for a direct comparison of the effects of spatial resolution on the fitting process without the variability of hyper-parameters broadening the parameter space. We also choose to use 4 Gaussians to fit each field, as this describes the region to our best knowledge from the 30 arcsecond resolution data. The amplitude, centroid velocity and velocity dispersion maps for each of the 4 components for each convolved field are shown in

Appendix A.3.1. We find that the maps with resolutions from 1 arcminute to 4 arcminutes are still able to resolve key structures of the cold filament as seen in the original map, with the G_1 Gaussian in each fit continuing to describe the gas at 12 km s^{-1} belonging to the filament. However beyond this resolution, the filament becomes harder to detect, before eventually becoming unresolved between 8 and 16-arcminute resolution. At this point, we lose information on the small-scale structures of the cold H I gas within this filament, with the gas smeared into broader clouds of gas.

For each of these Gaussian decompositions, we compute the CNM mass fraction as was done in Section 4.4.3 for the original field. For the purposes of direct comparison, we choose to compute the CNM mass fraction with only the Gaussian that was coldest in the original resolution image, G_1, tracing the filament's structure at approximately 12 km s^{-1}, as shown in Figure 4.3. With decreasing resolution, beam smearing results in less accurate separation of the Gaussian components and so focussing on one Gaussian allows for a more direct test of resolution effects. The CNM mass fraction maps of each resolution field are shown in Figure 4.12. We note that a blob-like structure appears at a longitude of ~ 298.3 degrees and latitude of -42.4, especially in the 4, 8 and 16 arcminute resolutions. This is not an artefact and is instead a result of the beam smoothing of the original H I cube combined with the ROHSA decomposition algorithm propagating this smoothed shape.

To quantitatively compare the CNM mass fractions as a function of resolution, we produce 1-dimensional histograms of the maps shown in Figure 4.12, forming violin plots shown in Figure 4.13. We find that the mean and median values of each CNM mass fraction map are consistent regardless of resolution. This consistency even extends up to the resolution of 128 arcminutes per beam, at which point the gas in the region is beam-smeared to a point where the filament is no longer detected. This result implies that at physical resolutions of ~ 8 parcecs per beam, the CNM mass fractions obtained are consistent with those at sub-parsec resolutions. This result is likely due to the fact that the data-cubes used in this work all have the same spectral resolution of 0.5 km s^{-1}, where CNM peaks are easily resolved despite their typically narrow line-widths (Nguyen et al. 2024). For surveys which match these observational requirements, such as the observations of the Magellanic system with the GASKAP-HI survey, mean and median measurements of CNM mass fraction across regions of these extra-galactic bodies, like those from Buckland-Willis et al. (2025) are likely well-aligned with measurements if they were to be made at sub-parsec resolution. This result likely also extends to more distant galaxies such as NGC 6822, where H I absorption sightlines have been detected (Pingel et al. 2024).

While such work only focuses on H I absorption, the CNM mass fraction values still rely on H I emission sightlines that have larger physical beam-sizes of $\sim$ 15 pc. With this in mind, the mean and median CNM mass fractions would likely be representative of the real values, provided enough sightlines to build a statistically significant sample.

The main discrepancy between the different resolutions however is the peak CNM mass fraction detected. With decreasing resolution, we find the peak CNM mass fraction also decreases. This is likely due to the fact that with a constant CNM volume filling fraction, larger pixel sizes will observe lower fractions of CNM gas within them relative to the total amount of gas. This effect, combined with the beam-smearing decreasing the amplitudes of the Gaussians detected, as seen in Figure 4.11, leads to a decrease in the peak CNM mass fraction. The trend appears to reverse at resolutions of around 128 arcminutes. However, this is likely due to the beamsize of this map being on the order of the field-of-view itself, and as such the structures within it are statistically insignificant. Hence, the 128 arcminute map may not be able to accurately measure the CNM.

We also note that despite our resolution range going down to 30 arcseconds per beam, which converts to a physical resolution of 0.03 parsecs, we still have not seen a plateau on the higher-end of the peak CNM mass fraction. This result also explains why the H I absorption surveys have higher CNM mass fractions than this work as seen in Figure 1.4, due to their higher spatial resolutions compared to H I emission maps, observing point-sources of gas towards background sources. This implies that higher resolution maps of local H I gas are needed to accurately resolve the highest concentrations of CNM gas within structures like the filament in this work. The varying range of CNM mass fraction values with resolution also implies extragalactic work such as that mentioned earlier for the SMC and NGC 6822 may need to take resolution into account when reporting the maximum and minimum CNM mass fractions found.

4.6 Summary

In this work, we have used recent H I emission observations as part of the GASKAP-HI Survey of Milky Way gas in the foreground towards the the SMC. From this $\sim$ 50-hour observation, we have utilised spatially coherent Gaussian decomposition through the tool ROHSA to uncover the H I cold gas within a local Galactic filament, and to test the variation in CNM mass fraction results with spatial resolution. The main conclusions of this work are:

- The region chosen contains a portion of a nearby Galactic filament that is observed at a line-of-sight velocity range of 6 to 15 km s^{-1}. Through 3D dust spectra, we match the filament structure to the wall of the Local Bubble.
- We decompose the local region with four Gaussians, two of which have linewidths that yield maximum kinetic temperatures of 290 K and 340 K, respectively. The other two Gaussians are broader, with maximum kinetic temperatures of 5300 and 5900 K.
- The main structure of the portion of the filament within the survey region can be best described with a single narrow Gaussian component. The other broader Gaussians represent diffuse gas that envelops the structure.
- The filament hosts structures similar to Rayleigh-Taylor instabilities, with both large-scale and small-scale modes being observed with mean wavelengths of 4 and 0.9 parsecs, respectively.
- The CNM mass fraction of the region, calculated using only the narrow component that describes the filament, has a mean value of 0.14 ± 0.11. The highest CNM mass fraction values are concentrated within the filament, predominantly in instability features imbedded inside the filament.
- The field has fewer high CNM mass fraction values than that measured through previous Galactic H I absorption surveys, due to the optically thin limitation of H I emission and the bias of absorption surveys towards sightlines where cold H I gas is detected. Likewise, the ROHSA decomposition has a lower peak CNM mass fraction compared to absorption measurements.
- We convolve the field to lower spatial resolutions with a Gaussian beam, up to a resolution of 128 arcminutes per beam, representing current physical resolutions of the Magellanic Cloud at ~ 8 parsecs per beam.
- Using ROHSA on these de-resolved fields, the mean and median CNM mass fractions obtained are consistent regardless of resolution. This is likely due to the spectral resolution of the survey remaining constant at 0.5 km s^{-1} leading to consistent component separation of the data.
- The peak CNM mass fraction decreases with decreasing resolution, as beam-smearing leads to a loss of small-scale structure.

Given the consistent mean CNM mass fraction found in the region used in this work regardless of spatial resolution, Gaussian decomposition tools such as ROHSA appear safe to use on extra-galactic surveys even when cold gas is not fully resolved.

However, this ability likely relies heavily on the condition of high spectral resolution, and on observing sightlines with few components. Further work will be needed with varying the spectral resolution in a similar manner to how the spatial resolution has been altered, to determine its effect on CNM mass fraction estimates and if a similar trend occurs with mean and median values. Toy models and synthetic H I spectra via numerical simulations will also be needed to improve reproducibility of the work in this chapter rather than relying solely on a single region of observational data.

While the mean and median CNM mass fractions extracted by ROHSA appears to be reliable regardless of resolution, the peak CNM mass fraction differs greatly. Obtaining accurate measurements of the potential range of CNM mass fractions within the ISM allows for numerical simulations and theoretical models of the ISM to be correctly constrained. The variability of this range with spatial resolution as shown in this work signals the importance of using spatially resolved data, and alludes to the potential for extra-galactic studies of H I emission phase decomposition to be biased away from higher CNM mass fractions.

No plateau was measured in the peak CNM mass fraction at higher spatial resolution, implying that the small-scale structure of the CNM is not yet fully resolved at physical resolutions of ~ 0.03 parsecs. With this in mind, higher spatial resolution surveys will be required in the future to test whether a plateau can be found, and if the small-scale structures of the CNM can be fully resolved through Gaussian decomposition of H I emission maps.

Acknowledgements

GASKAP-HI is partially funded by the Australian Government through an Australian Research Council Australian Laureate Fellowship (project number FL210100039 awarded to NM-G).

This research made use of `Astropy`, a community-developed core Python package for astronomy (Astropy Collaboration et al. 2013), `NumPy` (van der Walt et al. 2011), `matplotlib`, a Python library for the publication of quality graphics (Hunter 2007), and `SciPy` (Virtanen et al. 2020).

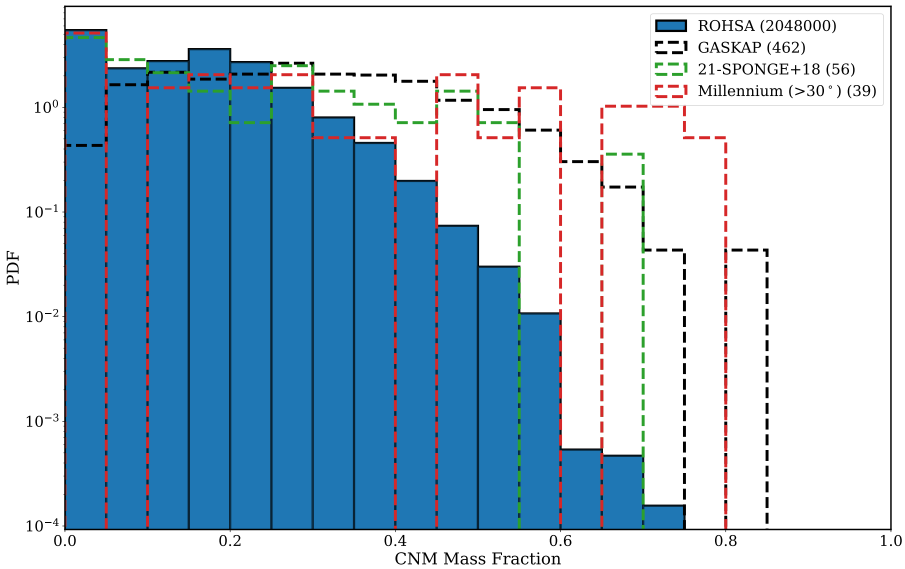

Figure 4.9: 1-Dimensional probability distribution functions of the CNM Mass fraction map shown in Figure 4.5, alongside distributions of CNM mass fraction from previous Galactic H I absorption surveys of the GASKAP-HI Pilot survey, (Nguyen et al. 2024), Millenium Survey sightlines with $|b| > 30°$ (Heiles & Troland 2003), and 21-SPONGE survey (Murray et al. 2018). The number of sightlines used in each survey are shown in their respective labels.

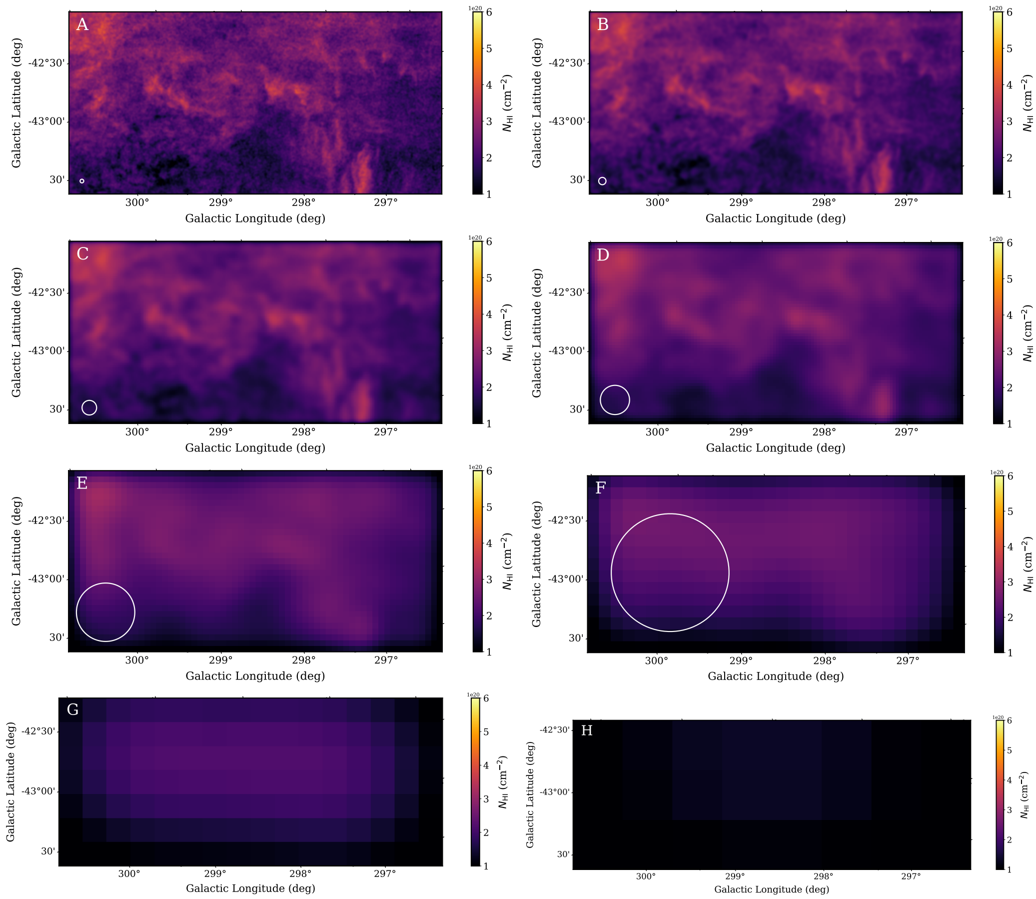

Figure 4.10: H I column density maps of the GASKAP-HI survey field discussed in Section 4.2.1, convolved to different spatial resolutions. The white circles indicate the beam-sizes of 1 arcminute (A), 2 arcminutes (B), 4 arcminutes (C), 8 arcminutes (D), 16 arcminutes (E), 32 arcminutes (F), 64 arcminutes (G), and 128 arcminutes per beam (H). Fields where the beam-size is not indicated have beam-sizes larger than the field and are hence not spatially resolved. The column densities are calculated over a velocity range of -30 to 30 km s^{-1}.

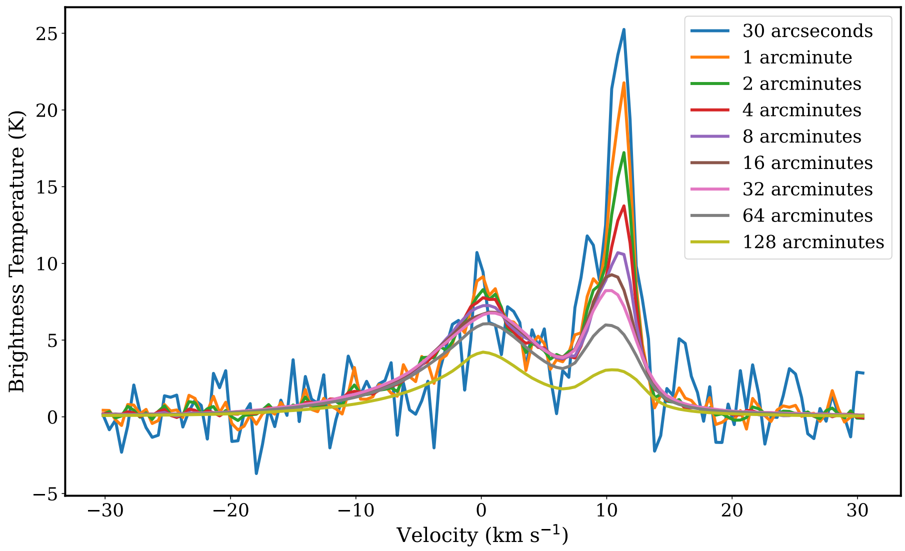

Figure 4.11: H I emission spectra of the 30 arcsecond resolution field in Section 4.2.1 along a sightline at Galactic latitude, b and longitude, l of $(l, b) = (-43.37°, 297.1°)$ compared to the same sightline for each of the spatial resolutions discussed in Section 4.5.1.

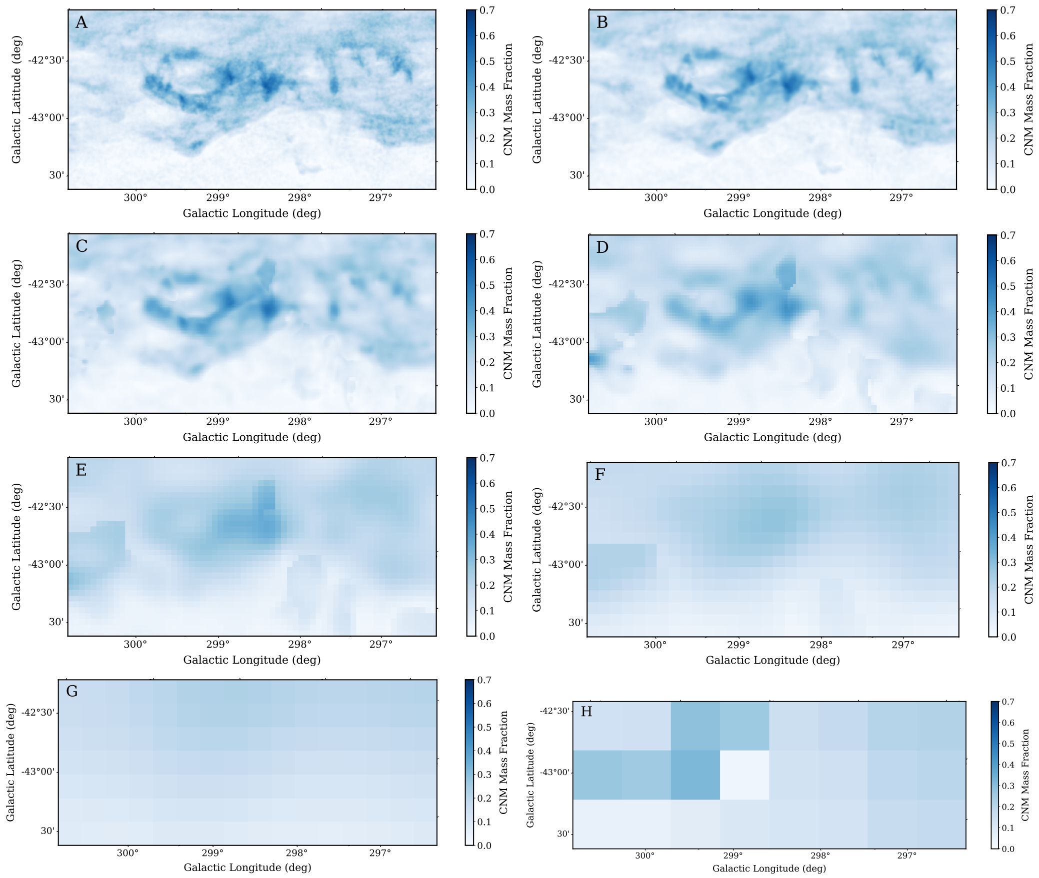

Figure 4.12: CNM mass fraction map of the de-resolved fields shown in Figure 4.10, marked with the same letter labels.

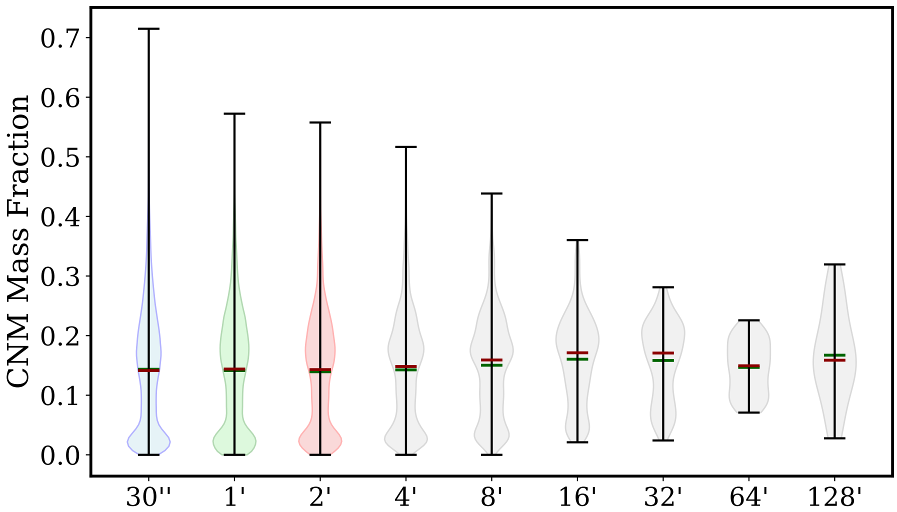

Figure 4.13: Violin plot of the CNM mass fraction distribution of each field from Figures 4.1 and 4.10 for each spatial resolution discussed in Section 4.5.1. The green and red lines indicate the mean and median of each distribution, respectively.

Chapter 5

Conclusions

5.1 Summary

With its close proximity, the interstellar medium (ISM) of the Milky Way provides us with a prime laboratory to explore the structure of galaxies at sub-parsec resolution and the dynamical processes that govern the transitions of neutral hydrogen (H I) between the different stages of the baryon cycle. Within this thesis, I have utilised H I emission and absorption data from the GASKAP-HI Pilot survey using the Australian Square Kilometre Array Pathfinder telescope that has produced the highest resolution H I emission maps of the Milky Way to-date (Pingel et al. 2022), and has detected hundreds of sightlines of H I absorption within a localised region in the foreground towards the Magellanic Clouds (Nguyen et al. 2024). The survey observed a filamentary region containing large-scale dense filaments (Kamal Youssef & Grenier 2024; Lynn et al. 2025), alongside diffuse H I gas enveloping the structures. This combination makes the GASKAP-HI Pilot survey ideal for understanding the properties of H I gas as it transitions between its warm and cold phases on the interface of cold filaments, within a typical region of the ISM in the Solar neighbourhood.

H I absorption sightlines are typically dominated by colder temperature gas, due to its higher optical depth and densities (Lazareff 1975; Dickey et al. 1977; Mohan et al. 2004). As such, detecting the warmer phases of gas requires higher sensitivity observations through longer observation times (Carilli et al. 1998). As a result, there have been very few detections of H I gas from the unstable neutral medium (UNM) or warm neutral medium (WNM) in absorption. In the case where long exposure time becomes unfeasible, spectral stacking has been utilised in the past to improve the noise characteristics of the H I spectra to observe low optical depth H I gas (Murray et al. 2014). The main limitation to these previous spectral stacks however, is that they average spectra of line-of-sights across the entire sky, incorporating gas that is not physically connected to each other. While this is useful for global averages of the temperature properties of the warmer phases, we have previously been limited in our ability to locally stack absorption sightlines due to the low density of bright background sources detected. With the GASKAP-HI survey detecting hundreds of H I absorption sightlines within a localised region of ~ 250 square-degrees (Nguyen et al. 2024), we are now at a point where we can locally stack spectra to observe spatial variations in the temperature of H I gas warmer than the cold neutral medium without relying on long observation times.

In Chapter 2, I have used spectral stacking to improve the signal-to-noise capabilities of the GASKAP-HI survey for detecting higher temperature H I gas in absorption. Through stacking the 462 sightlines where H I absorption was detected in the Milky Way, the noise level was reduced from a mean rms noise of $\sigma_\tau = 4.2 \times 10^{-2}$ by almost a factor of 40 to around $\sigma_\tau = 1.1 \times 10^{-3}$. This improved noise revealed a warmer component of H I gas with a spin temperature of approximately $T_s = 1300$ K. The 2240 sightlines where H I absorption was not detected were also used to produce a stack where cold neutral medium (CNM) gas was detected within the noise of individual sightlines, with a spin temperature warmer than that of the rest of the original GASKAP-HI catalogue. Additionally, another new avenue first tested in this work was the ability to locally stack spectra by spatial location across the plane-of-sky, a feat only achievable with the high density of sources found through the GASKAP-HI survey. Through binning the H I absorption sightlines with no detection based on their plane-of-sky distance to regions of known cold gas, the plane-of-sky variation in absorption properties were able to be quantitatively mapped. The optical depth of absorption features decreased with larger distances away from cold gas, but the spin temperature of cold gas remained relatively stable regardless of plane-of-sky distance. Aside from detecting additional warm and cold gas components to the original GASKAP-HI survey, the work also tested the accuracy of measuring spin temperature with spectrally stacked sightlines. Through use of the H I absorption detection catalogue of 462 sightlines as well as toy model examples, I was able to test the efficacy of spectral stacking, finding that while optical depth measurements on stacked spectra provide lower limit estimates, the spin temperature recovered is accurately measuring the average spin temperature of the original sightlines.

Our knowledge on the spatial structure of the CNM is mainly understood through both phase decomposition of spatially resolved maps of H I emission and optical depths maps of cold H I gas against single background sources (Deshpande et al. 2000; Dutta et al. 2014). The H I emission maps used distinguish between H I phases using the linewidth of Gaussian composed extracted from the spectra through Gaussian decomposition. However, these linewidths contain contributions from both thermal and turbulent components, meaning using linewidths for direct temperature estimates is not always accurate. On the other hand, optical depth maps, which mainly trace the cold H I gas due to higher optical depths, are limited by the relative size of bright background sources, typically to only several hundred AU to a few parsecs (Roy et al. 2010, 2012). To analyse the spatial structure of cold H I gas on larger scales accurately, we require both H I emission and H I absorption sightlines of the same gas. With this combination, we obtain the full radiative transfer process and are able to calculate spin temperatures to correctly separate H I phases by temperature. It is only recently with the GASKAP-HI survey where we have enough sightlines of H I absorption to spatially map the variation of cold gas absorption properties up to 100 parsecs across the plane-of-sky within a localised field and connect any variations to physical structures seen through H I column density.

In Chapter 3, I have utilised the 462 GASKAP-HI Pilot survey absorption sightlines to observe the spatial variation of absorption properties of optical depth, spin temperature and column density across the plane-of-sky. Qualitatively, the high optical depth values were concentrated towards regions of the Pilot survey lower in Galactic latitude, with low optical depth absorption components being ubiquitous across the filamentary region. However, the spin temperatures measured for each decomposed cold gas component showed no spatial correlation with any physical feature within the survey region. Probing more quantitatively, I employed the structure function to analyse the spatial variation of integrated optical depth, CNM column density, and for the first time, spin temperature of cold H I gas. The optical depth and column density structure functions formed power-law slopes of 0.23 ± 0.10 and 0.34 ± 0.12, respectively indicating that there is more variation of the two properties on larger scales, relating to the turbulent cascade of energy within the ISM. The optical depth slope was found to be on the shallower end of typical slopes from previous work on optical depth maps over single absorption sources on smaller spatial scales (Deshpande et al. 2000; Roy et al. 2010, 2012; Dutta et al. 2014). The slope of the H I column density structure function was converted into an equivalent spatial power spectrum (SPS) slope of ~ 2.3, which while shallower than typical H I SPS slopes of the Milky Way, is likely due to the CNM having more power on smaller scales Pingel et al. (2018). The overall trend of both the optical depth and H I column density slopes being shallower than normal could be due to the anisotropic structure of the region, primarily composed of two large-scale filaments. This anisotropy would cause turbulent slopes to be shallower than typical 3-dimensional turbulent power-law slopes (Roy et al. 2009). The shallower power-law slope at the larger scales probed by the GASKAP-HI survey of 0.4 to 100 parsecs compared to the slopes of optical depth over scales of 100's of AU could point to a transitionary stage between these two size scales where the structure of cold H I gas changes. Using the optical depth spectra of the H I absorption sightlines, I also computed the structure function for total H I column density in the optically thick regime, which has an equivalent SPS slope of approximately ~ -2.6. With the optically thick contribution, these provide a more accurate power-law description of H I gas than previous SPS work that uses solely H I emission maps in the optically thin regime. This slope is also equal to the SPS slope found for the H I column density of the residual warmer gas not found in absorption, implying that the spatial structure of the warmer phases are the dominant contributor to the structure of the total H I column density.

The structure function for the spin temperature however was flat, showing no dependence on spatial scale. This conflicts with MHD simulations such as the TIGRESS simulation (Kim & Ostriker 2017) where line-of-sight average spin temperatures of cold H I gas do form non-zero power-law slopes on the physical scales probed by the GASKAP-HI Pilot survey. However, when introducing noise similar to the properties of the GASKAP survey, the simulated structure functions also become flat, hinting that the result found in Chapter 3 is likely due to observational bias. Despite this, the small uncertainties on the spin temperature structure function allude to the possibility that current methods for determining spin temperature through the Heiles & Troland (2003) method do not accurately encapsulate all of the sources for error, and underestimate uncertainties on spin temperature measurements. For example, the ordering of Gaussian components physically along the line-of-sight remains a mystery when fitting the resulting spectra of hundreds of parsecs worth of radiative transfer. The arbitrary ordering of components based on fractional amounts of cold gas behind or in-front of the warm components is difficult to propagate into error analysis.

While the combination of H I absorption and emission enables the accurate estimation of temperature, this is still ultimately limited to point sources where background sources are visible. Even with the source density of the GASKAP-HI survey, the full spatially-sampled maps H I emission provides allow for more detailed analysis of H I spatial structure. As mentioned earlier, separating H I phases using H I emission maps has been historically completed by Gaussian decomposition of spectra along each sightline. Tools such as ROHSA have been developed to include spatial coherency to enforce similar decompositions to neighbouring pixels (Marchal et al. 2019). These techniques have been applied to both Galactic and extra-galactic regions (Marchal & Miville-Deschênes 2021; Marchal et al. 2021; Buckland-Willis et al. 2025). However, at extra-galactic distances, even of nearby galaxies like those of the Magellanic system, physical resolutions do not resolve gas at sub-parsec resolution.

For the GASKAP-HI survey of the Magellanic system, the physical resolution obtained with state-of-the-art telescopes is approximately 8 parsecs per beam (Pingel et al. 2022). The cold H I gas is often formed through colliding flows and dynamical processes on scales smaller than this (Hennebelle & Pérault 1999, 2000; Audit & Hennebelle 2005; Heitsch et al. 2006). With this in mind, it is uncertain as to how accurate Gaussian decomposition tools are for extracting H I phases when the small-scale structure of cold gas is not resolved.

In Chapter 4, I use recent H I emission data from the GASKAP-HI survey of a zoom-in of a nearby Galactic filament to observe the phase distribution of H I gas within gas close to the Local Bubble. When examined through individual velocity slices, there are structures similar to Rayleigh-Taylor instabilities imbedded within the filament. Through matching the H I data with 3D dust maps from Edenhofer et al. (2024) and models from O'Neill et al. (2024), we find the filament is connected to the Local Bubble Wall at a line-of-sight distance of approximately 215 ± 2 parsecs from us. The wavelengths of the Rayleigh-Taylor instabilities observed are on two scales: a large scale with an average wavelength of $\lambda \sim 4$ parsecs, and a smaller, critical wavelength of $\lambda \sim 0.9$ parsecs, below which smaller modes are suppressed.

Through the use of ROHSA, we decompose the field into 4 Gaussian components, each with 2D fields for their amplitudes, central velocities and velocity dispersions. Two of these Gaussians have linewidths that would yield maximum kinetic temperatures of approximately 300 K, with the other two having temperatures of around 5300 and 5900 K. Of these 4 Gaussians, only one of the cold components is aligned with and has spatial structure resembling the filament seen in the total H I emission datacube, with the other Gaussians related to other velocity structures. Using only the cold Gaussian belonging to the filamentary structure, I computed a map of the CNM mass fraction, where higher fractions are concentrated within the instabilities, which are perpendicular to the overall orientation of the filament. The mean CNM mass fraction is approximately 0.14 ± 0.11, and the distribution of values does not reach as high as those seen in previous H I absorption surveys. This result is likely due to the H I absorption surveys being biased towards sightlines where cold gas is detected as non-detections are usually discarded. The ROHSA decomposition is also concentrated heavily towards low CNM mass fractions due to the low volume filling fraction of the CNM.

While the ROHSA decomposition of this field along is on its own a useful analysis on the small-scale instabilities within nearby filaments, the main purpose of this Chapter is analysing ROHSA results as a function of spatial resolution. Convolving the original H I datacube spatially with a Gaussian beam up to resolutions of 128 arcminutes per beam, I apply ROHSA to these different resolution fields. Regardless of spatial resolution, the mean CNM mass fraction observed is consistent and similar to the value for the original 30 arcsecond resolution observation. This consistency is likely due to the fields still having high spectral resolution of 0.5 km s^{-1}, and because the field is spectrally simple with only a few Gaussian components needed. The peak CNM mass fraction on the other hand decreases with decreasing resolution, due to a combination of beam-smearing washing out high amplitude H I signals, and larger pixels collecting CNM gas and lowering the per-pixel amount of CNM gas on individual sightlines. This implies that while extra-galactic H I phase decomposition with sufficient spectral resolution, such as those of Buckland-Willis et al. (2025), may result in accurate mean CNM mass fractions, their peak values are limited, and do not reach the real range of fractions of CNM within the ISM. Even at the 30 arcsecond resolution of the GASKAP-HI survey, there is not plateau observed in peak CNM mass fraction. This implies that there are still some CNM structures that remain to be fully resolved, below a physical resolution of $\sim$ 0.03 parsecs. Information about the amount and concentration of CNM gas within the ISM is vital for numerical simulations to test theoretical models about turbulence and the dynamical processes of the baryon cycle. Observationally limited knowledge of the CNM mass fraction would hence also lead to inaccurate estimates on the relative strengths of heating and cooling dynamics in the ISM. With this in mind, high spatial resolution and obtaining sub-parsec resolution is incredibly important to derive the full CNM mass fraction range and to fully resolve the small-scale structure of CNM gas.

Overall, the work in this thesis attempts to explore new avenues that are now achievable with the state-of-the-art data from the GASKAP-HI survey: both in the high spatial resolution H I emission data and the high source density of H I absorption sightlines. Through testing the efficacy of spectral stacking of H I absorption and emission sightlines, using structure functions on H I absorption sightlines across the plane-of-sky, and analysing the effect of H I emission Gaussian decomposition with spatial resolution, I have demonstrated how current H I surveys enable new methods for studying the spatial variation of H I phases across the plane-of-sky.

5.2 Perspectives on Future Work

While the work in this thesis has demonstrated the ability of high-resolution H I emission data and a high density of H I absorption sightlines to analyse the structural properties of the CNM and other warmer gas phases, there are some limitations that could naturally be improved upon with both the continuation of the GASKAP-HI survey, and with the application of the tools used in this thesis to new data. Such improvements include increases to sensitivity, enabling observations of warmer H I gas phases in absorption spectra and their spatial variation, greater spatial sampling of H Iabsorption to provide more accurate structure functions over wider spatial ranges, and the application of new Bayesian forward fitting models to decompose H Iemission and absorption spectra. These avenues can be explored not just within the region of the Pilot survey discussed in this thesis, but the upcoming regions of the survey towards the Galactic plane.

5.2.1 Future Improvements on This Thesis

With the restricted observation time of 20 hours per field of the GASKAP-HI Pilot survey, the observational noise for H I absorption sightlines was too high to detect the warm neutral medium (WNM), even after spectral stacking. Currently, we know almost nothing about the spatial variations in the temperature of warm gas within our Galaxy. When observing the warmer phases of H I in absorption, we are typically limited by sensitivity and require long exposure times due to the gas' low optical depths and densities. Few surveys have been able to detect the WNM in absorption (Carilli et al. 1998; Dwarakanath et al. 2002; Patra et al. 2018), albeit with only a small handful of sources. Since we require absorption measurements to confidently calculate the spin temperature and kinetic temperature of gas, this makes determining the temperature of warm H I gas within the Milky Way incredibly challenging. The spectral stacking work completed with data from the 21-SPONGE survey was able to observe the WNM in absorption (Murray et al. 2014, 2018). However one downside of this work was that it utilised sightlines across the entire sky separated by large angular distances, meaning the average spectra comprised of gas not physically related to each other on different sides of the sky. To really understand the WNM we need to localise these stacks. Multiple spatially localised stacked measurements of the WNM will allow us to observe the spatial variation of the WNM's temperature across the plane-of-sky.

The GASKAP-HI survey (Dickey et al. 2013) is still ongoing, with one of its objectives to achieve additional observations of the original Pilot fields, giving a total observation time of 200 hours. This increased integration time will lead to a reduction in noise-levels in not just the H I absorption sightlines with already-detected cold gas, but also lower the noise of the sightlines were cold gas was originally not detected. From Chapter 2, it was found that the CNM also exists along the non-detection sightlines hidden below the noise. Increasing observation times along these sightlines would lower the noise-level to a point where this lower optical depth CNM gas would be detected along individual H I absorption sightlines. As such, the full GASKAP-HI survey will drastically increase the number of sightlines where cold H I gas will be detected in absorption compared to the Pilot sample. Assuming the spectra used in this thesis were observed with the full 200 hour observation time, the noise-level of the spectral stacks completed in Chapter 2 would reach a level similar to that of the 21-SPONGE survey, where the WNM was detected in absorption (Murray et al. 2014, 2018) (with stacked optical depth noise sensitivities of $\sigma_\tau \sim 2 \times 10^{-4}$). Through the high source density of H I absorption achieved by the ASKAP telescope, it will be possible to complete a similar task to that of Chapter 2, instead determining the temperature of the WNM in this region of the sky, and its variation across the plane-of-sky. Doing so will allow us to find any dependence on WNM temperature and local environment such as molecular tracers or UV-radiation field, to better inform numerical simulations in modelling phenomena such the Lyman-alpha radiation field, and other processes which balance energy in the ISM (Murray et al. 2014).

The structure functions calculated in Chapter 3 were limited by the spatial extent of the survey, only being reliable between ~ 0.4 and 100 parsecs. The lower limit of this range was mainly restricted due to low sample-sizes of pairs at smaller distances. With the full 200 hours of the GASKAP survey within this region, there will be an increase in the number of absorption sightlines detected, enabling a boost in sample-size to explore the smaller-scale nature of these structure functions. This will also enable a more direct comparison between previous structure function work that has mainly focused on AU scales using optical depth maps over single absorption sources like Cassiopeia A (Deshpande et al. 2000). Additionally the noise reduction from the improved observation time will enable for the detection of small-scale variation in cold H I gas, known as tiny-scale atomic structure, through observing the differences in optical depth spectra between sightlines very close on the plane-of-sky. While previous works have detected dozens of pairs with significant variation in density over scales on the order of 1000s of AU (Dickey 1979; Crovisier et al. 1985; Greisen & Liszt 1986; Rybarczyk et al. 2020), the sample size across the plane-of-sky is still small relative to total absorption detections. The higher sensitivity observations of the full 200 hour GASKAP-HI survey fields will enable the search for more evidence of tiny scale atomic structure, to place upper limits and estimates on the CNM 3D number density and to see if they align with that of previous measurements in the Northern hemisphere.

Within the Pilot region's spatial extent, no plateau points in the structure functions were found for any of the H I phases or their individual properties. Over the next few years, the GASKAP-HI survey will observe new fields, towards high Galactic latitudes and towards the Galactic centre and plane, as shown in Figure 5.1. This expansion of survey range, combined with the H I absorption source finding capabilities of the ASKAP telescope, will allow for H I absorption structure functions to be made across much larger physical distances. The increased spatial extent will enable continued efforts to detect the plateau point of the structure functions of each H I phase, allowing for us to determine the correlation length scale of the CNM, and the warmer gas phases, an observational probe for the average statistical size-scale of the H I phases. The increased spatial extent will also allow for larger-scale structure functions of the opacity-corrected column density of H I gas, allowing for a direct comparison between global spatial power spectra of H I emission across large patches of the Milky Way. With new survey regions also comes the ability to apply structure functions on new sets of absorption sightlines to search for variation in the power-law behaviour of the structure functions and spatial power spectra. Doing so would enable us to gather more information on the variation of spatial structure of cold H I gas between regions of the ISM undergoing different dynamical processes inside our Galaxy.

While the expanded range of the GASKAP-HI survey will improve our understanding of the optical depth and column density structure functions, the flat spin temperature structure functions derived in Chapter 3 allude to a need for new methods in determining H I spin temperatures. While the original method formulated by Heiles & Troland (2003) has become the staple for the past two decades, relying on Gaussian decomposition of the received emission and absorption spectra leads to degenerate solutions and non-quantifiable errors in estimating spin temperatures when testing different permutations of ordering the Gaussian components along the line of sight after fitting. To solve these limitations, new methods are being developed based on Bayesian forward modelling tools to fit H I emission and absorption spectra CARIBOU[1] is a H I Bayesian fitting model recently developed to model slabs along a line-of-sight representing clouds of different temperatures and densities, and then producing resulting spectra through radiative transfer. The model optimises the physical properties of the gas clouds along the sightline such as the kinetic temperature, three-dimensional number density and turbulent Mach numbers to produce the best fit to the received spectra. Compared to the Heiles and Troland method, the forward modelling approach provides a more physically motivated method for disentangling the cold and warm gas along sightlines. The model itself remains to

[1] https://github.com/tvwenger/caribou_hi

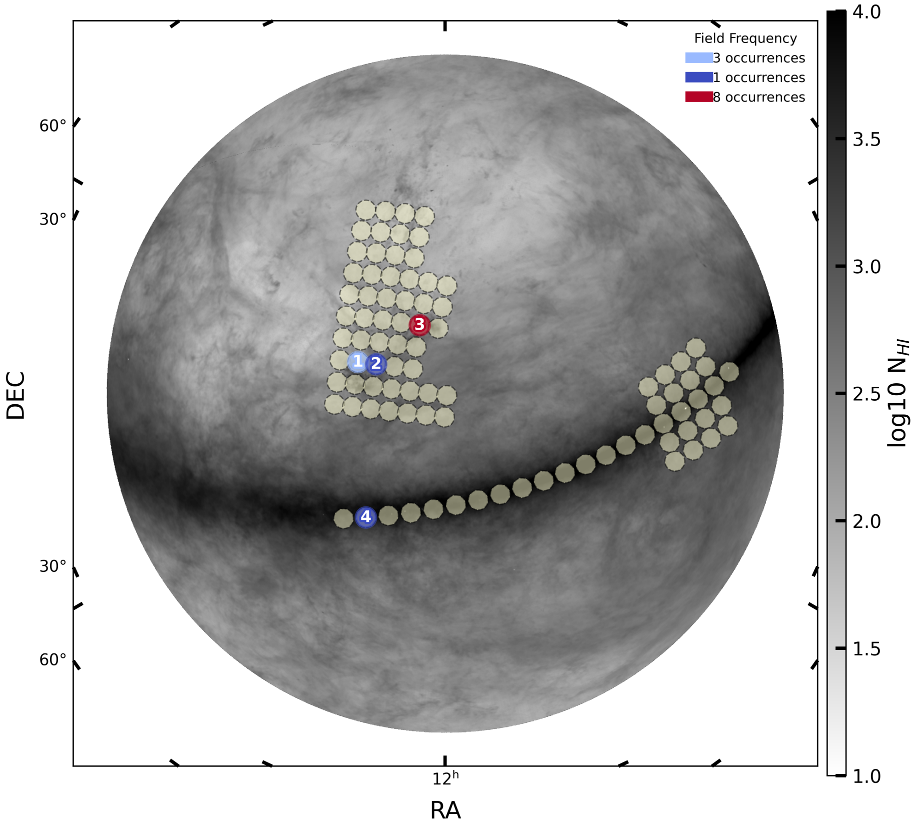

Figure 5.1: Locations of the fields being observed during the GASKAP-HI survey. The greyscale background map is a H I column density map of the Milky Way. Each circle represents a 5×5 degree field with 30 arcsecond resolution that will be observed over the next few years. The main targets are towards the Magellanic system (and high Galactic latitude), and towards the Galactic centre and plane. The filled-in circles represent fields already observed.

be fully tested on large scale surveys. Given the GASKAP-HI surveys' large sample of absorption sightlines, the survey offers an ideal test for this new method to determine physical temperatures and densities of the hundreds of sightlines towards the high Galactic latitudes of the Pilot survey for direct comparison with the work in this thesis. Additionally, this tool can be extended to be used with the future fields of the GASKAP-HI survey towards the Galactic plane. With high Galactic latitudes and the Galactic plane containing vastly different amounts of gas as well as involving different dynamical processes, the physical information fitted by these Bayesian models will improve our understanding on how dynamical processes affect the presence and properties of the different H I phases in our Galaxy.

5.2.2 Future Possibilities in Galactic H I Astronomy

The previously mentioned avenues all ultimately address limitations of the individual chapters contained within this thesis. However, with the advancement in H I absorption finding of the GASKAP-HI survey, there will also be new avenues to explore in improving our understanding of the Milky Way's ISM.

Past H I absorption surveys observed cold gas along the Galactic plane, finding that the cold gas mass fraction shows little variation out to a Galactic radius of ~ 25 kpc (Dickey et al. 2009). This result is perplexing, given the large variation in the heating and cooling mechanisms throughout the disk. To investigate the cause of this phenomenon with higher sensitivity and resolution, the GASKAP-HI survey will move into observing the Galactic plane within the next year, observing multiple fields at 0 degrees latitude, increasing in longitude away from the Galactic centre (as seen in Figure 5.1). Assuming the density of extragalactic background radio sources is similar in the Galactic plane to that of the pilot survey at high Galactic latitudes, GASKAP will find hundreds of absorption sources spread throughout the plane. Through the use of both Gaussian decomposition and Bayesian methods described earlier, it will be possible to analyse the physical properties of optical depth and spin temperature of the CNM as a function of Galactocentric radius, to determine if the Dickey et al. (2009) result holds with higher resolution data and which certain processes within the Galactic disk are responsible. Investigating the variation of cold H I gas properties within the Galactic disk with the high source density of GASKAP will enable more accurate studies on the location of cold gas.

Another fundamental question in interstellar medium research is what are the properties of turbulence in the inter-cloud medium, the cirrus gas that envelops cold clouds. The inter-cloud medium is dominated by the WNM, however extracting turbulent information about the WNM remains difficult. This is because Gaussian decomposition separating phases by H I emission contains both thermal and turbulent contributions to the linewidths observed, and so gas temperatures are required to isolate the thermal and turbulent contributions to determine turbulent Mach numbers. In the past, Gaussian decomposition tools used on H I emission such as ROHSA (Marchal et al. 2019) have been implemented to separate the WNM and CNM to estimate the physical properties of the WNM (Marchal & Miville-Deschênes 2021). This work has since become an important point of reference for the turbulent Mach number of the WNM in the Milky Way, however there have not been any more estimates of the WNM Mach number since then. The GASKAP survey will produce observations of both high Galactic latitude and Galactic plane environments, with a higher spatial resolution compared to previous surveys. With this comes the opportunity to follow on from Chapter 4 in separating the GASKAP survey H I emission into its distinct phases using ROHSA, instead to estimate the turbulent Mach number of the WNM in different Galactic environments, to see if there is any dependence on UV radiation field or other features in the region. With these separated H I phases in emission, there will also be the opportunity to compute spatial power spectra of each phase to analyse the power on different physical scales. The aim of this will be to determine if the difference in power law slope observed between the CNM and WNM in the past (Martin et al. 2015; Kalberla & Haud 2019) is universal or not. Being able to complete this on separate but nearby fields will enable the linking of WNM and CNM turbulent properties to the existence of physical structures and ongoing physical processes, such as converging flows or shocks.

The CNM forms through the condensation of warmer phases of neutral H I gas during periods of shocks and instabilities. With these instabilities typically occurring on parsec-scales, this has driven many works to focus on finding variations in optical depth as a function of angular separation between background radio sources. These small-scale fluctuations in density can be attributed to the turbulent nature of the CNM and density profiles of small cold gas clouds. While previous works have detected dozens of pairs with significant variation in density over scales on the order of 1000s of AU (Dickey 1979; Crovisier et al. 1985; Greisen & Liszt 1986; Rybarczyk et al. 2020), the sample size across the plane-of-sky is still small relative to total absorption detections. While the current GASKAP-HI Pilot survey did not reach the sensitivity to detect tiny scale atomic structure with 20 hour observations, the 200 hour total observation time of the Pilot survey fields

The GASKAP-HI survey is currently viewing the Milky Way gas towards the Magellanic system with exposure times of up to 200 hours per field over 10, 25 square-degree fields. The current GASKAP pilot survey did not reach the sensitivity to detect tiny scale atomic structure with 20 hour observations, however with this increased observation time, the survey will lead to an order of magnitude increase in the number of detections of close pairs of radio background sources. I intend to use these higher sensitivity observations to search for more evidence of tiny scale atomic structure, to place upper limits and estimates on the CNM 3D number density and to see if they align with that of previous measurements in the Northern hemisphere.

Future interferometric telescopes such as the Deep Synoptic Array (DSA) and the SKA will enable even greater spatial detail and higher spectral sensitivity while maintaining velocity resolutions similar to that of ASKAP for Galactic H I astronomy. With both of these telescopes able to survey the northern and southern skies respectively, large-scale observations of sub-parsec features within our local Galactic neighbourhood will be possible not just within key regions of the Milky Way, but across the entire sky.

All of these research avenues, inspired by the work completed in this thesis, will help to improve our understanding on the spatial structure and spatial variation of H I gas properties across the sky within both the Milky Way and nearby galaxies. This will lead to not just a test and refinement of the observational techniques used in preparation for the more powerful telescopes of tomorrow, but also help place restrictions to confine theoretical models and numerical simulations of the ISM.

Appendix

A.1 Appendix for Chapter 2

A.1.1 Toy Model Theoretical Considerations

In this section, we use toy models to investigate the biases introduced by mixing complex multiphase emission and absorption spectra through stacking.

Single component

We first begin our toy model by assuming the simple case of all sightlines containing a single component. Here, every component is perfectly shifted to 0 km s^{-1} by the peak of the spectrum in emission. However as mentioned in Section 2.3.1, this shifting may be inaccurate to $\sim 1-2$ km s^{-1} from the misalignment of absorption and emission peaks due to differing noise levels and sightlines used.

To test how stacking these components affects measurements such as the spin temperature, we set up a toy model with 2000 sightlines, each with an emission and absorption spectrum. In each sightline, a single component was created with a width and amplitudes in brightness temperature and optical depth typical of cold gas in the CNM. The properties for the 2000 sightlines were sampled from Gaussian distributions with the mean value uniformly chosen within $5 \leq T_{\mathrm{B,peak}} \leq 15$ K, $0.02 \leq \tau_{\mathrm{peak}} \leq 0.3$, FWHM ~ 5 km s^{-1} and standard deviations of $\sigma_{T_{\mathrm{B}}} = 4$ K, $\sigma_{\tau_{\mathrm{peak}}} = 0.01$ and $\sigma_{\mathrm{FWHM}} = 0.2$. The central velocities of these components is centred around 0 km s^{-1}, with a slight deviation to account for the $1-2$ km s^{-1} deviation between emission and absorption components found in reality (a central velocity dispersion of ~ 0.5 in the toy model). Stacking these spectra, we then calculate the spin temperature, T_s of the stacked component via:

$$T_s = \frac{T_{\mathrm{B,\ peak}}}{1 - e^{-\tau_{\mathrm{peak}}}} \tag{A.1}$$

Alongside this, we also compute the spin temperature of the individual sightlines and take the average to create a spin temperature that should be measured. Repeating this scenario 200 times (using a different sampled mean value of $T_{\rm B,peak}$ and $\tau_{\rm peak}$ for each iteration), we find the spin temperature of the stack is well correlated with the average spin temperature of the individual sightlines (figure not shown).

Multiple components

As discussed in Section 2.3.1, the most sensitive detection sources contain multiple components: a narrow primary component aligned with the peak in the corresponding emission profile, and a broader secondary component offset in velocity.

The primary component tied to the peak in emission will be aligned well at 0 km $\rm s^{-1}$ after shifting, whereas the additional peaks will merge into a broader secondary component.

To explore these effects of stacking multicomponent spectra, we create a similar toy model to that of Section A.1.1. We create 2000 mock sightlines, each with an absorption and emission spectrum. We create primary components similar to the previous section. In addition, we add a broader component. This secondary component has a width and brightness temperature and optical depth amplitude randomly sampled within typical values of warmer CNM and colder UNM gas. The properties for the 2000 sightlines were sampled from Gaussian distributions with the mean value uniformly chosen within $3 \leq T_{\rm B,peak} \leq 15$ K, $0.02 \leq \tau_{\rm peak} \leq 0.03$, FWHM ~ 15 km $\rm s^{-1}$ and standard deviations of $\sigma_{T_{\rm B}} = 4$ K, $\sigma_{\tau_{\rm peak}} = 0.01$ and $\sigma_{\rm FWHM} = 0.6$ respectively. The central velocity of this component is randomly sampled over a normal distribution centred on 0 km $\rm s^{-1}$ but with a dispersion of ~ 15 km $\rm s^{-1}$, simulating the potential of a non-zero central velocity of these secondary components after shifting.

Fig. A.1 demonstrates the effects of stacking these multicomponent absorption sightlines featuring a primary component, shifted correctly to 0 km $\rm s^{-1}$, and a broader secondary component whose central velocity is chosen from a normal distribution with a deviation of 15 km $\rm s^{-1}$. The values for the peaks and widths of the two components were chosen based on the parameter space mentioned earlier. The primary components, being correctly centred, produce an averaged component after Gaussian decomposition equivalent to an average of the individual primary components. However, due to the velocity variation of the secondary components, the average secondary component found after Gaussian decomposition varies drastically in amplitude and width from the average of the individual sightlines of the secondary components if they were all centred at 0 km $\rm s^{-1}$.

Repeating this experiment 100 times (with a different sampled mean value of $T_{\mathrm{B,peak}}$ and τ_{peak} for each iteration within the ranges mentioned above), we compared the measured amplitudes of the components with that of the average amplitude of the components in emission and absorption in individual sightlines. This comparison is shown in Fig. A.2. Only the secondary component's properties are displayed since the primary component's values agree with the average of individual primary components due to the correct centring of the features prior to stacking. For the secondary components however, the measured amplitudes are always lower. This is because the total flux is conserved in the average regardless of the Gaussian's central velocities. Increasing the velocity spread of the Gaussians broadens the final stack, and to compensate the averaged amplitude must diminish. Therefore, regardless of the severity of the range of central velocities of secondary components in individual sightlines, the peak of the secondary component will always be lower and its width always greater than the average of the individual sightline values.

Despite this lower limit, the stacked secondary components' amplitudes are still linearly correlated with the average values. Since the central velocities of the secondary components are approximately equal in emission and absorption, the overall effect of the velocity dispersion on the stack is equivalent in emission and absorption. As a result, the gradient of the linear correlation of measured peak brightness temperature and optical depth with the individual sightline average is the same.

When calculating the spin temperature of the secondary component through this toy model, we find that these gradients cancel out through the division of emission and absorption amplitudes. The spin temperature of the secondary component is therefore well correlated with the average of the individual secondary components' spin temperatures, as shown in Fig. A.2.

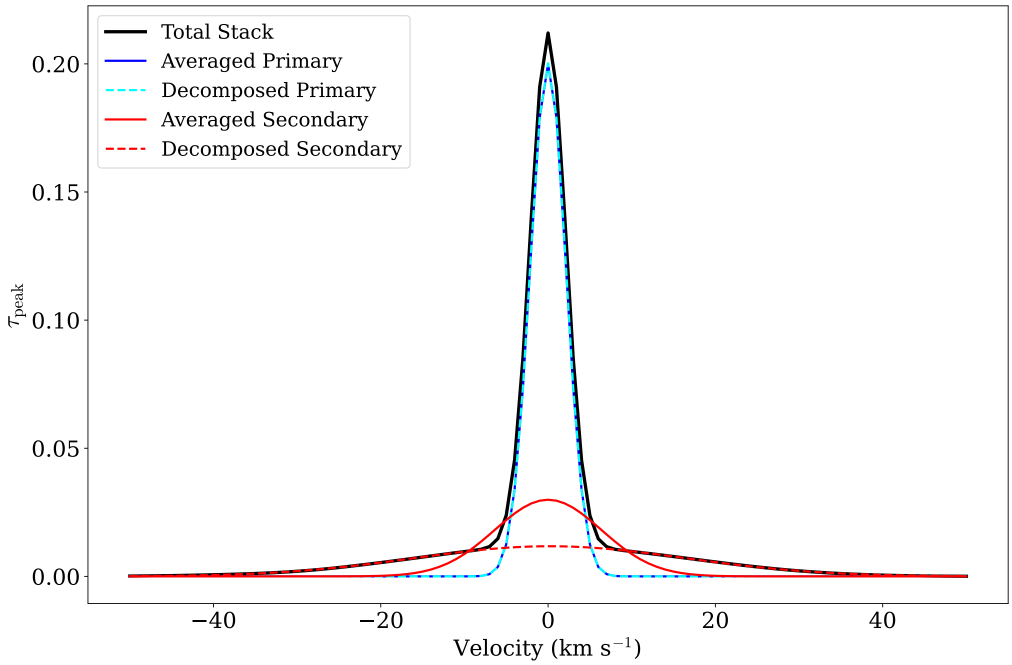

Figure A.1: Comparison of the primary and secondary component from Gaussian decomposition of a toy model stacked absorption spectra with the separated stacks of the individual primary and secondary components. The total stack (black) is produced as described in Section A.1.1. We note the primary component in the stack (cyan-dashed) is identical to the separately averaged primary component (solid blue). The secondary component (red-dashed) is shallower and has a greater FWHM than the separately averaged secondary component (solid red) where each component was centered to 0 km s^{-1}.

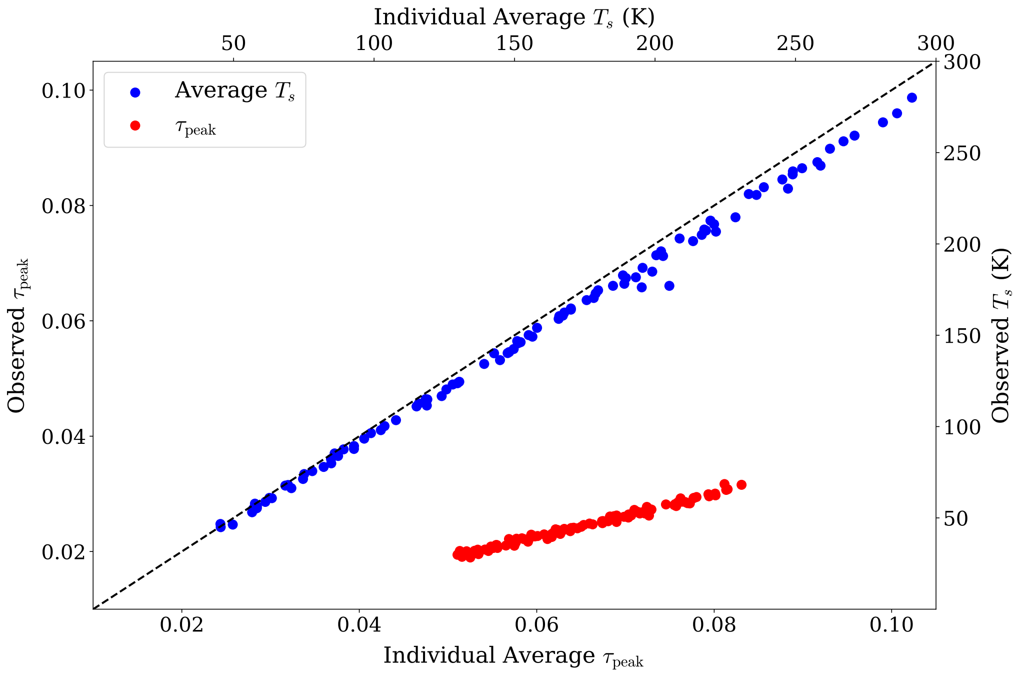

Figure A.2: Comparison of observed peak optical depth (red) and average spin temperature (blue) of the secondary components from 100 runs of stacking 2000 two-component spectra, as described in Section A.1.1. The peak brightness temperature is not displayed but shows a similar trend to the peak optical depth due to the velocity offsets being the same in both emission and absorption. The observed peak optical depth is always less than the average peak optical depth of the individual sightlines' secondary components. However, the observed spin temperature of the secondary component correlates well with the average spin temperature of each sightline's secondary component.

A.2 Appendix for Chapter 3

A.2.1 Noise Cutoff for Structure Function Data

To properly compute the structure functions used in this work, we first needed to remove high noise values from the datasets that would otherwise wash-out any observable structure. To do this, we make cutoffs based on the fractional error for each dataset used. For the CNM gas related quantities, only the integrated optical depth data contained sightlines with high percentage errors, shown in Figure A.3. We chose a fractional noise-cutoff of 0.6, where the 50 sightlines above this limit were removed from the dataset before computing the structure functions in Section 3.4.2. The other quantities of average spin temperature and CNM optically thick H I column density did not contain a noteworthy population of high error values that would plague the structure functions and therefore no cutoff was applied for those datasets.

We also applied noise-cutoffs for the WNM column density and the optically thick total column density values discussed in Section 3.4.3. Histograms of the fractional uncertainty of both of these datasets are shown in Figure A.4. For these datasets, we chose a fractional noise-cutoff of 0.4, where above this 9 and 16 values were removed from the WNM and optically thick total H I column density datasets, respectively. The additional quantity of optically thin total H I column density did not require a noise-cutoff as there were no sightlines with fractional uncertainty above the 0.4 cutoff.

A.2.2 Fitting error calculation

In order to correctly estimate the errors in the both the structure function and spatial power spectrum fits described in this work, we need to incorporate both the errors in the original fit as well as the statistical uncertainty from having a limited number of data points.

To account for the latter effect, we consider four different subsets of the structure function bins and spatial power spectrum points, shown below:

- Every second data-point (both the odd set and even set)
- Every third data-point (completed three times for each subset)
- The first half of the data-points
- The second half of the data-points

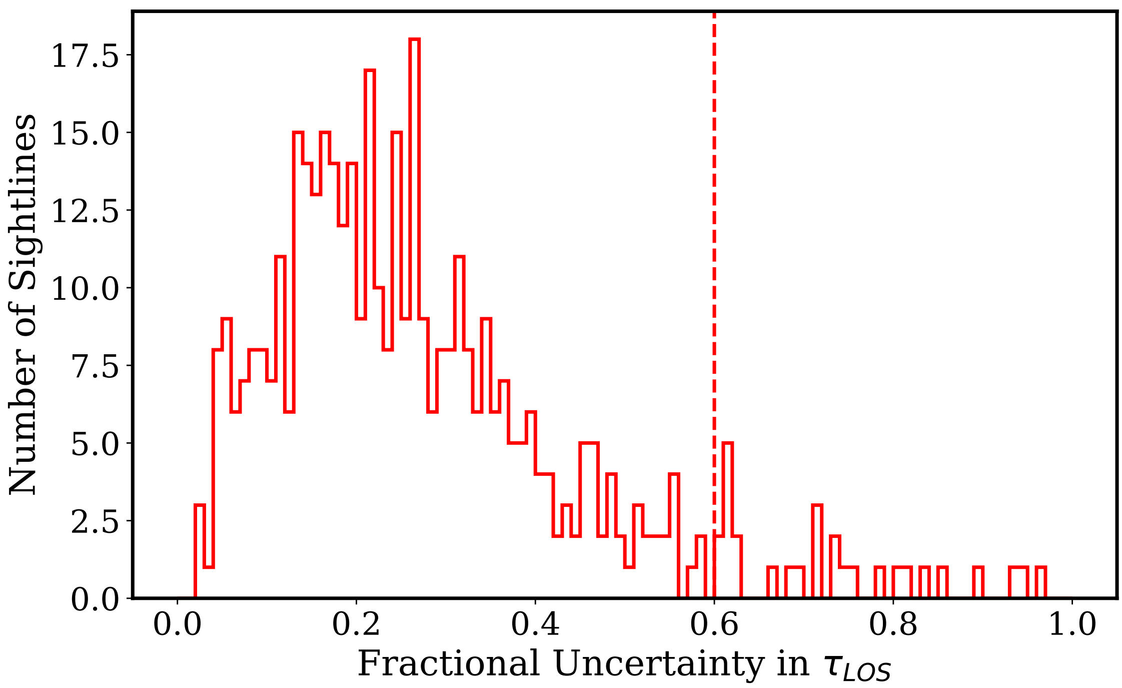

Figure A.3: Histogram of the Fractional uncertainty in the values for integrated optical depth, used in Section 3.4.2. The vertical dashed line represents the chosen noise cutoff limit of 0.6, where the 50 values above this were removed from the dataset before computing the structure function.

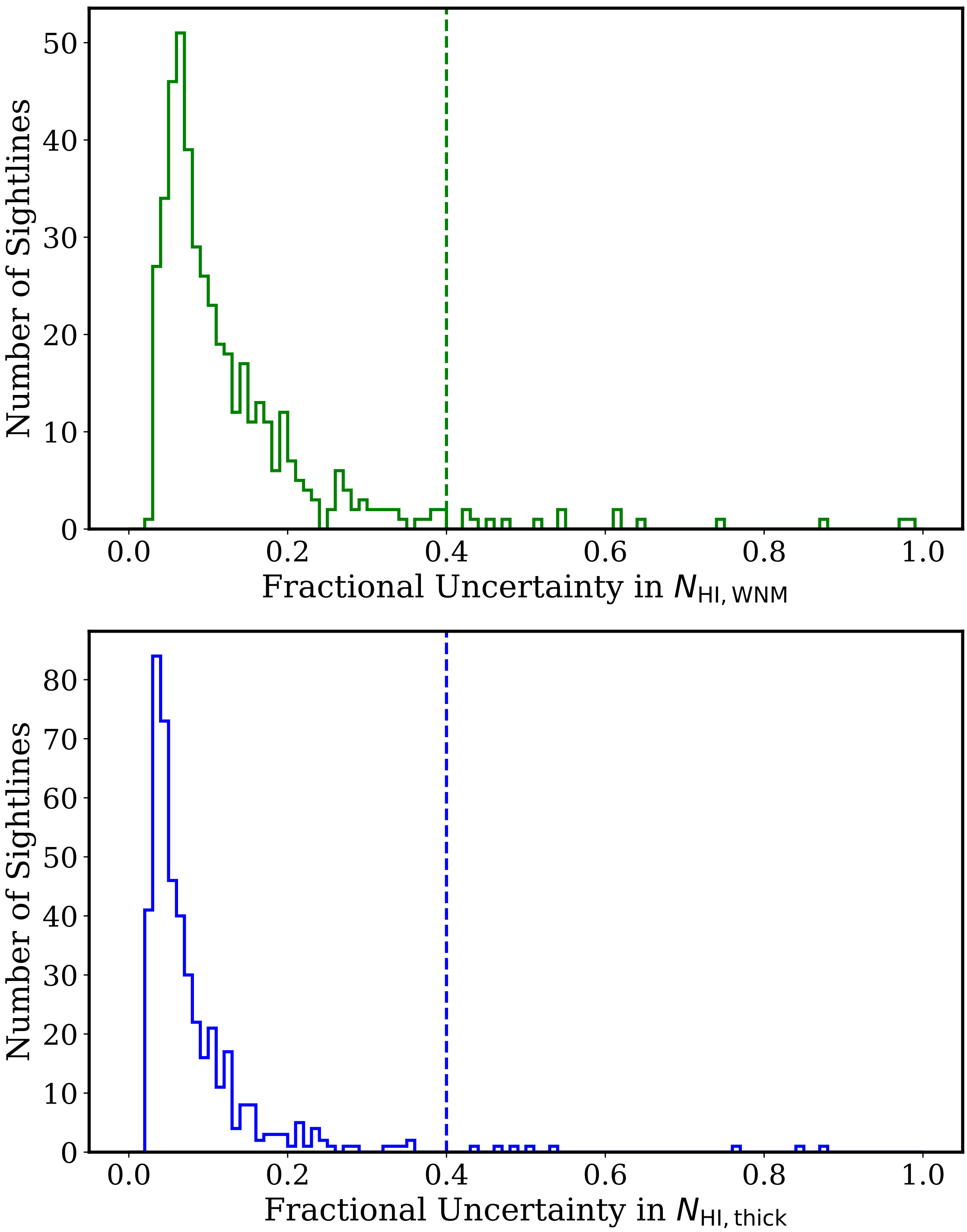

Figure A.4: Histogram of the Fractional uncertainty in the values for the opacity-corrected WNM (top) and total (bottom) H I column densities, used in Section 3.4.3. The vertical dashed lines represent the chosen noise cutoff limit of 0.4. Above this, 16 and 9 values were removed from the WNM and total H I column density datasets, respectively, before computing the structure functions.

From each of these subsets, we re-fit the functions in the same manner as for the original fit. The statistical uncertainty of the fit is then calculated through the standard deviation of each fitted parameter across all the subsets.

The total uncertainty in a fitted parameter can then be formed through quadratic sum of this statistical uncertainty, denoted as $\sigma_{\mathrm{statistical}}$, and the error of the original fit, $\sigma_{\mathrm{original\,fit}}$, such that:

$$\sigma_{\mathrm{total}} = \sqrt{\sigma^2_{\mathrm{original\,fit}} + \sigma^2_{\mathrm{statistical}}} \tag{A.2}$$

This error is the uncertainty recorded next to each of the fitted parameters for the structure functions and spatial power spectra throughout this work.

A.2.3 Sightline Location Bias

One potential bias in structure functions is dependent on the location of the discrete measurements used within the region one wishes to probe. If our sightlines are dominantly located along a specific direction, for example along a H I filament, then the spatial scale dependence we find will be biased towards that direction rather than being an isotropic measurement.

To test the reliability and symmetry of our source locations, we construct a scenario where our spin temperature values are sampled from a single Gaussian distribution. Since a Gaussian distribution should result in a flat structure function (since the values are entirely random and not spatially correlated), then any deviation from this flatness would be a sign of our sightlines being dominated by a single direction.

In our scenario, we generate a sample of 462 line-of-sight temperatures based on a normal spin temperature distribution with a mean of 60 K and standard deviation of 20 K. This distribution is chosen to be similar to the original GASKAP sample of individual absorption sources from Nguyen et al. (2024). For this generated sample, we generate uncertainties of 10%, mimicking an average error on spin temperature from Gaussian Decomposition. These spin temperatures are then paired with the original coordinate locations of the GASKAP Milky Way absorption survey discussed in this work.

Following the same procedure from Section 3.4.2, we compute the structure function of this artificial sample of average sightline temperatures. We repeat this process 100 times with different samples from the same normal distribution. The 100 structure functions are then averaged to produce a mean structure function from a random sample of spin temperatures, shown in Figure A.5. The uncertainties for these binned points in the structure function are made from a sum in quadrature of the original errors in each individual structure function and the standard deviations of individual bin values at that specific separation scale.

The structure function produced has a flat profile, indicating that our sightline sample used in this work is reliable and not biased in any particular direction or axis.

A.2.4 Other Synthetic Quantity Structure Functions

While Section 3.6.2 primarily focusses on comparing the spin temperature structure functions of the TIGRESS simulation with and without noise, we can also compare the other integrated quantities used in this work. Following the procedure of Section 3.6.2, we produced structure functions of the optically thick column density, $N_{\mathrm{HI,\,thick}}$ and of the integrated optical depth, τ_{LOS} using the brightness temperature and optical depth spectra produced which only contain cells with $T_k < 500$ K. This limit allows us to analyse the structure of only cold gas, similar to that of Section 3.4.2. From the four regions marked in Figure 3.10, we produced the structure functions of integrated optical depth, shown in Figure A.6, and for the optically thick column density, shown in Figure A.7.

Overall, we find that when adding noise of a similar order of magnitude to the brightness temperature and optical depth errors from the GASKAP-HI Pilot survey, there is not much variation in the structure functions for the optical depth and column density. This, in contrast with the large variation shown in Section 3.6.2 for the line-of-sight harmonic mean-weighted spin temperature, suggests that while the spin temperature structure function is heavily biased by the observational noise of the GASKAP-HI survey, the other quantities are not as affected.

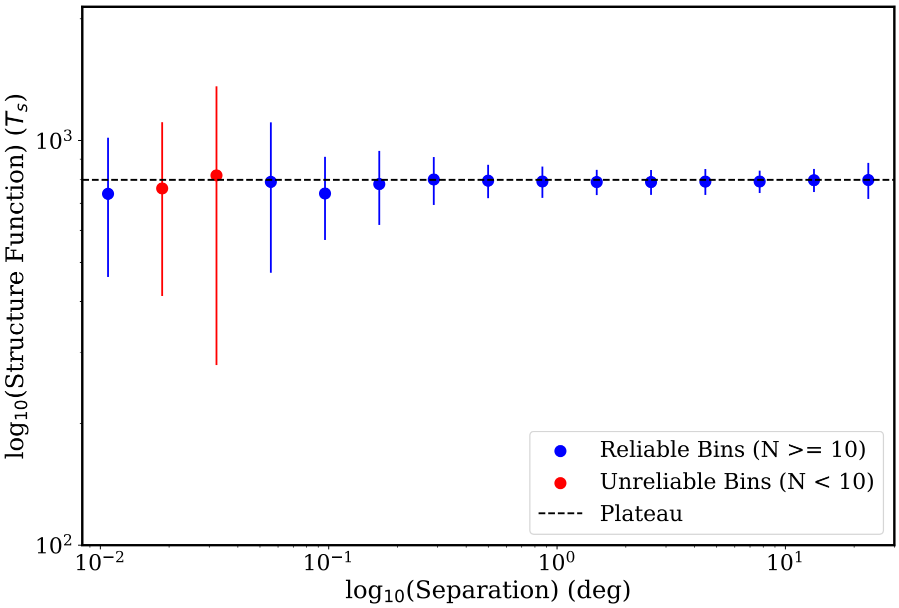

Figure A.5: Log-log plot of the binned average 2-point structure function measurements for a random Gaussian distribution of spin temperature measurements. The 2-point structure function is marked by the blue circles, with the red points indicating bins with low sampling and which are hence unreliable. The plateau point is marked by the dotted black lines, equal to $2\sigma^2$ for the 2-point structure function, where σ is the standard deviation of the original sample (Seta et al. 2023).

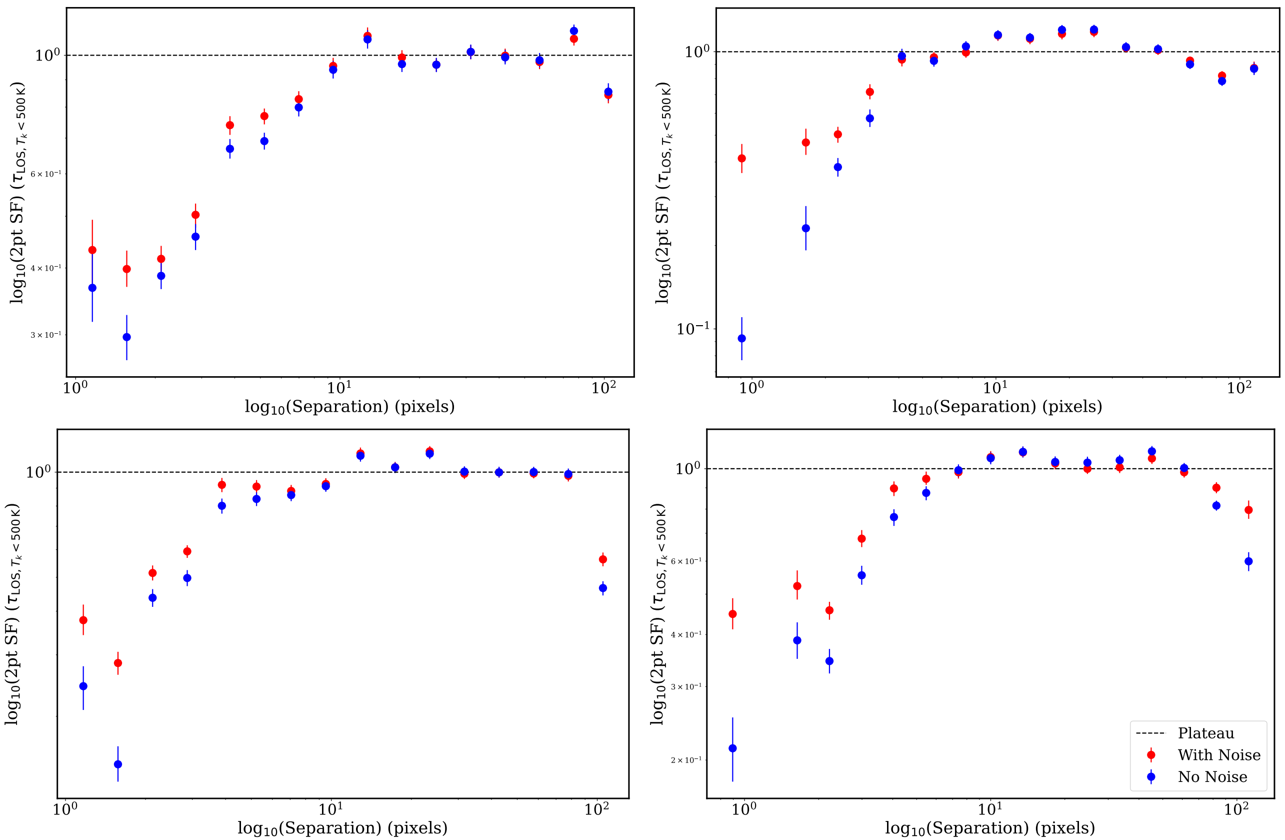

Figure A.6: Normalised structure functions of the TIGRESS simulation using data from the H I synthetic observation and regions A (top left), B (top right), C (bottom left), and D (bottom right) shown in Figure 3.10. The blue points are the structure function of the TIGRESS line-of-sight integrated optical depth of gas with $T_k < 500$ K as given through radiate transfer. The red points are from the same sightlines, but with optical depth errors added similar to the GASKAP survey. Both structure functions are normalised for comparison by the plateau point of the 2-point structure function equal to $2\sigma^2$ (Seta et al. 2023).

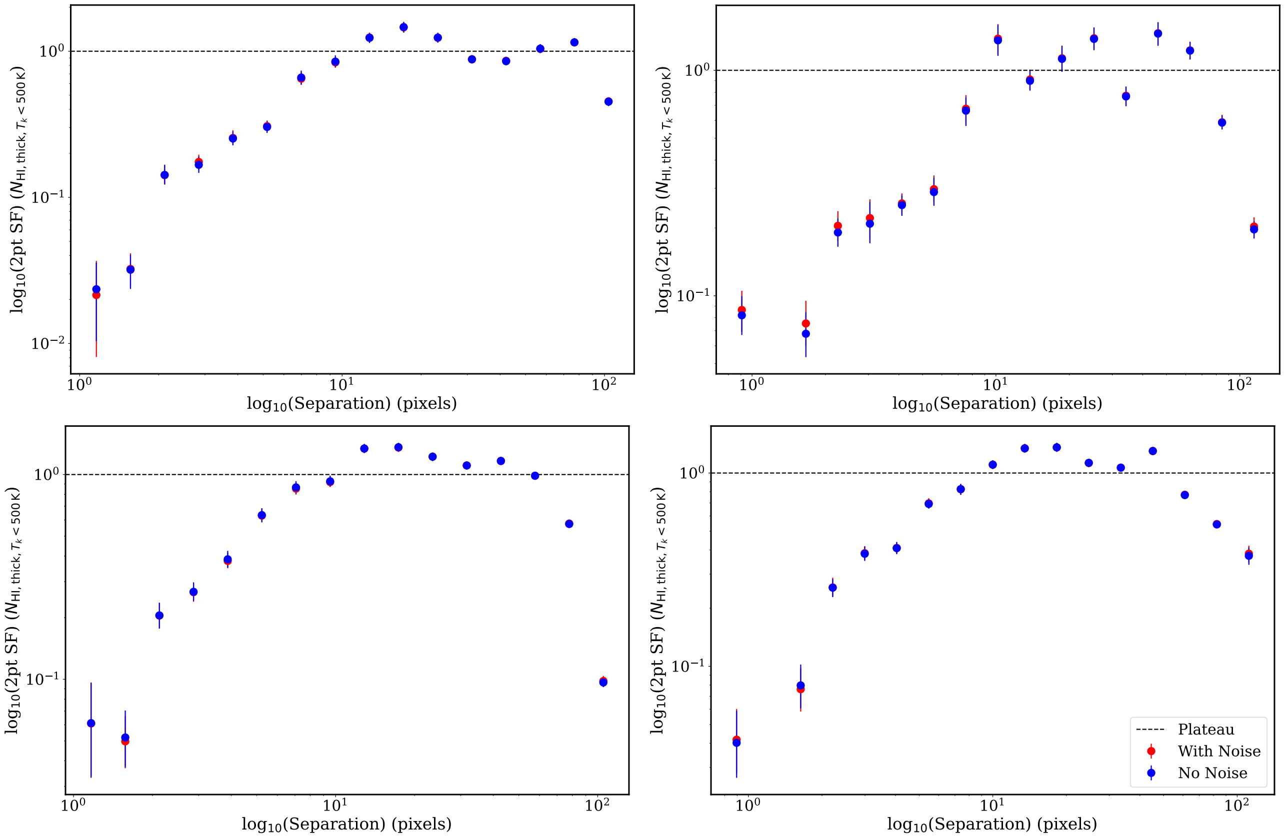

Figure A.7: Normalised structure functions of the TIGRESS simulation using data from the H I synthetic observation and regions A (top left), B (top right), C (bottom left), and D (bottom right) shown in Figure 3.10. The blue points are the structure function of the TIGRESS line-of-sight optically thick column density of gas with $T_k < 500$ K as given through radiate transfer. The red points are from the same sightlines, but with brightness temperature errors added similar to the GASKAP survey. Both structure functions are normalised for comparison by the plateau point of the 2-point structure function equal to $2\sigma^2$ (Seta et al. 2023).

A.3 Appendix for Chapter 4

A.3.1 Lower Resolution Parameter Maps

As discussed in Section 4.5.1, we can utilise the GASKAP-HI data at sub-parsec resolution to test the effect resolution has on Gaussian decomposition to separate the CNM from H I emission. Using the original 30 arcsecond resolution data from Section 4.2.1, we convolve the data using Gaussian beams of 1 arcminute, 2 arcminutes, 4 arcminutes, 8 arcminutes, 16 arcminutes, 32 arcminutes, 64 arcminutes, and 128 arcminutes, producing 8 maps in total. These maps were then re-binned to have the same number of pixels per beam as the original data-product to avoid over-sampling of the data. These fields were then decomposed using ROHSA, each fitted with 4 Gaussians, as discussed in Section 4.5.1. The resulting parameter maps for each of the Gaussians for each resolution are displayed in Figures A.8 to A.15. It is worth noting that for the fields where the beam-size is close to or on the order of the region itself, such as the 64 and 128 arcminute resolutions, we find the dispersions for Gaussians G_3 and G_4 become smooth. The other Gaussians of G_1 and G_2 have structure in their dispersion maps at these low resolutions. However, this is not statistically significant since the structure exists on scales smaller than the beam.

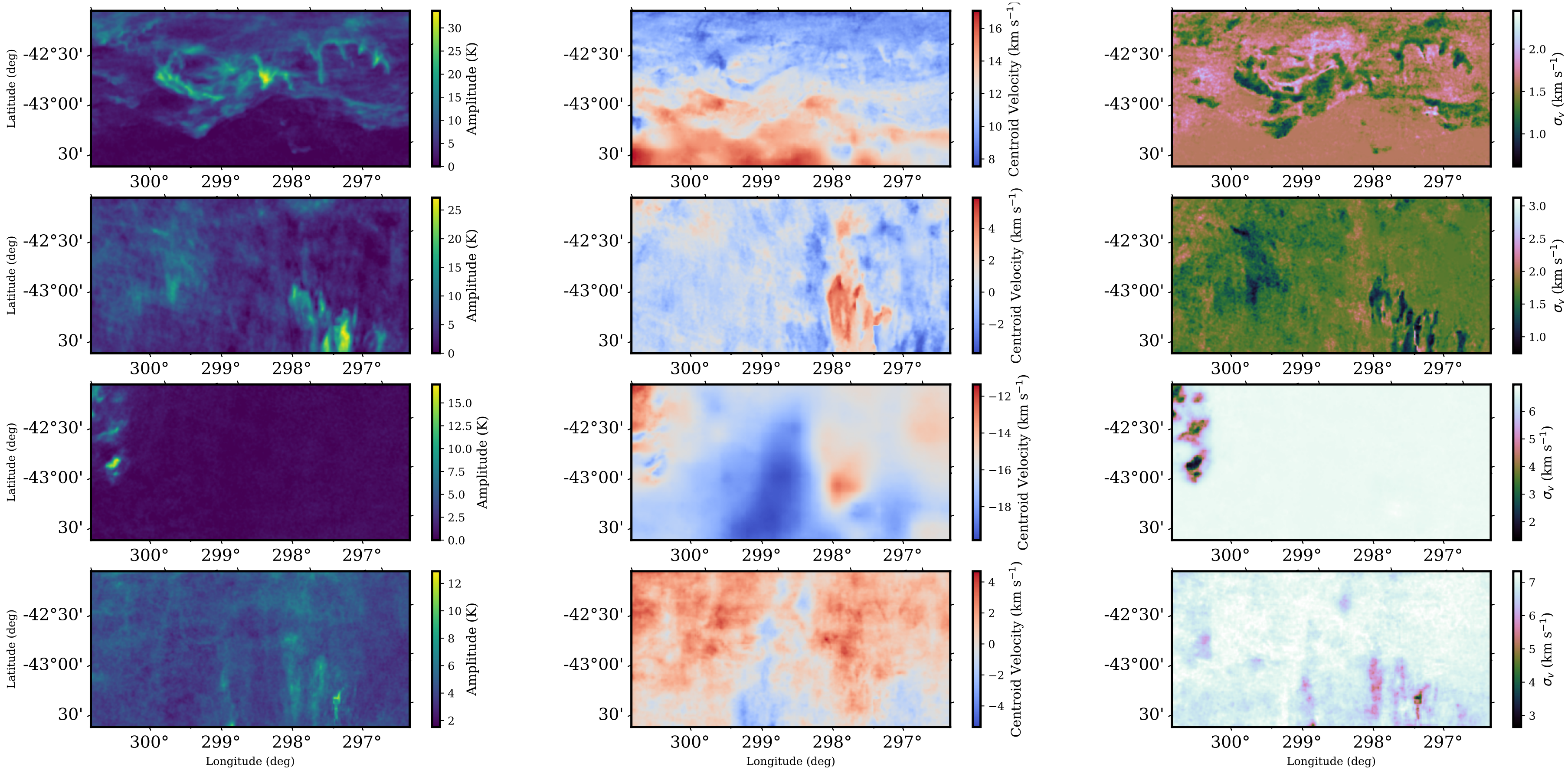

Figure A.8: Collection of fields for the amplitude (left), central velocity (middle) and velocity dispersion (right) of each Gaussian field (G_1, G_2, G_3, and G_4) fitted from the 1 arcminute resolution data discussed in Section 4.5.1.

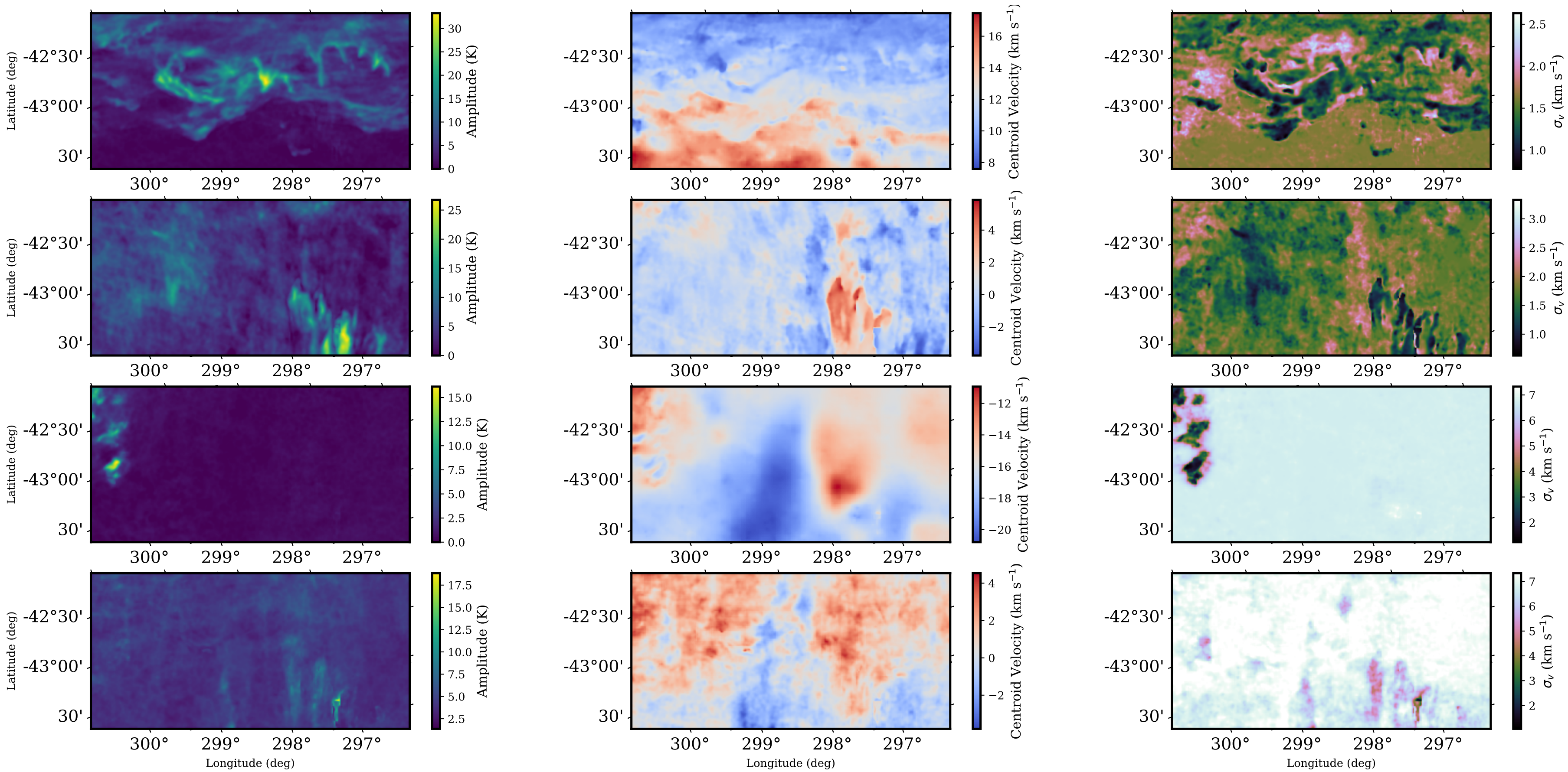

Figure A.9: Collection of fields for the amplitude (left), central velocity (middle) and velocity dispersion (right) of each Gaussian field (G_1, G_2, G_3, and G_4) fitted from the 2 arcminute resolution data discussed in Section 4.5.1.

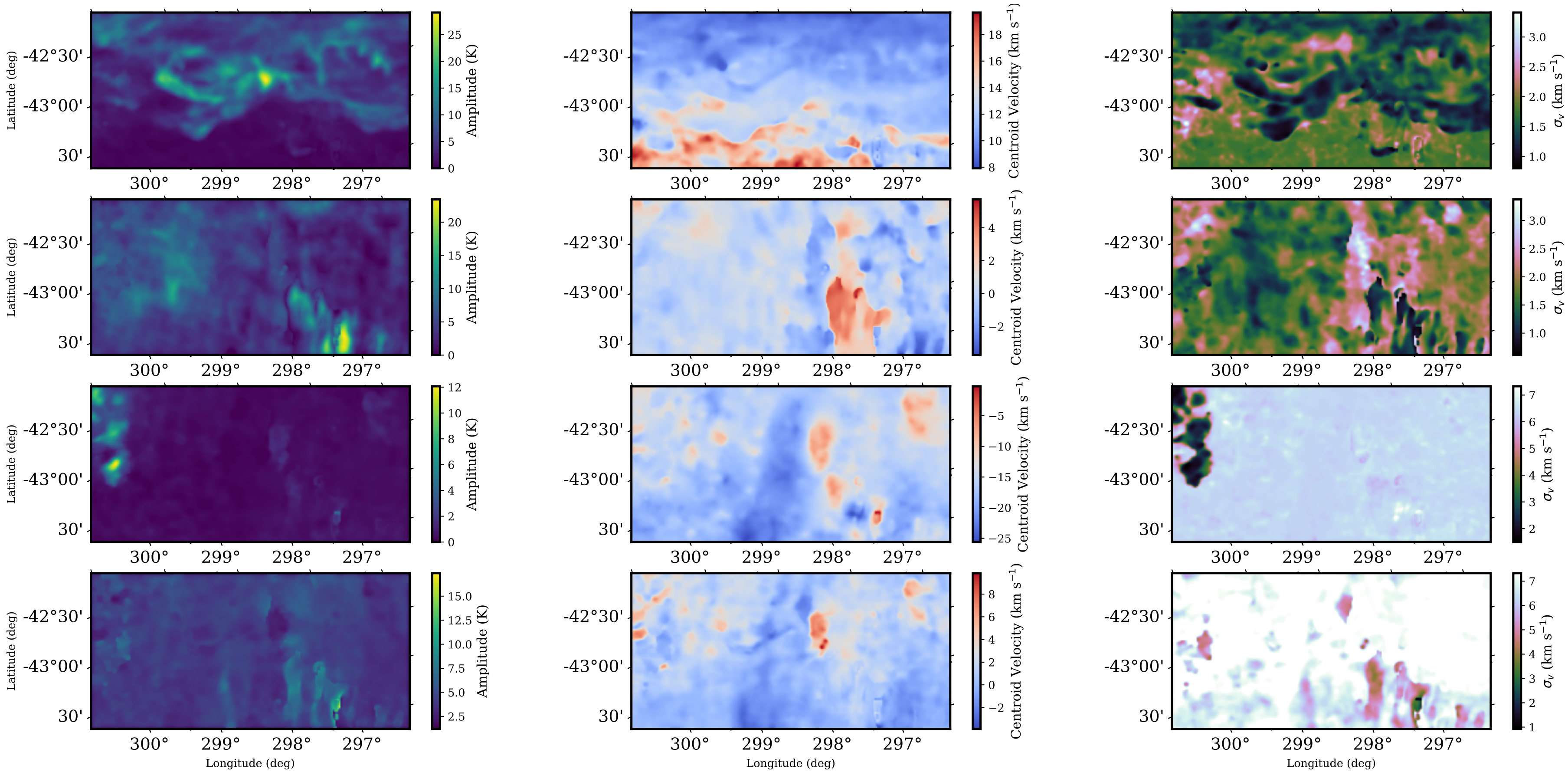

Figure A.10: Collection of fields for the amplitude (left), central velocity (middle) and velocity dispersion (right) of each Gaussian field (G_1, G_2, G_3, and G_4) fitted from the 4 arcminute resolution data discussed in Section 4.5.1.

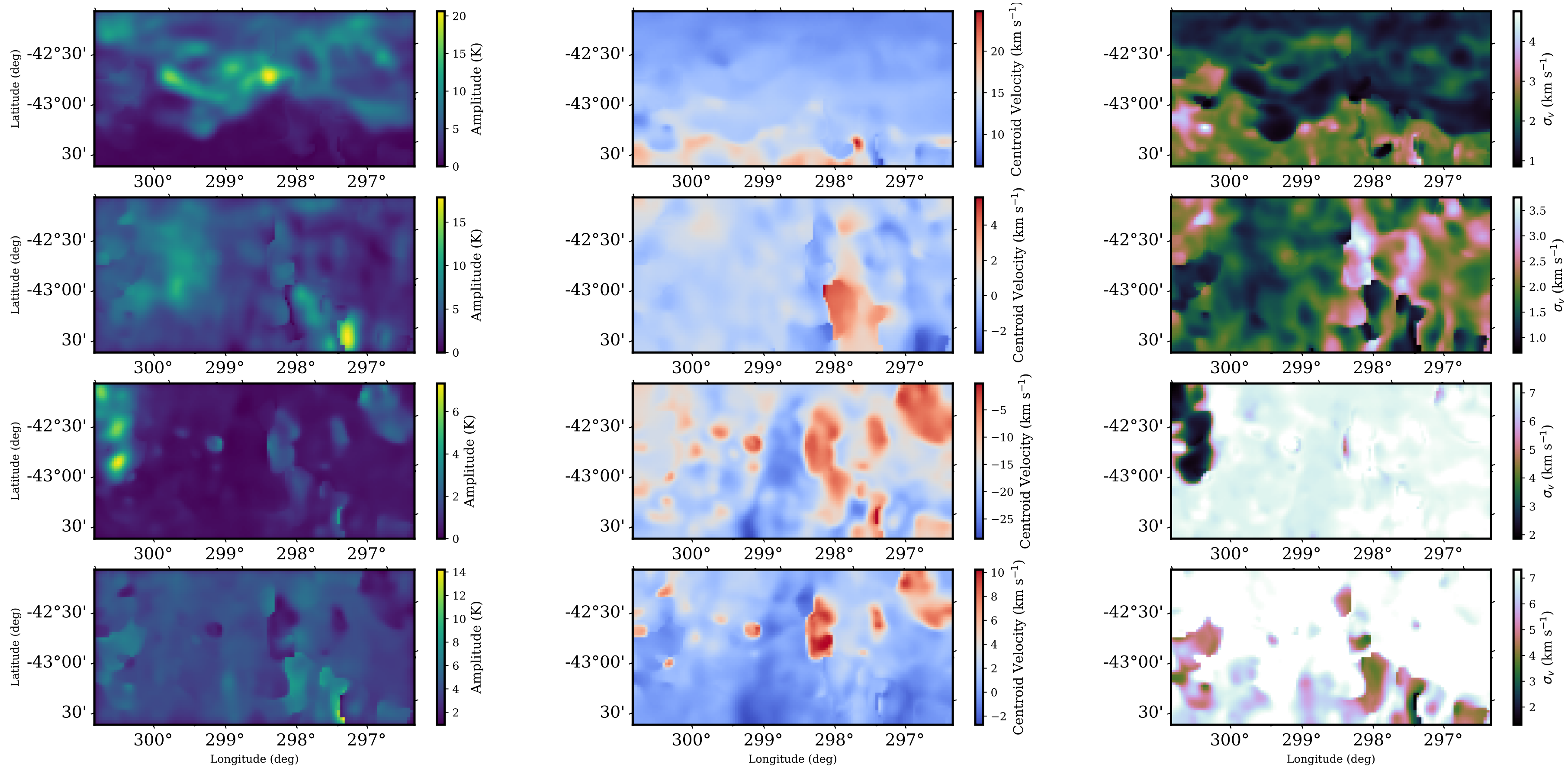

Figure A.11: Collection of fields for the amplitude (left), central velocity (middle) and velocity dispersion (right) of each Gaussian field (G_1, G_2, G_3, and G_4) fitted from the 8 arcminute resolution data discussed in Section 4.5.1.

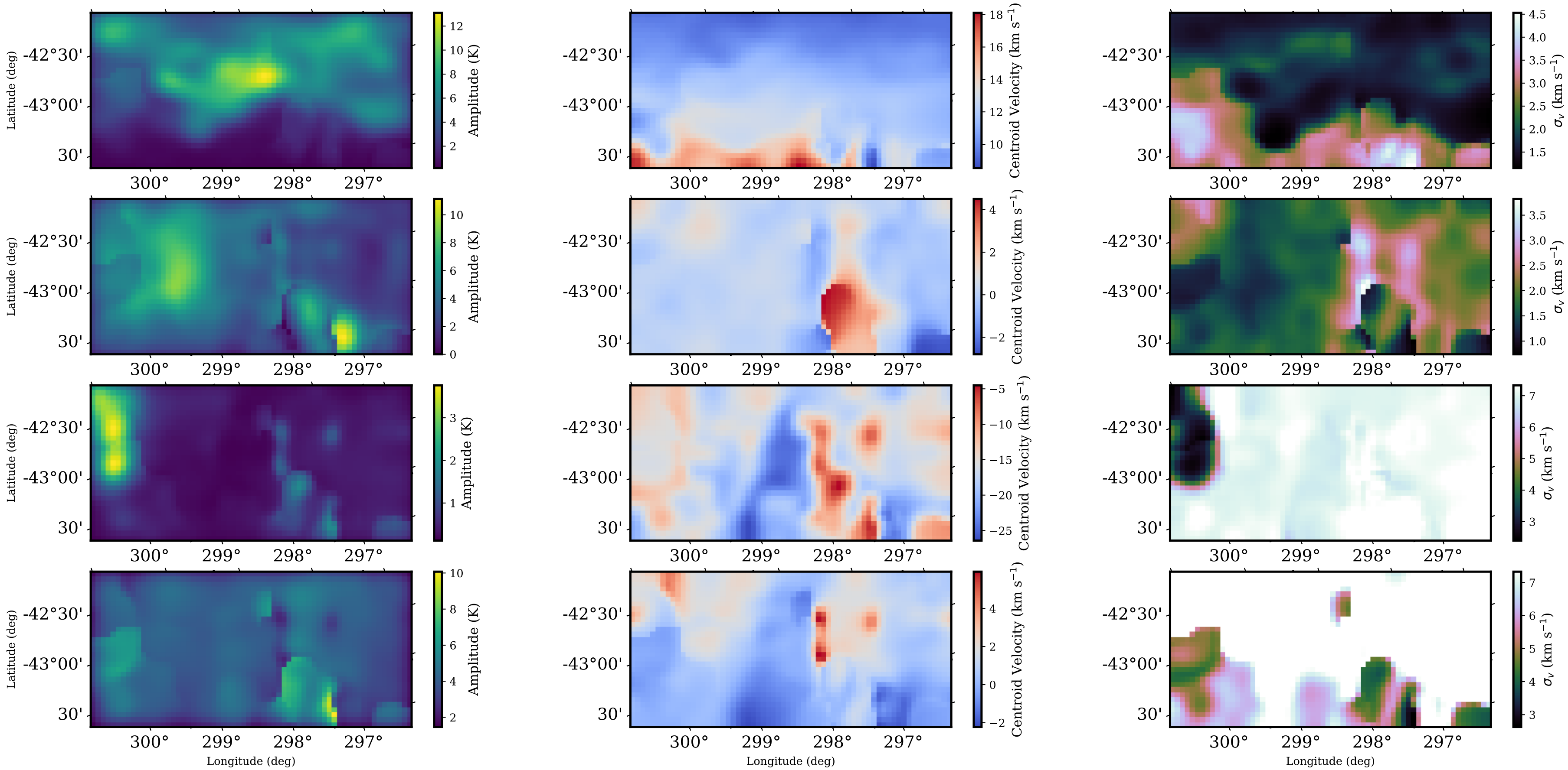

Figure A.12: Collection of fields for the amplitude (left), central velocity (middle) and velocity dispersion (right) of each Gaussian field (G_1, G_2, G_3, and G_4) fitted from the 16 arcminute resolution data discussed in Section 4.5.1.

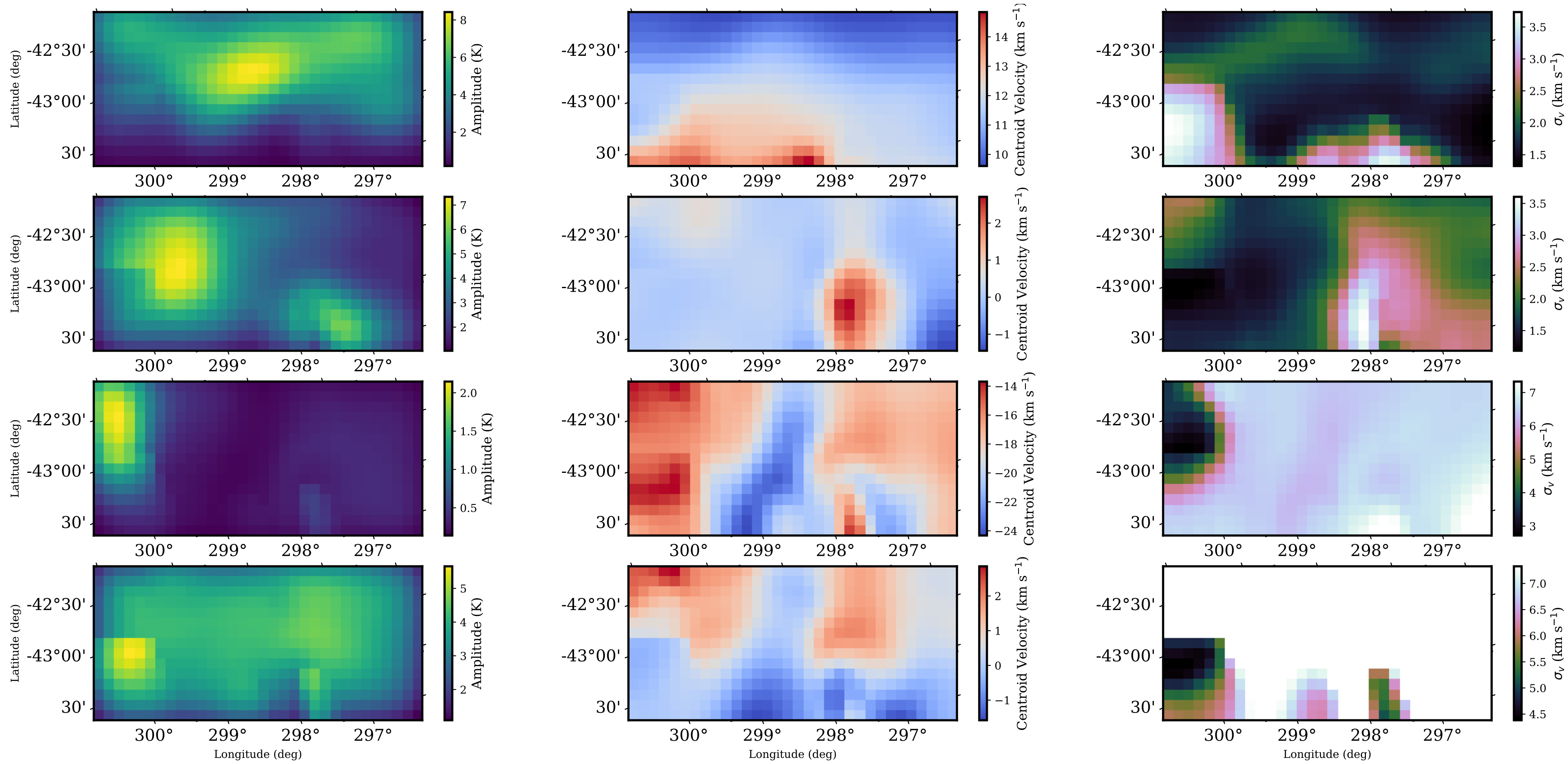

Figure A.13: Collection of fields for the amplitude (left), central velocity (middle) and velocity dispersion (right) of each Gaussian field (G_1, G_2, G_3, and G_4) fitted from the 32 arcminute resolution data discussed in Section 4.5.1.

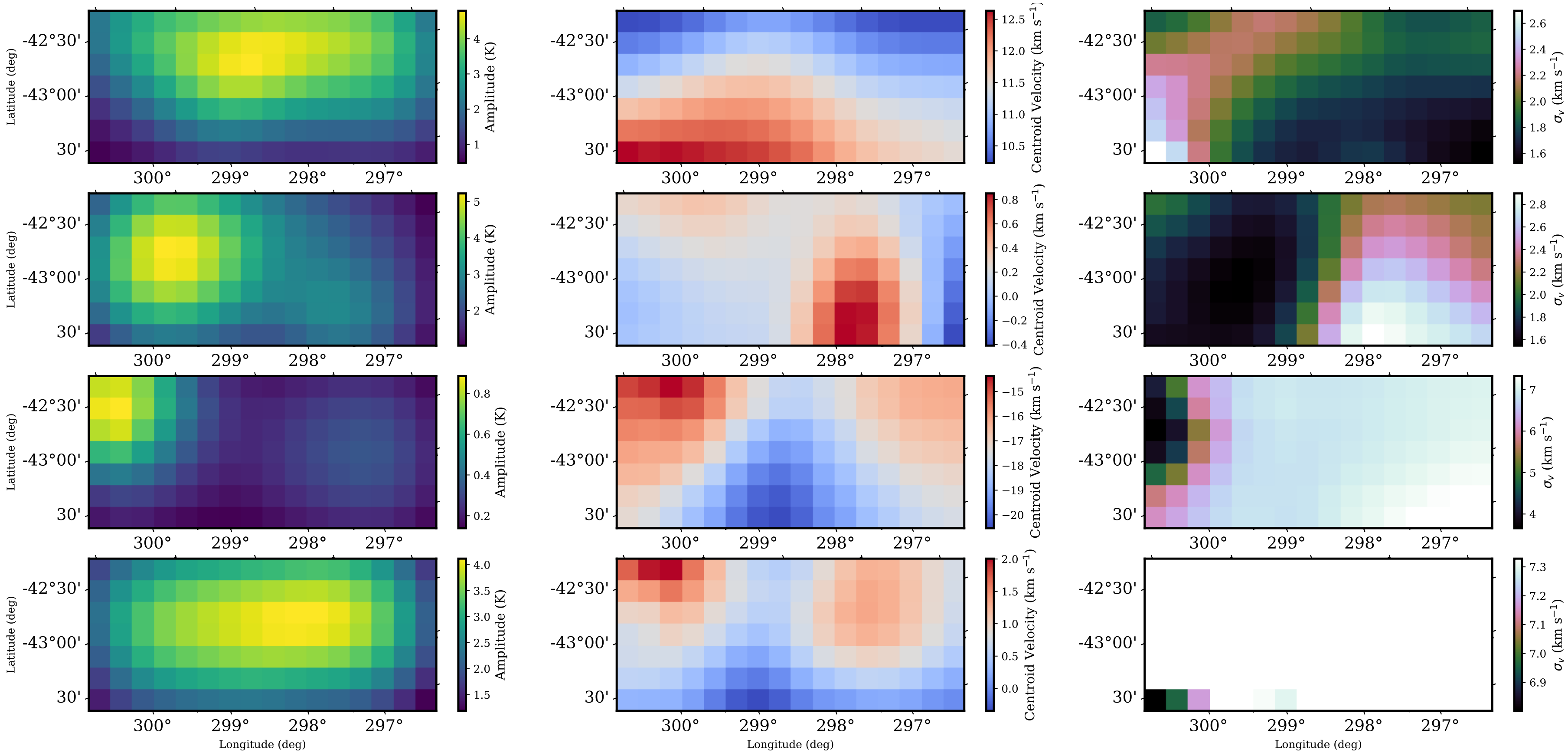

Figure A.14: Collection of fields for the amplitude (left), central velocity (middle) and velocity dispersion (right) of each Gaussian field (G_1, G_2, G_3, and G_4) fitted from the 64 arcminute resolution data discussed in Section 4.5.1.

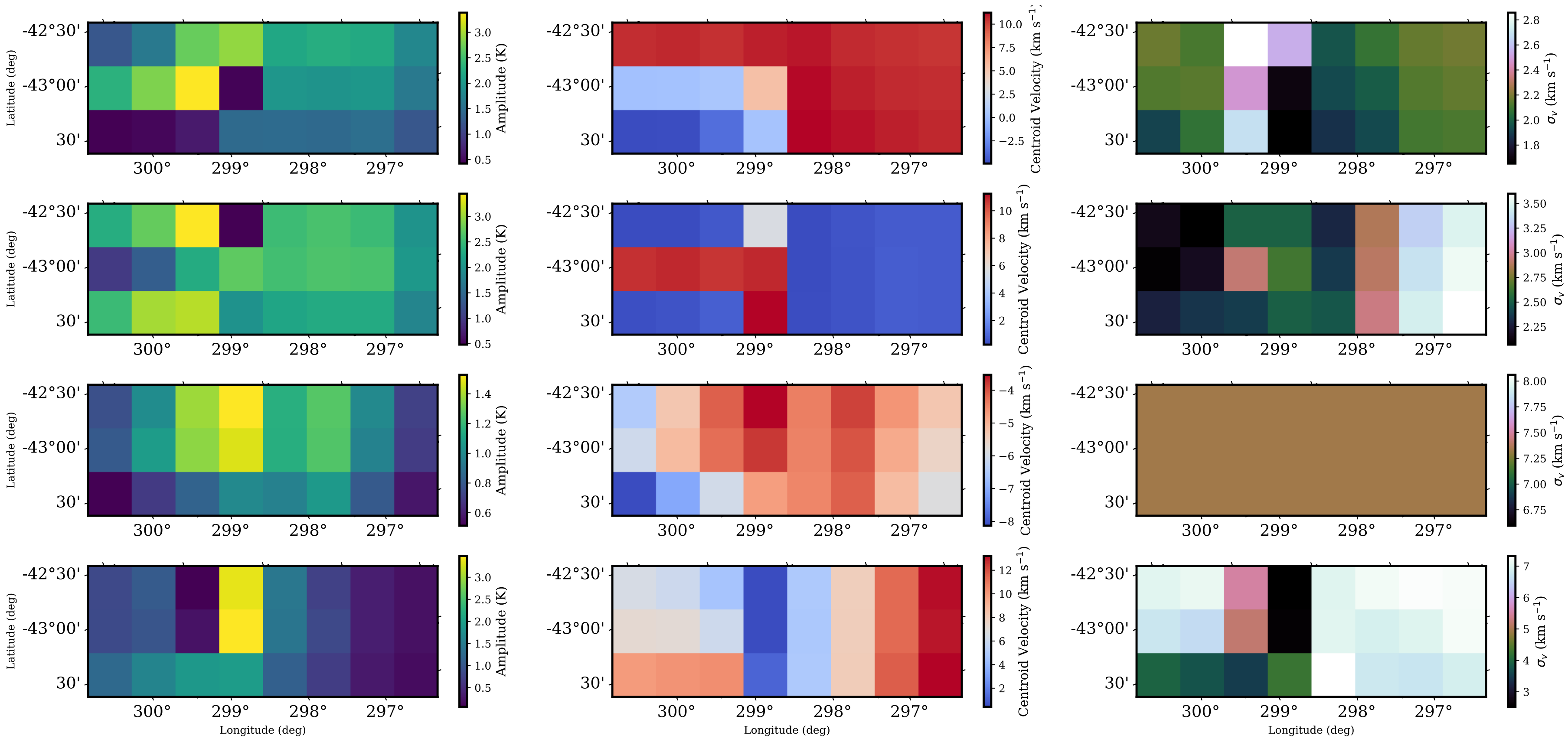

Figure A.15: Collection of fields for the amplitude (left), central velocity (middle) and velocity dispersion (right) of each Gaussian field (G_1, G_2, G_3, and G_4) fitted from the 128 arcminute resolution data discussed in Section 4.5.1.

Bibliography

Astropy Collaboration et al. 2013, A&A, 558, A33 (ADS entry)

Audit, E., & Hennebelle, P. 2005, A&A, 433, 1 (ADS entry)

Banerjee, R., Vázquez-Semadeni, E., Hennebelle, P., & Klessen, R. S. 2009, MNRAS, 398, 1082 (ADS entry)

Begum, A., Stanimirović, S., Goss, W. M., Heiles, C., Pavkovich, A. S., & Hennebelle, P. 2010, ApJ, 725, 1779 (ADS entry)

Belfort, P., & Crovisier, J. 1984, A&A, 136, 368 (ADS entry)

Beresnyak, A., Lazarian, A., & Cho, J. 2005, ApJL, 624, L93 (ADS entry)

Beuther, H., et al. 2016, A&A, 595, A32 (ADS entry)

Bhattacharjee, S., Roy, N., Sharma, P., Seta, A., & Federrath, C. 2024, MNRAS, 527, 8475 (ADS entry)

Bialy, S., & Sternberg, A. 2019, ApJ, 881, 160 (ADS entry)

Blagrave, K., Martin, P. G., Joncas, G., Kothes, R., Stil, J. M., Miville-Deschênes, M. A., Lockman, F. J., & Taylor, A. R. 2017, ApJ, 834, 126 (ADS entry)

Boulanger, F., Abergel, A., Bernard, J. P., Burton, W. B., Desert, F. X., Hartmann, D., Lagache, G., & Puget, J. L. 1996, A&A, 312, 256 (ADS entry)

Braun, R., Walterbos, R. A. M., & Kennicutt, Robert C., J. 1992, Nat, 360, 442 (ADS entry)

Buckland-Willis, F., et al. 2025, A&A, 693, A239 (ADS entry)

Burkhart, B., Stanimirović, S., Lazarian, A., & Kowal, G. 2010, ApJ, 708, 1204 (ADS entry)

Carilli, C. L., Dwarakanath, K. S., & Goss, W. M. 1998, ApJL, 502, L79 (ADS entry)

Chandrasekhar, S. 1961, Hydrodynamic and hydromagnetic stability (Oxford University Press) (ADS entry)

Christiansen, W. N., & Hindman, J. V. 1952, Obs, 72, 149 (ADS entry)

Clark, P. C., Glover, S. C. O., Klessen, R. S., & Bonnell, I. A. 2012, MNRAS, 424, 2599 (ADS entry)

Colman, T., et al. 2022, MNRAS, 514, 3670 (ADS entry)

Condon, J. J., & Ransom, S. M. 2016, Essential Radio Astronomy (Princeton University Press) (ADS entry)

Crovisier, J., & Dickey, J. M. 1983, A&A, 122, 282 (ADS entry)

Crovisier, J., Dickey, J. M., & Kazes, I. 1985, A&A, 146, 223 (ADS entry)

Crovisier, J., Kazes, I., & Aubry, D. 1978, A&AS, 32, 205 (ADS entry)

Dempsey, J., et al. 2022, PASA, 39, e034 (ADS entry)

Deshpande, A. A., Dwarakanath, K. S., & Goss, W. M. 2000, ApJ, 543, 227 (ADS entry)

Dickey, J. M. 1979, ApJ, 233, 558 (ADS entry)

Dickey, J. M., & Lockman, F. J. 1990, ARA&A, 28, 215 (ADS entry)

Dickey, J. M., McClure-Griffiths, N. M., Gaensler, B. M., & Green, A. J. 2003, ApJ, 585, 801 (ADS entry)

Dickey, J. M., McClure-Griffiths, N. M., Stanimirović, S., Gaensler, B. M., & Green, A. J. 2001, ApJ, 561, 264 (ADS entry)

Dickey, J. M., Salpeter, E. E., & Terzian, Y. 1977, ApJL, 211, L77 (ADS entry)

Dickey, J. M., Strasser, S., Gaensler, B. M., Haverkorn, M., Kavars, D., McClure-Griffiths, N. M., Stil, J., & Taylor, A. R. 2009, ApJ, 693, 1250 (ADS entry)

Dickey, J. M., et al. 2013, PASA, 30, e003 (ADS entry)

Draine, B. T. 2011, Physics of the Interstellar and Intergalactic Medium (Princeton University Press) (ADS entry)

Dutta, P., Chengalur, J. N., Roy, N., Goss, W. M., Arjunwadkar, M., Minter, A. H., Brogan, C. L., & Lazio, T. J. W. 2014, MNRAS, 442, 647 (ADS entry)

Dwarakanath, K. S., Carilli, C. L., & Goss, W. M. 2002, ApJ, 567, 940 (ADS entry)

Edenhofer, G., Zucker, C., Frank, P., Saydjari, A. K., Speagle, J. S., Finkbeiner, D., & Enßlin, T. A. 2024, A&A, 685, A82 (ADS entry)

Ekers, R. D., & Rots, A. H. 1979, in Astrophysics and Space Science Library, Vol. 76, IAU Colloquium 49: Image Formation from Coherence Functions in Astronomy, ed. C. van Schooneveld, 61 (ADS entry)

Elmegreen, B. G., Kim, S., & Staveley-Smith, L. 2001, ApJ, 548, 749 (ADS entry)

Elmegreen, B. G., & Scalo, J. 2004, ARA&A, 42, 211 (ADS entry)

Ewen, H. I., & Purcell, E. M. 1951, Natur, 168, 356 (ADS entry)

Fensch, J., Bournaud, F., Brucy, N., Dubois, Y., Hennebelle, P., & Rosdahl, J. 2023, A&A, 672, A193 (ADS entry)

Field, G. B. 1958, PIRE, 46, 240 (ADS entry)

Field, G. B. 1965, ApJ, 142, 531 (Link)

Field, G. B., Goldsmith, D. W., & Habing, H. J. 1969, ApJL, 155, L149 (Link)

Gibson, S. J. 2002, in Astronomical Society of the Pacific Conference Series, Vol. 276, Seeing Through the Dust: The Detection of HI and the Exploration of the ISM in Galaxies, ed. A. R. Taylor, T. L. Landecker, & A. G. Willis, 235 (ADS entry)

Goldreich, P., & Sridhar, S. 1997, ApJ, 485, 680 (ADS entry)

Green, D. A. 1993, MNRAS, 262, 327 (ADS entry)

Greisen, E. W., & Liszt, H. S. 1986, ApJ, 303, 702 (ADS entry)

Gupta, N., et al. 2025, A&A, 698, A120 (ADS entry)

Haud, U. 2000, A&A, 364, 83 (Link)

Haverkorn, M., Brown, J. C., Gaensler, B. M., & McClure-Griffiths, N. M. 2008, ApJ, 680, 362 (ADS entry)

Haverkorn, M., Gaensler, B. M., McClure-Griffiths, N. M., Dickey, J. M., & Green, A. J. 2004, ApJ, 609, 776 (ADS entry)

Heeschen, D. S. 1955, ApJ, 121, 569 (ADS entry)

—. 1981, in Telescopes for the 1980s, Annual Reviews Monograph, ed. G. Burbidge & A. Hewitt, 1–61 (ADS entry)

Heiles, C., & Jenkins, E. B. 1976, A&A, 46, 333 (ADS entry)

Heiles, C., & Troland, T. H. 2003, ApJ, 586, 1067 (Link)

Heiles, C., & Troland, T. H. 2003, ApJS, 145, 329 (ADS entry)

Heitsch, F., Slyz, A. D., Devriendt, J. E. G., Hartmann, L. W., & Burkert, A. 2006, ApJ, 648, 1052 (ADS entry)

Henderson, A. P., Jackson, P. D., & Kerr, F. J. 1982, ApJ, 263, 116 (ADS entry)

Hennebelle, P., & Audit, E. 2007, A&A, 465, 431 (ADS entry)

Hennebelle, P., Banerjee, R., Vázquez-Semadeni, E., Klessen, R. S., & Audit, E. 2008, A&A, 486, L43 (ADS entry)

Hennebelle, P., & Falgarone, E. 2012, A&ARv, 20, 55 (ADS entry)

Hennebelle, P., & Pérault, M. 1999, A&A, 351, 309 (Link)

—. 2000, A&A, 359, 1124 (Link)

HI4PI Collaboration et al. 2016, A&A, 594, A116 (ADS entry)

Hill, A. S., Mac Low, M.-M., Gatto, A., & Ibáñez-Mejía, J. C. 2018, ApJ, 862, 55 (ADS entry)

Hotan, A. W., et al. 2021, PASA, 38, e009 (ADS entry)

Hughes, M. P., Thompson, A. R., & Colvin, R. S. 1971, ApJS, 23, 323 (ADS entry)

Hunter, J. D. 2007, CSE, 9, 90 (ADS entry)

Iroshnikov, P. S. 1963, AZh, 40, 742 (ADS entry)

Jonas, J., & MeerKAT Team. 2016, in MeerKAT Science: On the Pathway to the SKA, 1 (ADS entry)

Kado-Fong, E., Kim, J.-G., Ostriker, E. C., & Kim, C.-G. 2020, ApJ, 897, 143 (ADS entry)

Kalberla, P. M. W., Burton, W. B., Hartmann, D., Arnal, E. M., Bajaja, E., Morras, R., & Pöppel, W. G. L. 2005, A&A, 440, 775 (ADS entry)

Kalberla, P. M. W., & Haud, U. 2015a, A&A, 578, A78 (ADS entry)

—. 2015b, A&A, 578, A78 (ADS entry)

—. 2018, A&A, 619, A58 (ADS entry)

—. 2019, A&A, 627, A112 (ADS entry)

Kalberla, P. M. W., et al. 2010, A&A, 521, A17 (ADS entry)

Kamal Youssef, F. R., & Grenier, I. A. 2024, A&A, 685, A102 (ADS entry)

Kanekar, N., Braun, R., & Roy, N. 2011, ApJL, 737, L33 (ADS entry)

Kanekar, N., Subrahmanyan, R., Chengalur, J. N., & Safouris, V. 2003, MNRAS, 346, L57 (ADS entry)

Kim, C.-G., Choi, S. K., & Flauger, R. 2019, ApJ, 880, 106 (ADS entry)

Kim, C.-G., & Ostriker, E. C. 2017, ApJ, 846, 133 (ADS entry)

Kim, C.-G., Ostriker, E. C., & Kim, W.-T. 2014, ApJ, 786, 64 (ADS entry)

Kim, J., & Ryu, D. 2005, ApJL, 630, L45 (ADS entry)

Klessen, R. S., & Glover, S. C. O. 2016, SAAS, 43, 85 (ADS entry)

Klessen, R. S., & Hennebelle, P. 2010, A&A, 520, A17 (ADS entry)

Knapp, G. R., & Verschuur, G. L. 1972, AJ, 77, 717 (ADS entry)

Kobayashi, M. I. N., Iwasaki, K., Tomida, K., Inoue, T., Omukai, K., & Tokuda, K. 2023, ApJ, 954, 38 (ADS entry)

Koch, E. W., Chiang, I.-D., Utomo, D., Chastenet, J., Leroy, A. K., Rosolowsky, E. W., & Sandstrom, K. M. 2020, MNRAS, 492, 2663 (ADS entry)

Kolmogorov, A. 1941, DoSSR, 30, 301 (ADS entry)

Körtgen, B., Pingel, N., & Killerby-Smith, N. 2021, MNRAS, 505, 1972 (ADS entry)

Kowal, G., & Lazarian, A. 2007, ApJL, 666, L69 (ADS entry)

Koyama, H., & Inutsuka, S.-I. 2000, ApJ, 532, 980 (ADS entry)

Koyama, H., & Inutsuka, S.-i. 2002, ApJL, 564, L97 (ADS entry)

Kraichnan, R. H., & Nagarajan, S. 1967, PhFl, 10, 859 (ADS entry)

Krumholz, M. R., & Burkhart, B. 2016, MNRAS, 458, 1671 (ADS entry)

Krumholz, M. R., Burkhart, B., Forbes, J. C., & Crocker, R. M. 2018, , 477, 2716 (ADS entry)

Krumholz, M. R., Matzner, C. D., & McKee, C. F. 2006, ApJ, 653, 361 (ADS entry)

Lazareff, B. 1975, A&A, 42, 25 (ADS entry)

Lazarian, A., & Pogosyan, D. 2000, ApJ, 537, 720 (ADS entry)

—. 2008, ApJ, 686, 350 (ADS entry)

Lee, B., et al. 2025, ApJ, 994, 80 (ADS entry)

Lee, M.-Y., Stanimirović, S., Murray, C. E., Heiles, C., & Miller, J. 2015, ApJ, 809, 56 (ADS entry)

Lenz, D., Hensley, B. S., & Doré, O. 2017, ApJ, 846, 38 (ADS entry)

Li, D., Nan, R., & Pan, Z. 2013, in IAU Symposium, Vol. 291, Neutron Stars and Pulsars: Challenges and Opportunities after 80 years, ed. J. van Leeuwen, 325–330 (ADS entry)

Lindner, R. R., et al. 2015, AJ, 149, 138 (ADS entry)

Liszt, H. 2001, A&A, 371, 698 (ADS entry)

Livingston, J. D., McClure-Griffiths, N. M., Gaensler, B. M., Seta, A., & Alger, M. J. 2021, MNRAS, 502, 3814 (ADS entry)

Low, F. J., et al. 1984, ApJL, 278, L19 (ADS entry)

Lynn, C., et al. 2025, MNRAS, 536, 3538 (ADS entry)

Marchal, A., Martin, P. G., & Gong, M. 2021, ApJ, 921, 11 (ADS entry)

Marchal, A., & Miville-Deschênes, M.-A. 2021, ApJ, 908, 186 (ADS entry)

Marchal, A., Miville-Deschênes, M.-A., Orieux, F., Gac, N., Soussen, C., Lesot, M.-J., d'Allonnes, A. R., & Salomé, Q. 2019, A&A, 626, A101 (ADS entry)

Martin, P. G., Blagrave, K. P. M., Lockman, F. J., Pinheiro Gonçalves, D., Boothroyd, A. I., Joncas, G., Miville-Deschênes, M. A., & Stephan, G. 2015, ApJ, 809, 153 (ADS entry)

McClure-Griffiths, N. M., Dickey, J. M., Gaensler, B. M., & Green, A. J. 2003, ApJ, 594, 833 (ADS entry)

McClure-Griffiths, N. M., Dickey, J. M., Gaensler, B. M., Green, A. J., Haverkorn, M., & Strasser, S. 2005, ApJS, 158, 178 (ADS entry)

McClure-Griffiths, N. M., Stanimirović, S., & Rybarczyk, D. R. 2023, ARA&A, 61, 19 (ADS entry)

McClure-Griffiths, N. M., et al. 2009, ApJS, 181, 398 (ADS entry)

McKee, C. F., & Ostriker, E. C. 2007, ARA&A, 45, 565 (ADS entry)

McKee, C. F., & Ostriker, J. P. 1977, ApJ, 218, 148 (ADS entry)

Mebold, U., Düsterberg, C., Dickey, J. M., Staveley-Smith, L., & Kalberla, P. 1997, ApJL, 490, L65 (ADS entry)

Mebold, U., Winnberg, A., Kalberla, P. M. W., & Goss, W. M. 1982, A&A, 115, 223 (ADS entry)

Mittal, A. K., Babler, B. L., Stanimirović, S., & Pingel, N. 2023, ApJ, 958, 192 (ADS entry)

Miville-Deschênes, M.-A., Levrier, F., & Falgarone, E. 2003, ApJ, 593, 831 (ADS entry)

Miville-Deschênes, M.-A., et al. 2017, A&A, 599, A109 (ADS entry)

Mohan, R., Dwarakanath, K. S., & Srinivasan, G. 2004, Journal of Astrophysics and Astronomy, 25, 143 (ADS entry)

Muller, C. A. 1957, ApJ, 125, 830 (ADS entry)

Muller, C. A., & Oort, J. H. 1951, Natur, 168, 357 (ADS entry)

Murray, C. E., Peek, J. E. G., & Kim, C.-G. 2020, ApJ, 899, 15 (ADS entry)

Murray, C. E., Stanimirović, S., Goss, W. M., Heiles, C., Dickey, J. M., Babler, B., & Kim, C.-G. 2018, ApJS, 238, 14 (ADS entry)

Murray, C. E., Stanimirović, S., Heiles, C., Dickey, J. M., McClure-Griffiths, N. M., Lee, M.-Y., M. Goss, W., & Killerby-Smith, N. 2021, ApJS, 256, 37 (ADS entry)

Murray, C. E., Stanimirović, S., Kim, C.-G., Ostriker, E. C., Lindner, R. R., Heiles, C., Dickey, J. M., & Babler, B. 2017, ApJ, 837, 55 (ADS entry)

Murray, C. E., et al. 2014, ApJL, 781, L41 (ADS entry)

—. 2015, ApJ, 804, 89 (ADS entry)

Nan, R., et al. 2011, IJMPD, 20, 989 (ADS entry)

Nelson, G. J. 1992, JEEEA, 12, 113 (ADS entry)

Nguyen, H., Dawson, J. R., Lee, M.-Y., Murray, C. E., Stanimirović, S., Heiles, C., Miville-Deschênes, M. A., & Petzler, A. 2019, ApJ, 880, 141 (ADS entry)

Nguyen, H., Tang, H., Alger, M., Marchal, A., Muller, E. G. M., Ong, C. S., & McClure-Griffiths, N. M. 2025a, MNRAS, 536, 962 (ADS entry)

Nguyen, H., et al. 2024, MNRAS, 534, 3478 (ADS entry)

—. 2025b, MNRAS, 543, 3474 (ADS entry)

Nidever, D. L., Majewski, S. R., & Butler Burton, W. 2008, ApJ, 679, 432 (ADS entry)

O'Neill, T. J., Zucker, C., Goodman, A. A., & Edenhofer, G. 2024, ApJ, 973, 136 (ADS entry)

Ostriker, E. C., McKee, C. F., & Leroy, A. K. 2010, ApJ, 721, 975 (ADS entry)

Padoan, P., Pan, L., Haugbølle, T., & Nordlund, Å. 2016, ApJ, 822, 11 (ADS entry)

Patra, N. N., Kanekar, N., Chengalur, J. N., & Roy, N. 2018, MNRAS, 479, L7 (ADS entry)

Patra, N. N., & Roy, N. 2024, MNRAS, 529, 4037 (ADS entry)

Peek, J. E. G., et al. 2011, ApJS, 194, 20 (ADS entry)

—. 2018, ApJS, 234, 2 (ADS entry)

Perley, R., et al. 2009, IEEEP, 97, 1448 (ADS entry)

Pingel, N. M., Lee, M.-Y., Burkhart, B., & Stanimirović, S. 2018, ApJ, 856, 136 (ADS entry)

Pingel, N. M., et al. 2013, ApJ, 779, 36 (ADS entry)

—. 2022, PASA, 39, e005 (ADS entry)

—. 2024, ApJ, 974, 93 (ADS entry)

Plume, R., et al. 2000, ApJL, 539, L133 (ADS entry)

Porter, D. H., Pouquet, A., & Woodward, P. R. 1994, PhFl, 6, 2133 (ADS entry)

Radhakrishnan, V., & Goss, W. M. 1972, ApJS, 24, 161 (ADS entry)

Riener, M., Kainulainen, J., Henshaw, J. D., Orkisz, J. H., Murray, C. E., & Beuther, H. 2019, A&A, 628, A78 (ADS entry)

Roberts, M. S. 1975, in Galaxies and the Universe, ed. A. Sandage, M. Sandage, & J. Kristian (University of Chicago Press), 309 (ADS entry)

Roy, N., Bharadwaj, S., Dutta, P., & Chengalur, J. N. 2009, MNRAS, 393, L26 (ADS entry)

Roy, N., Chengalur, J. N., Dutta, P., & Bharadwaj, S. 2010, MNRAS, 404, L45 (ADS entry)

Roy, N., Kanekar, N., Braun, R., & Chengalur, J. N. 2013a, MNRAS, 436, 2352 (Link)

Roy, N., Kanekar, N., & Chengalur, J. N. 2013b, MNRAS, 436, 2366 (Link)

Roy, N., Minter, A. H., Goss, W. M., Brogan, C. L., & Lazio, T. J. W. 2012, ApJ, 749, 144 (ADS entry)

Rybarczyk, D. R., Stanimirović, S., Zweibel, E. G., Murray, C. E., Dickey, J. M., Babler, B., & Heiles, C. 2020, ApJ, 893, 152 (ADS entry)

Sault, R. J. 1994, A&AS, 107, 55 (ADS entry)

Saury, E., Miville-Deschênes, M.-A., Hennebelle, P., Audit, E., & Schmidt, W. 2014, Astronomy & Astrophysics, 567, A16 (Link)

Scalo, J. M. 1987, in Interstellar Processes, ed. D. J. Hollenbach & H. A. Thronson, Jr., Vol. 134, 349 (ADS entry)

Schulreich, M. M., & Breitschwerdt, D. 2022, MNRAS, 509, 716 (ADS entry)

Seon, K.-i., & Kim, C.-G. 2020, ApJS, 250, 9 (ADS entry)

Seta, A., & Federrath, C. 2024, MNRAS, 533, 1875 (ADS entry)

Seta, A., Federrath, C., Livingston, J. D., & McClure-Griffiths, N. M. 2023, MNRAS, 518, 919 (ADS entry)

Shklovsky, I. S. 1982, Monochromatic Radio Emission from the Galaxy and the Possibility of its Observation (Dordrecht: Springer Netherlands), 318–324 (Link)

Stanimirović, S., Murray, C. E., Lee, M.-Y., Heiles, C., & Miller, J. 2014, ApJ, 793, 132 (ADS entry)

Stanimirovic, S., Staveley-Smith, L., Dickey, J. M., Sault, R. J., & Snowden, S. L. 1999, MNRAS, 302, 417 (ADS entry)

Stil, J. M., Taylor, A. R., & Sunstrum, C. 2011, ApJ, 726, 4 (ADS entry)

Stil, J. M., et al. 2006, AJ, 132, 1158 (ADS entry)

Stone, J. M., & Gardiner, T. 2007, ApJ, 671, 1726 (ADS entry)

Stutzki, J., Bensch, F., Heithausen, A., Ossenkopf, V., & Zielinsky, M. 1998, A&A, 336, 697 (ADS entry)

Szotkowski, S., et al. 2019, ApJ, 887, 111 (ADS entry)

Taank, M., Marchal, A., Martin, P. G., & Vujeva, L. 2022, ApJ, 937, 81 (ADS entry)

Taylor, A. R., et al. 2003, AJ, 125, 3145 (ADS entry)

Tielens, A. G. G. M. 2005, The Physics and Chemistry of the Interstellar Medium (Cambridge University Press) (ADS entry)

Treister, E., Schawinski, K., Volonteri, M., Natarajan, P., & Gawiser, E. 2011, Natur, 474, 356 (ADS entry)

van de Hulst, H. C. 1945, NTvN, 11, 210 (ADS entry)

van der Walt, S., Colbert, S. C., & Varoquaux, G. 2011, CSE, 13, 22 (ADS entry)

Vazquez-Semadeni, E. 2012, arXiv, arXiv:1202.4498 (ADS entry)

Vázquez-Semadeni, E., Ryu, D., Passot, T., González, R. F., & Gazol, A. 2006, ApJ, 643, 245 (ADS entry)

Virtanen, P., et al. 2020, NatMe, 17, 261 (ADS entry)

Wall, J. V., & Jenkins, C. R. 2003, Cambridge Observing Handbooks for Research Astronomers, Vol. 3, Practical Statistics for Astronomers (Cambridge Univ. Press, Cambridge, UK) (ADS entry)

Wang, Y., et al. 2020, A&A, 634, A139 (ADS entry)

Wiese, W. L., & Fuhr, J. R. 2009, JPCRD, 38, 565 (ADS entry)

Winkel, B., Kerp, J., Kalberla, P. M. W., & Ben Bekhti, N. 2010, in Astronomical Society of the Pacific Conference Series, Vol. 438, The Dynamic Interstellar Medium: A Celebration of the Canadian Galactic Plane Survey, ed. R. Kothes, T. L. Landecker, & A. G. Willis, 381 (ADS entry)

Wolfire, M. G., Hollenbach, D., McKee, C. F., Tielens, A. G. G. M., & Bakes, E. L. O. 1995, ApJ, 443, 152 (ADS entry)

Wolfire, M. G., McKee, C. F., Hollenbach, D., & Tielens, A. G. G. M. 2003, ApJ, 587, 278 (ADS entry)

Yuen, K. H., Ho, K. W., & Lazarian, A. 2021, ApJ, 910, 161 (ADS entry)

Zamora-Avilés, M., Vázquez-Semadeni, E., & Colín, P. 2012, ApJ, 751, 77 (ADS entry)

Zhang, K., et al. 2021, MNRAS, 500, 1741 (ADS entry)

Zhang, X., Green, G. M., & Rix, H.-W. 2023, MNRAS, 524, 1855 (ADS entry)